PHYSICS • CHEMISTRY • MATERIALS SCIENCE

NANOMATERIALS

Fundamentals of Nanomaterials

Quantum Phenomena • Synthesis • Characterization • Applications

Dr. Irfan Toqeer

PhD Physics, MSc Computer Science

To all students and researchers

who dare to explore

the fascinating world

at the nanoscale

Preface

The field of nanoscience and nanotechnology has emerged as one of the most exciting and rapidly developing areas of modern science. This textbook, *Nanomaterials: Part I – Fundamentals of Nanomaterials*, is designed to provide a comprehensive introduction to the fundamental concepts, synthesis methods, characterization techniques, and applications of nanomaterials.

This book is structured to serve both undergraduate and graduate students in physics, chemistry, materials science, and engineering disciplines. Each chapter integrates theoretical foundations with practical examples, mathematical derivations, and hands-on analyses to facilitate deep understanding.

Key Features:

- Comprehensive coverage from basic concepts to advanced applications
- Mathematical rigor with detailed derivations
- Extensive examples and case studies
- Integration of characterization techniques
- Focus on both fundamental physics and practical applications
- Special emphasis on applications relevant to developing countries

The chapters are organized to build knowledge progressively, starting from fundamental quantum phenomena and progressing through synthesis, characterization, and finally to diverse applications in energy, environment, biomedicine, and electronics.

I hope this textbook will inspire students to pursue research in nanoscience and provide researchers with a valuable reference for their work.

Dr. Irfan Toqeer
Faisalabad, Pakistan

Acknowledgments

I would like to express my sincere gratitude to all those who have contributed to the completion of this textbook.

First and foremost, I am grateful to Riphah International University Faisalabad for providing the academic environment and resources necessary for this work.

I thank my colleagues in the Department of Physics for their valuable discussions and feedback throughout the writing process. Special thanks to my students whose questions and curiosity have shaped the pedagogical approach of this book.

I acknowledge the numerous researchers whose work is cited throughout this textbook. The advancement of nanoscience is truly a collaborative global effort.

Finally, I am deeply grateful to my family for their patience, support, and encouragement during the many hours devoted to this project.

Dr. Irfan Toqeer

Contents

Preface iii

Acknowledgments v

List of Figures xv

List of Tables xvii

List of Abbreviations xx

Symbols and Notation xxiii

Contents

Part I: Fundamentals of Nanomaterials

Chapter 1: Introduction to Nanoscience and Nanotechnology

1.1 Introduction 1
1.2 Historical Evolution of Nanoscience 1
1.2.1 Ancient and Medieval Nanotechnology 2
1.3 Scale of Nanometer: Size Comparison and Quantum Effects 3
1.3.1 Understanding the Nanoscale 3
1.3.2 Surface-to-Volume Ratio Effects 4
1.3.3 Quantum Confinement Effects 5
1.3.4 Other Size-Dependent Properties 8
1.4 Top-Down vs. Bottom-Up Approaches 8
1.4.1 Top-Down Approach 9
1.4.2 Bottom-Up Approach 10
1.4.3 Hybrid Approaches 12
1.5 Classification of Nanomaterials 12
1.5.1 Dimensionality-Based Classification 13
1.5.2 Comprehensive Classification Table 17
1.6 Examples of Nanomaterials 18
1.6.1 Naturally Occurring Nanomaterials 18
1.6.2 Engineered Nanomaterials 19
1.7 Importance and Scope in Pakistan's Context 21
1.8 Summary 25
Exercises 26
Bibliography 29

Chapter 2: Quantum Phenomena in Nanomaterials

2.1 Introduction 31
2.2 Quantum Confinement Effect 31
2.2.1 Physical Origin of Quantum Confinement 31
2.2.2 Particle in a Box: Foundation 33
2.2.3 Size-Dependent Band Gap 36
2.3 Density of States in Lower Dimensions 38
2.3.1 General Formulation 38
2.3.2 Three-Dimensional (3D) Bulk 38
2.3.3 Two-Dimensional (2D) Quantum Well 39
2.3.4 One-Dimensional (1D) Nanowire 40
2.3.5 Zero-Dimensional (0D) Quantum Dot 41
2.3.6 Physical Consequences 42
2.4 Surface-to-Volume Ratio 43
2.4.1 Quantitative Analysis 43
2.4.2 Impact on Thermodynamic Properties 43
2.4.3 Impact on Chemical Properties 45
2.4.4 Impact on Optical Properties 45
2.5 Quantum Tunneling in Nanostructures 45
2.5.1 Fundamentals of Quantum Tunneling 45
2.5.2 Scanning Tunneling Microscopy 47
2.5.3 Resonant Tunneling 47
2.6 Coulomb Blockade and Single-Electron Transistor 47
2.7 Quantized Conductance 49
2.8 Quantum Wells, Wires, and Dots 50
2.9 Simulation Example 52
2.10 Summary 58
Exercises 59
Bibliography 63

Chapter 3: Structural, Electrical, Optical, and Magnetic Properties

3.1 Introduction 65
3.2 Crystal Structure and Defects 65
3.2.1 Structural Considerations at Nanoscale 66
3.2.2 Defects in Nanomaterials 67
3.3 Electronic Structure Modifications 68
3.3.1 Band Structure Evolution with Size 68
3.3.2 Density of States Modifications 69
3.3.3 Work Function Modifications 70
3.4 Optical Absorption and Photoluminescence 70
3.4.1 Optical Absorption in Nanomaterials 70
3.4.2 Photoluminescence 71
3.5 Magnetic Properties 72
3.5.1 Magnetic Behavior at Nanoscale 72
3.5.2 Superparamagnetism 73
3.5.3 Exchange Bias 74
3.6 Mechanical Properties at Nanoscale 74
3.7 Practical Focus: Band Gap Tuning in ZnO 75
3.8 Summary 77
Exercises 77
Bibliography 81

Chapter 4: Physical and Chemical Synthesis Routes

4.1 Introduction 83
4.2 Top-Down Approaches 84
4.2.1 Mechanical Milling 84
4.2.2 Lithographic Techniques 86
4.2.3 Laser Ablation 88
4.3 Bottom-Up Approaches 90
4.3.1 Sol-Gel Process 90
4.3.2 Chemical Vapor Deposition 92
4.3.3 Hydrothermal and Solvothermal Synthesis 94
4.3.4 Coprecipitation 96
4.3.5 Green Synthesis 98
4.4 Comparison of Synthesis Routes 100
4.5 Laboratory Note: Coprecipitation 101
4.6 Summary 104
Exercises 104
Bibliography 109

Chapter 5: Functionalization and Surface Modification

5.1 Introduction 111
5.2 Importance of Surface Chemistry 112
5.2.1 Surface Energy and Surface Tension 112
5.2.2 Colloidal Stability: DLVO Theory 114
5.2.3 Steric Stabilization 115
5.3 Functionalization Techniques 116
5.3.1 Chemical Grafting 116
5.3.2 Plasma Treatment 118
5.3.3 Polymer Coating 119
5.4 Surfactants and Capping Agents 121
5.4.1 Fundamentals of Surfactants 121
5.4.2 Capping Agent Mechanisms 122
5.5 Role in Stability and Applications 124
5.6 Example: Surface Modification of Graphene Oxide 125
5.7 Summary 128
Exercises 129
Bibliography 133

Chapter 6: Thin Films and Nanocomposites

6.1 Introduction 135
6.2 Thin Film Deposition Techniques 136
6.2.1 Spin Coating 136
6.2.2 Sputtering 138
6.2.3 Pulsed Laser Deposition 140
6.2.4 Atomic Layer Deposition 141
6.3 Nanocomposites 143
6.3.1 Polymer-Based Nanocomposites 143
6.3.2 Ceramic Nanocomposites 145
6.3.3 Metal Oxide-Graphene Hybrids 146
6.4 Structure-Property Correlation 148
6.5 Experiment: GO-MgO Nanocomposites 151
6.6 Summary 152
Exercises 152
Bibliography 157

Part II: Characterization of Nanomaterials

Chapter 7: Structural Characterization Techniques

7.1 Introduction 163
7.2 X-ray Diffraction (XRD) 164
7.2.1 Fundamental Principles 164
7.2.2 Bragg's Law 165
7.2.3 XRD Instrumentation 167
7.2.4 Debye-Scherrer Equation 167
7.2.5 Rietveld Refinement 169
7.3 Raman Spectroscopy 172
7.3.1 Fundamental Principles 172
7.3.2 Raman Instrumentation 173
7.3.3 Phase Identification 174
7.4 Data Analysis: XRD Pattern of ZnO 176
7.5 Summary 177
Exercises 177
Bibliography 181

Chapter 8: Morphological and Elemental Characterization

8.1 Introduction 183
8.2 Scanning Electron Microscopy (SEM) 184
8.2.1 Fundamental Principles 184
8.2.2 SEM Instrumentation 186
8.2.3 Imaging Modes and Contrast 186
8.3 Transmission Electron Microscopy (TEM) 187
8.3.1 Fundamental Principles 187
8.3.2 TEM Instrumentation 188
8.3.3 Imaging Modes 188
8.3.4 Selected Area Diffraction 189
8.4 Atomic Force Microscopy (AFM) 190
8.4.1 Fundamental Principles 190
8.4.2 Operating Modes 191
8.4.3 Resolution and Artifacts 191
8.5 Energy Dispersive X-ray (EDX) Analysis 192
8.5.1 Fundamental Principles 192
8.5.2 Quantitative Analysis 193
8.5.3 Spatial Resolution 193
8.6 Hands-On: Interpreting SEM/EDX Images 195
8.7 Summary 196
Exercises 196
Bibliography 201

Chapter 9: Optical and Magnetic Characterization

9.1 Introduction 203
9.2 UV-Vis Spectroscopy and Tauc Plot 204
9.2.1 Fundamental Principles 204
9.2.2 Band Gap Determination 205
9.2.3 Tauc Plot Analysis 206
9.2.4 Size-Dependent Band Gap 207
9.3 Photoluminescence Spectroscopy 207
9.3.1 Fundamental Principles 207
9.3.2 PL Spectral Features 208
9.3.3 Temperature-Dependent PL 209
9.4 Vibrating Sample Magnetometer (VSM) 209
9.4.1 Fundamental Principles 210
9.4.2 Magnetic Properties Measured 210
9.4.3 Types of Magnetic Behavior 211
9.5 FTIR Spectroscopy for Bonding Analysis 212
9.5.1 Fundamental Principles 212
9.5.2 FTIR Instrumentation 213
9.5.3 Spectral Analysis 214
9.6 Case Study: Magnetic Analysis of Ferrite 215
9.7 Summary 216
Exercises 216
Bibliography 221

Part III: Applications of Nanomaterials

Chapter 10: Energy and Environmental Applications

10.1 Introduction 227
10.2 Photocatalysis and Wastewater Remediation 227
10.2.1 Fundamental Principles 227
10.2.2 Kinetics of Photocatalytic Degradation 228
10.2.3 Quantum Efficiency 229
10.2.4 Nanomaterial Photocatalysts 229
10.2.5 Enhancement Strategies 229
10.2.6 Example: Ferrite Nanocomposites 231
10.3 Solar Cells and Supercapacitors 232
10.3.1 Nanomaterials in Photovoltaics 232
10.3.2 Supercapacitors 233
10.4 Hydrogen Production and Storage 234
10.4.1 Photocatalytic Water Splitting 234
10.4.2 Hydrogen Storage in Nanomaterials 235
10.5 Thermal and Electrical Conductivity 236
10.5.1 Thermal Conductivity 236
10.5.2 Thermoelectric Applications 236
10.6 Chapter Summary 237
References 237

Chapter 11: Biomedical and Pharmaceutical Applications

11.1 Introduction 239
11.2 Drug Delivery and Targeted Therapy 239
11.2.1 Fundamentals of Nanoparticle Drug Delivery 239
11.2.2 Drug Release Kinetics 240
11.2.3 Types of Nanocarriers 242
11.2.4 Active Targeting Strategies 242
11.3 Antibacterial and Antifungal Nanoparticles 243
11.3.1 Mechanisms of Antimicrobial Action 243
11.3.2 Quantifying Antibacterial Activity 243
11.3.3 Example: Ag-Doped ZnO 245
11.4 Biosensors and Bioimaging 246
11.4.1 Nanomaterial-Based Biosensors 246
11.4.2 Types of Biosensors 247
11.4.3 Bioimaging with Nanomaterials 247
11.5 Toxicological Aspects and Safety Regulations 248
11.5.1 Nanotoxicology: Fundamental Concepts 248
11.5.2 Toxicity Assessment Methods 249
11.5.3 Biodistribution and Clearance 249
11.5.4 Regulatory Framework 250
11.6 Chapter Summary 250
References 251

Chapter 12: Electronic and Photonic Applications

12.1 Introduction 253
12.2 Nanoelectronics and Logic Devices 253
12.2.1 Scaling and Quantum Effects 253
12.2.2 Carbon Nanotube FETs 254
12.2.3 Graphene Transistors 255
12.2.4 Quantum Dot Cellular Automata 256
12.3 Graphene-Based Photonic Structures 257
12.3.1 Optical Properties of Graphene 257
12.3.2 Graphene Photodetectors 257
12.3.3 Graphene Modulators 258
12.4 Terahertz Metamaterials and Plasmonics 258
12.4.1 Terahertz Gap and Applications 258
12.4.2 Split-Ring Resonators 258
12.4.3 Effective Medium Parameters 259
12.4.4 Negative Index Materials 259
12.4.5 Plasmonic Enhancement 260
12.5 Quantum Dots in Optoelectronics 260
12.5.1 Quantum Confinement and Emission 260
12.5.2 Optical Properties 260
12.5.3 QD Light-Emitting Diodes 261
12.5.4 QD Solar Cells 262
12.6 Advanced Topic: Graphene-Chiral Metamaterials 263
12.6.1 Chirality and Circular Dichroism 263
12.6.2 Graphene-Enhanced Chiral Metamaterials 263
12.6.3 Fabrication Considerations 265
12.7 Summary 266
References 266

List of Figures

Chapter 1

1.1 Timeline of major milestones in nanoscience 3

1.2 Logarithmic scale comparison of nanoscale regime 3

1.3 Size-dependent band gap energy for CdSe quantum dots 7

1.4 Schematic comparison of top-down and bottom-up approaches 9

1.5 Classification based on dimensionality 13

Chapter 2

2.1 Energy levels and wavefunctions for particle in 1D box 35

2.2 Size-dependent band gap of CdSe quantum dots 38

2.3 Density of states for different dimensional confinement 42

2.4 DLVO potential energy diagram 115

2.5 Type-II heterojunction band alignment 230

Chapter 3

3.1 Schematic of photocatalytic mechanism 228

3.2 Type-II heterojunction for charge separation 230

3.3 I-V characteristics of solar cell 232

3.4 Energy diagram for photocatalytic water splitting 235

Chapter 7

7.1 Geometry for derivation of Bragg's law 166

7.2 Schematic of X-ray diffractometer 167

7.3 Energy level diagram for Raman scattering 172

7.4 Simulated XRD pattern of ZnO nanoparticles 176

Chapter 8

8.1 Electron-specimen interaction volume in SEM 184

8.2 Schematic diagram of SEM instrumentation 186

8.3 Schematic of TEM column 188

8.4 Tip-sample force vs. distance in AFM 190

8.5 Characteristic X-ray generation mechanism 192

8.6 Simulated SEM image of ZnO nanoparticles 195

Chapter 10

10.1 Photocatalytic mechanism in semiconductor nanoparticles 228

10.2 Type-II heterojunction showing charge transfer 230

10.3 Current-voltage characteristics of solar cell 232

10.4 Energy diagram for water splitting 235

Chapter 11

11.1 Drug release profiles following different kinetic models 241

11.2 Multifaceted antibacterial mechanisms 243

Chapter 12

12.1 Transfer characteristics comparing FET types 256

12.2 Schematic of split-ring resonator 259

12.3 Size-dependent emission of quantum dots 261

List of Tables

Chapter 1

1.1 Comparative sizes of various objects and entities 3

1.2 Percentage of surface atoms vs. particle size 5

1.3 Exciton Bohr radius for common semiconductors 6

1.4 Top-down approach: advantages and limitations 10

1.5 Bottom-up approach: advantages and limitations 12

1.6 Comprehensive classification of nanomaterials 17

1.7 Economic impact of nanotechnology in Pakistan 24

Chapter 2

2.1 Exciton Bohr radius and effective masses 33

2.2 Summary of density of states in different dimensions 42

2.3 Grain boundary volume fraction vs. grain size 44

2.4 Comparison of quantum wells, wires, and dots 52

Chapter 4

4.1 Comparison of different ball mill types 85

4.2 Mechanical milling: advantages and limitations 85

4.3 Comparison of lithographic techniques 88

4.4 PLD process parameters 91

4.5 Sol-gel approach: advantages and limitations 92

4.6 Effect of hydrothermal parameters on particle size 96

4.7 Comparison of green synthesis methods 100

4.8 Comprehensive comparison of major synthesis methods 100

4.9 Synthesis method selection guide by application 100

Chapter 5

5.1 Surface energies of common nanomaterials 113

5.2 Plasma gases and their surface modifications 118

5.3 Polymers used for nanomaterial coating 120
5.4 CMC values of common surfactants 122
5.5 Characterization techniques for GO functionalization 128

Chapter 6

6.1 Key parameters affecting spin coating 138
6.2 Comparison of sputtering techniques 139
6.3 PLD process parameters 141
6.4 Comparison of thin film deposition techniques 143
6.5 Polymer nanocomposite classification 144

Chapter 7

7.1 Comparison of structural characterization techniques 163
7.2 Quality indicators for Rietveld refinement 171
7.3 Raman modes of ZnO (wurtzite) 174
7.4 Peak positions: Experimental vs. Standard 176

Chapter 8

8.1 Comparison of morphological characterization techniques 184
8.2 Backscatter coefficient for selected elements 187
8.3 AFM operating modes 191
8.4 Characteristic X-ray energies for selected elements 193

Chapter 9

9.1 Comparison of optical and magnetic techniques 203
9.2 Nanomaterial-based biosensing platforms 247
9.3 Regulatory guidelines for nanomedicine 250

Chapter 10

10.1 Properties of photocatalytic nanomaterials 229
10.2 Specific capacitance of nanomaterial electrodes 234
10.3 Hydrogen storage capacities of nanomaterials 236

Chapter 11

11.1 Common nanoparticle drug delivery systems 242
11.2 Classification of magnetic materials 211
11.3 Regulatory guidelines for nanomedicine 250

Chapter 12

12.1 Nanomaterial electrodes for supercapacitors 234
12.2 Hydrogen storage in nanomaterials 236

List of Abbreviations

0D, 1D, 2D, 3D	Zero-, One-, Two-, Three-Dimensional
AFM	Atomic Force Microscopy
ALD	Atomic Layer Deposition
APTES	3-Aminopropyltriethoxysilane
AUC	Area Under the Curve
BPR	Ball-to-Powder Ratio
BSE	Backscattered Electrons
CB	Conduction Band
CCD	Charge-Coupled Device
CMC	Critical Micelle Concentration
CNT	Carbon Nanotube
CNTFET	Carbon Nanotube Field-Effect Transistor
CVD	Chemical Vapor Deposition
DLS	Dynamic Light Scattering
DLVO	Derjaguin-Landau-Verwey-Overbeek (Theory)
DNA	Deoxyribonucleic Acid
DOS	Density of States
E-beam	Electron Beam
EDC	1-Ethyl-3-(3-dimethylaminopropyl)carbodiimide
EDLC	Electric Double-Layer Capacitor
EDX/EDS	Energy Dispersive X-ray Spectroscopy
EMA	European Medicines Agency
EMI	Electromagnetic Interference
EPR	Enhanced Permeability and Retention
EQE	External Quantum Efficiency
FDA	Food and Drug Administration (USA)
FET	Field-Effect Transistor
FIB	Focused Ion Beam
FTIR	Fourier Transform Infrared Spectroscopy
FWHM	Full Width at Half Maximum
GNR	Graphene Nanoribbon
GO	Graphene Oxide
GPC	Growth Per Cycle
h-BN	Hexagonal Boron Nitride
HRTEM	High-Resolution Transmission Electron Microscopy
HTL	Hole Transport Layer
IC_{50}	Half-Maximal Inhibitory Concentration
JCPDS	Joint Committee on Powder Diffraction Standards
LBL	Layer-by-Layer
LCP/RCP	Left/Right Circularly Polarized
LED	Light-Emitting Diode
LOD	Limit of Detection
LRV	Log Reduction Value
MEG	Multiple Exciton Generation
MIC	Minimum Inhibitory Concentration
MOCVD	Metal-Organic Chemical Vapor Deposition
MOF	Metal-Organic Framework
MRI	Magnetic Resonance Imaging
MTT	3-(4,5-Dimethylthiazol-2-yl)-2,5-diphenyltetrazolium bromide
MWCNT	Multi-Walled Carbon Nanotube
NBE	Near Band Edge
NEP	Noise-Equivalent Power
NHS	N-Hydroxysuccinimide
NIR	Near-Infrared
NP	Nanoparticle
PCA	Process Control Agent
PCE	Power Conversion Efficiency

Symbols and Notation

Physical Constants

h	Planck's constant	6.626×10^{-34}	Jůs
$\hbar$	Reduced Planck's constant	1.055×10^{-34}	Jůs
c	Speed of light	2.998×10^{8}	m/s
e	Elementary charge	1.602×10^{-19}	C
k_B	Boltzmann constant	1.381×10^{-23}	J/K
m_e	Electron mass	9.109×10^{-31}	kg
N_A	Avogadro's number	6.022×10^{23}	mol^{-1}
ϵ_0	Vacuum permittivity	8.854×10^{-12}	F/m
μ_0	Vacuum permeability	$4\pi \times 10^{-7}$	H/m

Common Symbols

λ	Wavelength	nm, μm
ν	Frequency	Hz, s^{-1}
E	Energy	eV, J
E_g	Band gap energy	eV
m^*	Effective mass	kg
μ	Reduced mass, mobility	kg, cm^2/Vůs
σ	Conductivity	S/m
κ	Thermal conductivity	W/můK
α	Absorption coefficient	cm^{-1}
η	Efficiency	%
Φ	Quantum yield, potential	%, V
ψ	Wave function	–
ρ	Density	g/cm^3
ϵ_r	Relative permittivity	–
χ	Susceptibility	–
T	Temperature	K, řC
V	Volume, voltage	m^3, V
A	Area, absorbance	m^2, a.u.
d	Diameter, thickness	nm, μm
r, R	Radius	nm
n	Refractive index, quantum number	–
θ	Angle	degrees, radians
ω	Angular frequency	rad/s

Nanomaterials

Part I: Fundamentals of Nanomaterials

Dr. Irfan Toqeer

Assistant Professor
Department of Physics
Riphah International University Faisalabad (RIUF)
Pakistan

November 7, 2025

Chapter 1

Introduction to Nanoscience and Nanotechnology

"There's plenty of room at the bottom."
— Richard P. Feynman, 1959

1.1 Introduction

The advent of nanoscience and nanotechnology represents one of the most profound scientific revolutions of the 21st century. The ability to manipulate matter at the atomic and molecular scale has opened unprecedented opportunities across diverse fields including electronics, medicine, energy, materials science, and environmental remediation. This chapter provides a comprehensive introduction to the fundamental concepts, historical development, and classification schemes that form the foundation of nanomaterials science.

Nanomaterials are defined as materials with at least one dimension in the range of 1 to 100 nanometers (nm). At this scale, materials exhibit unique physical, chemical, optical, electrical, and magnetic properties that differ significantly from their bulk counterparts. These size-dependent properties arise primarily due to two fundamental effects: the increased surface-to-volume ratio and quantum confinement effects.

Understanding nanomaterials requires an interdisciplinary approach, drawing upon principles from physics, chemistry, materials science, biology, and engineering. This chapter will guide you through the essential concepts needed to appreciate the remarkable world of the nanoscale.

1.2 Historical Evolution of Nanoscience

1.2.1 Ancient and Medieval Nanotechnology

While the term "nanotechnology" is modern, humans have unknowingly utilized nanomaterials for millennia. The historical evolution of nanoscience can be traced through several distinct periods:

Ancient Applications (4th Century - 17th Century)

The earliest documented use of nanomaterials dates back to ancient civilizations:

- **Lycurgus Cup (4th century AD):** This Roman glass cup exhibits dichroism—appearing green in reflected light and red in transmitted light. Modern analysis revealed that this remarkable optical property results from gold and silver nanoparticles (approximately 70 nm diameter) embedded in the glass matrix. The ratio of gold to silver (Au:Ag = 7:3) creates plasmonic effects responsible for the color change [1].

- **Damascus Steel (circa 300 BC - 1700 AD):** The legendary strength and sharpness of Damascus steel swords have been attributed to carbon nanotubes and cementite nanowires that form during the forging process. Analysis shows that these nanostructures range from 10-100 nm in diameter [2].

- **Medieval Stained Glass:** The vibrant colors in medieval cathedral windows were achieved using metal nanoparticles. Gold nanoparticles (10-50 nm) produce ruby red colors, while silver nanoparticles create yellow hues through surface plasmon resonance effects.

Foundation Period (1857-1959)

- **1857 - Michael Faraday:** Conducted systematic studies on colloidal gold, preparing what we now recognize as gold nanoparticles. His work, "Experimental Relations of Gold (and Other Metals) to Light," laid the groundwork for understanding nanoscale optical properties [3].

- **1905 - Albert Einstein:** Published his work on Brownian motion, providing theoretical framework for understanding particle behavior at the nanoscale.

- **1931 - Max Knoll and Ernst Ruska:** Invented the transmission electron microscope (TEM), enabling visualization of nanoscale structures.

- **1959 - Richard Feynman:** Delivered his visionary lecture "There's Plenty of Room at the Bottom" at Caltech, conceptualizing the manipulation of individual atoms and molecules, essentially predicting nanotechnology [4].

Modern Era (1974-Present)

- **1974 - Norio Taniguchi:** Coined the term "nanotechnology" to describe precision engineering at the nanometer scale [5].

- **1981 - Gerd Binnig and Heinrich Rohrer:** Invented the scanning tunneling microscope (STM) at IBM Zurich, enabling atomic-level imaging and manipulation (Nobel Prize 1986) [6].

- **1985 - Discovery of Fullerenes:** Harold Kroto, Richard Smalley, and Robert Curl discovered C_{60} buckminsterfullerene (Nobel Prize 1996) [7].

- **1991 - Sumio Iijima:** Discovered carbon nanotubes, opening new frontiers in nanomaterials research [8].

- **2000s - Present:** Explosive growth in nanomaterial synthesis, characterization, and applications, with global research funding exceeding billions of dollars annually.

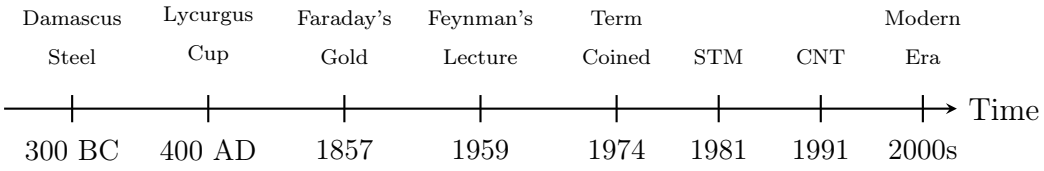

Figure 1.1: Timeline of major milestones in the evolution of nanoscience and nanotechnology

1.3 Scale of Nanometer: Size Comparison and Quantum Effects

1.3.1 Understanding the Nanoscale

The nanometer (nm) is one billionth of a meter:

$$1 \text{ nm} = 10^{-9} \text{ m} = 10^{-7} \text{ cm} = 10 \text{ Å} \tag{1.1}$$

To appreciate the nanoscale, consider the following size comparisons:

Table 1.1: Comparative sizes of various objects and entities

Object/Entity	**Size (approximate)**	**Scale**
Hydrogen atom (diameter)	0.1 nm	Atomic
Small molecule (water)	0.3 nm	Molecular
DNA double helix (diameter)	2 nm	Biomolecular
Protein (hemoglobin)	5 nm	Biomolecular
Virus (polio)	30 nm	Biological
Quantum dots	2-10 nm	Nanomaterial
Carbon nanotubes (diameter)	1-100 nm	Nanomaterial
Wavelength of visible light	400-700 nm	Optical
Bacteria (E. coli)	1,000 nm (1 μm)	Biological
Red blood cell	7,000 nm (7 μm)	Biological
Human hair (diameter)	80,000 nm (80 μm)	Macroscopic

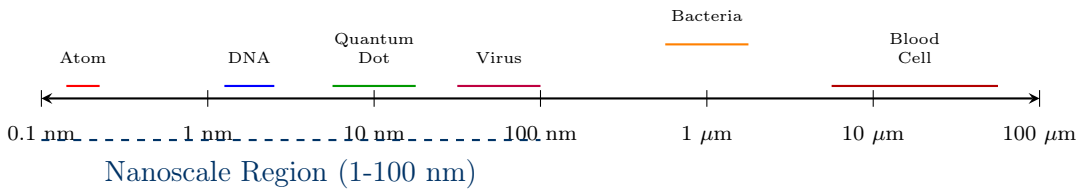

Figure 1.2: Logarithmic scale comparison showing the nanoscale regime

1.3.2 Surface-to-Volume Ratio Effects

One of the most significant characteristics of nanomaterials is their exceptionally high surface-to-volume ratio. As particle size decreases, the fraction of atoms located at or near the surface increases dramatically.

For a spherical particle of radius r, the surface area A and volume V are:

$$A = 4\pi r^2 \tag{1.2}$$

$$V = \frac{4}{3}\pi r^3 \tag{1.3}$$

The surface-to-volume ratio is:

$$\frac{A}{V} = \frac{4\pi r^2}{\frac{4}{3}\pi r^3} = \frac{3}{r} \tag{1.4}$$

This inverse relationship with radius means that as particle size decreases, the surface-to-volume ratio increases dramatically.

Example

Calculate the surface-to-volume ratio for gold particles of diameter 1 cm, 1 mm, 1 μm, and 1 nm.
Solution:
Using $\frac{A}{V} = \frac{3}{r}$ where r is the radius:

- For $d = 1$ cm, $r = 0.5$ cm: $\frac{A}{V} = \frac{3}{0.5} = 6$ cm^{-1}
- For $d = 1$ mm, $r = 0.5$ mm: $\frac{A}{V} = \frac{3}{0.0005} = 6000$ cm^{-1}
- For $d = 1$ μm, $r = 0.5$ μm: $\frac{A}{V} = \frac{3}{5\times10^{-7}} = 6 \times 10^6$ cm^{-1}
- For $d = 1$ nm, $r = 0.5$ nm: $\frac{A}{V} = \frac{3}{5\times10^{-10}} = 6 \times 10^9$ cm^{-1}

The surface-to-volume ratio increases by a factor of 10^9 when going from centimeter to nanometer scale!

Percentage of Surface Atoms

For a crystalline nanoparticle, we can estimate the percentage of atoms at the surface. Consider a spherical nanoparticle with N_{total} total atoms. The number of surface atoms N_{surf} can be approximated as:

$$\frac{N_{surf}}{N_{total}} \approx \frac{4d}{D} \tag{1.5}$$

where d is the atomic diameter and D is the particle diameter.

Table 1.2: Percentage of surface atoms as a function of particle size (assuming atomic diameter ≈ 0.3 nm)

Particle Diameter	**Number of Atoms**	**% Surface Atoms**
1 nm	$\sim$30	$\sim$99%
2 nm	$\sim$250	$\sim$60%
5 nm	$\sim$4,000	$\sim$24%
10 nm	$\sim$30,000	$\sim$12%
100 nm	$\sim 3 \times 10^7$	$\sim$1.2%
1 μm	$\sim 3 \times 10^{10}$	$\sim$0.12%

This high percentage of surface atoms leads to:

- Enhanced chemical reactivity
- Modified catalytic properties
- Altered mechanical properties
- Modified melting points
- Unique optical properties

1.3.3 Quantum Confinement Effects

When the dimensions of a material become comparable to or smaller than the de Broglie wavelength of charge carriers (electrons and holes), quantum confinement effects become significant. This leads to quantization of energy levels and dramatic changes in electronic and optical properties.

De Broglie Wavelength

The de Broglie wavelength of a particle is given by:

$$\lambda = \frac{h}{p} = \frac{h}{\sqrt{2m^* E}} \tag{1.6}$$

where:

- h is Planck's constant (6.626×10^{-34} J·s)
- p is momentum
- m^* is the effective mass
- E is the kinetic energy

For a free electron at room temperature, the thermal de Broglie wavelength is:

$$\lambda_{th} = \frac{h}{\sqrt{2\pi m k_B T}} \tag{1.7}$$

where k_B is Boltzmann's constant (1.381×10^{-23} J/K) and T is temperature.
At $T = 300$ K for an electron:

$$\lambda_{th} \approx 6.6 \text{ nm} \tag{1.8}$$

Exciton Bohr Radius

An exciton is a bound state of an electron and hole in a semiconductor. The exciton Bohr radius a_B represents the average separation between electron and hole:

$$a_B = \frac{\varepsilon_r \hbar^2}{m_r e^2} = \varepsilon_r \frac{m_0}{m_r} a_0 \tag{1.9}$$

where:

- ε_r is the relative permittivity
- $\hbar$ is the reduced Planck's constant
- $m_r = \frac{m_e^* m_h^*}{m_e^* + m_h^*}$ is the reduced effective mass
- e is the elementary charge
- a_0 is the Bohr radius (0.053 nm)

Table 1.3: Exciton Bohr radius for common semiconductors

Material	**Exciton Bohr Radius (nm)**	**Bulk Band Gap (eV)**
CdSe	5.6	1.74
CdS	2.8	2.42
CdTe	7.3	1.50
PbS	20	0.41
PbSe	46	0.28
Si	4.9	1.12
GaAs	11.5	1.42

Particle in a Box: Energy Quantization

When a particle is confined in a potential well (box), its energy becomes quantized. For a one-dimensional infinite potential well of length L, the allowed energy levels are:

$$E_n = \frac{n^2 h^2}{8mL^2} = \frac{n^2 \pi^2 \hbar^2}{2mL^2}, \quad n = 1, 2, 3, ... \tag{1.10}$$

For a three-dimensional spherical quantum dot of radius R, the energy levels are:

$$E_{n,l} = \frac{\hbar^2 \chi_{n,l}^2}{2m^* R^2} \tag{1.11}$$

where $\chi_{n,l}$ are the zeros of spherical Bessel functions.
The energy gap between levels scales as:

$$\Delta E \propto \frac{1}{R^2} \tag{1.12}$$

This means smaller particles have larger energy spacing and consequently larger band gaps.

Quantum Confinement Regimes

Quantum confinement effects are categorized based on the dimensionality of confinement:

1. **Weak Confinement Regime:** $R >> a_B$

$$E_g(R) = E_g^{bulk} + \frac{\hbar^2\pi^2}{2R^2}\left(\frac{1}{m_e^*} + \frac{1}{m_h^*}\right) - \frac{1.8e^2}{4\pi\varepsilon_0\varepsilon_r R} \tag{1.13}$$

2. **Strong Confinement Regime:** $R << a_B$

   Electron and hole are confined independently:

$$E_g(R) = E_g^{bulk} + \frac{\hbar^2\pi^2}{2m_e^*R^2} + \frac{\hbar^2\pi^2}{2m_h^*R^2} - \frac{1.8e^2}{4\pi\varepsilon_0\varepsilon_r R} \tag{1.14}$$

The terms represent:

- Bulk band gap energy
- Quantum confinement energy (kinetic energy)
- Coulombic attraction energy

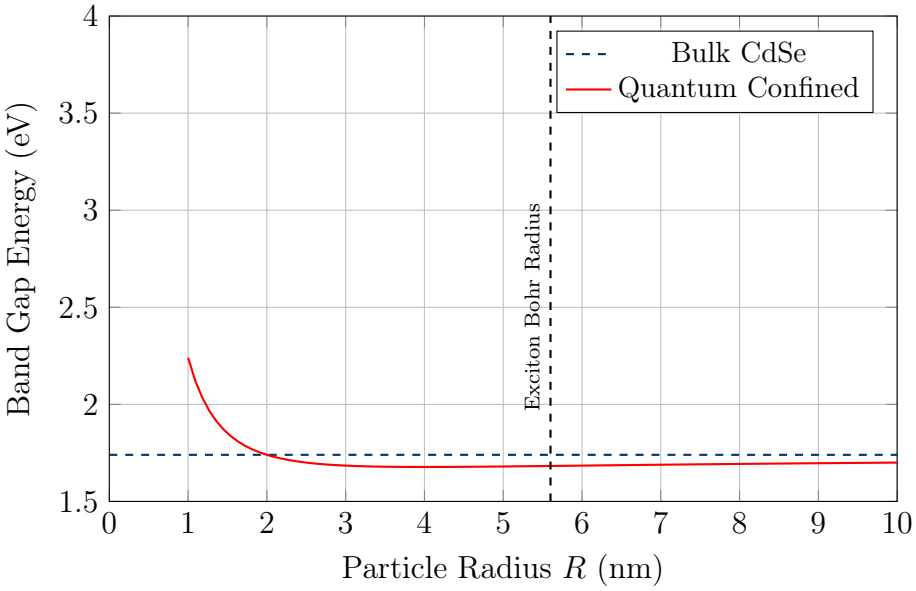

Figure 1.3: Size-dependent band gap energy for CdSe quantum dots showing quantum confinement effect

Key Point

Quantum confinement leads to:

- **Blue shift** in optical absorption and emission as particle size decreases
- Discrete, atom-like energy levels
- Size-tunable electronic and optical properties
- Enhanced oscillator strength and radiative recombination rates

1.3.4 Other Size-Dependent Properties

Melting Point Depression

Nanoparticles exhibit significantly lower melting points compared to bulk materials. The melting temperature $T_m(r)$ of a spherical particle of radius r is approximated by:

$$T_m(r) = T_m^{bulk}\left(1 - \frac{\alpha}{r}\right) \tag{1.15}$$

where α is a material-dependent constant typically in the range of 1-10 nm.
For gold nanoparticles:

$$T_m(r) = T_m^{bulk}\left(1 - \frac{2\gamma V_m}{r\Delta H_f}\right) \tag{1.16}$$

where γ is surface energy, V_m is molar volume, and ΔH_f is the heat of fusion.

Optical Properties: Surface Plasmon Resonance

Metal nanoparticles exhibit surface plasmon resonance (SPR)—collective oscillation of conduction electrons when excited by electromagnetic radiation. For a small spherical particle with radius $r << \lambda$, the extinction cross-section is given by:

$$C_{ext} = 9\frac{\omega}{c}\varepsilon_m^{3/2}V\frac{\varepsilon_2}{(\varepsilon_1 + 2\varepsilon_m)^2 + \varepsilon_2^2} \tag{1.17}$$

where:

- ω is angular frequency
- c is speed of light
- ε_m is the dielectric constant of the medium
- V is particle volume
- $\varepsilon = \varepsilon_1 + i\varepsilon_2$ is the complex dielectric function

Resonance occurs when: $\varepsilon_1 = -2\varepsilon_m$ (Fröhlich condition)

1.4 Top-Down vs. Bottom-Up Approaches

Nanomaterial synthesis strategies are broadly classified into two categories based on the direction of material assembly: top-down and bottom-up approaches.

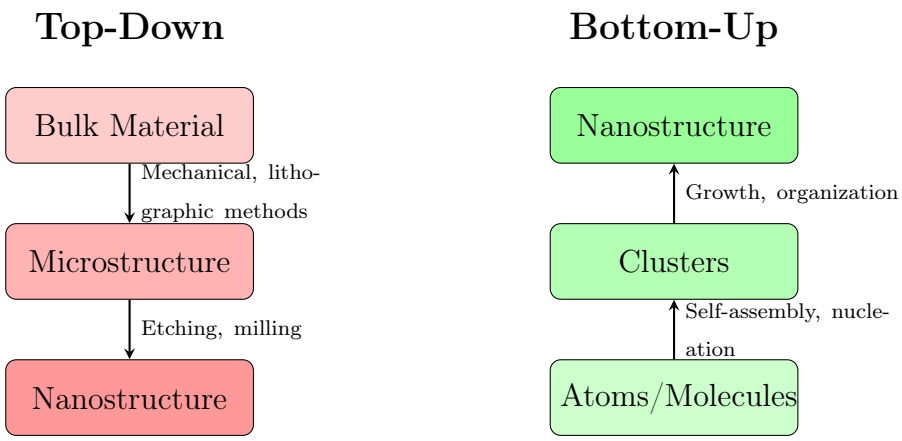

Figure 1.4: Schematic comparison of top-down and bottom-up approaches

1.4.1 Top-Down Approach

In the top-down approach, bulk materials are progressively broken down into nanoscale structures through various physical or chemical processes.

Characteristics

- **Starting point:** Bulk or macroscopic materials
- **Process direction:** Large → Small
- **Principle:** Removal/subtraction of material
- **Control:** External manipulation and patterning

Common Techniques

1. **Mechanical Methods**
   - *Ball milling:* High-energy collisions between balls and powder in a rotating chamber
   - *Grinding:* Progressive size reduction through mechanical forces
   - *Exfoliation:* Mechanical separation of layers (e.g., graphene from graphite)
2. **Lithographic Techniques**
   - *Photolithography:* Pattern transfer using light and photoresist (resolution $\sim$ 100 nm)
   - *Electron-beam lithography:* Direct writing with electron beam (resolution $<$ 10 nm)
   - *Nanoimprint lithography:* Mechanical embossing with a mold
3. **Etching Processes**
   - *Wet etching:* Chemical dissolution
   - *Dry etching:* Plasma or reactive ion etching

- *Focused ion beam (FIB):* Milling with accelerated ions

4. **Laser Ablation**
    - Material removal by high-intensity laser pulses
    - Particularly useful for nanoparticle generation

Advantages and Limitations

Table 1.4: Top-down approach: Advantages and limitations

Advantages	Limitations
Well-established industrial processes	Surface structure imperfections
Good control over macroscopic features	High energy consumption
Compatible with existing technologies	Waste generation
Scalable for mass production	Limited control at atomic level
Suitable for integration	Introduction of defects and contamination
	Expensive equipment
	Difficulty achieving sub-10 nm features

1.4.2 Bottom-Up Approach

The bottom-up approach builds nanomaterials from atomic or molecular components through self-assembly, chemical synthesis, or controlled growth processes.

Characteristics

- **Starting point:** Atoms, molecules, or clusters
- **Process direction:** Small → Large
- **Principle:** Assembly/addition of building blocks
- **Control:** Chemical interactions and thermodynamics

Common Techniques

1. **Chemical Synthesis**
    - *Sol-gel process:* Hydrolysis and condensation of precursors
    - *Precipitation:* Controlled nucleation from supersaturated solutions
    - *Hydrothermal/Solvothermal:* Synthesis in high-temperature/pressure solutions
    - *Microemulsion:* Synthesis in confined nanoreactors

2. **Vapor Phase Methods**

   - *Chemical Vapor Deposition (CVD):* Decomposition of gaseous precursors
   - *Physical Vapor Deposition (PVD):* Condensation of evaporated material
   - *Atomic Layer Deposition (ALD):* Sequential self-limiting surface reactions

3. **Self-Assembly**

   - *Molecular self-assembly:* Spontaneous organization driven by non-covalent interactions
   - *Colloidal self-assembly:* Organization of colloidal particles
   - *DNA-directed assembly:* Using DNA complementarity for precise positioning

4. **Biological Methods**

   - *Biomimetic synthesis:* Using biological molecules as templates
   - *Biosynthesis:* Using living organisms (bacteria, fungi, plants)

Thermodynamic Considerations

Bottom-up synthesis often relies on achieving thermodynamic equilibrium or controlled kinetic pathways. The Gibbs free energy change determines spontaneity:

$$\Delta G = \Delta H - T\Delta S \tag{1.18}$$

For nanoparticle formation, the total free energy includes contributions from:

$$\Delta G_{total} = \Delta G_{volume} + \Delta G_{surface} \tag{1.19}$$

For a spherical particle:

$$\Delta G = \frac{4}{3}\pi r^3 \Delta G_v + 4\pi r^2 \gamma \tag{1.20}$$

where ΔG_v is the free energy change per unit volume and γ is the surface energy. The critical nucleus radius r^* is found by setting $\frac{d(\Delta G)}{dr} = 0$:

$$r^* = -\frac{2\gamma}{\Delta G_v} \tag{1.21}$$

Advantages and Limitations

Table 1.5: Bottom-up approach: Advantages and limitations

Advantages	**Limitations**
Atomic-level control possible	Complex process control
Less waste generation	Scaling up challenges
Lower energy consumption	Purity and reproducibility issues
Formation of complex structures	Time-consuming optimization
Can produce crystalline, defect-free materials	Requires sophisticated characterization
Cost-effective for some applications	Limited long-range ordering
Nanoscale precision	Sensitive to environmental conditions

1.4.3 Hybrid Approaches

Modern nanofabrication often employs hybrid strategies combining both approaches:

- Top-down lithography combined with bottom-up deposition
- Template-assisted synthesis (templates created top-down, materials grown bottom-up)
- Directed self-assembly using lithographically defined patterns

1.5 Classification of Nanomaterials

Nanomaterials are classified based on various criteria including dimensionality, composition, origin, and morphology. The most fundamental classification is based on the number of dimensions in the nanoscale regime (1-100 nm).

1.5.1 Dimensionality-Based Classification

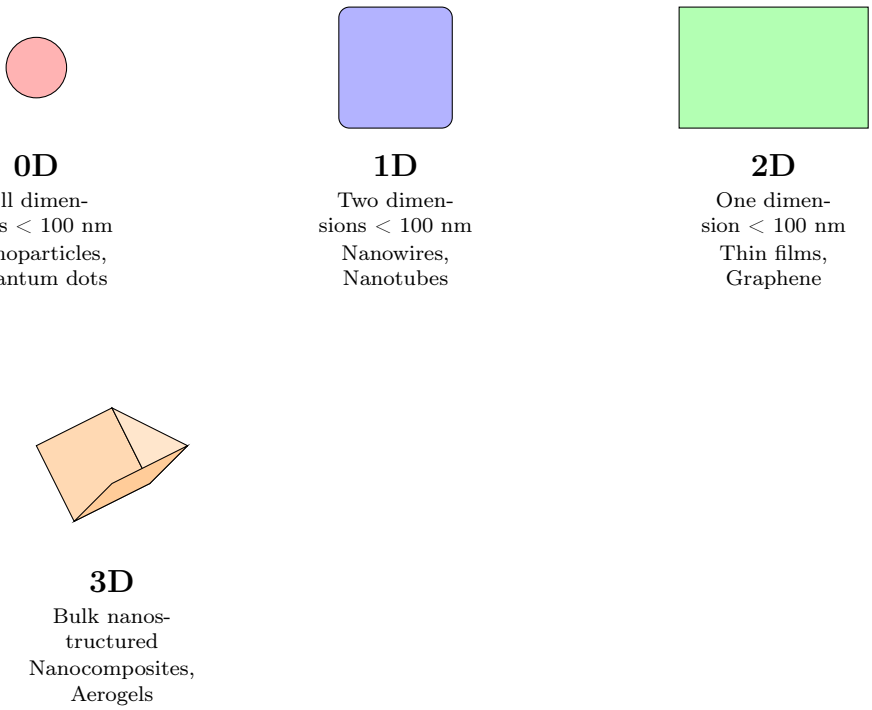

Figure 1.5: Classification of nanomaterials based on dimensionality

Zero-Dimensional (0D) Nanomaterials

Definition

Zero-dimensional nanomaterials have all three dimensions confined to the nanoscale (< 100 nm). They are also called nanoparticles or quantum dots.

Characteristics:

- Complete three-dimensional quantum confinement
- Discrete, atomic-like density of states
- Size-tunable properties
- Very high surface-to-volume ratio

Examples:

1. **Quantum Dots (QDs):** Semiconductor nanocrystals (CdSe, CdS, PbS, InP)

$$\text{Typical size: } 2 - 10 \text{ nm} \tag{1.22}$$

2. **Metal Nanoparticles:** Au, Ag, Pt, Fe nanoparticles
   - Gold nanoparticles: Biomedical applications, catalysis
   - Silver nanoparticles: Antimicrobial agents

3. **Fullerenes:** C_{60}, C_{70}, etc.

$$C_{60} \text{ diameter: } 0.7 \text{ nm} \tag{1.23}$$

4. **Oxide Nanoparticles:** TiO_2, ZnO, Fe_3O_4
5. **Core-Shell Nanoparticles:** CdSe/ZnS, Au/SiO_2

Applications:

- Biomedical imaging and drug delivery
- Catalysis
- Optoelectronics (LEDs, displays)
- Solar cells
- Sensors

One-Dimensional (1D) Nanomaterials

Definition

One-dimensional nanomaterials have two dimensions in the nanoscale while the third dimension is significantly larger. They include nanowires, nanorods, nanotubes, and nanofibers.

Characteristics:

- Two-dimensional quantum confinement
- High aspect ratio (length/diameter > 10)
- Anisotropic properties
- Efficient charge transport along length

Examples:

1. **Carbon Nanotubes (CNTs):**
   - Single-walled CNTs (SWCNTs): diameter 0.4-3 nm
   - Multi-walled CNTs (MWCNTs): diameter 2-100 nm
   - Length: micrometers to millimeters

   The structure is described by the chiral vector:

$$\vec{C}_h = n\vec{a}_1 + m\vec{a}_2 = (n, m) \tag{1.24}$$

   Diameter:

$$d = \frac{a}{\pi}\sqrt{n^2 + nm + m^2} \tag{1.25}$$

   where $a = 0.246$ nm is the graphene lattice constant.

2. **Semiconductor Nanowires:** Si, GaN, ZnO, InP nanowires
3. **Metal Nanowires:** Ag, Au, Cu nanowires
4. **Oxide Nanorods/Nanowires:** TiO_2, SnO_2, V_2O_5
5. **Nanofibers:** Electrospun polymer nanofibers

Applications:

- Nanoelectronics and transistors
- Energy storage (batteries, supercapacitors)
- Sensors (chemical, biological)
- Composites for mechanical reinforcement
- Field emission devices

Two-Dimensional (2D) Nanomaterials

Definition

Two-dimensional nanomaterials have one dimension in the nanoscale (thickness) while extending to larger dimensions in the other two directions. They include thin films, nanosheets, and nanoplates.

Characteristics:

- One-dimensional quantum confinement
- Planar structure
- Large surface area
- Unique electronic band structure

Examples:

1. **Graphene:** Single layer of carbon atoms in hexagonal lattice
   - Thickness: 0.335 nm (single layer)
   - Exceptional electronic properties
   - Linear dispersion relation near Dirac points:

$$E(\vec{k}) = \pm\hbar v_F |\vec{k}| \tag{1.26}$$

   where $v_F \approx 10^6$ m/s is the Fermi velocity

2. **Transition Metal Dichalcogenides (TMDs):**
   - MoS_2, WS_2, $MoSe_2$, WSe_2
   - Thickness: 0.6-0.7 nm per layer

- Transition from indirect (bulk) to direct (monolayer) band gap

3. **Hexagonal Boron Nitride (h-BN):** Insulating 2D material
4. **MXenes:** $Ti_3C_2T_x$, Mo_2CT_x (where T = O, OH, F)
5. **Phosphorene:** Single layer of black phosphorus
6. **Thin Films:** Metal, semiconductor, and oxide thin films

Applications:

- Electronics (transistors, interconnects)
- Optoelectronics (photodetectors, LEDs)
- Energy storage and conversion
- Catalysis
- Barrier coatings
- Sensors

Three-Dimensional (3D) Nanomaterials

Definition

Three-dimensional nanomaterials are bulk materials composed of nanoscale building blocks or containing nanoscale features throughout their structure.

Characteristics:

- No dimensional confinement in the material itself
- Bulk form composed of nanostructured units
- Properties influenced by grain boundaries and interfaces
- Three-dimensional network of nanoscale features

Examples:

1. **Nanocomposites:**
   - Polymer-nanoparticle composites
   - Metal matrix nanocomposites
   - Ceramic matrix nanocomposites
2. **Nanocrystalline Materials:**
   - Grain size < 100 nm

- Enhanced mechanical properties (Hall-Petch relation):

$$\sigma_y = \sigma_0 + k_y d^{-1/2} \tag{1.27}$$

  where σ_y is yield stress, d is grain size

3. **Porous Nanomaterials:**
   - Aerogels: 3D networks with $> 90\%$ porosity
   - Mesoporous silica: Ordered porous structure with 2-50 nm pores
   - Metal-organic frameworks (MOFs): Crystalline porous materials
4. **Nanoporous Metals:** Nanoporous gold, platinum
5. **Nanostructured Bulk Materials:** Compacted nanopowders

Applications:

- Structural materials with enhanced strength
- Catalysis (high surface area supports)
- Adsorption and separation
- Energy storage
- Thermal insulation (aerogels)

1.5.2 Comprehensive Classification Table

Table 1.6: Comprehensive classification of nanomaterials

Type	Confinement	Examples	Key Applications
0D	3D	Quantum dots (CdSe, PbS) Metal nanoparticles (Au, Ag) Fullerenes (C_{60})	Displays, bioimaging Catalysis, plasmonics Drug delivery, electronics
1D	2D	Carbon nanotubes Nanowires (Si, ZnO, GaN) Nanofibers	Electronics, composites Sensors, transistors Filtration, tissue engineering
2D	1D	Graphene TMDs (MoS_2, WS_2) Thin films	Electronics, sensors Optoelectronics, catalysis Coatings, devices
3D	0D	Nanocomposites Aerogels Nanocrystalline materials	Structural materials Insulation, catalysis High-strength alloys

1.6 Examples of Nanomaterials

1.6.1 Naturally Occurring Nanomaterials

Nature has been creating and utilizing nanomaterials long before human intervention. Understanding natural nanomaterials provides inspiration for synthetic approaches and applications.

Biological Nanomaterials

1. **Proteins and Enzymes**
   - Size: 1-100 nm
   - Function: Catalysis, structural support, transport
   - Example: Hemoglobin ($\sim$5 nm), performs oxygen transport
2. **DNA and RNA**
   - DNA double helix diameter: 2 nm
   - Length: Micrometers to centimeters (when extended)
   - Applications: Information storage, nanotechnology templates
3. **Virus Particles**
   - Size: 20-300 nm
   - Highly organized nanostructures
   - Example: Tobacco mosaic virus (18 nm diameter, 300 nm length)
4. **Ferritin**
   - Protein cage: 12 nm outer diameter
   - Contains iron oxide nanoparticles (6-8 nm)
   - Function: Iron storage in organisms
5. **Magnetosomes**
   - Magnetic nanoparticles (Fe_3O_4, Fe_3S_4) in bacteria
   - Size: 35-120 nm
   - Function: Magnetotaxis (navigation along magnetic field lines)

Mineral and Geological Nanomaterials

1. **Clay Minerals**
   - Layered aluminosilicates
   - Individual layer thickness: $\sim$1 nm
   - Examples: Montmorillonite, kaolinite

2. **Natural Nanoparticles in Soil and Water**
    - Colloidal particles
    - Size range: 1-100 nm
    - Composition: Iron oxides, aluminum oxides, organic matter
3. **Atmospheric Nanoparticles**
    - Volcanic ash nanoparticles
    - Sea salt nanoparticles
    - Mineral dust
4. **Opals**
    - Self-assembled silica nanospheres (150-300 nm)
    - Create photonic crystal structure
    - Produce iridescent colors through diffraction

Combustion-Derived Nanoparticles

- Forest fire smoke particles
- Volcanic emissions
- Natural gas seepage oxidation products

1.6.2 Engineered Nanomaterials

Engineered nanomaterials are intentionally designed and synthesized for specific applications.

Carbon-Based Nanomaterials

1. **Fullerenes (C_{60}, C_{70})**
    - Discovery: 1985 by Kroto, Curl, and Smalley
    - Structure: Closed-cage carbon molecules
    - C_{60}: Soccer ball structure, 60 carbon atoms
    - Properties: High electron affinity, superconductivity when doped
    - Applications: Drug delivery, organic photovoltaics, lubricants
2. **Carbon Nanotubes**
    - Discovery: 1991 by Sumio Iijima
    - Structure: Rolled graphene sheets
    - Electrical conductivity: Metallic or semiconducting depending on chirality
    - Mechanical properties: Young's modulus $\sim$ 1 TPa
    - Thermal conductivity: Up to 6000 W/m·K

- Applications: Nanoelectronics, composites, sensors, field emitters

3. **Graphene**
   - Isolation: 2004 by Geim and Novoselov (Nobel Prize 2010)
   - Properties:

$$\text{Charge carrier mobility: } > 200,000 \text{ cm}^2/\text{V·s} \tag{1.28}$$

$$\text{Thermal conductivity: } \sim 5000 \text{ W/m·K} \tag{1.29}$$

$$\text{Optical absorption: } 2.3\% \text{ per layer} \tag{1.30}$$

   - Applications: Electronics, sensors, energy storage, composites

4. **Carbon Quantum Dots**
   - Size: < 10 nm
   - Properties: Photoluminescence, biocompatibility
   - Applications: Bioimaging, sensing, LEDs

Metal and Metal Oxide Nanoparticles

1. **Gold Nanoparticles (Au NPs)**
   - Size-dependent color due to surface plasmon resonance
   - 20 nm Au NPs: Red color ($\lambda_{SPR} \approx 520$ nm)
   - Applications: Diagnostics, therapeutics, catalysis, electronics

2. **Silver Nanoparticles (Ag NPs)**
   - Strong antimicrobial properties
   - Plasmonic properties
   - Applications: Antibacterial coatings, wound dressings, sensors

3. **Titanium Dioxide ($\mathbf{TiO_2}$)**
   - Band gap: 3.2 eV (anatase), 3.0 eV (rutile)
   - Photocatalytic activity under UV light
   - Applications: Self-cleaning surfaces, water purification, solar cells

4. **Zinc Oxide (ZnO)**
   - Band gap: 3.37 eV
   - Piezoelectric properties
   - Applications: UV filters, gas sensors, LEDs

5. **Iron Oxide ($\mathbf{Fe_3O_4}$, γ-$\mathbf{Fe_2O_3}$)**
   - Superparamagnetic at nanoscale
   - Applications: MRI contrast agents, hyperthermia, drug delivery

Semiconductor Quantum Dots

1. **CdSe Quantum Dots**
    - Size-tunable emission: 450-650 nm
    - High quantum yield
    - Applications: Displays (QLED), bioimaging, solar cells
2. **PbS Quantum Dots**
    - Near-infrared emission
    - Large exciton Bohr radius (20 nm)
    - Applications: IR photodetectors, solar cells
3. **InP Quantum Dots**
    - Cadmium-free alternative
    - Lower toxicity
    - Applications: Displays, lighting

1.7 Importance and Scope in Pakistan's Industrial and Research Context

1.7.1 Current Research Landscape in Pakistan

Pakistan has shown growing interest in nanotechnology research and development over the past two decades. Several institutions have established dedicated research centers and programs:

Major Research Institutions

1. **National Center for Physics (NCP), Islamabad**
    - Nanoscience and Technology Department
    - Focus: Synthesis and characterization of nanomaterials
    - Facilities: Electron microscopy, X-ray diffraction, spectroscopy
2. **National Institute for Biotechnology and Genetic Engineering (NIBGE), Faisalabad**
    - Nanobiotechnology research
    - Biosynthesis of nanoparticles
    - Agricultural nanotechnology applications
3. **Pakistan Institute of Engineering and Applied Sciences (PIEAS), Islamabad**
    - Nanomaterials synthesis and applications

- Nuclear and radiation sciences with nanomaterials

4. **University Centers**

   - Quaid-i-Azam University, Islamabad
   - University of the Punjab, Lahore
   - GC University, Lahore
   - NUST, Islamabad
   - Riphah International University, Faisalabad (RIUF)

1.7.2 Potential Applications in Pakistan

Water Purification and Treatment

Pakistan faces significant water quality challenges. Nanomaterials offer promising solutions:

- **TiO_2 photocatalysis:** Degradation of organic pollutants and bacteria
- **Silver nanoparticles:** Antimicrobial water treatment
- **Carbon nanotubes and graphene:** Heavy metal removal through adsorption
- **Nanofiltration membranes:** Removal of arsenic, fluoride, and other contaminants

Impact potential: With over 60% of population lacking access to safe drinking water, nanotechnology-based water treatment could significantly improve public health.

Agriculture and Food Security

- **Nanofertilizers:** Controlled release of nutrients, improved efficiency

$$\text{Nutrient use efficiency increase: } 20 - 40\% \tag{1.31}$$

- **Nanopesticides:** Targeted delivery, reduced environmental impact
- **Nanosensors:** Soil quality monitoring, early disease detection in crops
- **Food packaging:** Antimicrobial nanocoatings to extend shelf life

Economic impact: Agriculture contributes 19.2% to Pakistan's GDP; nanotechnology could increase yields by 15-30%.

Energy Sector

1. **Solar Energy**
    - Quantum dot solar cells
    - Perovskite nanocrystal solar cells
    - Antireflective nanocoatings
    - Potential efficiency increase: 20-45%
2. **Energy Storage**
    - Graphene-based supercapacitors
    - Silicon nanowire batteries
    - Metal oxide nanoparticles for Li-ion batteries
    - Energy density improvement: 2-5 times
3. **Hydrogen Production and Storage**
    - Nanostructured catalysts for water splitting
    - Metal hydride nanoparticles for hydrogen storage

Strategic importance: Pakistan faces energy deficit of 4000-5000 MW; nanotechnology-enhanced renewable energy could address this gap.

Healthcare and Biomedicine

- **Diagnostics:**
    - Gold nanoparticle-based rapid diagnostic tests
    - Quantum dot biomarkers for disease detection
    - Nanosensors for glucose monitoring (diabetes management)
- **Drug Delivery:**
    - Targeted cancer therapy using nanoparticles
    - Liposomal drug formulations
    - Reduced side effects and improved efficacy
- **Antimicrobial Applications:**
    - Silver nanoparticle wound dressings
    - Nanocoatings for medical devices
    - Combat antibiotic resistance

Textiles

Pakistan's textile industry contributes 8.5% to GDP and 60% to exports:

- **Functional textiles:** Water-repellent, stain-resistant nanocoatings
- **Antimicrobial fabrics:** Silver and copper nanoparticle treatments
- **UV-protective clothing:** TiO_2 and ZnO nanoparticle incorporation
- **Smart textiles:** Temperature-regulating nanofibers

Value addition: Premium pricing of 30-100% for functional textiles.

Environmental Remediation

- **Air quality:** Nano-TiO_2 coatings on buildings for NOx reduction
- **Soil remediation:** Nanoscale zero-valent iron for heavy metal removal
- **Industrial waste treatment:** Photocatalytic degradation of dyes and chemicals

1.7.3 Economic Potential

Table 1.7: Estimated economic impact of nanotechnology applications in Pakistan

Sector	Current Value (USD)	Potential Increase
Textiles	\$16 billion	20-30%
Agriculture	\$50 billion	15-25%
Healthcare	\$3 billion	30-50%
Water treatment	\$500 million	100-200%
Energy	\$8 billion	25-40%
Electronics	\$2 billion	50-100%

1.7.4 Challenges and Opportunities

Challenges

1. **Infrastructure:** Limited advanced characterization facilities
2. **Funding:** Research funding $< 0.3\%$ of GDP
3. **Skilled workforce:** Need for specialized training programs
4. **Industry-academia gap:** Limited technology transfer
5. **Regulatory framework:** Lack of comprehensive nanotechnology regulations
6. **Safety concerns:** Need for nanotoxicology studies

Opportunities

1. **Growing awareness:** Increasing government and industry interest
2. **International collaboration:** Partnerships with advanced research centers
3. **Young population:** Large pool of potential researchers and innovators
4. **Niche applications:** Focus on water, agriculture, and textiles where immediate impact possible
5. **Regional hub potential:** Strategic location for South Asian nanotechnology development

1.7.5 Policy Recommendations

1. Establish National Nanotechnology Research Centers in major cities
2. Increase R&D funding to 1% of GDP with dedicated nanotechnology allocation
3. Develop industry-specific nanotechnology roadmaps
4. Create incentives for private sector investment in nanotechnology
5. Implement nanotechnology curriculum in universities
6. Establish safety and regulatory guidelines
7. Promote international research collaborations
8. Support startup ecosystem for nanotechnology commercialization

Key Point

Nanotechnology has immense potential to address Pakistan's challenges in water, energy, agriculture, healthcare, and industry. Strategic investment in research infrastructure, human resource development, and industry-academia collaboration can position Pakistan as a regional leader in nanotechnology applications.

1.8 Summary

This chapter has provided a comprehensive introduction to nanoscience and nanotechnology, covering:

- The historical evolution from ancient unintentional use to modern engineered nanomaterials
- The nanoscale regime (1-100 nm) and its unique size-dependent properties
- Surface-to-volume ratio effects and quantum confinement phenomena
- Top-down and bottom-up synthesis approaches

- Classification based on dimensionality (0D, 1D, 2D, 3D)
- Examples of natural and engineered nanomaterials
- Applications and potential impact in Pakistan's context

The fundamental principle underlying nanomaterial science is that properties at the nanoscale differ dramatically from bulk due to:

$$\text{Size effects} = \begin{cases} \text{Increased surface-to-volume ratio} \\ \text{Quantum confinement} \\ \text{Modified electronic structure} \\ \text{Enhanced surface reactivity} \end{cases} \tag{1.32}$$

Understanding these principles is essential for designing and utilizing nanomaterials effectively across diverse applications.

Exercises

Conceptual Questions

1. Explain why Richard Feynman's 1959 lecture is considered the conceptual foundation of nanotechnology even though the term wasn't coined until 1974.
2. Discuss how the Lycurgus Cup demonstrates plasmonic effects. What is the physical origin of its dichroism?
3. Compare and contrast quantum confinement effects in 0D, 1D, and 2D nanomaterials. How does dimensionality affect the density of states?
4. Explain why nanoparticles have lower melting points than bulk materials. Derive a simple relationship between melting point and particle size.
5. Discuss the advantages and limitations of top-down vs. bottom-up approaches for synthesizing: (a) quantum dots, (b) nanowires, (c) thin films.
6. Why do gold nanoparticles appear red while bulk gold is yellow? Explain in terms of surface plasmon resonance.
7. Describe three naturally occurring nanomaterials and explain how nature utilizes their nanoscale properties.
8. How can nanotechnology address Pakistan's water crisis? Propose a specific nanomaterial-based solution with technical justification.
9. Discuss the potential environmental and health concerns associated with engineered nanomaterials. What safety measures should be implemented?
10. Explain how carbon nanotubes can be either metallic or semiconducting based on their structure. What determines this property?

Numerical Problems

1. Calculate the surface-to-volume ratio for a spherical gold nanoparticle with diameter:

   (a) 10 nm

   (b) 50 nm

   (c) 100 nm

   Express your answers in nm^{-1} and compare with bulk gold.

2. A CdSe quantum dot has a diameter of 3 nm. Given that the exciton Bohr radius of CdSe is 5.6 nm and the bulk band gap is 1.74 eV:

   (a) Determine if the dot is in weak or strong confinement regime

   (b) Estimate the band gap of the quantum dot using:

   $$E_g(R) = E_g^{bulk} + \frac{\hbar^2 \pi^2}{2R^2}\left(\frac{1}{m_e^*} + \frac{1}{m_h^*}\right)$$

   where $m_e^* = 0.13m_0$ and $m_h^* = 0.45m_0$

   (c) Calculate the emission wavelength

3. Consider a spherical silver nanoparticle with radius 20 nm:

   (a) Calculate the total number of silver atoms (atomic radius of Ag = 0.144 nm, FCC structure)

   (b) Estimate the percentage of atoms at the surface

   (c) Calculate the total surface area

4. The de Broglie wavelength of an electron is given by $\lambda = h/\sqrt{2m_e E}$:

   (a) Calculate λ for an electron with kinetic energy 1 eV

   (b) At what kinetic energy does $\lambda = 10$ nm?

   (c) Compare this with thermal energy at room temperature (300 K)

5. A single-walled carbon nanotube has chiral vector (10, 5):

   (a) Calculate its diameter using $d = \frac{a}{\pi}\sqrt{n^2 + nm + m^2}$ where $a = 0.246$ nm

   (b) Determine if it's metallic or semiconducting (Rule: metallic if $n - m$ is divisible by 3)

   (c) If the length is 1 μm, calculate the aspect ratio

6. For a particle in a 1D infinite potential well of length L:

   (a) Calculate the first three energy levels for an electron confined in $L = 5$ nm

   (b) Calculate the energy difference between ground state and first excited state

   (c) What is the wavelength of photon emitted in transition from $n = 2$ to $n = 1$?

7. A nanocrystalline material has grain size 20 nm. Using the Hall-Petch relation:

$$\sigma_y = 50 + 500d^{-1/2} \text{ MPa}$$

where d is grain size in nm:

   (a) Calculate the yield stress
   (b) Compare with grain sizes of 100 nm and 1000 nm
   (c) Plot yield stress vs. grain size

8. The melting point depression of nanoparticles is given by:

$$T_m(r) = T_m^{bulk}\left(1 - \frac{4\sigma V_m}{r\Delta H_f}\right)$$

For gold: $T_m^{bulk} = 1064$C, $\sigma = 1.4$ J/m^2, $V_m = 10.2$ cm^3/mol, $\Delta H_f = 12.5$ kJ/mol:

   (a) Calculate T_m for particles with $r = 2, 5, 10, 20$ nm
   (b) Plot T_m vs. r
   (c) At what radius does T_m drop below 500°C?

9. A quantum dot has emission wavelength 600 nm (red). If you want to shift the emission to 450 nm (blue):

   (a) Should you increase or decrease the dot size?
   (b) By what factor should the energy gap change?
   (c) If the original diameter was 5 nm, estimate the new diameter (assume $E_g \propto 1/R^2$)

10. Pakistan's textile industry uses 100 million meters of fabric daily. If silver nanoparticle treatment (10 ppm Ag) is applied:

   (a) Calculate total silver required per day (assume fabric density 150 g/m^2)
   (b) If Ag nanoparticles are 20 nm diameter, estimate number of particles per cm^2
   (c) Calculate the cost if silver is \$600/kg and nanoparticle synthesis adds 50% cost

Advanced Problems

1. Derive the expression for the energy levels of a particle in a three-dimensional cubic box with sides $L_x = L_y = L_z = L$. Show that degeneracy exists and give examples.

2. Using Mie theory, show that the extinction cross-section of a small spherical particle is proportional to V^2 for Rayleigh scattering and to V for resonant absorption.

3. Develop a business plan for implementing nanotechnology-based water purification in a rural Pakistani community of 5000 people. Include: technical specifications, cost analysis, and environmental impact assessment.

4. Design a graphene-based sensor for detecting pesticide residues in agricultural products. Provide: working principle, sensitivity estimation, and fabrication approach suitable for Pakistan.

Bibliography

[1] Freestone, I., Meeks, N., Sax, M., & Higgitt, C. (1990). The Lycurgus Cup—A Roman nanotechnology. *Gold Bulletin*, 23(4), 270-277.

[2] Reibold, M., Paufler, P., Levin, A. A., Kochmann, W., Pätzke, N., & Meyer, D. C. (2006). Carbon nanotubes in an ancient Damascus sabre. *Nature*, 444(7117), 286-286.

[3] Faraday, M. (1857). Experimental relations of gold (and other metals) to light. *Philosophical Transactions of the Royal Society of London*, 147, 145-181.

[4] Feynman, R. P. (1960). There's plenty of room at the bottom. *Engineering and Science*, 23(5), 22-36.

[5] Taniguchi, N. (1974). On the basic concept of nano-technology. *Proceedings of the International Conference on Production Engineering, Tokyo*, Part II, 18-23.

[6] Binnig, G., & Rohrer, H. (1982). Scanning tunneling microscopy. *Helvetica Physica Acta*, 55(6), 726-735.

[7] Kroto, H. W., Heath, J. R., O'Brien, S. C., Curl, R. F., & Smalley, R. E. (1985). C_{60}: Buckminsterfullerene. *Nature*, 318(6042), 162-163.

[8] Iijima, S. (1991). Helical microtubules of graphitic carbon. *Nature*, 354(6348), 56-58.

[9] Novoselov, K. S., Geim, A. K., Morozov, S. V., Jiang, D., Zhang, Y., Dubonos, S. V., Grigorieva, I. V., & Firsov, A. A. (2004). Electric field effect in atomically thin carbon films. *Science*, 306(5696), 666-669.

[10] Roduner, E. (2006). Size matters: why nanomaterials are different. *Chemical Society Reviews*, 35(7), 583-592.

[11] Cao, G., & Wang, Y. (2004). *Nanostructures and Nanomaterials: Synthesis, Properties and Applications*. Imperial College Press, London.

[12] Poole, C. P., & Owens, F. J. (2003). *Introduction to Nanotechnology*. John Wiley & Sons, New Jersey.

[13] Kelsall, R. W., Hamley, I. W., & Geoghegan, M. (Eds.). (2005). *Nanoscale Science and Technology*. John Wiley & Sons, Chichester.

[14] Klabunde, K. J. (Ed.). (2001). *Nanoscale Materials in Chemistry*. John Wiley & Sons, New York.

[15] Rao, C. N. R., Müller, A., & Cheetham, A. K. (Eds.). (2004). *The Chemistry of Nanomaterials: Synthesis, Properties and Applications*. Wiley-VCH, Weinheim.

[16] Bhushan, B. (Ed.). (2017). *Springer Handbook of Nanotechnology* (4th ed.). Springer, Berlin.

[17] Gleiter, H. (2000). Nanostructured materials: basic concepts and microstructure. *Acta Materialia*, 48(1), 1-29.

[18] Schmid, G. (Ed.). (2004). *Nanoparticles: From Theory to Application*. Wiley-VCH, Weinheim.

[19] Alivisatos, A. P. (1996). Semiconductor clusters, nanocrystals, and quantum dots. *Science*, 271(5251), 933-937.

[20] Murray, C. B., Kagan, C. R., & Bawendi, M. G. (2000). Synthesis and characterization of monodisperse nanocrystals and close-packed nanocrystal assemblies. *Annual Review of Materials Science*, 30(1), 545-610.

[21] Burda, C., Chen, X., Narayanan, R., & El-Sayed, M. A. (2005). Chemistry and properties of nanocrystals of different shapes. *Chemical Reviews*, 105(4), 1025-1102.

[22] Xia, Y., Xiong, Y., Lim, B., & Skrabalak, S. E. (2009). Shape-controlled synthesis of metal nanocrystals: simple chemistry meets complex physics? *Angewandte Chemie International Edition*, 48(1), 60-103.

[23] Whitesides, G. M., & Grzybowski, B. (2002). Self-assembly at all scales. *Science*, 295(5564), 2418-2421.

[24] Ozin, G. A., & Arsenault, A. C. (2009). *Nanochemistry: A Chemical Approach to Nanomaterials* (2nd ed.). Royal Society of Chemistry, Cambridge.

[25] Ministry of Science and Technology, Government of Pakistan. (2012). *National Nanotechnology Policy and Strategic Plan 2012-2020*. Islamabad, Pakistan.

[26] Hussain, S., Hussain, I., Sayed, S. M., Ikram, M., & Maqsood, A. (2020). Nanotechnology research and development in Pakistan: Prospects and challenges. *Nanotechnology Reviews*, 9(1), 348-364.

Chapter 2

Quantum Phenomena in Nanomaterials

> *"The underlying physical laws necessary for the mathematical theory of a large part of physics and the whole of chemistry are thus completely known, and the difficulty is only that the exact application of these laws leads to equations much too complicated to be soluble."*
> — Paul Dirac, 1929

2.1 Introduction

The transition from bulk materials to nanomaterials introduces fundamental changes in physical behavior governed by quantum mechanics. When the physical dimensions of a material become comparable to characteristic length scales such as the de Broglie wavelength, exciton Bohr radius, or mean free path of charge carriers, classical physics becomes inadequate, and quantum mechanical descriptions become essential.

This chapter explores the rich quantum phenomena that emerge in nanoscale systems. We will examine how spatial confinement leads to quantization of energy levels, how the density of electronic states transforms in reduced dimensions, and how quantum mechanical effects such as tunneling, Coulomb blockade, and conductance quantization manifest in nanomaterials. These quantum phenomena are not merely theoretical curiosities—they form the foundation for revolutionary technologies including quantum dots for displays and biomedical imaging, single-electron transistors, quantum computing devices, and ultra-sensitive sensors.

Understanding quantum effects in nanomaterials requires a solid foundation in quantum mechanics, solid-state physics, and statistical mechanics. We will develop these concepts systematically, starting from first principles and building toward practical applications and computational simulations.

2.2 Quantum Confinement Effect

2.2.1 Physical Origin of Quantum Confinement

Quantum confinement occurs when the motion of charge carriers (electrons and holes) is restricted in one or more spatial dimensions to a length scale comparable to or smaller

than their de Broglie wavelength. This spatial restriction leads to quantization of momentum and energy in the confined directions, fundamentally altering the electronic structure of the material.

De Broglie Wavelength and Characteristic Length Scales

The de Broglie wavelength of a particle with momentum p is given by:

$$\lambda_{dB} = \frac{h}{p} = \frac{h}{\sqrt{2m^* E}} \tag{2.1}$$

where h is Planck's constant, m^* is the effective mass, and E is the kinetic energy.

For a free electron at thermal equilibrium at temperature T, the thermal de Broglie wavelength is:

$$\lambda_{th} = \frac{h}{\sqrt{2\pi m^* k_B T}} \tag{2.2}$$

At room temperature ($T = 300$ K) for electrons with $m^* \approx m_e$:

$$\lambda_{th} \approx 6.6 \text{ nm} \tag{2.3}$$

Key Point

Quantum confinement effects become significant when the characteristic dimension L of the nanostructure satisfies:

$$L \lesssim \lambda_{dB}, \quad L \lesssim a_B, \quad \text{or} \quad L \lesssim \ell_{mfp} \tag{2.4}$$

where a_B is the exciton Bohr radius and ℓ_{mfp} is the mean free path.

The Exciton and Bohr Radius in Semiconductors

An exciton is a bound state of an electron and hole attracted to each other by the Coulomb force. In semiconductor nanocrystals, the exciton Bohr radius defines a critical length scale:

$$a_B^* = \frac{4\pi\varepsilon_0\varepsilon_r\hbar^2}{\mu e^2} = \varepsilon_r \frac{m_0}{\mu} a_0 \tag{2.5}$$

where:

- ε_0 is the vacuum permittivity
- ε_r is the relative dielectric constant
- $\mu = \frac{m_e^* m_h^*}{m_e^* + m_h^*}$ is the reduced effective mass
- e is the elementary charge
- $a_0 = 0.053$ nm is the Bohr radius of hydrogen

Table 2.1: Exciton Bohr radius and effective masses for common semiconductors

Material	a_B^* **(nm)**	m_e^*/m_0	m_h^*/m_0	ε_r
CdSe	5.6	0.13	0.45	10.0
CdS	2.8	0.21	0.80	8.9
CdTe	7.3	0.11	0.35	10.4
PbS	20.0	0.25	0.25	17.0
PbSe	46.0	0.27	0.27	23.0
Si	4.9	0.98	0.49	11.7
GaAs	11.5	0.067	0.45	12.9
InP	10.1	0.077	0.60	12.4
ZnO	2.3	0.24	0.59	8.5

2.2.2 Particle in a Box: Foundation of Quantum Confinement

The simplest model for quantum confinement is the particle in a box, where a particle is confined within infinite potential walls.

One-Dimensional Confinement

Consider a particle of mass m confined in a one-dimensional infinite potential well:

$$V(x) = \begin{cases} 0, & 0 < x < L \\ \infty, & \text{otherwise} \end{cases} \tag{2.6}$$

Mathematical Derivation

Solution of the Schrödinger Equation

The time-independent Schrödinger equation inside the well is:

$$-\frac{\hbar^2}{2m}\frac{d^2\psi}{dx^2} = E\psi \tag{2.7}$$

This can be rewritten as:

$$\frac{d^2\psi}{dx^2} + k^2\psi = 0, \quad \text{where} \quad k^2 = \frac{2mE}{\hbar^2} \tag{2.8}$$

The general solution is:

$$\psi(x) = A\sin(kx) + B\cos(kx) \tag{2.9}$$

Applying boundary conditions $\psi(0) = 0$ and $\psi(L) = 0$:
From $\psi(0) = 0$: $B = 0$
From $\psi(L) = 0$: $A\sin(kL) = 0$
For non-trivial solutions: $kL = n\pi$, where $n = 1, 2, 3, ...$
Therefore:

$$k_n = \frac{n\pi}{L} \tag{2.10}$$

The energy eigenvalues are:

$$E_n = \frac{\hbar^2 k_n^2}{2m} = \frac{n^2\pi^2\hbar^2}{2mL^2} = \frac{n^2h^2}{8mL^2} \tag{2.11}$$

The normalized eigenfunctions are:

$$\psi_n(x) = \sqrt{\frac{2}{L}}\sin\left(\frac{n\pi x}{L}\right) \tag{2.12}$$

Key Point

Key features of the confined system:

1. Energy quantization: $E_n \propto n^2/L^2$
2. Ground state energy is non-zero: $E_1 = \frac{h^2}{8mL^2}$ (zero-point energy)
3. Energy spacing increases with decreasing L
4. Energy spacing between adjacent levels: $\Delta E_{n,n+1} = E_{n+1} - E_n = \frac{h^2(2n+1)}{8mL^2}$

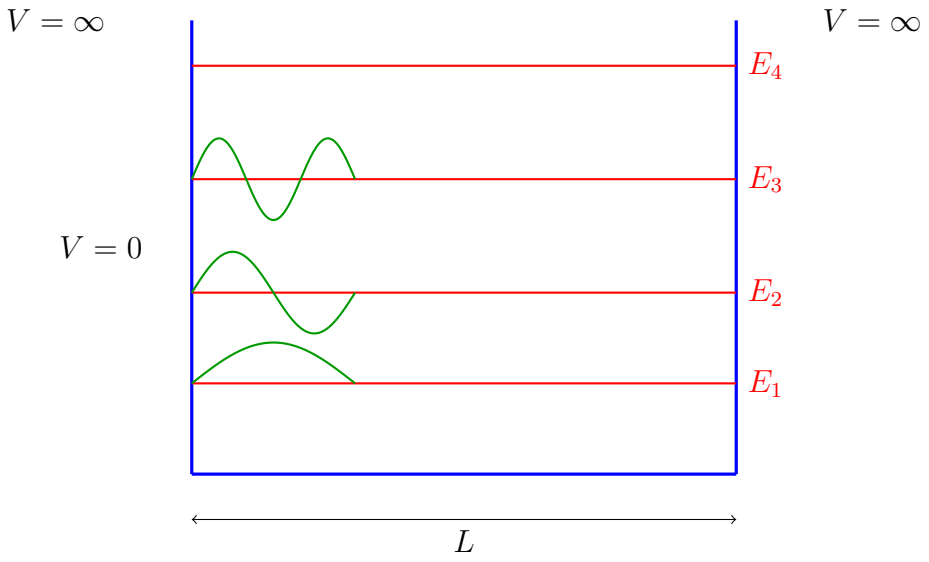

Figure 2.1: Energy levels and wavefunctions for a particle in a 1D infinite potential well

Three-Dimensional Confinement: Quantum Dot

For a particle confined in a cubic box with sides L_x, L_y, L_z, the Schrödinger equation separates into three independent one-dimensional problems:

$$E_{n_x,n_y,n_z} = \frac{\hbar^2\pi^2}{2m}\left(\frac{n_x^2}{L_x^2} + \frac{n_y^2}{L_y^2} + \frac{n_z^2}{L_z^2}\right) \tag{2.13}$$

For a cubic box ($L_x = L_y = L_z = L$):

$$E_{n_x,n_y,n_z} = \frac{\hbar^2\pi^2}{2mL^2}(n_x^2 + n_y^2 + n_z^2) = \frac{h^2}{8mL^2}n^2 \tag{2.14}$$

where $n^2 = n_x^2 + n_y^2 + n_z^2$.
Degeneracy: Multiple quantum states can have the same energy. For example:

- $(n_x, n_y, n_z) = (2,1,1), (1,2,1), (1,1,2)$ all give $n^2 = 6$ (3-fold degenerate)

Spherical Quantum Dot

For a spherical quantum dot of radius R, the Schrödinger equation in spherical coordinates leads to:

$$E_{n,l} = \frac{\hbar^2}{2m^*R^2}\chi_{n,l}^2 \tag{2.15}$$

where $\chi_{n,l}$ are the zeros of the spherical Bessel functions $j_l(x)$.
For $l = 0$ (s-states): $\chi_{1,0} = \pi$, $\chi_{2,0} = 2\pi$, $\chi_{3,0} = 3\pi$, etc.
The ground state energy is:

$$E_{1,0} = \frac{\pi^2\hbar^2}{2m^*R^2} \tag{2.16}$$

2.2.3 Size-Dependent Band Gap in Semiconductor Nanocrystals

The most dramatic consequence of quantum confinement is the size-dependent optical band gap of semiconductor nanocrystals (quantum dots).

Effective Mass Approximation

In the effective mass approximation, electrons and holes are treated as particles with effective masses m_e^* and m_h^* moving in a potential well created by confinement. The total energy shift from the bulk band gap is:

$$\Delta E = E_{e,conf} + E_{h,conf} + E_{Coulomb} \tag{2.17}$$

Brus Equation

For a spherical quantum dot in the strong confinement regime ($R < a_B^*$), the Brus equation gives the size-dependent band gap:

$$E_g(R) = E_g^{bulk} + \frac{\hbar^2\pi^2}{2R^2}\left(\frac{1}{m_e^*} + \frac{1}{m_h^*}\right) - \frac{1.8e^2}{4\pi\varepsilon_0\varepsilon_r R} + \text{smaller terms} \tag{2.18}$$

where:

- First term: Bulk band gap energy
- Second term: Quantum confinement energy (kinetic energy, $\propto 1/R^2$)
- Third term: Coulombic attraction between electron and hole ($\propto -1/R$)
- Fourth term includes electron-hole correlation effects

Key Point

The quantum confinement term dominates, leading to a **blue shift** (increase) in band gap as particle size decreases. This is the fundamental principle behind size-tunable optical properties of quantum dots.

Example

Band Gap Calculation for CdSe Quantum Dot
Calculate the band gap of a CdSe quantum dot with radius $R = 2$ nm.
Given:

- $E_g^{bulk} = 1.74$ eV
- $m_e^* = 0.13m_0$
- $m_h^* = 0.45m_0$
- $\varepsilon_r = 10.0$
- $R = 2$ nm $= 2 \times 10^{-9}$ m

Solution:
Confinement energy:

$$E_{conf} = \frac{\hbar^2\pi^2}{2R^2}\left(\frac{1}{m_e^*} + \frac{1}{m_h^*}\right) \tag{2.19}$$

$$= \frac{(1.055 \times 10^{-34})^2 \times \pi^2}{2 \times (2 \times 10^{-9})^2}\left(\frac{1}{0.13 \times 9.109 \times 10^{-31}} + \frac{1}{0.45 \times 9.109 \times 10^{-31}}\right) \tag{2.20}$$

$$\approx 0.52 \text{ eV} \tag{2.21}$$

Coulomb term:

$$E_{Coulomb} = -\frac{1.8 \times (1.602 \times 10^{-19})^2}{4\pi \times 8.854 \times 10^{-12} \times 10.0 \times 2 \times 10^{-9}} \tag{2.22}$$

$$\approx -0.065 \text{ eV} \tag{2.23}$$

Total band gap:

$$E_g(2 \text{ nm}) = 1.74 + 0.52 - 0.065 \approx 2.20 \text{ eV} \tag{2.24}$$

Corresponding emission wavelength:

$$\lambda = \frac{hc}{E_g} = \frac{1240 \text{ eV·nm}}{2.20 \text{ eV}} \approx 564 \text{ nm (green)} \tag{2.25}$$

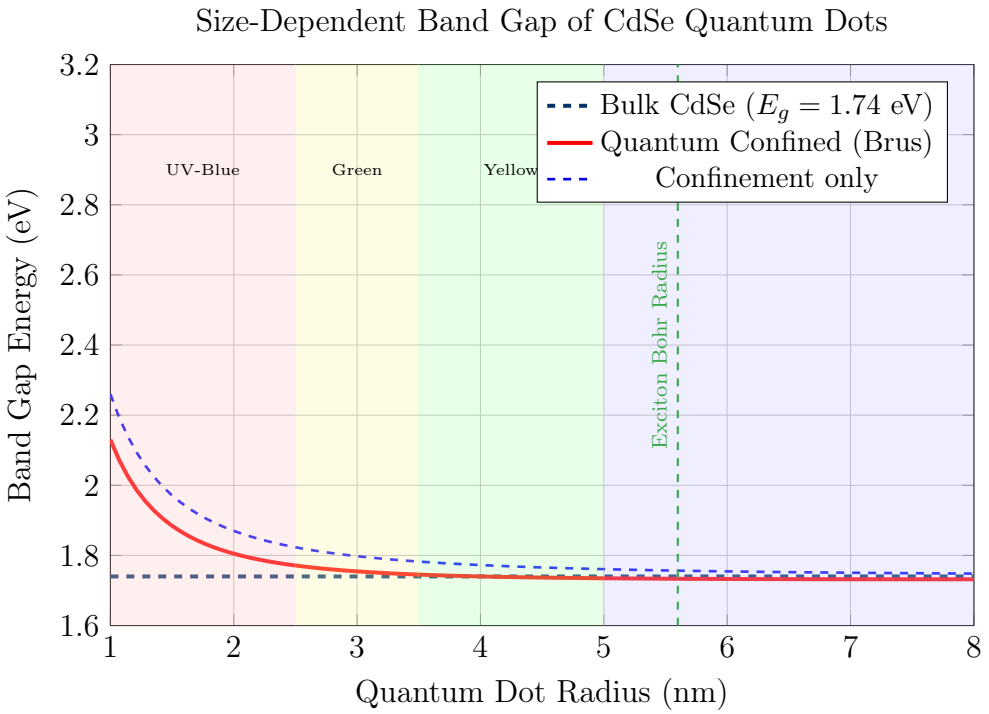

Figure 2.2: Size-dependent band gap of CdSe quantum dots showing quantum confinement effect and corresponding emission colors

2.3 Density of States in Lower Dimensions

The density of states (DOS) describes the number of available quantum states per unit energy per unit volume. Quantum confinement dramatically alters the DOS, which in turn affects optical, electrical, and thermal properties.

2.3.1 Density of States: General Formulation

The density of states $g(E)$ is defined such that $g(E)dE$ gives the number of quantum states in the energy interval $[E, E + dE]$ per unit volume.

For a system with dispersion relation $E(\vec{k})$, the DOS can be calculated from:

$$g(E) = \frac{1}{(2\pi)^d} \int_{\text{surface } E(\vec{k})=E} \frac{dS_k}{|\nabla_k E(\vec{k})|} \tag{2.26}$$

where d is the dimensionality and the integral is over the constant energy surface in k-space.

2.3.2 Three-Dimensional (3D) Bulk Semiconductor

For a bulk semiconductor with parabolic bands near the band edge:

$$E(\vec{k}) = \frac{\hbar^2 k^2}{2m^*} \tag{2.27}$$

where $k^2 = k_x^2 + k_y^2 + k_z^2$.

Mathematical Derivation

3D Density of States

The number of states in a spherical shell of radius k and thickness dk in k-space is:

$$dN = 2 \times \frac{V}{(2\pi)^3} \times 4\pi k^2 dk \tag{2.28}$$

where the factor of 2 accounts for spin degeneracy and V is the volume.
Converting from k to energy using $E = \frac{\hbar^2 k^2}{2m^*}$:

$$k = \sqrt{\frac{2m^* E}{\hbar^2}}, \quad dk = \frac{1}{2}\sqrt{\frac{2m^*}{\hbar^2 E}} dE \tag{2.29}$$

The density of states per unit volume is:

$$g_{3D}(E) = \frac{1}{V}\frac{dN}{dE} = \frac{2}{(2\pi)^3} \times 4\pi k^2 \frac{dk}{dE} \tag{2.30}$$

$$= \frac{1}{\pi^2}\left(\frac{2m^*}{\hbar^2}\right)^{3/2} \sqrt{E} \tag{2.31}$$

This can be written as:

$$g_{3D}(E) = \frac{1}{2\pi^2}\left(\frac{2m^*}{\hbar^2}\right)^{3/2} E^{1/2} \tag{2.32}$$

Key feature: $g_{3D}(E) \propto E^{1/2}$ — square root dependence on energy.

2.3.3 Two-Dimensional (2D) Quantum Well

In a quantum well, confinement in one direction (say z) leads to discrete subbands. Within each subband, motion is free in the x-y plane.

The energy is:

$$E_n(k_x, k_y) = E_n^{conf} + \frac{\hbar^2(k_x^2 + k_y^2)}{2m^*} \tag{2.33}$$

where $E_n^{conf} = \frac{n^2\pi^2\hbar^2}{2m^* L_z^2}$ is the confinement energy in the n-th subband.

Mathematical Derivation

2D Density of States

For the n-th subband, considering the free motion in 2D:
The number of states in an annular ring in 2D k-space:

$$dN = 2 \times \frac{A}{(2\pi)^2} \times 2\pi k dk \tag{2.34}$$

where A is the area.
With $E_{2D} = \frac{\hbar^2 k^2}{2m^*}$:

$$k = \sqrt{\frac{2m^* E_{2D}}{\hbar^2}}, \quad dk = \frac{m^*}{\hbar^2 k} dE_{2D} \tag{2.35}$$

The 2D DOS per unit area for one subband:

$$g_{2D}(E_{2D}) = \frac{1}{A}\frac{dN}{dE_{2D}} = \frac{2}{(2\pi)^2} \times 2\pi k \frac{dk}{dE_{2D}} \tag{2.36}$$

$$= \frac{m^*}{\pi\hbar^2} \tag{2.37}$$

Result:

$$g_{2D} = \frac{m^*}{\pi\hbar^2} = \text{constant} \tag{2.38}$$

Key feature: $g_{2D}(E) = \text{constant}$ — independent of energy! This is a characteristic signature of 2D systems.

For the total DOS including all subbands:

$$g_{2D}^{total}(E) = \frac{m^*}{\pi\hbar^2} \sum_{n=1}^{\infty} \Theta(E - E_n^{conf}) \tag{2.39}$$

where Θ is the Heaviside step function.

2.3.4 One-Dimensional (1D) Nanowire

In a nanowire, confinement occurs in two directions, leaving one direction free.

The energy is:

$$E_{n_y,n_z}(k_x) = E_{n_y,n_z}^{conf} + \frac{\hbar^2 k_x^2}{2m^*} \tag{2.40}$$

Mathematical Derivation

1D Density of States

For motion along the wire axis (x-direction):
Number of states in interval dk_x:

$$dN = 2 \times \frac{L}{2\pi} \times dk_x \tag{2.41}$$

With $E_{1D} = \frac{\hbar^2 k_x^2}{2m^*}$:

$$k_x = \sqrt{\frac{2m^* E_{1D}}{\hbar^2}}, \quad dk_x = \frac{1}{2}\sqrt{\frac{2m^*}{\hbar^2 E_{1D}}} dE_{1D} \tag{2.42}$$

The 1D DOS per unit length for one subband:

$$g_{1D}(E_{1D}) = \frac{1}{L}\frac{dN}{dE_{1D}} = \frac{2}{2\pi} \times \frac{dk_x}{dE_{1D}} \tag{2.43}$$

$$= \frac{1}{\pi}\sqrt{\frac{2m^*}{\hbar^2 E_{1D}}} = \frac{1}{\pi\hbar}\sqrt{\frac{2m^*}{E_{1D}}} \tag{2.44}$$

Result:

$$g_{1D}(E) \propto E^{-1/2} \tag{2.45}$$

Key feature: $g_{1D}(E) \propto E^{-1/2}$ — diverges as $E \to 0$ (Van Hove singularities at subband edges).

2.3.5 Zero-Dimensional (0D) Quantum Dot

In a quantum dot, all three dimensions are confined, leading to complete quantization of energy levels.

$$E_{n_x,n_y,n_z} = \text{discrete values only} \tag{2.46}$$

The density of states becomes a series of delta functions:

$$g_{0D}(E) = \sum_{n_x,n_y,n_z} \delta(E - E_{n_x,n_y,n_z}) \tag{2.47}$$

Key feature: Completely discrete spectrum — atom-like density of states.

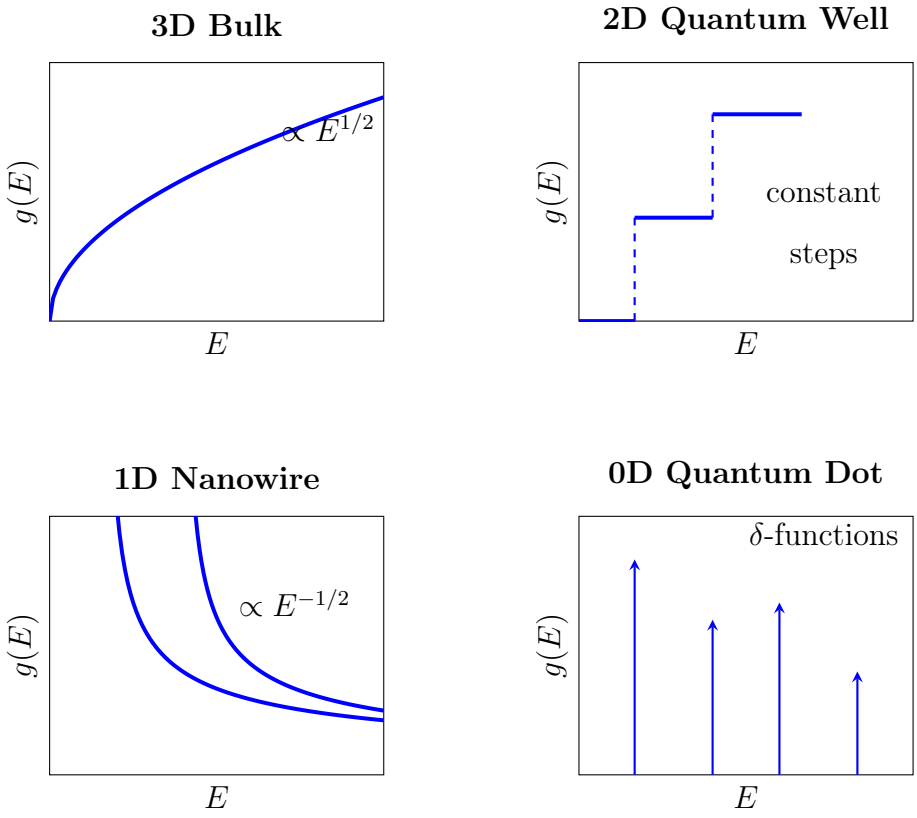

Figure 2.3: Density of states for different dimensional confinement regimes

Table 2.2: Summary of density of states in different dimensions

Dimensionality	**Structure**	**DOS**	**Energy Dependence**
3D	Bulk	$\frac{1}{2\pi^2}\left(\frac{2m^*}{\hbar^2}\right)^{3/2} E^{1/2}$	$E^{1/2}$
2D	Quantum Well	$\frac{m^*}{\pi\hbar^2}$	Constant (per subband)
1D	Nanowire	$\frac{1}{\pi\hbar}\sqrt{\frac{2m^*}{E}}$	$E^{-1/2}$
0D	Quantum Dot	$\sum_n \delta(E - E_n)$	Discrete δ-functions

2.3.6 Physical Consequences of Modified DOS

The modification of DOS in lower dimensions has profound effects on material properties:

1. **Optical Properties:**
   - Sharper absorption features in lower dimensions
   - Enhanced oscillator strength
   - Narrower emission linewidths in quantum dots
2. **Electrical Properties:**
   - Modified carrier concentration: $n = \int g(E)f(E)dE$

- Enhanced mobility in 2D systems (reduced scattering)
- Conductance quantization in 1D

3. **Thermoelectric Properties:**
   - Enhanced Seebeck coefficient in low-D systems
   - Improved thermoelectric figure of merit ZT
4. **Laser Applications:**
   - Lower threshold current in quantum well lasers
   - Temperature-insensitive operation

2.4 Surface-to-Volume Ratio and Its Impact on Properties

2.4.1 Quantitative Analysis of Surface-to-Volume Ratio

As established in Chapter 1, the surface-to-volume ratio scales inversely with characteristic dimension. We now examine the specific physical and chemical consequences.

For a spherical nanoparticle of radius R:

$$\frac{S}{V} = \frac{4\pi R^2}{\frac{4}{3}\pi R^3} = \frac{3}{R} \tag{2.48}$$

The fraction of atoms at or near the surface can be estimated as:

$$f_{surface} = 1 - \left(1 - \frac{t}{R}\right)^3 \approx \frac{3t}{R} \quad \text{for } t << R \tag{2.49}$$

where t is the thickness of the surface layer (typically one or few atomic layers).

Table 2.3: Surface fraction for nanoparticles of different sizes (assuming $t = 0.3$ nm)

Diameter (nm)	Total Atoms	Surface Atoms	Surface Fraction (%)
1	∼30	∼30	99
2	∼250	∼150	60
5	∼4,000	∼960	24
10	∼30,000	∼3,600	12
50	$\sim 4 \times 10^6$	∼96,000	2.4
100	$\sim 3 \times 10^7$	∼380,000	1.2

2.4.2 Impact on Thermodynamic Properties

Melting Point Depression

The Gibbs-Thomson equation relates melting point to particle size:

$$T_m(R) = T_m^\infty \left(1 - \frac{4\sigma_{sl} V_m}{R\Delta H_f}\right) \tag{2.50}$$

where:

- T_m^∞ is the bulk melting temperature
- σ_{sl} is the solid-liquid interfacial energy
- V_m is the molar volume
- ΔH_f is the molar enthalpy of fusion
- R is the particle radius

Physical origin: Surface atoms have fewer nearest neighbors, lower coordination, and are more weakly bound. This destabilizes the solid phase, lowering the melting point.

Example

Melting Point of Gold Nanoparticles
For gold:

- $T_m^\infty = 1337$ K $(1064C)$
- $\sigma_{sl} \approx 0.132$ J/m^2
- $V_m = 10.2 \times 10^{-6}$ m^3/mol
- $\Delta H_f = 12,550$ J/mol

Calculate T_m for Au nanoparticles with $R = 5$ nm:

$$T_m(5 \text{ nm}) = 1337 \times \left(1 - \frac{4 \times 0.132 \times 10.2 \times 10^{-6}}{5 \times 10^{-9} \times 12,550}\right) \tag{2.51}$$

$$= 1337 \times (1 - 0.086) \tag{2.52}$$

$$= 1222 \text{ K} = 949C \tag{2.53}$$

The melting point drops by $115C$ compared to bulk gold!

Surface Energy Contribution

The total energy of a nanoparticle includes bulk and surface contributions:

$$E_{total} = E_{bulk} + E_{surface} = \rho V \epsilon_{bulk} + \sigma S \tag{2.54}$$

where ρ is atomic density, ϵ_{bulk} is energy per atom in bulk, and σ is surface energy per unit area.

For a sphere:

$$E_{total} = \frac{4}{3}\pi R^3 \rho \epsilon_{bulk} + 4\pi R^2 \sigma \tag{2.55}$$

The surface energy becomes dominant for $R < R_{critical} \sim \sigma/(\rho\epsilon_{bulk})$.

2.4.3 Impact on Chemical Properties

Enhanced Catalytic Activity

The catalytic activity often scales with the number of surface atoms. For a mass m of catalyst divided into particles of radius R:

$$\text{Active sites} \propto \frac{m}{R} \tag{2.56}$$

Smaller particles provide more active surface area per unit mass, explaining why metal nanoparticles (Pt, Pd, Au) are exceptional catalysts.

Size-Dependent Reactivity

The adsorption energy of molecules on nanoparticle surfaces depends on particle size due to:

1. Modified electronic structure (quantum confinement)
2. Increased fraction of low-coordination surface sites (edges, corners)
3. Lattice strain effects

Ostwald Ripening

In colloidal suspensions, smaller particles have higher solubility (Gibbs-Thomson effect):

$$\ln\left(\frac{C(R)}{C_\infty}\right) = \frac{2\sigma V_m}{RTR} \tag{2.57}$$

This leads to Ostwald ripening: dissolution of small particles and growth of larger ones.

2.4.4 Impact on Optical Properties

Surface states and surface plasmons become increasingly important:

1. **Surface plasmon resonance:** Collective oscillation of surface electrons
2. **Surface states:** Create additional electronic levels within the band gap
3. **Surface passivation:** Essential for photoluminescence quantum yield

2.5 Quantum Tunneling in Nanostructures

2.5.1 Fundamentals of Quantum Tunneling

Quantum tunneling is the phenomenon where particles penetrate through potential barriers that are classically forbidden. This purely quantum mechanical effect becomes significant in nanoscale devices.

Tunneling Through a Rectangular Barrier

Consider a particle with energy E incident on a potential barrier:

$$V(x) = \begin{cases} 0, & x < 0 \\ V_0, & 0 \leq x \leq a \\ 0, & x > a \end{cases} \tag{2.58}$$

For $E < V_0$ (classically forbidden):

Mathematical Derivation

Transmission Coefficient

In the three regions, the wavefunction has the form:

Region I ($x < 0$):

$$\psi_I(x) = Ae^{ik_1 x} + Be^{-ik_1 x}, \quad k_1 = \sqrt{\frac{2mE}{\hbar^2}} \tag{2.59}$$

Region II ($0 \leq x \leq a$):

$$\psi_{II}(x) = Ce^{\kappa x} + De^{-\kappa x}, \quad \kappa = \sqrt{\frac{2m(V_0 - E)}{\hbar^2}} \tag{2.60}$$

Region III ($x > a$):

$$\psi_{III}(x) = Fe^{ik_1 x} \tag{2.61}$$

Applying boundary conditions (continuity of ψ and ψ' at $x = 0$ and $x = a$), the transmission coefficient is:

$$T = \frac{|F|^2}{|A|^2} = \frac{1}{1 + \frac{V_0^2 \sinh^2(\kappa a)}{4E(V_0 - E)}} \tag{2.62}$$

For $\kappa a >> 1$ (thick barrier or high barrier):

$$T \approx \frac{16E(V_0 - E)}{V_0^2} e^{-2\kappa a} = T_0 e^{-2a\sqrt{2m(V_0 - E)}/\hbar} \tag{2.63}$$

Key Point

Key features of quantum tunneling:

1. Exponential dependence on barrier width: $T \propto e^{-2\kappa a}$
2. Exponential dependence on barrier height: $\kappa \propto \sqrt{V_0 - E}$
3. Non-zero probability even when $E < V_0$
4. Tunneling probability increases dramatically as dimensions shrink to nanoscale

2.5.2 Scanning Tunneling Microscopy (STM)

STM exploits quantum tunneling to image surfaces with atomic resolution. The tunneling current between a sharp metallic tip and conducting surface is:

$$I \propto V e^{-2\kappa d} \tag{2.64}$$

where d is the tip-sample distance and $\kappa \approx 1$ Å^{-1} for typical work functions.

A change of just 1 Å in distance changes the current by a factor of $e^2 \approx 7.4$, providing extreme sensitivity.

2.5.3 Resonant Tunneling

In a double-barrier structure, tunneling probability shows sharp resonances when the electron energy matches a quasi-bound state in the quantum well.

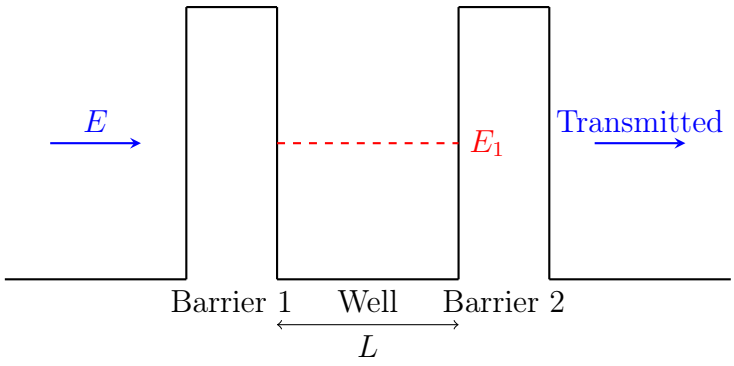

Figure 2.4: Double-barrier resonant tunneling structure

The transmission coefficient shows peaks when:

$$E = E_n = \frac{n^2 \pi^2 \hbar^2}{2m^* L^2}, \quad n = 1, 2, 3, ... \tag{2.65}$$

2.6 Coulomb Blockade and Single-Electron Transistor

2.6.1 Charging Energy of Nanoparticles

When a nanoparticle is small enough, the energy required to add a single electron becomes significant and observable.

The electrostatic energy (charging energy) of a particle with charge $Q = ne$ is:

$$E_C = \frac{Q^2}{2C} = \frac{n^2 e^2}{2C} \tag{2.66}$$

where C is the capacitance of the particle.

For a spherical particle of radius R in vacuum:

$$C = 4\pi\varepsilon_0 R \tag{2.67}$$

The energy to add the n-th electron is:

$$E(n) - E(n-1) = \frac{e^2}{2C}(2n-1) \tag{2.68}$$

The single-electron charging energy is:

$$E_C = \frac{e^2}{2C} = \frac{e^2}{8\pi\varepsilon_0 R} \tag{2.69}$$

Example

Charging Energy Calculation
For a gold nanoparticle with $R = 5$ nm in vacuum:

$$E_C = \frac{(1.602 \times 10^{-19})^2}{8\pi \times 8.854 \times 10^{-12} \times 5 \times 10^{-9}} \tag{2.70}$$

$$= 2.3 \times 10^{-20} \text{ J} = 0.14 \text{ eV} \tag{2.71}$$

Thermal energy at room temperature:

$$k_B T = 0.026 \text{ eV at } T = 300 \text{ K} \tag{2.72}$$

Since $E_C > k_B T$, Coulomb blockade effects should be observable at room temperature!

2.6.2 Coulomb Blockade Phenomenon

Definition

Coulomb Blockade: The suppression of electron tunneling through a small metallic island at low bias voltages due to electrostatic charging energy.

For Coulomb blockade to be observable:

$$E_C >> k_B T \quad \text{and} \quad R_T >> R_Q = \frac{h}{e^2} \approx 26 \text{ k}\Omega \tag{2.73}$$

where R_T is the tunnel junction resistance and R_Q is the quantum resistance.

2.6.3 Single-Electron Transistor (SET)

A SET consists of a small metallic island connected to source and drain electrodes through tunnel junctions, with a gate electrode capacitively coupled to the island.

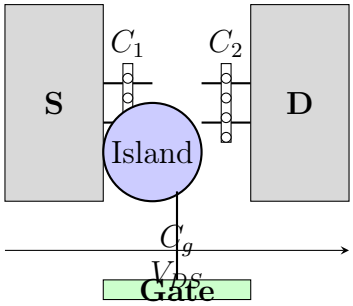

Figure 2.5: Schematic of a single-electron transistor (SET)

The total energy of the system with n excess electrons on the island is:

$$E(n) = \frac{(ne - C_g V_g)^2}{2C_\Sigma} - neV_{DS}/2 \tag{2.74}$$

where $C_\Sigma = C_1 + C_2 + C_g$ is the total capacitance.

Electron tunneling is allowed when:

$$E(n+1) < E(n) \quad \Rightarrow \quad |V_g - V_g^{(n)}| > \frac{e}{2C_g} \tag{2.75}$$

This leads to Coulomb oscillations in conductance as a function of gate voltage, with period:

$$\Delta V_g = \frac{e}{C_g} \tag{2.76}$$

2.7 Quantized Conductance

2.7.1 Landauer Formula

In mesoscopic systems, conductance is not simply determined by Ohm's law. The Landauer formula relates conductance to transmission probability:

$$G = \frac{2e^2}{h} \sum_n T_n \tag{2.77}$$

where the sum is over all conducting channels (modes) and T_n is the transmission probability of the n-th channel.

The quantity $G_0 = \frac{2e^2}{h} = \frac{1}{12.9\ \text{k}\Omega}$ is the conductance quantum.

2.7.2 Quantum Point Contact

In a narrow constriction (quantum point contact), the number of transverse modes is quantized. For a 2D electron gas with constriction width W:

The number of occupied modes at Fermi energy is:

$$N = \text{int}\left(\frac{k_F W}{\pi}\right) \tag{2.78}$$

where k_F is the Fermi wave vector.

For perfect transmission ($T_n = 1$), the conductance is:

$$G = N \times G_0 = N \times \frac{2e^2}{h} \tag{2.79}$$

This leads to conductance quantization in integer multiples of G_0:

$$G = n \times 77.5\ \mu\text{S}, \quad n = 1, 2, 3, ... \tag{2.80}$$

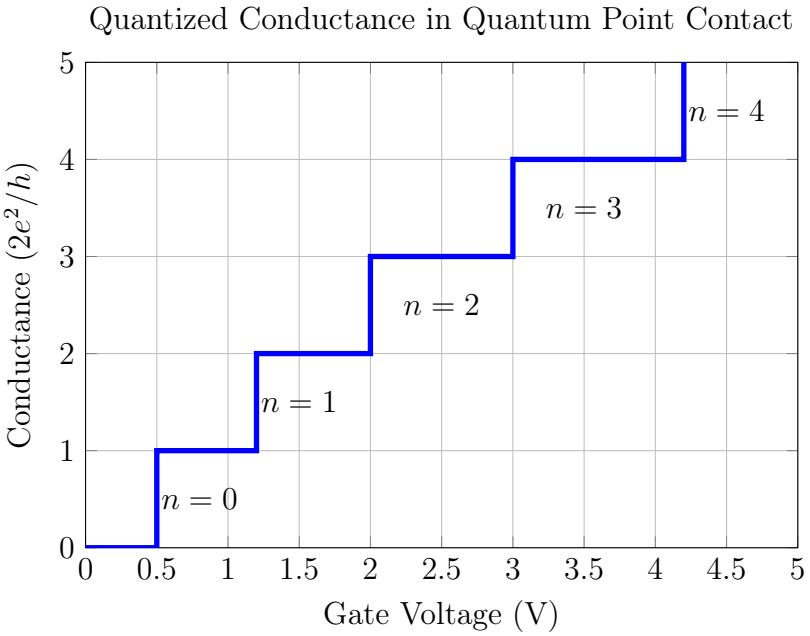

Figure 2.6: Quantized conductance plateaus in a quantum point contact

2.8 Quantum Wells, Wires, and Dots: Detailed Analysis

2.8.1 Quantum Wells

Square Quantum Well

A quantum well is formed when a thin layer of narrow-gap semiconductor is sandwiched between wide-gap barriers.

For a finite square well:

$$V(z) = \begin{cases} V_0, & |z| > L/2 \\ 0, & |z| \leq L/2 \end{cases} \tag{2.81}$$

The energy eigenvalues are found from transcendental equations:

Even states:

$$k \tan(kL/2) = \kappa \tag{2.82}$$

Odd states:

$$-k \cot(kL/2) = \kappa \tag{2.83}$$

where $k = \sqrt{2m^* E/\hbar^2}$ and $\kappa = \sqrt{2m^*(V_0 - E)/\hbar^2}$.

Optical Transitions in Quantum Wells

Selection rules for intersubband transitions:

$$\Delta n = \text{odd} \quad (\text{for } z\text{-polarized light}) \tag{2.84}$$

The absorption coefficient is enhanced compared to bulk due to the step-like DOS.

2.8.2 Quantum Wires

In quantum wires, 1D subbands are formed. For a rectangular wire with dimensions $L_y \times L_z$:

$$E_{n_y,n_z,k_x} = \frac{\hbar^2\pi^2}{2m^*}\left(\frac{n_y^2}{L_y^2} + \frac{n_z^2}{L_z^2}\right) + \frac{\hbar^2 k_x^2}{2m^*} \tag{2.85}$$

Applications:

- Nanowire transistors
- Quantum cascade lasers
- Thermoelectric devices
- Quantum information processing

2.8.3 Quantum Dots: Artificial Atoms

Electronic Structure

Quantum dots are often called "artificial atoms" because of their discrete energy spectrum:

$$E_{n,l,m} = E_{n,l}^{conf} + E_{Coulomb} + E_{exchange-correlation} \tag{2.86}$$

Shell structure emerges similar to atomic orbitals: s, p, d, f shells.

Addition Energy Spectrum

The energy to add the N-th electron:

$$\mu(N) = E_{total}(N) - E_{total}(N-1) \tag{2.87}$$

Shows peaks at "magic numbers" corresponding to closed shells.

Applications of Quantum Dots

1. **Display Technology:** QLED TVs using CdSe/ZnS quantum dots
2. **Biomedical Imaging:** Fluorescent labels with tunable emission
3. **Solar Cells:** Multiple exciton generation, intermediate band cells
4. **Quantum Computing:** Spin qubits in semiconductor quantum dots

5. **Single-Photon Sources:** For quantum cryptography
6. **Lasers:** Low-threshold, temperature-insensitive quantum dot lasers

Table 2.4: Comparison of quantum wells, wires, and dots

Property	**Quantum Well (2D)**	**Quantum Wire (1D)**	**Quantum Dot (0D)**
Confinement	One dimension	Two dimensions	Three dimensions
DOS	Step function	$E^{-1/2}$ singularities	δ-functions
Typical size	2-20 nm (thickness)	5-50 nm (diameter)	2-10 nm (all dimensions)
Energy spectrum	Discrete subbands	1D subbands	Fully discrete
Main applications	Lasers, modulators	Sensors, transistors	Displays, bioimaging, qubits
Fabrication	MBE, MOCVD	VLS, template	Colloidal synthesis, self-assembly

2.9 Simulation Example: Quantum Confinement in a Nanoparticle

In this section, we provide a Python simulation to visualize quantum confinement effects in a spherical quantum dot.

2.9.1 Theoretical Background for Simulation

We simulate a particle in a spherical potential well using the effective mass approximation. The energy eigenvalues for $l = 0$ (s-states) in a spherical well of radius R are:

$$E_n = \frac{\hbar^2 \chi_n^2}{2m^* R^2} \tag{2.88}$$

where $\chi_n = n\pi$ for an infinite well.
The radial wavefunctions are:

$$\psi_n(r) = A_n \frac{\sin(n\pi r/R)}{r}, \quad r \leq R \tag{2.89}$$

2.9.2 Python Code

```
import numpy as np
import matplotlib.pyplot as plt
from scipy.special import spherical_jn
from scipy.optimize import fsolve

# Physical constants
hbar = 1.055e-34  # J*s
```

```
e = 1.602e-19      # C
m_e = 9.109e-31    # kg

# Material parameters for CdSe
m_eff_electron = 0.13 * m_e  # Effective mass of electron
m_eff_hole = 0.45 * m_e      # Effective mass of hole
eps_r = 10.0                  # Relative permittivity
E_g_bulk = 1.74              # Bulk band gap (eV)

def calculate_energy_levels(R, n_max=5):
    """
    Calculate energy levels for a spherical quantum dot

    Parameters:
    R: radius in nm
    n_max: maximum quantum number

    Returns:
    energies: array of energy levels in eV
    """
    R_m = R * 1e-9  # Convert to meters
    energies = []

    for n in range(1, n_max + 1):
        # Confinement energy for electron
        E_e = (n**2 * np.pi**2 * hbar**2) / (2 * m_eff_electron *
           R_m**2)

        # Confinement energy for hole
        E_h = (n**2 * np.pi**2 * hbar**2) / (2 * m_eff_hole * R_m
           **2)

        # Coulomb interaction
        E_coulomb = -1.8 * e**2 / (4 * np.pi * 8.854e-12 * eps_r *
            R_m)

        # Total energy (in eV)
        E_total = E_g_bulk + (E_e + E_h) / e + E_coulomb / e
        energies.append(E_total)

    return np.array(energies)

def calculate_wavefunction(R, n, r_points=1000):
    """
    Calculate radial wavefunction for quantum number n

    Parameters:
    R: radius in nm
    n: quantum number
    r_points: number of points for plotting

```

```
    Returns:
    r: radial coordinates
    psi: wavefunction values
    """
    r = np.linspace(0, R, r_points)

    # Avoid division by zero at r=0
    r[0] = 1e-3

    # Wavefunction: sin(n*pi*r/R) / r
    psi = np.sin(n * np.pi * r / R) / r

    # Normalization
    norm = np.sqrt(np.trapz(psi**2 * r**2, r))
    psi = psi / norm

    return r, psi

def plot_size_dependent_bandgap():
    """
    Plot band gap as a function of quantum dot size
    """
    radii = np.linspace(1, 10, 100)  # nm
    bandgaps = []

    for R in radii:
        E = calculate_energy_levels(R, n_max=1)
        bandgaps.append(E[0])

    plt.figure(figsize=(10, 6))
    plt.plot(radii, bandgaps, 'b-', linewidth=2, label='Quantum
       Confined')
    plt.axhline(y=E_g_bulk, color='r', linestyle='--',
                linewidth=2, label=f'Bulk CdSe ({E_g_bulk} eV)')

    # Mark exciton Bohr radius
    plt.axvline(x=5.6, color='g', linestyle='--',
                linewidth=1.5, label='Exciton Bohr Radius')

    plt.xlabel('Quantum Dot Radius (nm)', fontsize=12)
    plt.ylabel('Band Gap Energy (eV)', fontsize=12)
    plt.title('Size-Dependent Band Gap of CdSe Quantum Dots',
              fontsize=14, fontweight='bold')
    plt.legend(fontsize=11)
    plt.grid(True, alpha=0.3)
    plt.tight_layout()
    plt.savefig('bandgap_vs_size.png', dpi=300)
    plt.show()

def plot_wavefunctions():
    """
```

```
    Plot wavefunctions for different quantum numbers
    """
    R = 5  # nm

    fig, (ax1, ax2) = plt.subplots(1, 2, figsize=(14, 5))

    colors = ['blue', 'red', 'green', 'purple']

    # Plot radial wavefunctions
    for n in range(1, 5):
        r, psi = calculate_wavefunction(R, n)
        ax1.plot(r, psi, linewidth=2, label=f'n={n}', color=colors
           [n-1])

    ax1.set_xlabel('Radius r (nm)', fontsize=12)
    ax1.set_ylabel('Wavefunction  (r)', fontsize=12)
    ax1.set_title('Radial Wavefunctions', fontsize=14, fontweight=
       'bold')
    ax1.legend(fontsize=11)
    ax1.grid(True, alpha=0.3)
    ax1.axhline(y=0, color='k', linewidth=0.5)

    # Plot probability densities
    for n in range(1, 5):
        r, psi = calculate_wavefunction(R, n)
        prob_density = psi**2 * r**2
        ax2.plot(r, prob_density, linewidth=2,
                label=f'n={n}', color=colors[n-1])

    ax2.set_xlabel('Radius r (nm)', fontsize=12)
    ax2.set_ylabel('Probability Density r |  (r)|  ', fontsize
       =12)
    ax2.set_title('Radial Probability Densities',
                  fontsize=14, fontweight='bold')
    ax2.legend(fontsize=11)
    ax2.grid(True, alpha=0.3)

    plt.tight_layout()
    plt.savefig('wavefunctions.png', dpi=300)
    plt.show()

def plot_energy_spectrum():
    """
    Plot energy level spectrum for different sizes
    """
    sizes = [2, 3, 5, 8]  # nm

    fig, ax = plt.subplots(figsize=(12, 8))

    for i, R in enumerate(sizes):
        energies = calculate_energy_levels(R, n_max=5)
```

```
        x_pos = i * 1.5

        for j, E in enumerate(energies):
            ax.hlines(E, x_pos - 0.3, x_pos + 0.3,
                      colors='blue', linewidth=3)
            if j == 0:
                ax.text(x_pos + 0.4, E, f'{E:.2f} eV',
                        fontsize=9, va='center')

        ax.text(x_pos, 1.5, f'R = {R} nm',
                fontsize=11, ha='center', fontweight='bold')

    # Bulk band gap line
    ax.axhline(y=E_g_bulk, color='red', linestyle='--',
               linewidth=2, label='Bulk CdSe')

    ax.set_ylabel('Energy (eV)', fontsize=13)
    ax.set_title('Energy Level Spectrum for Different QD Sizes',
                 fontsize=15, fontweight='bold')
    ax.set_xlim(-0.5, (len(sizes)-1)*1.5 + 0.5)
    ax.set_ylim(1.5, 4.0)
    ax.legend(fontsize=12)
    ax.grid(True, alpha=0.3, axis='y')
    ax.set_xticks([])

    plt.tight_layout()
    plt.savefig('energy_spectrum.png', dpi=300)
    plt.show()

def emission_wavelength_vs_size():
    """
    Calculate and plot emission wavelength vs size
    """
    radii = np.linspace(1.5, 8, 100)
    wavelengths = []

    for R in radii:
        E = calculate_energy_levels(R, n_max=1)[0]
        # Convert energy (eV) to wavelength (nm)
        wavelength = 1240 / E  # Using E(eV) *   (nm) = 1240
        wavelengths.append(wavelength)

    plt.figure(figsize=(10, 6))
    plt.plot(radii, wavelengths, 'b-', linewidth=2.5)

    # Color-coded regions
    plt.axhspan(400, 450, alpha=0.2, color='blue', label='Blue')
    plt.axhspan(450, 500, alpha=0.2, color='cyan', label='Cyan')
    plt.axhspan(500, 570, alpha=0.2, color='green', label='Green')
    plt.axhspan(570, 590, alpha=0.2, color='yellow', label='Yellow
        ')
```

```
    plt.axhspan(590, 620, alpha=0.2, color='orange', label='Orange')
    plt.axhspan(620, 750, alpha=0.2, color='red', label='Red')

    plt.xlabel('Quantum Dot Radius (nm)', fontsize=12)
    plt.ylabel('Emission Wavelength (nm)', fontsize=12)
    plt.title('Size-Tunable Emission from CdSe Quantum Dots',
              fontsize=14, fontweight='bold')
    plt.legend(loc='upper right', fontsize=10)
    plt.grid(True, alpha=0.3)
    plt.ylim(400, 750)
    plt.tight_layout()
    plt.savefig('emission_wavelength.png', dpi=300)
    plt.show()

# Run all simulations
if __name__ == "__main__":
    print("Quantum Confinement Simulation for CdSe Quantum Dots")
    print("=" * 60)

    # Generate all plots
    print("\n1. Generating band gap vs size plot...")
    plot_size_dependent_bandgap()

    print("2. Generating wavefunction plots...")
    plot_wavefunctions()

    print("3. Generating energy spectrum plot...")
    plot_energy_spectrum()

    print("4. Generating emission wavelength plot...")
    emission_wavelength_vs_size()

    # Print some example calculations
    print("\n" + "=" * 60)
    print("Example Calculations:")
    print("=" * 60)

    for R in [2, 3, 5]:
        E = calculate_energy_levels(R, n_max=1)[0]
        wavelength = 1240 / E
        print(f"\nRadius = {R} nm:")
        print(f"  Band gap = {E:.3f} eV")
        print(f"  Emission wavelength = {wavelength:.1f} nm")
        print(f"  Color: ", end="")
        if wavelength < 450:
            print("Blue")
        elif wavelength < 500:
            print("Cyan")
        elif wavelength < 570:
            print("Green")
```

```
        elif wavelength < 590:
            print("Yellow")
        elif wavelength < 620:
            print("Orange")
        else:
            print("Red")

    print("\n" + "=" * 60)
    print("Simulation complete! Plots saved as PNG files.")
    print("=" * 60)
```

Listing 2.1: Quantum confinement simulation for a spherical quantum dot

2.9.3 Expected Output and Interpretation

The simulation generates four plots:

1. **Band Gap vs. Size:** Shows the characteristic $1/R^2$ dependence of the quantum confinement energy
2. **Wavefunctions:** Displays the radial wavefunctions and probability densities for different quantum numbers
3. **Energy Spectrum:** Illustrates how the discrete energy levels change with quantum dot size
4. **Emission Wavelength:** Demonstrates size-tunable optical properties spanning the visible spectrum

Key Observations from Simulation:

- As QD radius decreases from 8 nm to 2 nm, band gap increases from ∼1.85 eV to ∼2.8 eV
- Corresponding emission shifts from red (670 nm) to blue (440 nm)
- Strong confinement regime ($R < a_B$) shows most dramatic effects
- Energy level spacing increases with decreasing size
- Number of nodes in wavefunctions increases with quantum number n

2.10 Summary

This chapter has explored the fundamental quantum phenomena that emerge in nanomaterials:

1. **Quantum Confinement:** Spatial restriction leads to energy quantization and size-dependent properties. The Brus equation describes band gap tuning in quantum dots.

2. **Density of States:** Dimensionality dramatically affects DOS:
   - 3D: $g(E) \propto E^{1/2}$
   - 2D: $g(E) = \text{constant}$
   - 1D: $g(E) \propto E^{-1/2}$
   - 0D: $g(E) = \sum \delta(E - E_n)$
3. **Surface Effects:** High surface-to-volume ratio affects melting point, reactivity, catalytic activity, and optical properties.
4. **Quantum Tunneling:** Exponential dependence on barrier width enables STM and resonant tunneling devices.
5. **Coulomb Blockade:** Single-electron charging effects in nanoparticles enable single-electron transistors.
6. **Quantized Conductance:** Mesoscopic transport shows discrete conductance values in units of $2e^2/h$.
7. **Low-Dimensional Systems:** Quantum wells, wires, and dots exhibit unique electronic structures with diverse applications.

These quantum phenomena form the foundation for nanoscale devices and provide unprecedented control over material properties through size and shape engineering.

Exercises

Conceptual Questions

1. Explain physically why quantum confinement leads to an increase in band gap energy. Why doesn't classical physics predict this effect?
2. Why does the density of states become constant in 2D systems? Derive this result geometrically by considering the area in k-space.
3. Discuss the relationship between exciton Bohr radius and quantum confinement regimes. What changes in the physics when $R < a_B$ vs. $R > a_B$?
4. Explain why the Coulomb term in the Brus equation is negative. Under what conditions can it be neglected?
5. How does the Van Hove singularity in 1D DOS affect optical absorption spectra?
6. Why is quantum tunneling probability exponentially sensitive to barrier width? Derive this dependence from the wavefunction decay.
7. Explain why Coulomb blockade requires both $E_C >> k_B T$ and $R_T >> R_Q$. What happens if only one condition is satisfied?
8. Discuss why conductance quantization occurs in integer multiples of $2e^2/h$. What is the physical significance of the factor of 2?

9. Compare and contrast quantum dots with natural atoms. In what ways are they similar and different?

10. Why do smaller nanoparticles have lower melting points? Discuss the thermodynamic origin.

Numerical Problems

1. An electron is confined in a 1D infinite potential well of width $L = 5$ nm.

   (a) Calculate the first three energy levels

   (b) Calculate the wavelength of light emitted in the $n = 3 \to n = 2$ transition

   (c) What is the zero-point energy?

2. A CdTe quantum dot has a radius of 3 nm. Given: $m_e^* = 0.11m_0$, $m_h^* = 0.35m_0$, $\varepsilon_r = 10.4$, $E_g^{bulk} = 1.50$ eV.

   (a) Calculate the quantum confinement energy for electron and hole

   (b) Calculate the Coulomb interaction energy

   (c) What is the total band gap?

   (d) What is the emission wavelength?

3. Calculate the 3D density of states for electrons in GaAs at $E = 0.1$ eV above the conduction band minimum. Given: $m^* = 0.067m_0$.

4. For a 2D quantum well of thickness 10 nm:

   (a) Calculate the confinement energies of the first three subbands

   (b) Calculate the 2D DOS per unit area

   (c) Sketch the total DOS including all subbands up to $E = 0.3$ eV

5. An electron with energy $E = 2$ eV approaches a potential barrier of height $V_0 = 5$ eV and width $a = 1$ nm.

   (a) Calculate the decay constant κ

   (b) Calculate the transmission probability

   (c) How does T change if barrier width doubles?

6. A gold nanoparticle has radius $R = 3$ nm.

   (a) Calculate the charging energy in eV

   (b) At what temperature is $E_C = 10k_BT$?

   (c) Calculate the period of Coulomb oscillations if $C_g = 1$ aF

7. A 2D electron gas forms a quantum point contact with Fermi wavelength $\lambda_F = 40$ nm.

   (a) Calculate the constriction width when exactly 5 modes are transmitted

   (b) What is the conductance in this configuration?

(c) What gate voltage change is needed to reduce to 4 modes if $\Delta V_g = 0.1$ V per mode?

8. For a PbS quantum dot with $a_B = 20$ nm and $E_g^{bulk} = 0.41$ eV:

   (a) Calculate the size needed for emission at 1000 nm (IR)

   (b) Calculate the size needed for emission at 600 nm (visible)

   (c) Plot band gap vs. radius from 5 nm to 25 nm

9. A nanowire has rectangular cross-section 10 nm × 15 nm. Calculate:

   (a) The confinement energies of the first 6 subbands

   (b) Which subbands are degenerate?

   (c) The 1D DOS for the lowest subband at $E_{1D} = 0.05$ eV

10. Calculate the fraction of surface atoms for:

    (a) Spherical Au nanoparticle, $R = 2$ nm

    (b) Cubic Si nanoparticle, side length = 5 nm

    (c) Compare surface-to-volume ratios

Advanced Problems

1. Derive the Brus equation starting from the effective mass Hamiltonian. Include all terms and discuss the validity of approximations.

2. Calculate the density of states for a 1D system with dispersion relation $E(k) = \alpha k^2 + \beta k^4$. How does it differ from the parabolic case?

3. Design a resonant tunneling diode using GaAs/AlGaAs heterostructures. Specify:

   (a) Layer thicknesses

   (b) Barrier heights

   (c) Expected resonance energies

   (d) I-V characteristics

4. Modify the Python simulation to:

   (a) Include finite barrier height (use scipy.special.spherical$_j n$)

   (a) Calculate oscillator strength for optical transitions

   (b) Model core/shell quantum dots (CdSe/ZnS)

   (c) Include temperature-dependent linewidth

5. Derive the Landauer formula from first principles using scattering theory. Include spin degeneracy and multiple channels.

Bibliography

[1] Harrison, P. (2005). *Quantum Wells, Wires and Dots: Theoretical and Computational Physics of Semiconductor Nanostructures* (2nd ed.). John Wiley & Sons, Chichester.

[2] Davies, J. H. (1998). *The Physics of Low-Dimensional Semiconductors: An Introduction*. Cambridge University Press, Cambridge.

[3] Singh, J. (2003). *Electronic and Optoelectronic Properties of Semiconductor Structures*. Cambridge University Press, Cambridge.

[4] Datta, S. (1995). *Electronic Transport in Mesoscopic Systems*. Cambridge University Press, Cambridge.

[5] Brus, L. E. (1984). Electron-electron and electron-hole interactions in small semiconductor crystallites: The size dependence of the lowest excited electronic state. *Journal of Chemical Physics*, 80(9), 4403-4409.

[6] Murray, C. B., Norris, D. J., & Bawendi, M. G. (1993). Synthesis and characterization of nearly monodisperse CdE (E = S, Se, Te) semiconductor nanocrystallites. *Journal of the American Chemical Society*, 115(19), 8706-8715.

[7] Efros, Al. L., & Efros, A. L. (1982). Interband absorption of light in a semiconductor sphere. *Soviet Physics Semiconductors*, 16(7), 772-775.

[8] Alivisatos, A. P. (1996). Perspectives on the physical chemistry of semiconductor nanocrystals. *Journal of Physical Chemistry*, 100(31), 13226-13239.

[9] Klimov, V. I. (Ed.). (2006). *Semiconductor and Metal Nanocrystals: Synthesis and Electronic and Optical Properties*. CRC Press, Boca Raton.

[10] Kouwenhoven, L. P., Austing, D. G., Tarucha, S. (2001). Few-electron quantum dots. *Reports on Progress in Physics*, 64(6), 701-736.

[11] Beenakker, C. W. J., van Houten, H. (1991). Quantum transport in semiconductor nanostructures. *Solid State Physics*, 44, 1-228.

[12] Landauer, R. (1957). Spatial variation of currents and fields due to localized scatterers in metallic conduction. *IBM Journal of Research and Development*, 1(3), 223-231.

[13] van Wees, B. J., van Houten, H., Beenakker, C. W. J., Williamson, J. G., Kouwenhoven, L. P., van der Marel, D., Foxon, C. T. (1988). Quantized conductance of point contacts in a two-dimensional electron gas. *Physical Review Letters*, 60(9), 848-850.

[14] Likharev, K. K. (1999). Single-electron devices and their applications. *Proceedings of the IEEE*, 87(4), 606-632.

[15] Fulton, T. A., Dolan, G. J. (1987). Observation of single-electron charging effects in small tunnel junctions. *Physical Review Letters*, 59(1), 109-112.

[16] Grabert, H., Devoret, M. H. (Eds.). (1992). *Single Charge Tunneling: Coulomb Blockade Phenomena in Nanostructures*. Springer, New York.

[17] Bastard, G. (1988). *Wave Mechanics Applied to Semiconductor Heterostructures*. Les Editions de Physique, Les Ulis.

[18] Weisbuch, C., Vinter, B. (1991). *Quantum Semiconductor Structures: Fundamentals and Applications*. Academic Press, Boston.

[19] Kelly, M. J. (2003). *Low-Dimensional Semiconductors: Materials, Physics, Technology, Devices*. Oxford University Press, Oxford.

Chapter 3

Structural, Electrical, Optical, and Magnetic Properties

"The properties of materials at the nanoscale are not simply scaled-down versions of bulk properties—they represent a fundamentally different regime of matter."
— G. A. Ozin

3.1 Introduction

The transition from bulk materials to nanoscale dimensions triggers profound changes in structural, electronic, optical, magnetic, and mechanical properties. These modifications arise from fundamental physical phenomena including quantum confinement, increased surface-to-volume ratio, surface energy effects, and altered inter-atomic interactions.

In this chapter, we explore how reducing material dimensions to the nanoscale transforms:

- **Structural properties:** Crystal structure stability, defect formation energies, and lattice parameters
- **Electronic properties:** Band structure, density of states, and charge transport
- **Optical properties:** Absorption spectra, photoluminescence, and plasmonic behavior
- **Magnetic properties:** Magnetic ordering, coercivity, and superparamagnetic transitions
- **Mechanical properties:** Strength, hardness, and elastic modulus

3.2 Crystal Structure and Defects in Nanomaterials

3.2.1 Structural Considerations at the Nanoscale

Lattice Parameter Variations

As particle size decreases, the lattice parameter (unit cell dimension) often deviates from bulk values due to surface stress and reduced coordination number of surface atoms.

For nanoparticles, the lattice parameter $a(r)$ varies with radius r according to:

$$\frac{a(r) - a_\infty}{a_\infty} = -\frac{2\alpha}{r} \tag{3.1}$$

where a_∞ is the bulk lattice parameter and α is a material-dependent constant related to surface stress.

This relationship derives from thermodynamic considerations. The equilibrium lattice parameter minimizes the total free energy:

$$G_{total} = G_{bulk}(a) + \gamma(a) \cdot A \tag{3.2}$$

where $\gamma(a)$ is the surface energy and A is the surface area.

Example

Lattice contraction in CdSe nanocrystals
For CdSe quantum dots:

- Bulk lattice parameter: $a_\infty = 6.05$ Å
- For $r = 1.5$ nm: $a \approx 6.02$ Å (0.5% contraction)
- For $r = 3.0$ nm: $a \approx 6.04$ Å (0.16% contraction)

This contraction affects electronic structure and optical properties.

Crystal Structure Stability

Nanomaterials can exhibit crystal structures different from their bulk counterparts due to surface energy minimization. The stable phase is determined by minimizing total Gibbs free energy:

$$G = G_V \cdot V + \gamma \cdot A \tag{3.3}$$

For a spherical particle of radius r:

$$G = \frac{4}{3}\pi r^3 G_V + 4\pi r^2 \gamma \tag{3.4}$$

Different crystal phases have different bulk free energies (G_V) and surface energies (γ). The critical size for phase transition:

$$r_c = \frac{3(\gamma_2 - \gamma_1)}{G_{V,1} - G_{V,2}} \tag{3.5}$$

Table 3.1: Size-dependent phase transitions in common nanomaterials

Material	Bulk Phase	Nanophase	Critical Size
TiO_2	Rutile	Anatase	< 14 nm
ZrO_2	Monoclinic	Tetragonal	< 30 nm
CdSe	Wurtzite	Rock salt	High pressure
Au	FCC	Icosahedral	< 3 nm
Si	Diamond	Amorphous	< 2 nm

3.2.2 Defects in Nanomaterials

Classification of Defects

Crystal defects are classified by dimensionality:

1. **Point defects (0D):** Vacancies, interstitials, substitutional atoms
2. **Line defects (1D):** Dislocations (edge, screw, mixed)
3. **Planar defects (2D):** Grain boundaries, stacking faults, twin boundaries
4. **Volume defects (3D):** Voids, precipitates, inclusions

Defect Formation Energy

The formation energy of a defect is the energy required to create it. For a vacancy:

$$E_f^{vac} = E_{N-1} - \frac{N-1}{N} E_N \tag{3.6}$$

The equilibrium concentration of vacancies follows Arrhenius behavior:

$$n_{vac} = N \exp\left(-\frac{E_f^{vac}}{k_B T}\right) \tag{3.7}$$

In nanomaterials, defect formation energies are size-dependent:

$$E_f(r) = E_f^{\infty}\left(1 - \frac{\beta}{r}\right) \tag{3.8}$$

Key Point

Nanomaterials often exhibit higher defect concentrations than bulk due to:

- Reduced defect formation energies
- Large surface-to-volume ratio
- Non-equilibrium synthesis conditions
- Surface reconstruction effects

Grain Boundaries in Nanocrystalline Materials

Nanocrystalline materials with grain sizes < 100 nm contain significant grain boundary volume fraction:

$$f_{GB} = \frac{3\delta}{d} \tag{3.9}$$

where δ is grain boundary thickness ($\sim 0.5 - 1$ nm) and d is grain size.
For $d = 10$ nm and $\delta = 0.5$ nm: $f_{GB} = 15\%$

Table 3.2: Grain boundary volume fraction vs. grain size

Grain Size (nm)	GB Thickness (nm)	GB Fraction (%)
5	0.5	30
10	0.5	15
20	0.5	7.5
50	0.5	3
100	0.5	1.5

3.3 Electronic Structure Modifications at Nanoscale

3.3.1 Band Structure Evolution with Size

From Discrete to Continuous: Molecular to Bulk

The electronic structure transitions from discrete molecular orbitals to continuous energy bands as the number of atoms increases:

$$\text{Atom} \rightarrow \text{Molecule} \rightarrow \text{Cluster} \rightarrow \text{Nanoparticle} \rightarrow \text{Bulk} \tag{3.10}$$

For a system of N identical atoms, tight-binding approximation gives:

$$E(k) = E_0 + 2t\cos(ka) \tag{3.11}$$

where E_0 is atomic energy level, t is hopping integral, and a is lattice constant.
For finite nanoparticles with N atoms, k is quantized:

$$k_n = \frac{n\pi}{(N+1)a}, \quad n = 1, 2, ..., N \tag{3.12}$$

giving N discrete energy levels:

$$E_n = E_0 + 2t\cos\left(\frac{n\pi}{N+1}\right) \tag{3.13}$$

Quantum Confinement Effects on Band Gap

For semiconductors, quantum confinement increases band gap energy. Using effective mass approximation:

Mathematical Derivation

Band gap modification due to quantum confinement
For strong confinement ($R < a_B$), the band gap becomes:

$$E_g(R) = E_g^{bulk} + \frac{\hbar^2\pi^2}{2R^2}\left(\frac{1}{m_e^*} + \frac{1}{m_h^*}\right) - \frac{1.8e^2}{4\pi\varepsilon_0\varepsilon_r R} \tag{3.14}$$

This can be written as:

$$E_g(R) = E_g^{bulk} + \frac{\hbar^2\pi^2}{2\mu R^2} - \frac{1.8e^2}{4\pi\varepsilon_0\varepsilon_r R} \tag{3.15}$$

where $\mu = \frac{m_e^* m_h^*}{m_e^* + m_h^*}$ is the reduced effective mass.
The three terms represent:

- Bulk band gap energy
- Quantum confinement (kinetic) energy $\propto R^{-2}$
- Coulombic attraction energy $\propto R^{-1}$

3.3.2 Density of States Modifications

The density of states (DOS) $g(E)$ describes the number of electronic states per unit energy per unit volume. It fundamentally changes with dimensionality.

DOS in Different Dimensions

For a free electron gas:

3D Bulk:

$$g_{3D}(E) = \frac{1}{2\pi^2}\left(\frac{2m}{\hbar^2}\right)^{3/2} E^{1/2} \propto E^{1/2} \tag{3.16}$$

2D Quantum Well:

$$g_{2D}(E) = \frac{m}{\pi\hbar^2}\sum_n \Theta(E - E_n) = \text{constant (step function)} \tag{3.17}$$

1D Nanowire:

$$g_{1D}(E) = \frac{1}{\pi}\sqrt{\frac{2m}{\hbar^2}}\sum_{n,m}\frac{1}{\sqrt{E - E_{n,m}}} \propto E^{-1/2} \tag{3.18}$$

0D Quantum Dot:

$$g_{0D}(E) = 2\sum_{n,l,m}\delta(E - E_{n,l,m}) = \text{discrete levels} \tag{3.19}$$

Table 3.3: Summary of density of states in different dimensions

System	Confinement	DOS Energy Dependence
3D Bulk	None	$E^{1/2}$ (continuous)
2D Quantum Well	1D	Constant (steps)
1D Nanowire	2D	$E^{-1/2}$ (singularities)
0D Quantum Dot	3D	δ-functions (discrete)

3.3.3 Work Function Modifications

The work function Φ (energy to remove electron from Fermi level to vacuum) changes with nanoparticle size:

$$\Phi(r) = \Phi_\infty + \frac{e^2}{8\pi\varepsilon_0 r} \tag{3.20}$$

This affects catalytic activity, contact resistance, field emission, and electrochemical behavior.

3.4 Optical Absorption and Photoluminescence

3.4.1 Optical Absorption in Nanomaterials

Fundamental Principles

Light absorption occurs when photon energy matches electronic transition energy. The absorption coefficient:

$$\alpha(\omega) = \frac{2\omega}{c}\kappa(\omega) \tag{3.21}$$

For direct band gap semiconductors:

$$\alpha(h\nu) = A\frac{\sqrt{h\nu - E_g}}{h\nu} \tag{3.22}$$

Quantum Size Effects

As nanoparticle size decreases:

- Band gap increases → absorption edge blue-shifts
- Discrete energy levels → sharp absorption features
- Enhanced oscillator strength

Surface Plasmon Resonance (SPR)

Metal nanoparticles exhibit strong absorption due to collective oscillation of conduction electrons. For spherical particles with radius $r << \lambda$:

$$C_{ext} = \frac{24\pi^2 r^3 \varepsilon_m^{3/2}}{\lambda} \frac{\varepsilon_2}{(\varepsilon_1 + 2\varepsilon_m)^2 + \varepsilon_2^2} \tag{3.23}$$

Resonance occurs when:

$$\varepsilon_1(\omega) = -2\varepsilon_m \quad \text{(Fröhlich condition)} \tag{3.24}$$

Table 3.4: Surface plasmon resonance wavelengths for metal nanoparticles

Metal	SPR (nm)	Color	Application
Ag	400-420	Yellow	SERS, sensors
Au	520-530	Red	Biodiagnostics
Cu	560-570	Red-orange	Catalysis
Au nanorods	650-900	Blue-IR	Photothermal therapy

3.4.2 Photoluminescence (PL) in Nanomaterials

PL Mechanisms

Photoluminescence involves:

1. **Absorption:** Photon excites electron from valence to conduction band
2. **Thermalization:** Carriers relax to band edges ($\sim$ ps)
3. **Radiative recombination:** Electron-hole recombination emitting photon

Quantum Yield

The photoluminescence quantum yield (PLQY):

$$\Phi_{PL} = \frac{\text{photons emitted}}{\text{photons absorbed}} = \frac{\Gamma_{rad}}{\Gamma_{rad} + \Gamma_{non-rad}} \tag{3.25}$$

The PL lifetime:

$$\tau_{PL} = \frac{1}{\Gamma_{rad} + \Gamma_{non-rad}} \tag{3.26}$$

For high-quality quantum dots: $\Phi_{PL} > 80\%$, $\tau_{PL} \sim 10 - 100$ ns.

Stokes Shift

The energy difference between absorption and emission peaks:

$$\Delta E_{Stokes} = E_{abs} - E_{PL} \tag{3.27}$$

Origins: thermalization to band edge, lattice relaxation (Franck-Condon effect), energy transfer to surface states.

Typical values: 50-200 meV for quantum dots.

Example

CdSe/ZnS Core-Shell Quantum Dots

- Core size: 3 nm CdSe, Shell: 2 monolayers ZnS
- Absorption peak: 540 nm (2.30 eV)
- Emission peak: 560 nm (2.21 eV)
- Stokes shift: 0.09 eV = 90 meV
- PLQY: 85%, PL lifetime: 25 ns

The ZnS shell passivates surface defects, increasing PLQY from ∼15% (bare CdSe) to 85%.

3.5 Magnetic Properties: Superparamagnetism and Exchange Bias

3.5.1 Magnetic Behavior at the Nanoscale

Single-Domain Transition

Bulk ferromagnetic materials contain multiple magnetic domains. The critical size for single-domain formation:

$$d_c \approx \frac{9\sqrt{AK_1}}{\mu_0 M_s^2} \tag{3.28}$$

where A is exchange stiffness, K_1 is anisotropy constant, M_s is saturation magnetization.

Table 3.5: Critical single-domain sizes for magnetic materials

Material	M_s **(kA/m)**	K_1 **(kJ/m^3)**	d_c **(nm)**
Fe	1707	48	15
Co	1422	450	35
Ni	485	-5	30
Fe_3O_4	480	-11	128
$CoFe_2O_4$	425	200	70

3.5.2 Superparamagnetism

Theory

For single-domain nanoparticles, thermal energy can overcome anisotropy energy barrier, causing spontaneous magnetization reversal.

Energy barrier for magnetization reversal:

$$E_b = KV \tag{3.29}$$

where K is effective anisotropy constant and V is particle volume.

Relaxation time (Néel-Brown model):

$$\tau = \tau_0 \exp\left(\frac{KV}{k_B T}\right) \tag{3.30}$$

where $\tau_0 \sim 10^{-9} - 10^{-11}$ s.

Mathematical Derivation

Blocking Temperature

The blocking temperature T_B separates superparamagnetic and blocked states:

$$\tau_m = \tau_0 \exp\left(\frac{KV}{k_B T_B}\right) \tag{3.31}$$

Solving for T_B:

$$T_B = \frac{KV}{k_B \ln(\tau_m/\tau_0)} \tag{3.32}$$

For typical values ($\tau_m = 100$ s, $\tau_0 = 10^{-10}$ s):

$$T_B \approx \frac{KV}{25 k_B} \tag{3.33}$$

Thus $T_B \propto V$ (or $T_B \propto d^3$ for spheres).

Langevin Function

In superparamagnetic state, magnetization follows Langevin function:

$$M(H) = M_s \left[\coth\left(\frac{\mu H}{k_B T}\right) - \frac{k_B T}{\mu H}\right] \tag{3.34}$$

where $\mu = M_s V$ is particle magnetic moment.

For small fields:

$$M(H) \approx \frac{M_s^2 V H}{3 k_B T} \tag{3.35}$$

Initial susceptibility:

$$\chi_{initial} = \frac{M_s^2 V}{3 k_B T} \propto \frac{1}{T} \tag{3.36}$$

3.5.3 Exchange Bias

Phenomenon and Origin

Exchange bias occurs in ferromagnetic (FM) / antiferromagnetic (AFM) interfaces:

- Shift of hysteresis loop along field axis
- Enhanced coercivity
- Asymmetric magnetization reversal

Exchange bias field:

$$H_{EB} = \frac{J_{EB}}{M_{FM} t_{FM}} \tag{3.37}$$

where J_{EB} is interfacial exchange energy, M_{FM} is FM magnetization, t_{FM} is FM thickness.

Meiklejohn-Bean Model

Predicted exchange bias:

$$H_{EB} = \frac{J_{int} S_{AFM}}{M_{FM} t_{FM}} \tag{3.38}$$

Experimental values typically 1-2 orders smaller due to compensated AFM interfaces, roughness, and AFM domain formation.

3.6 Mechanical Properties at Nanoscale

3.6.1 Hall-Petch and Inverse Hall-Petch Relations

Hall-Petch Strengthening

Reducing grain size increases strength:

$$\sigma_y = \sigma_0 + k_y d^{-1/2} \tag{3.39}$$

where σ_y is yield stress, σ_0 is friction stress, k_y is Hall-Petch constant, d is grain size.
Physical origin: Grain boundaries impede dislocation motion.

Inverse Hall-Petch Effect

Below critical grain size ($d_c \sim 10 - 20$ nm):

$$\sigma_y = \sigma_0 - k' d^{-1/2} \quad \text{for } d < d_c \tag{3.40}$$

Mechanisms:

- Grain boundary sliding
- Insufficient dislocation sources
- Grain boundary diffusion creep

3.6.2 Elastic Properties

Young's modulus varies with size:

$$E(d) = E_\infty \left(1 - \frac{C}{d}\right) \tag{3.41}$$

For nanocrystalline bulk:

$$E_{nc} = f_{grain} E_{grain} + f_{GB} E_{GB} \tag{3.42}$$

3.6.3 Hardness Enhancement

Nanocrystalline materials exhibit exceptional hardness:

$$H = H_0 + k_H d^{-1/2} \tag{3.43}$$

Table 3.6: Hardness enhancement in nanocrystalline materials

Material	Grain Size (nm)	Hardness (GPa)	Factor
Cu (conv.)	> 1000	0.4	–
Cu (nc)	20	2.1	5×
Ni (conv.)	> 1000	1.2	–
Ni (nc)	10	6.5	5.4×
Fe (conv.)	> 1000	1.5	–
Fe (nc)	15	5.8	3.9×

3.7 Practical Focus: Band Gap Tuning in ZnO Nanoparticles

3.7.1 ZnO as a Model System

Zinc oxide (ZnO) properties:

- Wide band gap: $E_g^{bulk} = 3.37$ eV (300 K)
- Large exciton binding energy: 60 meV
- Direct band gap → efficient light emission
- Applications: UV LEDs, solar cells, sensors, piezoelectrics

3.7.2 Size-Dependent Band Gap

ZnO quantum dots exhibit quantum confinement:

$$E_g(d) = E_g^{bulk} + \frac{\hbar^2 \pi^2}{2\mu d^2} - \frac{1.8e^2}{4\pi\varepsilon_0\varepsilon_r d} \tag{3.44}$$

For ZnO: $E_g^{bulk} = 3.37$ eV, $m_e^* = 0.24m_0$, $m_h^* = 0.59m_0$, $\mu = 0.17m_0$, $\varepsilon_r = 8.5$.

Example

Calculate band gap for 3 nm ZnO quantum dot
Solution:
Kinetic energy term:

$$E_{kinetic} = \frac{\hbar^2\pi^2}{2\mu d^2} = \frac{(1.055 \times 10^{-34})^2\pi^2}{2 \times 0.17 \times 9.11 \times 10^{-31} \times (3 \times 10^{-9})^2} \tag{3.45}$$

$$= 6.25 \times 10^{-20} \text{ J} = 0.39 \text{ eV} \tag{3.46}$$

Coulomb term:

$$E_{Coulomb} = \frac{1.8e^2}{4\pi\varepsilon_0\varepsilon_r d} = 0.054 \text{ eV} \tag{3.47}$$

Total:

$$E_g(3 \text{ nm}) = 3.37 + 0.39 - 0.054 = 3.71 \text{ eV} \tag{3.48}$$

Emission wavelength:

$$\lambda = \frac{hc}{E_g} = \frac{1240 \text{ eV·nm}}{3.71 \text{ eV}} = 334 \text{ nm (UV)} \tag{3.49}$$

3.7.3 Synthesis Methods

Sol-Gel Method

Controlled hydrolysis:

$$Zn^{2+} + 2OH^- \rightarrow Zn(OH)_2 \rightarrow ZnO + H_2O \tag{3.50}$$

Size control parameters: precursor concentration, pH, temperature, reaction time, surfactants.

Table 3.7: ZnO nanoparticle size control via synthesis parameters

Parameter	Value	Size (nm)	E_g (eV)
Temperature	60°C	8-10	3.45
Temperature	80°C	15-20	3.40
pH	9	5-7	3.52
pH	11	12-15	3.42 Precursor>Precursor
0.1 M	–	6-8	3.48 Precursor>Precursor
0.5 M	–	20-25	3.39

3.7.4 Characterization

UV-Vis Absorption: Band gap determination using Tauc plot:

$$(\alpha h\nu)^2 = A(h\nu - E_g) \tag{3.51}$$

Photoluminescence:

- Near band edge (NBE) emission: UV region
- Deep level emission: Visible (from defects)
- Quality indicator: I_{NBE}/I_{defect} ratio

3.7.5 Applications

- **UV Photodetectors:** Size-tuned for specific wavelengths
- **Transparent Conducting Oxides:** Al/Ga-doped ZnO
- **Gas Sensors:** Detection of CO, NO_2, H_2

3.8 Summary

This chapter explored how nanoscale dimensions alter material properties:

Key Point

Key Size-Dependent Relationships:

- **Structural:** Lattice parameter $\propto 1/r$
- **Electronic:** Band gap $\propto 1/r^2$
- **Optical:** Absorption blue-shift with decreasing size
- **Magnetic:** Blocking temperature $T_B \propto V \propto r^3$
- **Mechanical:** Strength increases (Hall-Petch) then decreases (inverse)

Applications enabled by property modifications:

- Optoelectronic devices (LEDs, solar cells, photodetectors)
- Magnetic storage and sensors
- High-strength structural materials
- Optimized catalysts
- Biomedical applications

Exercises

Conceptual Questions

1. Explain why anatase TiO_2 is stable at nanoscale while rutile is stable in bulk.
2. Describe Hall-Petch and inverse Hall-Petch effects. At what grain size does transition occur?

3. Why do semiconductor quantum dots show discrete absorption peaks while bulk shows continuous absorption?
4. Explain photoluminescence vs. surface plasmon resonance. Which nanomaterials exhibit each?
5. Derive the relationship between blocking temperature and nanoparticle volume.
6. Why is the Coulomb term negative in quantum confinement equation? What does it represent?
7. Compare density of states for 0D, 1D, 2D, 3D systems.
8. Why does ZnS shell coating on CdSe increase photoluminescence quantum yield?
9. How does grain boundary volume fraction affect nanocrystalline properties?
10. What is exchange bias and its importance for magnetic storage?

Numerical Problems

1. A CdSe quantum dot has diameter 4 nm. Calculate: (a) band gap energy, (b) emission wavelength, (c) number of unit cells, (d) surface atom percentage. Given: $E_g^{bulk} = 1.74$ eV, $m_e^* = 0.13m_0$, $m_h^* = 0.45m_0$, $\varepsilon_r = 10$, $a = 0.605$ nm.
2. For Fe_3O_4 nanoparticles with $K = 1.1 \times 10^4$ J/m^3: (a) Calculate energy barrier for 10 nm diameter, (b) determine blocking temperature, (c) at what size is $T_B = 300$ K?
3. Nanocrystalline Ni with grain size 15 nm. Using $\sigma_0 = 50$ MPa, $k_y = 300$ MPa·nm$^{1/2}$: (a) Calculate yield strength, (b) compare with 50 nm and 5 nm, (c) plot for $d = 5 - 100$ nm.
4. Gold nanoparticles (20 nm) in water ($\varepsilon_m = 1.77$): (a) Calculate SPR wavelength, (b) extinction cross-section, (c) SPR change in toluene ($\varepsilon_m = 2.38$).
5. ZnO quantum dots at temperatures 60°C (4 nm), 80°C (7 nm), 100°C (12 nm): (a) Calculate band gaps, (b) emission wavelengths, (c) plot vs. size.
6. Ag nanoparticles with $\frac{a(r)-a_\infty}{a_\infty} = -\frac{0.8}{r}$ (nm), $a_\infty = 4.09$ Å: (a) Calculate a for $r = 2, 5, 10$ nm, (b) percentage change for 2 nm, (c) size for $< 0.1\%$ change.
7. Quantum well width $L = 10$ nm, $m^* = 0.067m_0$: (a) First three energy levels, (b) energy spacing, (c) wavelength for $n = 2 \to n = 1$.
8. Nanocrystalline Cu (20 nm grain): (a) GB volume fraction ($\delta = 0.5$ nm), (b) effective diffusion if $D_{GB} = 10^{-15}$ m^2/s, $D = 10^{-18}$ m^2/s, (c) compare with 100 nm.
9. Superparamagnetic particle with $\tau = 10^{-7}$ s at 300 K. If volume doubled: (a) new relaxation time, (b) blocking temperatures, (c) temperature for $\tau = 1$ s.
10. CdS nanowire (8 nm diameter, 2 μm length): (a) Radial confinement energy, (b) length confinement?, (c) expected band gap (bulk 2.42 eV), (d) aspect ratio.

Advanced Problems

1. Derive size-dependent melting temperature from thermodynamic principles including surface energy.

2. Design experiment to measure blocking temperature distribution of polydisperse Fe_3O_4 nanoparticles.

3. Develop synthesis protocol for ZnO quantum dots with 370 nm emission. Include target size, method, parameters, characterization.

4. Calculate 1D density of states and explain van Hove singularities. Discuss optical implications.

Bibliography

[1] Cao, G., & Wang, Y. (2011). *Nanostructures and Nanomaterials* (2nd ed.). World Scientific, Singapore.

[2] Roduner, E. (2006). Size matters: why nanomaterials are different. *Chem. Soc. Rev.*, 35, 583-592.

[3] Alivisatos, A. P. (1996). Semiconductor clusters, nanocrystals, and quantum dots. *Science*, 271, 933-937.

[4] Murray, C. B., et al. (2000). Synthesis and characterization of monodisperse nanocrystals. *Annu. Rev. Mater. Sci.*, 30, 545-610.

[5] Brus, L. E. (1984). Electron-hole interactions in small semiconductor crystallites. *J. Chem. Phys.*, 80, 4403-4409.

[6] Burda, C., et al. (2005). Chemistry and properties of nanocrystals of different shapes. *Chem. Rev.*, 105, 1025-1102.

[7] Gleiter, H. (2000). Nanostructured materials: basic concepts and microstructure. *Acta Mater.*, 48, 1-29.

[8] Meyers, M. A., et al. (2006). Mechanical properties of nanocrystalline materials. *Prog. Mater. Sci.*, 51, 427-556.

[9] Néel, L. (1949). Magnetic behaviour of fine ferromagnetic particles. *Ann. Geophys.*, 5, 99-136.

[10] Bean, C. P., & Livingston, J. D. (1959). Superparamagnetism. *J. Appl. Phys.*, 30, S120-S129.

[11] Meiklejohn, W. H., & Bean, C. P. (1956). New magnetic anisotropy. *Phys. Rev.*, 102, 1413-1414.

[12] Nogués, J., & Schuller, I. K. (1999). Exchange bias. *J. Magn. Magn. Mater.*, 192, 203-232.

[13] Kelly, K. L., et al. (2003). Optical properties of metal nanoparticles. *J. Phys. Chem. B*, 107, 668-677.

[14] Link, S., & El-Sayed, M. A. (1999). Size and temperature dependence of plasmon absorption. *J. Phys. Chem. B*, 103, 4212-4217.

[15] Djurišić, A. B., & Leung, Y. H. (2006). Optical properties of ZnO nanostructures. *Small*, 2, 944-961.

[16] Spanhel, L., & Anderson, M. A. (1991). Semiconductor clusters in sol-gel process. *J. Am. Chem. Soc.*, 113, 2826-2833.

[17] Bawendi, M. G., et al. (1990). Quantum mechanics of larger semiconductor clusters. *Annu. Rev. Phys. Chem.*, 41, 477-496.

[18] Peng, X., et al. (1997). Epitaxial growth of highly luminescent CdSe/CdS core/shell nanocrystals. *J. Am. Chem. Soc.*, 119, 7019-7029.

[19] Rao, C. N. R., et al. (Eds.). (2004). *The Chemistry of Nanomaterials*. Wiley-VCH, Weinheim.

[20] Poole, C. P., & Owens, F. J. (2003). *Introduction to Nanotechnology*. Wiley, New Jersey.

[21] Bhushan, B. (Ed.). (2017). *Springer Handbook of Nanotechnology* (4th ed.). Springer, Berlin.

[22] Koch, C. C., et al. (2007). *Structural Nanocrystalline Materials*. Cambridge University Press.

[23] Hall, E. O. (1951). The deformation and ageing of mild steel. *Proc. Phys. Soc. B*, 64, 747.

[24] Petch, N. J. (1953). The cleavage strength of polycrystals. *J. Iron Steel Inst.*, 174, 25-28.

[25] Chokshi, A. H., et al. (1989). On the validity of Hall-Petch in nanocrystalline materials. *Scr. Metall.*, 23, 1679-1683.

[26] Ozin, G. A., & Arsenault, A. C. (2009). *Nanochemistry* (2nd ed.). RSC, Cambridge.

[27] Zhang, H., & Banfield, J. F. (1998). Thermodynamic analysis of phase stability of nanocrystalline titania. *J. Mater. Chem.*, 8, 2073-2076.

[28] Kovalenko, M. V., et al. (2015). Prospects of nanoscience with nanocrystals. *ACS Nano*, 9, 1012-1057.

Chapter 4

Physical and Chemical Synthesis Routes

"The art of synthesis is not just making new materials, but making them with the right size, shape, composition, and structure for the intended application."
— C. N. R. Rao

4.1 Introduction

The synthesis of nanomaterials is a critical aspect of nanotechnology, as the properties of nanomaterials are intimately connected to their size, shape, morphology, crystallinity, and chemical composition. The ability to precisely control these parameters during synthesis determines the ultimate performance of nanomaterials in applications ranging from catalysis and energy storage to biomedical devices and electronics.

Nanomaterial synthesis methods are broadly classified into two fundamental approaches:

- **Top-down approaches:** Starting from bulk materials and reducing dimensions through mechanical, physical, or chemical processes
- **Bottom-up approaches:** Building nanomaterials atom-by-atom or molecule-by-molecule from precursors

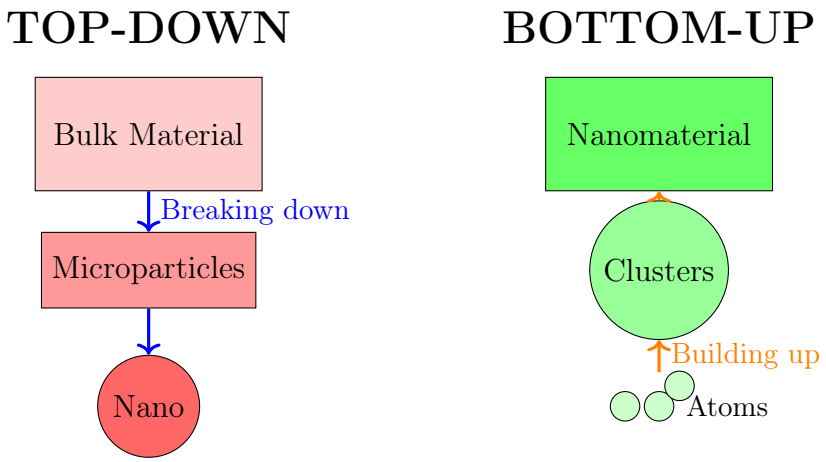

Figure 4.1: Schematic illustration of top-down and bottom-up synthesis approaches

This chapter provides a comprehensive overview of the most important physical and chemical synthesis routes, their underlying principles, advantages, limitations, and practical considerations.

4.2 Top-Down Approaches

Top-down approaches involve the reduction of bulk materials to nanoscale dimensions through mechanical, lithographic, or energetic processes. While these methods can produce large quantities of nanomaterials, they often face challenges in achieving uniform size distribution and may introduce defects.

4.2.1 Mechanical Milling

Principles and Mechanisms

Mechanical milling (also known as ball milling or mechanochemical synthesis) is one of the most straightforward and scalable top-down methods. The process involves placing bulk material with milling balls in a container that is subjected to high-energy collisions.

Definition

Mechanical Milling is a solid-state powder processing technique involving repeated welding, fracturing, and rewelding of powder particles in a high-energy ball mill.

The size reduction mechanism involves:

1. **Impact:** High-velocity collisions between balls and powder
2. **Attrition:** Grinding action between balls and container walls
3. **Shear:** Relative motion causing particle deformation

Energy Considerations

The kinetic energy transferred during collision is:

$$E_k = \frac{1}{2} m_b v_b^2 \tag{4.1}$$

where m_b is ball mass and v_b is ball velocity.
The critical velocity for effective milling:

$$v_c = \sqrt{2g(R - r)} \tag{4.2}$$

where g is gravitational acceleration, R is mill radius, and r is ball radius.
The power intensity can be estimated as:

$$P = \frac{m_b v_b^3}{2D} \tag{4.3}$$

where D is the mill diameter.

Types of Ball Mills

Table 4.1: Comparison of different ball mill types

Type	Energy	Speed (rpm)	Size Achievable	Scale
Planetary mill	Very high	100-800	5-50 nm	Lab
Attritor mill	High	250-500	50-500 nm	Pilot
Tumbler mill	Medium	50-100	100-1000 nm	Industrial
Vibratory mill	High	1000-2000	10-100 nm	Lab/Pilot
SPEX mill	Very high	1200-1500	10-50 nm	Lab

Critical Parameters

Key parameters affecting particle size and properties:

- **Ball-to-powder ratio (BPR):** Typically 5:1 to 20:1

$$BPR = \frac{m_{balls}}{m_{powder}} \tag{4.4}$$

- **Milling speed:** Must be optimized to avoid centrifugation

$$N_c = \frac{42.3}{\sqrt{D}} \tag{4.5}$$

  where N_c is critical speed (rpm) and D is diameter (m)

- **Milling time:** Extended milling can lead to contamination and amorphization
- **Milling atmosphere:** Inert (Ar, N_2), reactive (H_2, O_2), or vacuum
- **Process control agents (PCA):** Surfactants to prevent agglomeration

Advantages and Limitations

Table 4.2: Mechanical milling: advantages and limitations

Advantages	Limitations
Simple equipment and operation	Broad size distribution
Scalable to industrial production	Contamination from milling media
Applicable to wide range of materials	High defect density
Can process high melting point materials	Difficult to achieve <10 nm
Solid-state processing (no solvents)	High energy consumption
Can create alloys and composites	Limited morphology control
Cost-effective	Possible phase transformations

Example

Ball milling of ZnO
Starting material: Bulk ZnO powder (10 μm average size)
Conditions:

- Mill: Planetary ball mill
- Ball material: Zirconia (ZrO_2)
- BPR: 10:1
- Speed: 300 rpm
- Time: 6 hours
- Atmosphere: Air

Results: Average particle size reduced to 45 nm with wurtzite crystal structure preserved.

4.2.2 Lithographic Techniques

Lithography encompasses a family of top-down methods that use radiation (photons, electrons, ions) to pattern materials with nanoscale precision. These techniques are the foundation of semiconductor manufacturing.

Photolithography

Photolithography uses ultraviolet (UV) light to transfer geometric patterns from a photomask to a light-sensitive photoresist.

Process steps:

1. **Substrate cleaning:** Remove contaminants
2. **Photoresist coating:** Spin-coating of polymer resist
3. **Soft bake:** Evaporate solvents (90-120°C)
4. **Exposure:** UV light through mask
5. **Development:** Dissolve exposed (positive) or unexposed (negative) regions
6. **Hard bake:** Stabilize pattern
7. **Etching:** Transfer pattern to substrate
8. **Resist removal:** Strip remaining photoresist

Resolution limit:
The minimum feature size is determined by the Rayleigh criterion:

$$R = k_1 \frac{\lambda}{NA} \tag{4.6}$$

where:

- R is minimum resolvable feature size
- k_1 is process-dependent factor (typically 0.4-0.6)
- λ is wavelength of light
- NA is numerical aperture of lens system

For deep UV (DUV) lithography using 193 nm ArF excimer laser:

$$R = 0.5 \times \frac{193 \text{ nm}}{1.35} \approx 71 \text{ nm} \tag{4.7}$$

Extreme UV (EUV) lithography at 13.5 nm enables sub-10 nm features.

Electron Beam Lithography (EBL)

EBL uses focused electron beams to directly write patterns without masks, offering superior resolution.

Resolution:

The spot size is determined by electron wavelength:

$$\lambda_e = \frac{h}{\sqrt{2m_e eV}} \tag{4.8}$$

For 50 keV electrons:

$$\lambda_e = \frac{6.626 \times 10^{-34}}{\sqrt{2 \times 9.11 \times 10^{-31} \times 1.6 \times 10^{-19} \times 50000}} \approx 0.0055 \text{ nm} \tag{4.9}$$

Practical resolution: 5-10 nm (limited by scattering, not wavelength)

Exposure dose:

$$D = \frac{I \cdot t}{A} \tag{4.10}$$

where D is dose (μC/cm^2), I is beam current, t is exposure time, A is exposed area.

Focused Ion Beam (FIB) Lithography

FIB uses accelerated ions (typically Ga^+) for both imaging and milling.

Sputter yield (atoms removed per incident ion):

$$Y = \frac{N_{sputtered}}{N_{incident}} \tag{4.11}$$

Typical sputter yields: 1-10 atoms/ion for 30 keV Ga^+ on Si.

Table 4.3: Comparison of lithographic techniques

Parameter	**Photolithography**	**EBL**	**FIB**
Resolution	50-200 nm	5-10 nm	5-10 nm
Throughput	Very high	Low	Very low
Mask required	Yes	No	No
3D capability	Limited	Limited	Excellent
Substrate damage	Minimal	Low	High
Cost	High (masks)	Moderate	High

4.2.3 Laser Ablation

Laser ablation is a physical vapor deposition technique where high-intensity laser pulses vaporize material from a target, which then condenses as nanoparticles.

Principles

When a pulsed laser beam strikes a target surface:

1. **Photon absorption:** Electronic excitation
2. **Energy conversion:** Heat generation
3. **Melting/vaporization:** Phase transition
4. **Plasma formation:** Ionization of vapor
5. **Plume expansion:** Material ejection
6. **Nucleation:** Cluster formation
7. **Growth:** Nanoparticle formation

Energy Considerations

The energy density required for ablation:

$$\Phi_{th} = \frac{E}{A} = \frac{P \cdot t}{A} \tag{4.12}$$

where Φ_{th} is threshold fluence (J/cm^2), E is pulse energy, A is spot area, P is power, t is pulse duration.

Typical threshold fluences:

- Metals: 0.1-1 J/cm^2
- Semiconductors: 0.5-2 J/cm^2
- Ceramics: 1-5 J/cm^2

Ablation Rate

The ablation depth per pulse:

$$d = \alpha^{-1} \ln\left(\frac{\Phi}{\Phi_{th}}\right) \tag{4.13}$$

where α is optical absorption coefficient and Φ is applied fluence.
The mass removal rate:

$$\dot{m} = \rho \cdot A \cdot d \cdot f \tag{4.14}$$

where ρ is material density and f is laser repetition rate.

Pulsed Laser Ablation in Liquid (PLAL)

A variation where ablation occurs in liquid medium, offering advantages:

- Confined plume expansion
- Rapid quenching
- Better size control
- Surface functionalization by liquid

Particle size in PLAL can be estimated:

$$d_p \propto \left(\frac{\Phi}{\Phi_{th}}\right)^{-1/3} \tag{4.15}$$

Higher laser fluence produces smaller particles.

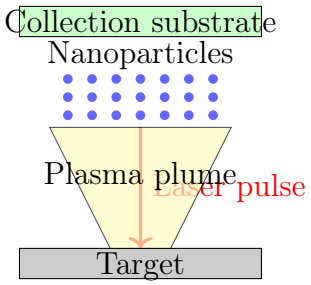

Figure 4.2: Schematic of laser ablation process

Table 4.4: Laser ablation parameters and their effects

Parameter	**Effect on Size**	**Effect on Yield**
Laser fluence ↑	Decreases	Increases
Pulse duration ↑	Increases	Increases
Wavelength ↓	Decreases	Varies
Repetition rate ↑	Varies	Increases
Background pressure ↑	Decreases	Decreases

4.3 Bottom-Up Approaches

Bottom-up approaches build nanomaterials from atomic or molecular precursors through chemical reactions, self-assembly, or vapor-phase processes. These methods generally offer better control over size, composition, and crystallinity.

4.3.1 Sol-Gel Process

The sol-gel process is a versatile wet-chemical technique for producing metal oxide nanomaterials through hydrolysis and condensation of molecular precursors.

Fundamental Chemistry

Definition

A **sol** is a colloidal suspension of solid particles (1-100 nm) in a liquid. A **gel** is a three-dimensional network of interconnected particles or polymers with liquid trapped in the pores.

For metal alkoxide precursors $M(OR)_n$:
Step 1: Hydrolysis

$$\mathrm{M(OR)_n + H_2O \longrightarrow M(OR)_{n-1}(OH) + ROH} \tag{4.16}$$

Step 2: Condensation
Water condensation:

$$\mathrm{M{-}OH + HO{-}M \longrightarrow M{-}O{-}M + H_2O} \tag{4.17}$$

Alcohol condensation:

$$\mathrm{M{-}OR + HO{-}M \longrightarrow M{-}O{-}M + ROH} \tag{4.18}$$

Kinetics and Control Parameters

Hydrolysis rate constant:

$$k_h = k_0 \exp\left(-\frac{E_a}{RT}\right) \tag{4.19}$$

The relative rates of hydrolysis (r_h) and condensation (r_c) determine structure:

$$\frac{r_h}{r_c} = f(\text{pH, temperature, } h = \frac{[\mathrm{H_2O}]}{[\mathrm{M}]}) \tag{4.20}$$

- $r_h >> r_c$: Linear chains, polymeric gels
- $r_h \approx r_c$: Branched structures
- $r_h << r_c$: Dense colloidal particles

pH effects:

- Low pH (< 3): Acid-catalyzed, $r_h > r_c$, polymeric structure
- High pH (> 7): Base-catalyzed, $r_c > r_h$, particulate structure
- Isoelectric point (IEP): Maximum condensation rate

Water ratio:

$$h = \frac{[\mathrm{H_2O}]}{[\mathrm{M(OR)}_n]} \tag{4.21}$$

Stoichiometric: $h = n/2$. Practical: h = 2-50.

Processing Steps

1. **Sol formation:** Mixing precursor, solvent, water, catalyst
2. **Gelation:** Formation of 3D network (hours to days)
3. **Aging:** Strengthening of gel network
4. **Drying:**
   - Evaporative drying → xerogel (shrinkage)
   - Supercritical drying → aerogel (maintains porosity)
   - Freeze drying → cryogel
5. **Calcination:** Heat treatment to remove organics, crystallize

Particle Size Control

The final particle size can be approximated by:

$$d_p = k \left(\frac{k_c}{k_n} \right)^{1/3} \tag{4.22}$$

where k_c is condensation rate constant and k_n is nucleation rate constant.
Stöber method for monodisperse silica:

$$d_{SiO_2} = A \cdot [\mathrm{NH_3}]^m \cdot [\mathrm{TEOS}]^n \cdot [\mathrm{H_2O}]^p \tag{4.23}$$

Empirically: $m \approx 0.3$, $n \approx 0.5$, $p \approx 0.1$

Example

Sol-gel synthesis of TiO_2 nanoparticles
Precursor: Titanium isopropoxide $Ti(OiPr)_4$
Reaction:

$$Ti(OiPr)_4 + 2\,H_2O \longrightarrow TiO_2 + 4\,iPrOH \tag{4.24}$$

Procedure:

- Dissolve 5 mL $Ti(OiPr)_4$ in 50 mL ethanol
- Add dropwise: 1 mL H_2O + 1 mL HNO_3 (0.1 M)
- Stir at room temperature for 2 hours (sol formation)
- Age at 60°C for 24 hours (gelation)
- Dry at 100°C
- Calcine at 450°C for 2 hours

Result: Anatase TiO_2 nanoparticles, 10-15 nm average size

4.3.2 Chemical Vapor Deposition (CVD)

CVD is a bottom-up technique where gaseous precursors react on a heated substrate to deposit solid materials.

General CVD Reaction

$$A_{(g)} + B_{(g)} \xrightarrow{\text{heat}} AB_{(s)} + C_{(g)} \tag{4.25}$$

CVD Process Steps

1. **Transport:** Precursor gases flow to reactor
2. **Mass transfer:** Diffusion through boundary layer to substrate
3. **Adsorption:** Precursor molecules adsorb on surface
4. **Surface reaction:** Chemical decomposition/reaction
5. **Nucleation:** Island formation
6. **Growth:** Island coalescence, film/nanowire growth
7. **Desorption:** By-products desorb
8. **Mass transfer:** By-products diffuse away

Growth Rate

The deposition rate depends on limiting step:

Surface reaction limited (low temperature):

$$r = k_s C_s = k_0 \exp\left(-\frac{E_a}{RT}\right) C_s \tag{4.26}$$

where k_s is surface reaction rate constant and C_s is surface concentration.

Mass transport limited (high temperature):

$$r = h_m(C_g - C_s) \approx h_m C_g \tag{4.27}$$

where h_m is mass transfer coefficient and C_g is gas-phase concentration.

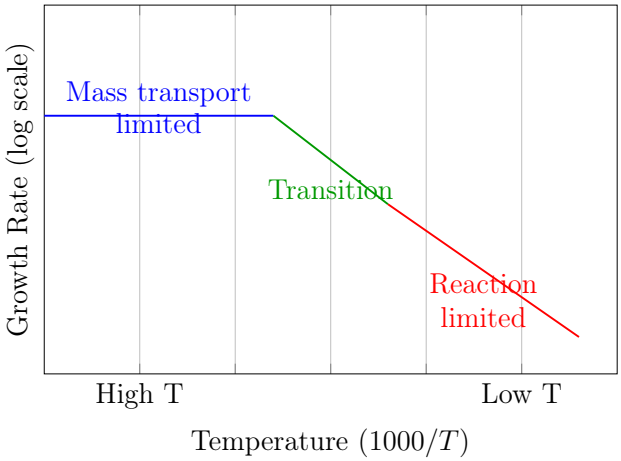

Figure 4.3: CVD growth rate vs. temperature showing different limiting regimes

Types of CVD

Table 4.5: CVD variants and their characteristics

Type	Pressure	Temperature (°C)	Advantages	Applications
APCVD	1 atm	600-1000	Simple, high rate	Coatings
LPCVD	0.1-10 Torr	400-900	Uniformity	Semiconductors
PECVD	0.1-10 Torr	200-400	Low temp	Flexible electronics
MOCVD	Varies	400-1000	High purity	LEDs, lasers
ALD	$<$ 1 Torr	150-400	Atomic control	Nanoelectronics

Nanostructure Synthesis by CVD

Carbon Nanotube Growth:

Vapor-Liquid-Solid (VLS) mechanism:

1. Catalyst particle (Fe, Ni, Co) forms liquid droplet
2. Carbon dissolves in liquid droplet

3. Supersaturation leads to carbon precipitation
4. Tubular structure grows from catalyst

Growth velocity:

$$v = \frac{dL}{dt} = \frac{D}{d_p}(C_{sat} - C_{eq}) \tag{4.28}$$

where D is diffusion coefficient, d_p is particle diameter, C_{sat} is saturation concentration.

Example

CVD synthesis of ZnO nanowires
Precursor: Zn powder at 600°C
Reaction:

$$2\,\mathrm{Zn_{(s)}} + \mathrm{O_{2(g)}} \longrightarrow 2\,\mathrm{ZnO_{(s)}} \tag{4.29}$$

Conditions:

- Source temperature: 600°C
- Substrate temperature: 400-500°C
- Carrier gas: Ar (100 sccm)
- O_2 flow: 5 sccm
- Pressure: 10 Torr
- Time: 30 min

Result: Aligned ZnO nanowires, 50-100 nm diameter, 5-10 μm length

4.3.3 Hydrothermal and Solvothermal Synthesis

Definition

Hydrothermal synthesis involves crystallization of substances from aqueous solution at high temperature (100-374°C) and high pressure (1-100 MPa) in a sealed vessel (autoclave).
Solvothermal synthesis uses organic solvents instead of water.

Thermodynamic Principles

At high temperature and pressure, water exhibits unique properties:

- Reduced dielectric constant → enhanced solubility of ionic compounds
- Increased ion product K_w → stronger acid/base behavior
- Lower viscosity → faster diffusion

The solubility of many oxides increases with temperature and pressure:

$$\log S = A - \frac{B}{T} + C \log \rho \tag{4.30}$$

where S is solubility, T is temperature, ρ is water density.

Process Mechanism

Dissolution-Crystallization:

1. Precursor dissolution at high T, P
2. Supersaturation generation
3. Nucleation
4. Crystal growth

In-situ Transformation:
Direct solid-state transformation under hydrothermal conditions.

Growth Kinetics

Crystal growth rate often follows:

$$\frac{dR}{dt} = k_g(\Delta C)^g \tag{4.31}$$

where R is crystal radius, k_g is growth rate constant, ΔC is supersaturation, g is growth order (typically 1-2).

Particle size can be controlled by:

$$d_p \propto T^\alpha t^\beta C^\gamma \tag{4.32}$$

Typical exponents: $\alpha = 0.5\text{-}1.5$, $\beta = 0.3\text{-}0.5$, $\gamma = 0.2\text{-}0.5$

Critical Parameters

- **Temperature:** 120-250°C for most oxides
- **Pressure:** Autogenous (self-generated) or externally controlled
- **Fill ratio:**

$$F = \frac{V_{solution}}{V_{autoclave}} = 0.4 - 0.8 \tag{4.33}$$

- **pH:** Controls solubility and morphology
- **Surfactants/templates:** Direct growth and shape
- **Reaction time:** Hours to days

Example

Hydrothermal synthesis of SnO_2 nanoparticles
Precursor: $SnCl_4 \cdot 5H_2O$
Reaction:

$$SnCl_4 + 2\,H_2O \longrightarrow SnO_2 + 4\,HCl \tag{4.34}$$

Procedure:

- Dissolve 2.25 g $SnCl_4 \cdot 5H_2O$ in 40 mL water
- Adjust pH to 10 with NaOH
- Transfer to 50 mL Teflon-lined autoclave
- Heat at 180°C for 12 hours
- Cool naturally
- Wash and dry precipitate

Result: Tetragonal SnO_2 nanoparticles, 5-10 nm

Table 4.6: Effect of hydrothermal parameters on particle size

Parameter	Increase	Effect on Particle Size
Temperature	↑	Increases
Time	↑	Increases
Precursor concentration	↑	Increases
pH (from IEP)	↑ or ↓	Decreases
Surfactant concentration	↑	Decreases

4.3.4 Coprecipitation

Coprecipitation is a simple, scalable wet-chemical method based on simultaneous precipitation of multiple components from solution.

Principles

General reaction:

$$M^{n+}_{(aq)} + nOH^-_{(aq)} \longrightarrow M(OH)_{n(s)} \tag{4.35}$$

followed by thermal decomposition:

$$M(OH)_n \xrightarrow{\Delta} MO_x + H_2O \tag{4.36}$$

Precipitation Theory

Nucleation:

Classical nucleation theory gives critical nucleus radius:

$$r^* = \frac{2\gamma V_m}{RT \ln S} \tag{4.37}$$

where γ is surface energy, V_m is molar volume, S is supersaturation ratio:

$$S = \frac{Q}{K_{sp}} \tag{4.38}$$

Q is ionic product, K_{sp} is solubility product.
The nucleation rate:

$$J = A \exp\left(-\frac{16\pi\gamma^3 V_m^2}{3(RT)^3(\ln S)^2}\right) \tag{4.39}$$

Growth:
Diffusion-controlled growth:

$$\frac{dr}{dt} = \frac{D(C_\infty - C_s)}{r} \tag{4.40}$$

Reaction-controlled growth:

$$\frac{dr}{dt} = k_r(C_s - C_{eq}) \tag{4.41}$$

LaMer Model

The LaMer model describes burst nucleation for monodisperse particles:

1. **Stage I:** Precursor generation, concentration rises
2. **Stage II:** Supersaturation exceeds critical level, rapid nucleation
3. **Stage III:** Nucleation ceases, growth on existing nuclei

For monodispersity: Short nucleation period, long growth period.

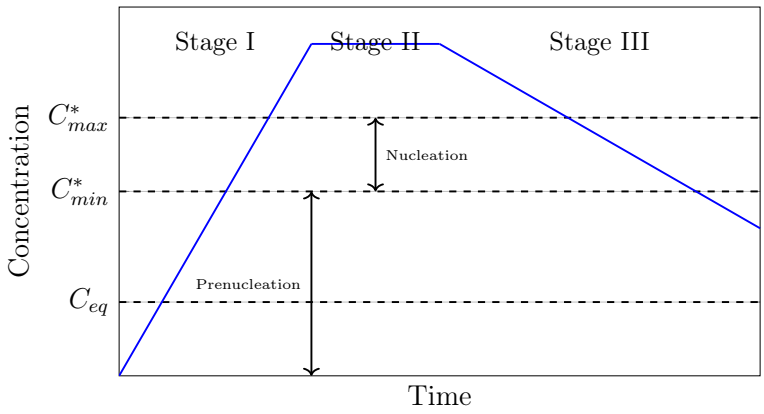

Figure 4.4: LaMer diagram showing nucleation and growth stages

Size Control Strategies

- **Rapid mixing:** Uniform supersaturation → narrow size distribution
- **Low temperature:** Slow growth → smaller particles
- **Surfactants:** Capping agents limit growth
- **pH control:** Affects solubility and growth rate
- **Aging:** Ostwald ripening → larger particles

Example

Coprecipitation of Fe_3O_4 nanoparticles
Reaction:

$$Fe^{2+} + 2\,Fe^{3+} + 8\,OH^- \longrightarrow Fe_3O_4 + 4\,H_2O \tag{4.42}$$

Procedure:

- Mix $FeCl_2 \cdot 4H_2O$ (1.99 g) and $FeCl_3 \cdot 6H_2O$ (5.41 g) in 50 mL water
- Fe^{2+}:Fe^{3+} ratio = 1:2
- Add dropwise 20 mL NH_4OH (25%) with vigorous stirring
- Stir at 80°C for 30 min
- Wash with water until pH = 7
- Dry at 60°C

Result: Superparamagnetic Fe_3O_4 nanoparticles, 10-15 nm

4.3.5 Green Synthesis

Green synthesis (biosynthesis) uses biological entities (plants, bacteria, fungi) or biologically derived molecules to synthesize nanoparticles in an environmentally benign manner.

Principles

Biological systems provide:

- **Reducing agents:** Proteins, polyphenols, flavonoids, terpenoids
- **Stabilizing agents:** Biomolecules prevent agglomeration
- **Shape-directing agents:** Templates for morphology control

General mechanism for metal nanoparticles:

$$M^{n+} + ne^- \xrightarrow{\text{biomolecule}} M^0 \tag{4.43}$$

Plant-Mediated Synthesis

Plant extracts contain polyphenols that act as reducing and capping agents:

$$\text{Polyphenol}_{(\text{reduced})} + \text{M}^{n+} \longrightarrow \text{Polyphenol}_{(\text{oxidized})} + \text{M}^{0} \tag{4.44}$$

Advantages:

- Readily available
- Non-toxic
- Cost-effective
- Single-step process
- No harsh chemicals

Microbial Synthesis

Bacteria:
Intracellular or extracellular synthesis
Mechanisms:

- Enzymatic reduction (NADH-dependent reductases)
- Electron transfer from respiratory chain
- Biosorption followed by reduction

Fungi:
Produce large amounts of proteins → higher yield
Secreted enzymes and metabolites reduce metal ions

Example

Green synthesis of AgNPs using Azadirachta indica (Neem) leaf extract
Procedure:

- Prepare extract: Boil 10 g fresh neem leaves in 100 mL water for 5 min, filter
- Add 10 mL extract to 90 mL $AgNO_3$ solution (1 mM)
- Observe color change to brown (indicates AgNP formation)
- Incubate at room temperature for 24 hours
- Centrifuge, wash, dry

Reaction:

$$\text{Ag}^{+} + \text{polyphenol}_{(\text{red})} \longrightarrow \text{Ag}^{0} + \text{polyphenol}_{(\text{ox})} \tag{4.45}$$

Result: Spherical Ag nanoparticles, 10-30 nm, stabilized by biomolecules

Table 4.7: Comparison of green synthesis methods

Method	Time	Yield	Size Control
Plant extract	Minutes-hours	Medium	Moderate
Bacteria	Hours-days	Low-medium	Good
Fungi	Hours-days	High	Good
Algae	Hours-days	Medium	Moderate

4.4 Comparison of Synthesis Routes

Selecting an appropriate synthesis method depends on multiple factors including desired material properties, scale, cost, and application requirements.

Table 4.8: Comprehensive comparison of major synthesis methods

Method	Size Range	Scalability	Cost	Size Control	Purity
Ball milling	10-500 nm	Excellent	Low	Poor	Moderate
Lithography	5-200 nm	Good	Very high	Excellent	Excellent
Laser ablation	1-100 nm	Limited	High	Moderate	Good
Sol-gel	2-100 nm	Good	Low	Good	Good
CVD	1-1000 nm	Good	High	Excellent	Excellent
Hydrothermal	5-500 nm	Good	Moderate	Good	Good
Coprecipitation	5-100 nm	Excellent	Very low	Moderate	Moderate
Green synthesis	10-200 nm	Good	Very low	Poor	Good

Table 4.9: Synthesis method selection guide by application

Application	Recommended Methods
Semiconductor devices	CVD, lithography, ALD
Catalysts	Sol-gel, hydrothermal, coprecipitation
Biomedical	Green synthesis, sol-gel, coprecipitation
Magnetic materials	Coprecipitation, hydrothermal
Structural nanocomposites	Ball milling, sol-gel
Optical materials	Sol-gel, hydrothermal, laser ablation
Energy storage	Hydrothermal, sol-gel, CVD
Sensors	Sol-gel, CVD, green synthesis

4.5 Laboratory Note: Coprecipitation of CuO and ZnO Nanoparticles

Laboratory Note

Objective

To synthesize copper oxide (CuO) and zinc oxide (ZnO) nanoparticles via coprecipitation method and compare their properties.

Introduction

Coprecipitation is a widely used method for synthesizing metal oxide nanoparticles due to its simplicity, cost-effectiveness, and scalability. This experiment demonstrates the synthesis of CuO and ZnO nanoparticles from their respective metal salt precursors using sodium hydroxide as the precipitating agent.

Chemicals and Materials

For CuO synthesis:

- Copper(II) sulfate pentahydrate ($CuSO_4 \cdot 5H_2O$)
- Sodium hydroxide (NaOH) pellets
- Distilled water

For ZnO synthesis:

- Zinc nitrate hexahydrate ($Zn(NO_3)_2 \cdot 6H_2O$)
- Sodium hydroxide (NaOH) pellets
- Distilled water

Equipment:

- Magnetic stirrer with hot plate
- Beakers (250 mL)
- pH meter
- Centrifuge
- Oven
- Muffle furnace

Safety Precautions

- Wear safety goggles, lab coat, and gloves at all times
- NaOH is corrosive - handle with care
- $CuSO_4$ is toxic - avoid skin contact and ingestion
- Work in well-ventilated area
- Dispose of chemical waste properly according to institutional guidelines

Laboratory Note

Procedure A: CuO Nanoparticle Synthesis

Step 1: Precursor Solution Preparation

1. Dissolve 2.5 g $CuSO_4 \cdot 5H_2O$ in 100 mL distilled water in a 250 mL beaker
2. Stir using magnetic stirrer at 300 rpm
3. Heat to 60°C

Step 2: Precipitation

1. Prepare 2 M NaOH solution (8 g NaOH in 100 mL water)
2. Add NaOH solution dropwise to $CuSO_4$ solution with constant stirring
3. Continue addition until pH reaches 12
4. Observe color change: Blue (Cu^{2+}) → Light blue precipitate $Cu(OH)_2$

Chemical reaction:

$$Cu^{2+}_{(aq)} + 2\,OH^-_{(aq)} \longrightarrow Cu(OH)_{2(s)} \tag{4.46}$$

Step 3: Aging and Washing

1. Continue stirring at 60°C for 1 hour
2. Allow to cool to room temperature
3. Centrifuge at 5000 rpm for 10 minutes
4. Discard supernatant
5. Wash precipitate 3 times with distilled water
6. Wash once with ethanol

Step 4: Drying and Calcination

1. Dry precipitate in oven at 80°C for 12 hours
2. Grind dried powder using mortar and pestle
3. Calcine at 400°C for 3 hours in muffle furnace
4. Observe color change: Light blue → Black (CuO formation)

Thermal decomposition:

$$Cu(OH)_{2(s)} \xrightarrow{\Delta} CuO_{(s)} + H_2O_{(g)} \tag{4.47}$$

Procedure B: ZnO Nanoparticle Synthesis

Step 1: Precursor Solution Preparation

1. Dissolve 2.975 g $Zn(NO_3)_2 \cdot 6H_2O$ in 100 mL distilled water
2. Stir at 300 rpm
3. Heat to 60°C

4.6 Summary

This chapter has provided a comprehensive overview of physical and chemical synthesis routes for nanomaterials:

Key Point

Key Takeaways:

- **Top-down methods** (milling, lithography, laser ablation) start from bulk materials and break them down, offering scalability but often limited size control
- **Bottom-up methods** (sol-gel, CVD, hydrothermal, coprecipitation, green synthesis) build from atomic/molecular precursors, providing better control over size, composition, and crystallinity
- Each synthesis method has distinct advantages and limitations regarding cost, scalability, size control, and purity
- Method selection depends on target application, required properties, available resources, and production scale
- Understanding the underlying chemistry and physics enables rational optimization of synthesis parameters

The future of nanomaterial synthesis lies in:

- Developing greener, more sustainable methods
- Achieving atomic-level precision in structure control
- Scaling up laboratory processes for industrial production
- Integrating computational modeling for synthesis prediction
- Continuous and automated synthesis platforms

Exercises

Conceptual Questions

1. Explain the fundamental difference between top-down and bottom-up synthesis approaches. Give three examples of each.
2. Why is contamination from milling media a concern in ball milling? How can it be minimized?
3. Derive the Rayleigh criterion for photolithography resolution. Discuss how resolution can be improved.
4. In sol-gel synthesis, explain how pH affects the ratio of hydrolysis to condensation rates and consequently the final structure.

5. Describe the VLS mechanism for nanowire growth in CVD. Why is catalyst size critical?

6. In hydrothermal synthesis, why does increasing temperature generally increase particle size?

7. Explain the LaMer model for particle nucleation and growth. What conditions favor monodisperse particles?

8. Why is rapid mixing important in coprecipitation for obtaining narrow size distribution?

9. Discuss the advantages and challenges of green synthesis methods compared to conventional chemical routes.

10. For synthesizing quantum dots with precise size control, which method would you recommend and why?

Numerical Problems

1. A planetary ball mill operates at 400 rpm with mill radius 15 cm. Calculate:
   (a) The critical speed
   (b) Whether the mill is operating in cascading or centrifuging mode
   (c) The kinetic energy of a 10 g zirconia ball at this speed

2. For photolithography using 248 nm KrF excimer laser with numerical aperture 0.85:
   (a) Calculate minimum feature size (assume $k_1 = 0.5$)
   (b) If switching to 193 nm ArF laser with same NA, what is the new resolution?
   (c) What NA would be needed to achieve 30 nm resolution at 193 nm?

3. In laser ablation of gold with 10 ns pulses at 1064 nm:
   (a) If threshold fluence is 0.5 J/cm^2 and applied fluence is 2 J/cm^2, calculate ablation depth per pulse (assume $\alpha = 1.2 \times 10^6$ cm^{-1})
   (b) For spot diameter 100 μm and repetition rate 10 Hz, calculate mass removal rate (Au density: 19.3 g/cm^3)

4. In Stöber synthesis of silica nanoparticles: [NH_3] = 0.5 M, [TEOS] = 0.1 M, [H_2O] = 2 M. If particle diameter follows:

$$d = 15 \times [NH_3]^{0.3} \times [\text{TEOS}]^{0.5} \times [H_2O]^{0.1}$$

   Calculate:
   (a) Expected particle diameter (nm)
   (b) New diameter if [NH_3] is doubled
   (c) New diameter if [TEOS] is halved

5. For hydrothermal synthesis at 180°C in 100 mL autoclave with 60 mL solution:

(a) Calculate the fill ratio

(b) If water vapor pressure at 180°C is 10 bar, estimate internal pressure (assume ideal gas behavior for vapor phase)

6. In coprecipitation of Fe_3O_4, 1.99 g $FeCl_2 \cdot 4H_2O$ and 5.41 g $FeCl_3 \cdot 6H_2O$ are used:

   (a) Verify the molar ratio of Fe^{2+}:Fe^{3+} is 1:2

   (b) Calculate theoretical yield of Fe_3O_4

   (c) If experimental yield is 1.8 g, calculate percentage yield

7. For CVD of Si from SiH_4 decomposition at 600°C:

$$SiH_{4(g)} \longrightarrow Si_{(s)} + 2\,H_{2(g)}$$

   If activation energy is 180 kJ/mol and pre-exponential factor is 10^{12} s^{-1}:

   (a) Calculate rate constant at 600°C

   (b) Calculate rate constant at 700°C

   (c) By what factor does rate increase?

8. In sol-gel TiO_2 synthesis, if nucleation rate $J = 10^{20}$ nuclei/m^3/s for 10 seconds, followed by growth for 2 hours with growth rate 0.1 nm/min:

   (a) Calculate number density of particles

   (b) Estimate final particle diameter

   (c) Calculate volume fraction if TiO_2 density is 3.8 g/cm^3

9. XRD analysis of ball-milled ZnO shows FWHM of (101) peak at 36.2° is 0.4°. Calculate crystallite size using Scherrer equation (K = 0.9, λ = 1.5406 Å, convert FWHM to radians).

10. For green synthesis of Ag nanoparticles, 10 mL plant extract is added to 90 mL of 1 mM $AgNO_3$:

    (a) Calculate total moles of Ag^+

    (b) If conversion efficiency is 80%, calculate mass of Ag nanoparticles formed

    (c) If particles are spherical with 20 nm diameter, estimate number of particles (Ag density: 10.5 g/cm^3)

Advanced Problems

1. Design a synthesis protocol for producing 5 nm CdSe quantum dots with narrow size distribution (< 10% RSD) using hot-injection method. Include precursor concentrations, temperatures, and time parameters. Justify your choices.

2. Compare the environmental impact of synthesizing 1 kg of ZnO nanoparticles by: (a) ball milling, (b) sol-gel, (c) green synthesis using plant extracts. Consider energy consumption, chemical waste, and carbon footprint.

3. Propose a CVD reactor design for growing vertically aligned carbon nanotubes on a 4-inch silicon wafer. Include gas flow rates, temperature zones, and expected growth rate calculations.

4. Develop a cost analysis for producing 100 g of Au nanoparticles (20 nm) comparing: (a) laser ablation in liquid, (b) citrate reduction method. Include materials, equipment, energy, and time costs.

Bibliography

[1] Cao, G., & Wang, Y. (2011). *Nanostructures and Nanomaterials: Synthesis, Properties, and Applications* (2nd ed.). World Scientific Publishing.

[2] Rao, C. N. R., Müller, A., & Cheetham, A. K. (2004). *The Chemistry of Nanomaterials: Synthesis, Properties and Applications*. Wiley-VCH.

[3] Suryanarayana, C. (2001). Mechanical alloying and milling. *Progress in Materials Science*, 46(1-2), 1-184.

[4] Vollath, D. (2008). *Nanomaterials: An Introduction to Synthesis, Properties and Applications*. Wiley-VCH.

[5] Brinker, C. J., & Scherer, G. W. (1990). *Sol-Gel Science: The Physics and Chemistry of Sol-Gel Processing*. Academic Press.

[6] Pierson, H. O. (1999). *Handbook of Chemical Vapor Deposition* (2nd ed.). Noyes Publications.

[7] Byrappa, K., & Yoshimura, M. (2001). *Handbook of Hydrothermal Technology*. William Andrew Publishing.

[8] LaMer, V. K., & Dinegar, R. H. (1950). Theory, production and mechanism of formation of monodispersed hydrosols. *Journal of the American Chemical Society*, 72(11), 4847-4854.

[9] Mittal, A. K., Chisti, Y., & Banerjee, U. C. (2013). Synthesis of metallic nanoparticles using plant extracts. *Biotechnology Advances*, 31(2), 346-356.

[10] Hench, L. L., & West, J. K. (1990). The sol-gel process. *Chemical Reviews*, 90(1), 33-72.

[11] Kodas, T. T., & Hampden-Smith, M. J. (1999). *Aerosol Processing of Materials*. Wiley-VCH.

[12] Suslick, K. S., Price, G. J. (1999). Applications of ultrasound to materials chemistry. *Annual Review of Materials Science*, 29(1), 295-326.

[13] Ozin, G. A., & Arsenault, A. C. (2009). *Nanochemistry: A Chemical Approach to Nanomaterials* (2nd ed.). Royal Society of Chemistry.

[14] Baraton, M. I. (Ed.). (2002). *Synthesis, Functionalization and Surface Treatment of Nanoparticles*. American Scientific Publishers.

[15] Wang, Z. L. (Ed.). (2000). *Characterization of Nanophase Materials*. Wiley-VCH.

[16] Schmid, G. (Ed.). (2004). *Nanoparticles: From Theory to Application*. Wiley-VCH.

[17] Cushing, B. L., Kolesnichenko, V. L., & O'Connor, C. J. (2004). Recent advances in the liquid-phase syntheses of inorganic nanoparticles. *Chemical Reviews*, 104(9), 3893-3946.

[18] Niederberger, M., Pinna, N. (2009). *Metal Oxide Nanoparticles in Organic Solvents: Synthesis, Formation, Assembly and Application*. Springer.

[19] Viswanathan, B., Ramaraj, R., Periasamy, A. P., et al. (2009). *Nanomaterials*. Narosa Publishing House.

[20] Koch, C. C. (2007). *Nanostructured Materials: Processing, Properties and Applications* (2nd ed.). William Andrew Publishing.

[21] Segets, D., Gradl, J., Taylor, R. K., et al. (2009). Analysis of optical absorbance spectra for the determination of ZnO nanoparticle size distribution. *ACS Nano*, 3(7), 1703-1710.

[22] Burda, C., Chen, X., Narayanan, R., & El-Sayed, M. A. (2005). Chemistry and properties of nanocrystals of different shapes. *Chemical Reviews*, 105(4), 1025-1102.

[23] Talapin, D. V., Lee, J. S., Kovalenko, M. V., & Shevchenko, E. V. (2010). Prospects of colloidal nanocrystals for electronic and optoelectronic applications. *Chemical Reviews*, 110(1), 389-458.

[24] Park, J., Joo, J., Kwon, S. G., et al. (2007). Synthesis of monodisperse spherical nanocrystals. *Angewandte Chemie International Edition*, 46(25), 4630-4660.

[25] Iravani, S. (2011). Green synthesis of metal nanoparticles using plants. *Green Chemistry*, 13(10), 2638-2650.

[26] Chaudhuri, R. G., & Paria, S. (2012). Core/shell nanoparticles: classes, properties, synthesis mechanisms, characterization, and applications. *Chemical Reviews*, 112(4), 2373-2433.

[27] Jun, Y. W., Choi, J. S., & Cheon, J. (2006). Shape control of semiconductor and metal oxide nanocrystals through nonhydrolytic colloidal routes. *Angewandte Chemie International Edition*, 45(21), 3414-3439.

Chapter 5

Functionalization and Surface Modification

"The surface of a nanomaterial is not just a boundary—it is the gateway to function, stability, and application."
— G. A. Ozin

5.1 Introduction

At the nanoscale, the surface-to-volume ratio becomes extraordinarily large, making the surface chemistry of nanomaterials a dominant factor in determining their overall properties and behavior. For a spherical nanoparticle of radius r, the surface-to-volume ratio scales as:

$$\frac{A}{V} = \frac{4\pi r^2}{\frac{4}{3}\pi r^3} = \frac{3}{r} \tag{5.1}$$

This inverse relationship means that as particle size decreases, an increasingly larger fraction of atoms reside at or near the surface. For a 5 nm particle, approximately 40-50% of atoms are surface atoms, compared to less than 1% for a 1 μm particle.

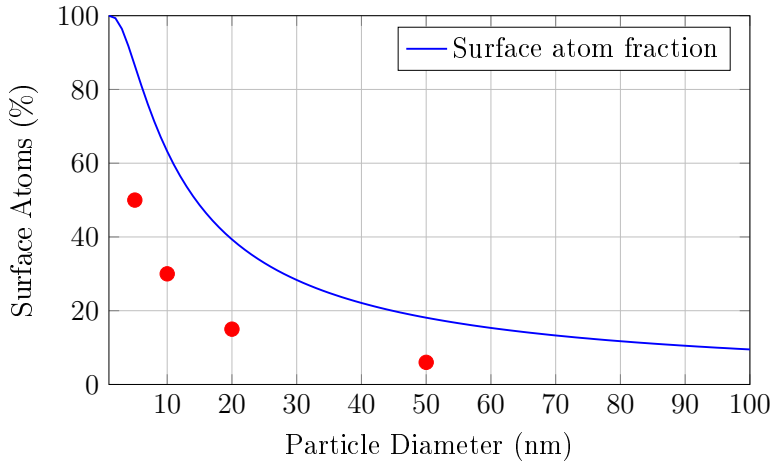

Figure 5.1: Percentage of surface atoms as a function of particle diameter

Surface functionalization—the deliberate modification of nanomaterial surfaces through chemical, physical, or biological means—is therefore critical for:

- **Stability enhancement:** Preventing agglomeration and degradation
- **Dispersion control:** Achieving uniform distribution in various media
- **Biocompatibility:** Reducing toxicity for biomedical applications
- **Targeted delivery:** Attaching recognition molecules for specific interactions
- **Catalytic activity:** Modifying surface active sites
- **Electrical properties:** Tuning conductivity and charge transfer
- **Optical properties:** Modifying absorption and emission characteristics

This chapter explores the fundamental principles, techniques, and applications of surface functionalization and modification in nanomaterials.

5.2 Importance of Surface Chemistry

5.2.1 Surface Energy and Surface Tension

Thermodynamic Perspective

Surface atoms have unsatisfied coordination compared to bulk atoms, resulting in excess free energy. The surface energy γ (J/m^2 or N/m) represents the work required to create a unit area of new surface:

$$\gamma = \left(\frac{\partial G}{\partial A}\right)_{T,P,n} \tag{5.2}$$

where G is Gibbs free energy and A is surface area.

For a nanoparticle, the total free energy includes surface contribution:

$$G_{total} = G_{bulk} + \gamma A \tag{5.3}$$

For a spherical particle:

$$G = \frac{4}{3}\pi r^3 g_v + 4\pi r^2 \gamma \tag{5.4}$$

where g_v is volumetric free energy density.

The chemical potential of atoms in a nanoparticle is size-dependent:

$$\mu(r) = \mu_\infty + \frac{2\gamma V_m}{r} \tag{5.5}$$

where μ_∞ is bulk chemical potential and V_m is molar volume.

Consequences of High Surface Energy

1. Agglomeration tendency:

Nanoparticles spontaneously agglomerate to minimize total surface area and thus total free energy. The driving force is:

$$\Delta G_{agg} = -\gamma \Delta A < 0 \tag{5.6}$$

2. Enhanced reactivity:

Surface atoms with dangling bonds are more reactive than bulk atoms. Reaction rate often scales with surface area:

$$r = k \cdot A_{surface} \tag{5.7}$$

3. Size-dependent solubility:

The Ostwald-Freundlich equation relates solubility to particle size:

$$\ln \frac{S(r)}{S_\infty} = \frac{2\gamma V_m}{rRT} \tag{5.8}$$

Smaller particles have higher solubility.

Table 5.1: Surface energies of common nanomaterials

Material	Surface Energy (J/m^2)	Contact Angle (°)
Au	1.5	High
Ag	1.2	High
SiO_2	0.3	40-50
TiO_2	0.6-0.9	10-20
Graphene	0.046-0.069	127 (water)
Carbon nanotubes	0.027-0.045	90-110
Polystyrene	0.040	90

5.2.2 Colloidal Stability: DLVO Theory

Definition

DLVO Theory (Derjaguin, Landau, Verwey, Overbeek) describes the stability of colloidal dispersions through the balance of attractive van der Waals forces and repulsive electrostatic forces.

Van der Waals Attraction

The attractive potential energy between two spherical particles of radius r separated by distance h:

$$V_A(h) = -\frac{A_H r}{12h} \tag{5.9}$$

where A_H is the Hamaker constant (typically 10^{-20} to 10^{-19} J).
For small separations ($h << r$):

$$V_A(h) \approx -\frac{A_H r}{12h} \tag{5.10}$$

Electrostatic Repulsion

For identically charged particles in aqueous medium:

$$V_R(h) = 2\pi\varepsilon_r\varepsilon_0 r\psi_0^2 \ln[1 + \exp(-\kappa h)] \tag{5.11}$$

where:

- ε_r is relative permittivity
- ε_0 is permittivity of free space
- ψ_0 is surface potential
- κ is Debye parameter:

$$\kappa = \sqrt{\frac{2N_A e^2 I}{\varepsilon_r\varepsilon_0 k_B T}} \tag{5.12}$$

- I is ionic strength

The Debye length $\lambda_D = 1/\kappa$ characterizes the electrostatic screening distance.

Total Interaction Energy

$$V_{total}(h) = V_A(h) + V_R(h) \tag{5.13}$$

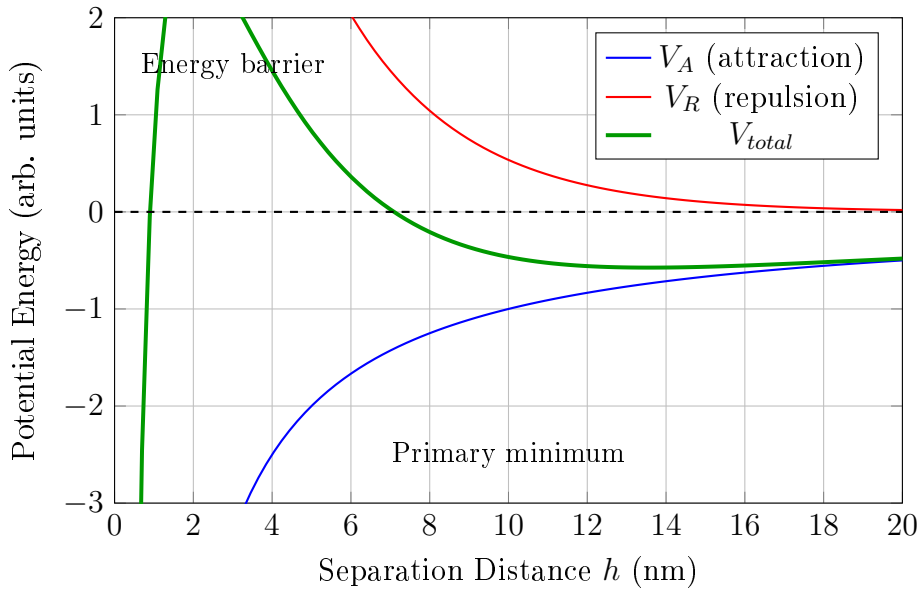

Figure 5.2: DLVO potential energy diagram showing stability of colloidal dispersion

Key Point

Stability Conditions:

- **High barrier:** Stable dispersion (no aggregation)
- **Low barrier:** Slow flocculation
- **No barrier:** Rapid coagulation

Surface functionalization modifies ψ_0 and can introduce steric repulsion, enhancing stability.

5.2.3 Steric Stabilization

Adsorbed polymer layers on nanoparticle surfaces provide steric (entropic) repulsion when particles approach. The steric potential:

$$V_S(h) = V_{mixing} + V_{elastic} \tag{5.14}$$

Mixing term (osmotic repulsion):

$$V_{mixing} \propto kT \left(\frac{1}{2} - \chi\right) \phi^2 \tag{5.15}$$

where χ is Flory-Huggins interaction parameter and ϕ is polymer volume fraction.
Elastic term (volume restriction):

$$V_{elastic} \propto kT \cdot (\text{compression energy}) \tag{5.16}$$

Good steric stabilizers have:

- Strong anchoring to surface

- Extended conformation in solvent
- Sufficient grafting density
- $\chi < 0.5$ (good solvent condition)

5.3 Functionalization Techniques

5.3.1 Chemical Grafting

Chemical grafting involves forming covalent bonds between functional molecules and the nanomaterial surface.

Grafting Strategies

1. **"Grafting-to" approach:**
   Pre-formed polymer chains react with surface groups:

$$\text{Surface}-\text{X} + \text{Y}-\text{Polymer} \longrightarrow \text{Surface}-\text{Polymer} + \text{XY} \tag{5.17}$$

   Advantages: Well-defined polymer structure
   Limitations: Low grafting density due to steric hindrance
2. **"Grafting-from" approach:**
   Polymerization initiated from surface-bound initiators:

$$\text{Surface}-\text{Initiator} \xrightarrow{\text{monomer}} \text{Surface}-\text{Polymer} \tag{5.18}$$

   Advantages: High grafting density
   Limitations: Less control over polymer structure

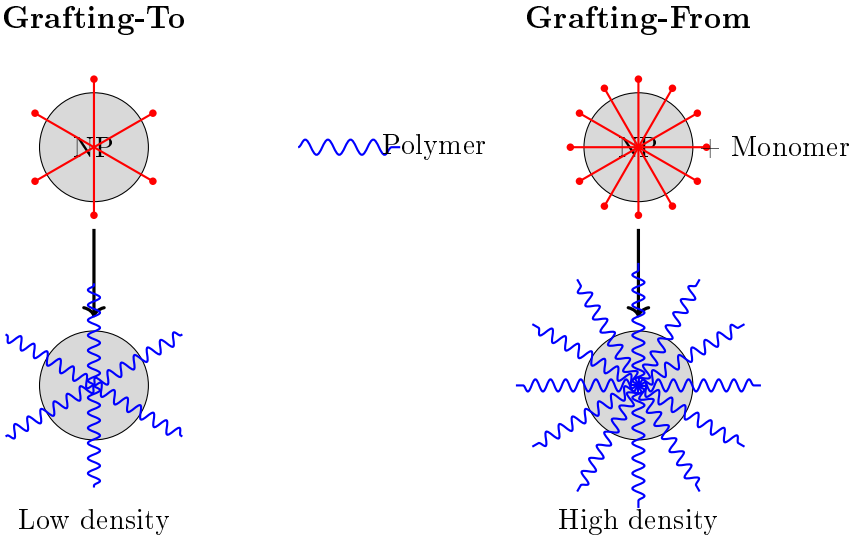

Figure 5.3: Comparison of grafting-to and grafting-from approaches

Surface Coupling Reactions

Silane coupling:
For oxide surfaces (SiO_2, TiO_2, etc.):

$$\text{Surface}{-}\text{OH} + (\text{RO})_3\text{Si}{-}\text{R'} \longrightarrow \text{Surface}{-}\text{O}{-}\text{Si}(\text{OR})_2{-}\text{R'} + \text{ROH} \tag{5.19}$$

Common silanes:

- APTES (3-aminopropyltriethoxysilane): Provides -NH_2 groups
- MPTS (3-mercaptopropyltrimethoxysilane): Provides -SH groups
- GPTS (3-glycidoxypropyltrimethoxysilane): Provides epoxy groups

Thiol chemistry:
For noble metal surfaces (Au, Ag):

$$\text{Au} + \text{R}{-}\text{SH} \longrightarrow \text{Au}{-}\text{S}{-}\text{R} + \frac{1}{2}\,\text{H}_2 \tag{5.20}$$

Self-assembled monolayers (SAMs) form with typical grafting density: 4-5 molecules/nm^2. The bond energy of Au-S: ∼180-200 kJ/mol (strong covalent character).
Carboxylic acid coupling:
For amine-functionalized surfaces:

$$\text{R}{-}\text{COOH} + \text{R'}{-}\text{NH}_2 \xrightarrow{\text{EDC/NHS}} \text{R}{-}\text{CO}{-}\text{NH}{-}\text{R'} + \text{H}_2\text{O} \tag{5.21}$$

EDC (1-ethyl-3-(3-dimethylaminopropyl)carbodiimide) and NHS (N-hydroxysuccinimide) activate carboxylic acids.

Grafting Density and Characterization

Grafting density σ (molecules/nm^2 or chains/nm^2):

$$\sigma = \frac{N_A \cdot w_{polymer}}{M_n \cdot A_{surface}} \tag{5.22}$$

where:

- $w_{polymer}$ is mass of grafted polymer
- M_n is number-average molecular weight
- $A_{surface}$ is specific surface area

Typical values:

- Grafting-to: 0.1-0.5 chains/nm^2
- Grafting-from: 0.5-2.0 chains/nm^2
- SAMs: 3-5 molecules/nm^2

5.3.2 Plasma Treatment

Plasma treatment uses ionized gas to modify nanomaterial surfaces through physical bombardment and/or chemical reactions.

Plasma Fundamentals

A plasma consists of:

- Electrons (high kinetic energy: 1-10 eV)
- Ions (positive and negative)
- Radicals (neutral reactive species)
- Photons (UV and visible)

Degree of ionization:

$$\alpha = \frac{n_i}{n_i + n_n} \tag{5.23}$$

where n_i is ion density and n_n is neutral density.
Low-temperature plasmas used for surface modification: $\alpha \sim 10^{-6}$ to 10^{-4}.

Plasma-Surface Interactions

1. Physical effects:

- Ion bombardment $\rightarrow$ surface cleaning, etching
- Energy transfer: $E = \frac{1}{2}m_i v_i^2 + eV_{plasma}$
- Sputtering yield: atoms removed per incident ion

2. Chemical effects:

- Radical reactions with surface atoms
- Formation of new functional groups
- Cross-linking of surface polymers

Common Plasma Treatments

Table 5.2: Plasma gases and their surface modifications

Plasma Gas	Functional Groups	Applications
O_2	-OH, -C=O, -COOH	Hydrophilization, cleaning
NH_3	-NH_2, -NH-	Amination for bioconjugation
CF_4	-CF_3, -CF_2-	Hydrophobization
Ar	None (physical)	Cleaning, activation
H_2	-H (reduction)	Reduction of oxides
Air	Mixed oxygenated	General activation

Process Parameters

Key parameters affecting modification:

- **Power:** 10-500 W (controls plasma density)
- **Pressure:** 0.1-1 Torr (affects mean free path)
- **Time:** Seconds to minutes
- **Frequency:** RF (13.56 MHz), microwave (2.45 GHz)

Surface modification depth:

$$d_{mod} \approx \lambda_{mfp} \cdot \sqrt{t \cdot D} \tag{5.24}$$

where λ_{mfp} is mean free path, t is time, D is diffusion coefficient.
Typical depths: 1-10 nm for polymers, sub-nm for metals.

Example

Oxygen plasma treatment of carbon nanotubes
Conditions:

- Gas: O_2 (99.9%)
- Power: 100 W
- Pressure: 0.5 Torr
- Time: 5 minutes

Results:

- Introduction of -OH, -COOH groups
- Oxygen content: 0% → 8-12%
- Contact angle: 85° → 25° (hydrophilic)
- Enhanced dispersibility in water

Mechanism:

$$\mathrm{C(CNT)} + \mathrm{O}^{\bullet} \longrightarrow \mathrm{C{-}O}^{\bullet} \xrightarrow{\mathrm{O_2}} \mathrm{C{=}O, C{-}OH} \tag{5.25}$$

5.3.3 Polymer Coating

Polymer coatings provide physical and chemical barriers on nanomaterial surfaces.

Coating Methods

1. **Physisorption:**
   Non-covalent adsorption through:

- Van der Waals forces
- Electrostatic interactions
- Hydrogen bonding
- Hydrophobic interactions

Adsorption energy: 5-50 kJ/mol

2. Layer-by-layer (LbL) assembly:

Alternating deposition of oppositely charged polyelectrolytes:

$$\mathrm{NP}^{+} + \mathrm{Polymer}^{-} \xrightarrow{\mathrm{NP-Polymer}} {}^{-} + \mathrm{Polymer}^{+} \xrightarrow{\mathrm{NP-Polymer-Polymer}} {}^{+} \tag{5.26}$$

Thickness per bilayer: 1-5 nm

3. In-situ polymerization:

Monomers polymerize on nanoparticle surface:

$$\mathrm{NP} + \mathrm{nMonomer} \xrightarrow{\mathrm{initiator}} \mathrm{NP@Polymer} \tag{5.27}$$

4. Encapsulation:

Nanoparticles trapped within polymer matrix during synthesis.

Common Coating Polymers

Table 5.3: Polymers used for nanomaterial coating

Polymer	Properties	Applications
PEG (polyethylene glycol)	Biocompatible, hydrophilic	Drug delivery, stealth coating
PVP (polyvinylpyrrolidone)	Stabilizer, hydrophilic	Dispersion, synthesis
PVA (polyvinyl alcohol)	Biocompatible, film-forming	Biomedical, packaging
Chitosan	Biodegradable, cationic	Antimicrobial, drug delivery
PMMA (polymethyl methacrylate)	Transparent, rigid	Optical applications
Polydopamine	Adhesive, multifunctional	Universal coating

Coating Thickness and Stability

For polymer-coated nanoparticles, the hydrodynamic diameter:

$$d_h = d_{core} + 2\delta_{coating} \tag{5.28}$$

Coating thickness δ depends on:

- Polymer molecular weight
- Grafting density
- Solvent quality
- Ionic strength

For grafted polymers in good solvent (Flory regime):

$$\delta \approx N^{3/5} a \tag{5.29}$$

where N is degree of polymerization and a is monomer size.
Desorption rate constant for physisorbed polymers:

$$k_d = k_0 \exp\left(-\frac{E_a}{RT}\right) \tag{5.30}$$

Stability increases with:

- Higher molecular weight
- Multiple anchor points
- Covalent attachment

5.4 Surfactants and Capping Agents

5.4.1 Fundamentals of Surfactants

Definition

Surfactants (surface-active agents) are amphiphilic molecules with hydrophobic tails and hydrophilic heads that preferentially adsorb at interfaces, reducing surface tension.

Surfactant Classification

1. Ionic surfactants:

- Anionic: R-COO^-, R-SO_3^- (e.g., SDS, AOT)
- Cationic: R-$N^+(CH_3)_3$ (e.g., CTAB, CTAC)
- Zwitterionic: Both charges (e.g., phospholipids)

2. Non-ionic surfactants:

- Ethoxylated: R-O-$(CH_2CH_2O)_n$-H (e.g., Triton X, Tween)
- Block copolymers: PEO-PPO-PEO (e.g., Pluronic)

Critical Micelle Concentration (CMC)

Below CMC: Surfactants adsorb at interfaces
Above CMC: Micelles form in bulk solution

$$\gamma = \gamma_0 - RT\Gamma \ln\left(1 + \frac{C}{a}\right) \tag{5.31}$$

where Γ is surface excess concentration and a is adsorption constant.
At CMC, surface tension reaches minimum and becomes constant.

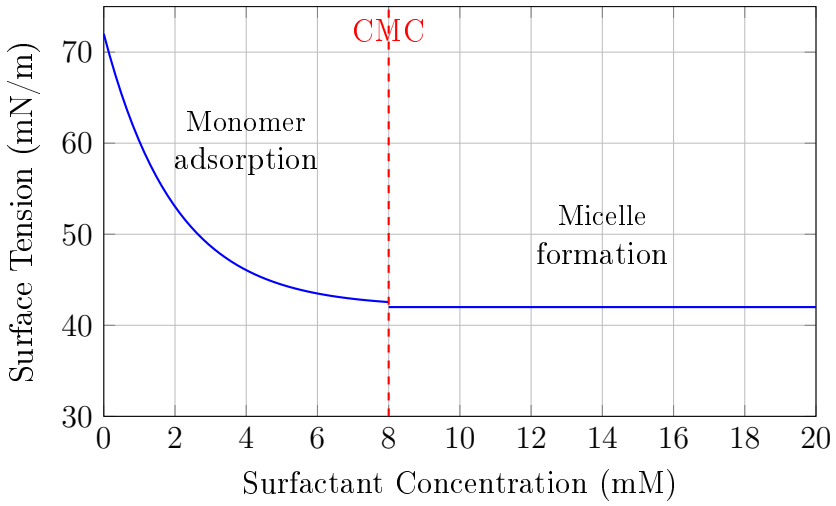

Figure 5.4: Surface tension vs. surfactant concentration showing CMC

Table 5.4: CMC values of common surfactants in water at 25°C

Surfactant	**Type**	**CMC (mM)**
SDS (sodium dodecyl sulfate)	Anionic	8.2
CTAB (cetyltrimethylammonium bromide)	Cationic	0.9
Triton X-100	Non-ionic	0.24
Tween 20	Non-ionic	0.06
AOT (sodium dioctyl sulfosuccinate)	Anionic	2.5

5.4.2 Capping Agent Mechanisms

Capping agents control nanoparticle nucleation and growth by:

1. **Adsorption:** Selective binding to specific crystal facets
2. **Growth inhibition:** Blocking addition sites
3. **Stabilization:** Preventing agglomeration
4. **Shape control:** Differential facet coverage

Adsorption Isotherms

Langmuir isotherm:

$$\theta = \frac{KC}{1 + KC} \tag{5.32}$$

where θ is fractional coverage, K is adsorption equilibrium constant, C is concentration.

Surface coverage:

$$\Gamma = \Gamma_{max} \frac{KC}{1 + KC} \tag{5.33}$$

Freundlich isotherm:

$$\Gamma = K_F C^{1/n} \tag{5.34}$$

Empirical equation for heterogeneous surfaces.

Facet-Selective Capping

Different capping agents bind preferentially to different crystal facets, controlling nanoparticle shape.

For FCC metals (Au, Ag, Pt):

- {111} facets: Most stable (lowest energy)
- {100} facets: Intermediate energy
- {110} facets: Highest energy

Binding energy order determines shape:

$$\text{Shape} = f\left(\frac{E_{binding,\{100\}}}{E_{binding,\{111\}}}\right) \tag{5.35}$$

- Ratio ≈ 1.73: Octahedron (all {111})
- Ratio ≈ 1.0: Cube (all {100})
- Intermediate: Cuboctahedron, truncated shapes

Example

Shape control of Ag nanoparticles using PVP
PVP (polyvinylpyrrolidone) preferentially binds to {100} facets of Ag:
High PVP concentration:

- Strong {100} protection
- Growth along ⟨111⟩ direction
- Product: Nanocubes (bounded by {100})

Low PVP concentration:

- Weak facet selectivity
- Isotropic growth
- Product: Nanospheres

Reaction:

$$Ag^+ + e^- \xrightarrow{\text{PVP}} Ag^0 \xrightarrow{\text{growth}} \text{Agnanocubes} \tag{5.36}$$

5.5 Role in Stability, Dispersion, and Targeted Applications

5.5.1 Enhanced Colloidal Stability

Functionalization improves stability through:

1. Electrostatic stabilization:
Introduction of charged groups increases zeta potential (ζ):

$$\zeta = \frac{4\pi\sigma d}{\varepsilon_r \varepsilon_0 \kappa} \tag{5.37}$$

Stability criterion: $|\zeta| > 25$ mV (good stability)

2. Steric stabilization:
Polymer layers prevent close approach:

$$V_{steric} = V_{mixing} + V_{elastic} > 0 \tag{5.38}$$

3. Combined electrosteric stabilization:
Charged polymers (e.g., PAA, PEI) provide both mechanisms.

5.5.2 Improved Dispersion

Wetting and dispersion characterized by contact angle θ:

$$\cos\theta = \frac{\gamma_{SV} - \gamma_{SL}}{\gamma_{LV}} \tag{5.39}$$

where subscripts S, L, V denote solid, liquid, vapor.
Surface modification changes γ_{SL} to improve wetting.
Dispersibility quantification:
Turbidity measurement using Beer-Lambert law:

$$A = \varepsilon \cdot C \cdot l \tag{5.40}$$

Higher absorbance $\rightarrow$ better dispersion
Sedimentation time:

$$t_{sed} = \frac{18\eta h}{(\rho_p - \rho_m) g d^2} \tag{5.41}$$

where η is viscosity, h is height, ρ are densities.

5.5.3 Biomedical Applications

Biocompatibility Enhancement

PEGylation (PEG coating) provides:

- "Stealth" effect: Evades immune recognition
- Prolonged circulation time

- Reduced protein adsorption

Protein adsorption (Vroman effect):

$$\Gamma_{protein} = \Gamma_{max} \left(1 - e^{-k_{ads}t}\right) \tag{5.42}$$

PEG reduces Γ_{max} by steric exclusion.

Targeted Drug Delivery

Surface conjugation with targeting ligands:

- Antibodies: Specific antigen recognition
- Peptides: RGD sequence for integrin binding
- Aptamers: Nucleic acid-based binding
- Small molecules: Folic acid for cancer cells

Binding affinity (dissociation constant):

$$K_D = \frac{k_{off}}{k_{on}} = \frac{[\text{Ligand}][\text{Receptor}]}{[\text{Complex}]} \tag{5.43}$$

Lower $K_D \rightarrow$ stronger binding
Typical values: nM to pM range for effective targeting.

5.5.4 Catalytic Applications

Surface modification affects catalytic performance:
Active site engineering:
Ligands can:

- Block unselective sites
- Create uniform active sites
- Modify electronic structure

Turnover frequency (TOF):

$$TOF = \frac{\text{moles of product}}{\text{moles of active sites} \times \text{time}} \tag{5.44}$$

Surface functionalization can increase TOF by 10-1000×.

5.6 Example: Surface Modification of Graphene Oxide

Graphene oxide (GO) serves as an excellent platform for studying surface functionalization due to its rich surface chemistry.

5.6.1 Structure and Chemistry of Graphene Oxide

GO contains multiple oxygen-containing functional groups:

- Epoxy groups (-O-) on basal plane
- Hydroxyl groups (-OH) on basal plane
- Carboxyl groups (-COOH) at edges
- Carbonyl groups (-C=O) at edges

Oxygen content: Typically 30-50 wt%
C/O ratio: 2:1 to 3:1

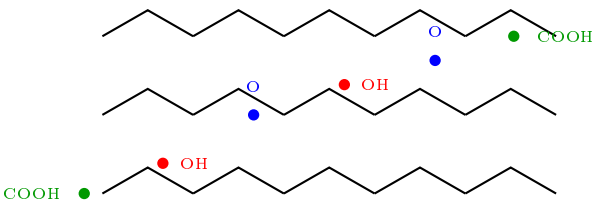

Figure 5.5: Schematic structure of graphene oxide showing various functional groups

5.6.2 Reduction of Graphene Oxide

Reduction removes oxygen groups, partially restoring sp^2 carbon network:

Chemical reduction:

$$\text{GO} + \text{Reducingagent} \longrightarrow \text{rGO} + \text{Oxidizedproducts} \tag{5.45}$$

Common reducing agents:

- Hydrazine (N_2H_4): Strong, toxic
- Sodium borohydride ($NaBH_4$): Moderate
- Ascorbic acid (Vitamin C): Mild, green
- Hydroiodic acid (HI): Strong

Thermal reduction:
Rapid heating (>1000°C/min) to 200-1000°C:

$$\text{C}-\text{Ogroups} \xrightarrow{\Delta} \text{CO}_2 + \text{CO} + \text{H}_2\text{O} \tag{5.46}$$

Electrochemical reduction:
Apply negative potential:

$$\text{GO} + \text{ne}^- + \text{nH}^+ \longrightarrow \text{rGO} + \text{H}_2\text{O} \tag{5.47}$$

Extent of reduction characterized by C/O ratio:

- GO: C/O = 2-3
- rGO: C/O = 8-15
- Pristine graphene: C/O > 100

5.6.3 Functionalization Strategies for GO

Covalent Functionalization

1. Esterification:

$$\text{GO}-\text{COOH} + \text{R}-\text{OH} \xrightarrow{\text{DCC}} \text{GO}-\text{COO}-\text{R} + \text{H}_2\text{O} \tag{5.48}$$

2. Amidation:

$$\text{GO}-\text{COOH} + \text{R}-\text{NH}_2 \xrightarrow{\text{EDC/NHS}} \text{GO}-\text{CO}-\text{NH}-\text{R} + \text{H}_2\text{O} \tag{5.49}$$

3. Epoxy ring-opening:

$$\text{GO}-\text{O}^-(\text{epoxy}) + \text{R}-\text{NH}_2 \longrightarrow \text{GO}-\text{O}-\text{CH}(\text{NH}-\text{R})-\text{CH}(\text{OH})^- \tag{5.50}$$

4. Diazonium coupling:

$$\text{GO} + \text{ArN}_2^+ \longrightarrow \text{GO}-\text{Ar} + \text{N}_2 \tag{5.51}$$

Non-covalent Functionalization

- π-π stacking with aromatic molecules
- Hydrogen bonding with polymers
- Electrostatic interactions with charged species
- Van der Waals interactions

Advantages:

- Preserves graphene electronic structure
- Reversible
- Simple processing

Application

GO-based drug delivery system
Procedure:

1. Reduce GO partially to improve biocompatibility
2. PEGylate rGO via amidation:

$$\text{rGO}-\text{COOH} + \text{H}_2\text{N}-\text{PEG}-\text{NH}_2 \longrightarrow \text{rGO}-\text{CONH}-\text{PEG}-\text{NH}_2 \quad (5.52)$$

3. Load anticancer drug (doxorubicin) via π-π stacking
4. Conjugate targeting antibody to terminal -NH_2

Properties:

- Drug loading: 1-2 mg drug/mg rGO-PEG
- pH-responsive release: Low pH (tumor) triggers release
- NIR photothermal effect: rGO absorbs NIR, generates heat
- Enhanced cellular uptake: Antibody targeting

Performance:

- 10× higher cancer cell killing vs. free drug
- Reduced side effects (targeting)
- Synergistic chemo-photothermal therapy

5.6.4 Characterization of Functionalized GO

Table 5.5: Characterization techniques for GO functionalization

Technique	Information	Key Indicators
XPS	Elemental composition	C/O ratio, functional groups
FTIR	Functional groups	C=O (1720), C-O (1050) cm^{-1}
Raman	Sp^2/sp^3 ratio	I_D/I_G ratio
TGA	Thermal stability	Mass loss steps
UV-Vis	Electronic structure	π-π^* transition
Zeta potential	Surface charge	Stability prediction
Contact angle	Hydrophilicity	Wettability

5.7 Summary

Surface functionalization and modification are essential tools in nanomaterials science, enabling:

Key Point

Key Concepts:

- High surface-to-volume ratio makes surface chemistry dominant in nanomaterials
- DLVO theory explains colloidal stability through balance of van der Waals attraction and electrostatic repulsion
- Chemical grafting provides covalent attachment with high stability
- Plasma treatment offers rapid, versatile surface activation
- Polymer coating provides steric stabilization and biocompatibility
- Surfactants and capping agents control nucleation, growth, and shape
- Functionalization enables targeted applications in biomedicine, catalysis, sensing, and energy
- Graphene oxide exemplifies versatile platform for diverse functionalization strategies

Future directions include:

- Atomically precise surface engineering
- Stimuli-responsive functionalization
- Self-healing surface coatings
- Bio-inspired functionalization
- Computational design of surface chemistry

Exercises

Conceptual Questions

1. Explain why surface energy becomes increasingly important as particle size decreases. Derive the expression for size-dependent chemical potential.
2. Describe the DLVO theory. How does surface functionalization modify the total interaction potential between nanoparticles?
3. Compare and contrast "grafting-to" and "grafting-from" approaches for polymer functionalization. Which would you choose for high grafting density and why?
4. Explain the mechanism of plasma-surface interaction. How does oxygen plasma differ from argon plasma in terms of surface modification?
5. Discuss the concept of CMC. Why is it important for nanomaterial synthesis and stabilization?

6. How do capping agents control nanoparticle shape? Provide a specific example.
7. Explain steric stabilization. Derive the conditions for effective steric repulsion.
8. Why is PEGylation important for biomedical applications of nanoparticles?
9. Describe three methods to reduce graphene oxide. Compare their advantages and limitations.
10. Discuss the difference between covalent and non-covalent functionalization of graphene oxide. When would you use each approach?

Numerical Problems

1. For a spherical Au nanoparticle with diameter 10 nm:
   (a) Calculate the surface-to-volume ratio
   (b) Estimate the percentage of surface atoms (assume FCC with $a = 4.08$ Å)
   (c) Calculate the excess chemical potential at the surface (Au surface energy: 1.5 J/m^2, $V_m = 10.2$ cm^3/mol)
2. Using DLVO theory, calculate the total interaction energy between two 50 nm SiO_2 particles at separation $h = 5$ nm:
   - Hamaker constant: $A_H = 6.5 \times 10^{-20}$ J
   - Surface potential: $\psi_0 = 50$ mV
   - Debye length: $\lambda_D = 10$ nm
   - Medium: Water ($\varepsilon_r = 80$)
3. For silane coupling on SiO_2 nanoparticles (specific surface area 200 m^2/g):
   (a) If 0.5 g SiO_2 reacts with APTES achieving grafting density of 2 molecules/nm^2, calculate mass of APTES attached
   (b) Calculate the number of -NH_2 groups per gram of functionalized SiO_2
4. A surfactant reduces surface tension from 72 mN/m to 35 mN/m at CMC. Using Gibbs adsorption equation at 25°C:

$$\Gamma = -\frac{1}{RT}\frac{d\gamma}{d\ln C}$$

   If CMC is 5 mM, estimate surface excess concentration Γ (assume linear decrease before CMC).
5. Polymer-coated nanoparticles have hydrodynamic diameter 80 nm measured by DLS. If core diameter is 50 nm:
   (a) Calculate coating thickness
   (b) If polymer molecular weight is 10,000 g/mol and grafting density is 0.5 chains/nm^2, calculate total polymer mass on one particle

(c) Estimate volume fraction of polymer in the shell (polymer density: 1.1 g/cm^3)

6. For Langmuir adsorption of a capping agent on nanoparticle surface with $K = 10^5$ M^{-1}:

   (a) Calculate fractional coverage θ at concentrations: 0.1 mM, 1 mM, 10 mM

   (b) At what concentration is $\theta = 0.9$?

   (c) If $\Gamma_{max} = 5$ molecules/nm^2, calculate surface concentration at 1 mM

7. A 20 nm diameter nanoparticle with zeta potential -40 mV is dispersed in water. Calculate:

   (a) Electrophoretic mobility using Hückel equation: $\mu_E = \frac{2\varepsilon_r \varepsilon_0 \zeta}{3\eta}$

   (b) Terminal velocity in electric field $E = 100$ V/cm (water viscosity: 0.001 Pa·s)

8. Graphene oxide (C:O = 2.5:1, formula: $C_{10}O_4H_4$) is reduced with hydrazine:

   (a) Calculate molecular weight of GO unit

   (b) If reduction increases C:O to 12:1, calculate percentage of oxygen removed

   (c) If starting with 1 g GO, calculate mass of rGO produced

9. For plasma treatment of carbon nanotubes at 100 W for 5 min:

   (a) If ion energy is 50 eV and ion flux is 10^{16} ions/cm^2/s, calculate total energy deposited per cm^2

   (b) If each ion creates 2 functional groups, estimate functionalization density

10. Calculate the sedimentation time for 50 nm SiO_2 nanoparticles in water over 1 cm height:

    - SiO_2 density: 2.2 g/cm^3
    - Water density: 1.0 g/cm^3
    - Water viscosity: 0.001 Pa·s

    Compare with 50 nm particles coated with 10 nm polymer layer (polymer density: 1.1 g/cm^3).

Advanced Problems

1. Design a functionalization strategy for Fe_3O_4 nanoparticles for targeted cancer therapy. Include:

   - Surface coating for biocompatibility
   - Targeting ligand and conjugation chemistry
   - Drug loading mechanism
   - Characterization plan

2. Propose an experimental protocol to determine the grafting density of PEG on Au nanoparticles. Include measurement techniques and calculation methods.

3. Develop a plasma treatment procedure to convert hydrophobic carbon nanotubes (contact angle 90°) to hydrophilic (contact angle $< 30°$). Specify gas, power, time, and pressure. How would you verify success?

4. Compare the stability of electrostatically stabilized vs. sterically stabilized Ag nanoparticles in high salt concentration (0.5 M NaCl). Use DLVO theory to support your analysis.

5. Design a synthesis protocol for shape-controlled Pt nanoparticles (cubes, octahedra, and wires) using different capping agents. Justify your choice of capping agents based on crystallographic considerations.

Bibliography

[1] Cao, G., & Wang, Y. (2011). *Nanostructures and Nanomaterials: Synthesis, Properties, and Applications* (2nd ed.). World Scientific Publishing.

[2] Ozin, G. A., & Arsenault, A. C. (2009). *Nanochemistry: A Chemical Approach to Nanomaterials* (2nd ed.). Royal Society of Chemistry.

[3] Rao, C. N. R., Müller, A., & Cheetham, A. K. (2004). *The Chemistry of Nanomaterials: Synthesis, Properties and Applications*. Wiley-VCH.

[4] Love, J. C., Estroff, L. A., Kriebel, J. K., Nuzzo, R. G., & Whitesides, G. M. (2005). Self-assembled monolayers of thiolates on metals as a form of nanotechnology. *Chemical Reviews*, 105(4), 1103-1170.

[5] Barbey, R., Lavanant, L., Paripovic, D., et al. (2009). Polymer brushes via surface-initiated controlled radical polymerization. *Chemical Reviews*, 109(11), 5437-5527.

[6] Israelachvili, J. N. (2011). *Intermolecular and Surface Forces* (3rd ed.). Academic Press.

[7] Hiemenz, P. C., & Rajagopalan, R. (2016). *Principles of Colloid and Surface Chemistry* (4th ed.). CRC Press.

[8] Dreyer, D. R., Park, S., Bielawski, C. W., & Ruoff, R. S. (2010). The chemistry of graphene oxide. *Chemical Society Reviews*, 39(1), 228-240.

[9] Zhu, Y., Murali, S., Cai, W., et al. (2010). Graphene and graphene oxide: synthesis, properties, and applications. *Advanced Materials*, 22(35), 3906-3924.

[10] Napper, D. H. (1983). *Polymeric Stabilization of Colloidal Dispersions*. Academic Press.

[11] Desai, M. P., Labhasetwar, V., Walter, E., Levy, R. J., & Amidon, G. L. (1997). The mechanism of uptake of biodegradable microparticles in Caco-2 cells is size dependent. *Pharmaceutical Research*, 14(11), 1568-1573.

[12] Sperling, R. A., & Parak, W. J. (2010). Surface modification, functionalization and bioconjugation of colloidal inorganic nanoparticles. *Philosophical Transactions of the Royal Society A*, 368(1915), 1333-1383.

[13] Xia, Y., Xiong, Y., Lim, B., & Skrabalak, S. E. (2009). Shape-controlled synthesis of metal nanocrystals. *Angewandte Chemie International Edition*, 48(1), 60-103.

[14] Grzelczak, M., Pérez-Juste, J., Mulvaney, P., & Liz-Marzán, L. M. (2008). Shape control in gold nanoparticle synthesis. *Chemical Society Reviews*, 37(9), 1783-1791.

[15] Hotze, E. M., Phenrat, T., & Lowry, G. V. (2010). Nanoparticle aggregation: challenges to understanding transport and reactivity. *Journal of Environmental Quality*, 39(6), 1909-1924.

[16] Walkey, C. D., & Chan, W. C. (2012). Understanding and controlling the interaction of nanomaterials with proteins in a physiological environment. *Chemical Society Reviews*, 41(7), 2780-2799.

[17] Nel, A. E., Mädler, L., Velegol, D., et al. (2009). Understanding biophysicochemical interactions at the nano–bio interface. *Nature Materials*, 8(7), 543-557.

[18] Jokerst, J. V., Lobovkina, T., Zare, R. N., & Gambhir, S. S. (2011). Nanoparticle PEGylation for imaging and therapy. *Nanomedicine*, 6(4), 715-728.

[19] Laurent, S., Forge, D., Port, M., et al. (2008). Magnetic iron oxide nanoparticles: synthesis, stabilization, vectorization, physicochemical characterizations, and biological applications. *Chemical Reviews*, 108(6), 2064-2110.

[20] Langer, R., & Tirrell, D. A. (2004). Designing materials for biology and medicine. *Nature*, 428(6982), 487-492.

[21] Peer, D., Karp, J. M., Hong, S., et al. (2007). Nanocarriers as an emerging platform for cancer therapy. *Nature Nanotechnology*, 2(12), 751-760.

[22] Farokhzad, O. C., & Langer, R. (2009). Impact of nanotechnology on drug delivery. *ACS Nano*, 3(1), 16-20.

[23] Schladt, T. D., Schneider, K., Schild, H., & Tremel, W. (2011). Synthesis and bio-functionalization of magnetic nanoparticles for medical diagnosis and treatment. *Dalton Transactions*, 40(24), 6315-6343.

[24] Chaudhuri, R. G., & Paria, S. (2012). Core/shell nanoparticles: classes, properties, synthesis mechanisms, characterization, and applications. *Chemical Reviews*, 112(4), 2373-2433.

[25] Feng, L., & Liu, Z. (2011). Graphene in biomedicine: opportunities and challenges. *Nanomedicine*, 6(2), 317-324.

[26] Sun, X., Liu, Z., Welsher, K., et al. (2008). Nano-graphene oxide for cellular imaging and drug delivery. *Nano Research*, 1(3), 203-212.

[27] Zhao, J., Pei, S., Ren, W., Gao, L., & Cheng, H. M. (2010). Efficient preparation of large-area graphene oxide sheets for transparent conductive films. *ACS Nano*, 4(9), 5245-5252.

Chapter 6

Thin Films and Nanocomposites

"The combination of materials at the nanoscale creates properties that neither component possesses alone—the essence of nanocomposite synergy."
— Paul Calvert

6.1 Introduction

Thin films and nanocomposites represent two of the most versatile and technologically important classes of nanomaterials. A thin film is a layer of material ranging from fractions of a nanometer to several micrometers in thickness, deposited on a substrate. Nanocomposites are multiphase materials where at least one phase has dimensions in the nanometer range (1-100 nm), resulting in unique properties that exceed those of conventional composites.

Definition

Thin Film: A layer of material with thickness ranging from atomic monolayers ($\sim$0.3 nm) to several micrometers, exhibiting properties different from bulk due to quantum confinement, surface effects, and interfacial phenomena.
Nanocomposite: A multiphase solid material where one of the phases has one, two, or three dimensions less than 100 nm, or structures having nanoscale repeat distances between the different phases.

The unique properties of thin films arise from:

- High surface-to-volume ratio
- Quantum confinement effects (for very thin films)
- Interface and surface energy contributions
- Strain effects from lattice mismatch
- Modified electronic band structure

For a thin film of thickness t, the volume-to-surface ratio:

$$\frac{V}{A} = \frac{A \cdot t}{2A + \text{edge}} \approx \frac{t}{2} \tag{6.1}$$

As t decreases, surface effects dominate.

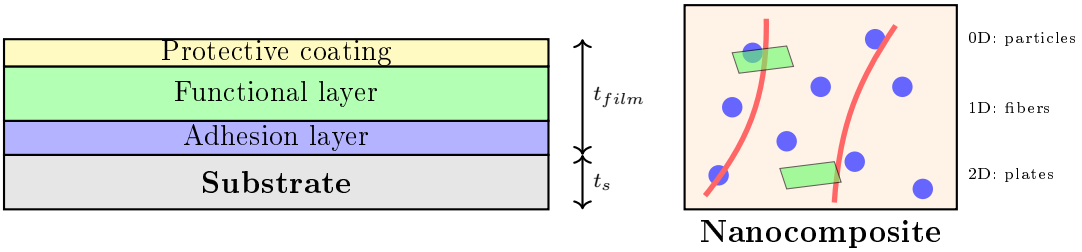

Figure 6.1: Schematic representation of multilayer thin film structure (left) and nanocomposite with different dimensional fillers (right)

This chapter explores deposition techniques for thin films, various types of nanocomposites, and the structure-property relationships that make these materials invaluable for modern technology.

6.2 Thin Film Deposition Techniques

Thin film deposition methods are classified into two main categories:

- **Physical Vapor Deposition (PVD):** Material transfer through physical processes (evaporation, sputtering)
- **Chemical Vapor Deposition (CVD):** Film growth through chemical reactions of gaseous precursors

Additionally, solution-based methods like spin coating provide cost-effective alternatives for certain applications.

6.2.1 Spin Coating

Spin coating is a widely used solution-processing technique for depositing uniform thin films on flat substrates.

Process Description

The spin coating process consists of four stages:

1. **Deposition:** Solution dispensed onto substrate center
2. **Spin-up:** Substrate accelerates to final rotation speed
3. **Spin-off:** Excess solution expelled by centrifugal force
4. **Evaporation:** Solvent evaporates, film solidifies

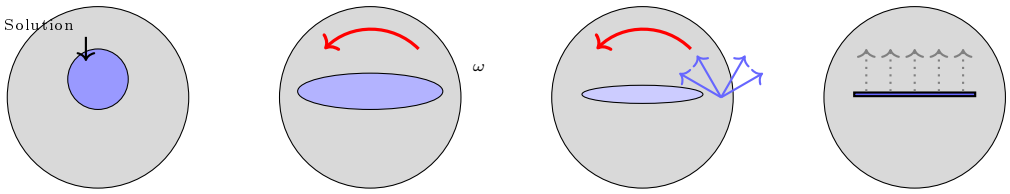

Figure 6.2: Four stages of spin coating process

Theory and Mathematical Modeling

The final film thickness is determined by the balance between centrifugal force expelling the solution and viscous forces resisting flow.

For a Newtonian fluid on a rotating disk, the thinning rate during spin-off is:

$$\frac{dh}{dt} = -\frac{2\omega^2 h^2}{3\nu} \tag{6.2}$$

where:

- h is film thickness
- ω is angular velocity (rad/s)
- ν is kinematic viscosity

Integrating from initial thickness h_0 at $t = 0$ to final thickness h_f:

$$h_f = h_0 \left(1 + \frac{2\omega^2 h_0 t}{3\nu}\right)^{-1} \tag{6.3}$$

During evaporation-dominated regime, the empirical relationship:

$$h_f = K \frac{C^{1/3}}{\omega^{1/2}} \tag{6.4}$$

where:

- K is a constant depending on solution properties
- C is solute concentration
- ω is spin speed

More generally:

$$h_f \propto \frac{\eta^a C^b}{\omega^c} \tag{6.5}$$

with typical exponents: $a \approx 0.5$, $b \approx 0.3 - 1.0$, $c \approx 0.5 - 1.0$.

Process Parameters

Table 6.1: Key parameters affecting spin coating

Parameter	Effect on Thickness	Typical Range
Spin speed (ω)	$h \propto \omega^{-0.5}$	1000-8000 rpm
Solution viscosity (η)	$h \propto \eta^{0.5}$	1-100 cP
Concentration (C)	$h \propto C^{0.3-1}$	0.5-10 wt%
Spin time	Affects uniformity	10-60 s
Acceleration	Affects uniformity	500-1500 rpm/s

Example

Spin coating of PMMA
Solution: 3 wt% PMMA in chlorobenzene ($\eta = 5$ cP)
Spin speed: 3000 rpm
Using empirical relation with $K = 50$:

$$h_f = 50 \times \frac{(3)^{0.33}}{(3000)^{0.5}} = 50 \times \frac{1.44}{54.77} \approx 1.3 \text{ nm} \tag{6.6}$$

Actual thickness: 130 nm (correction factor needed)
More accurately: $h_f \approx 100 \times (C/\omega^{0.5})$ gives ∼140 nm

6.2.2 Sputtering

Sputtering is a PVD technique where energetic ions bombard a target material, ejecting atoms that deposit on a substrate.

Sputtering Mechanism

When an energetic ion (typically Ar^+) strikes the target surface:

1. Ion penetrates surface (depth ∼ 1-10 nm)
2. Collision cascade transfers momentum to target atoms
3. Surface atoms with sufficient energy overcome binding energy
4. Sputtered atoms travel to substrate and condense

Sputter yield Y (atoms ejected per incident ion):

$$Y = \frac{3\alpha}{4\pi^2} \frac{M_1}{M_2} \frac{E}{U_s} \tag{6.7}$$

where:

- α is energy transfer efficiency
- M_1 is ion mass, M_2 is target atom mass

- E is ion energy
- U_s is surface binding energy

For optimum momentum transfer: $M_1 \approx M_2$ (Ar for most metals)

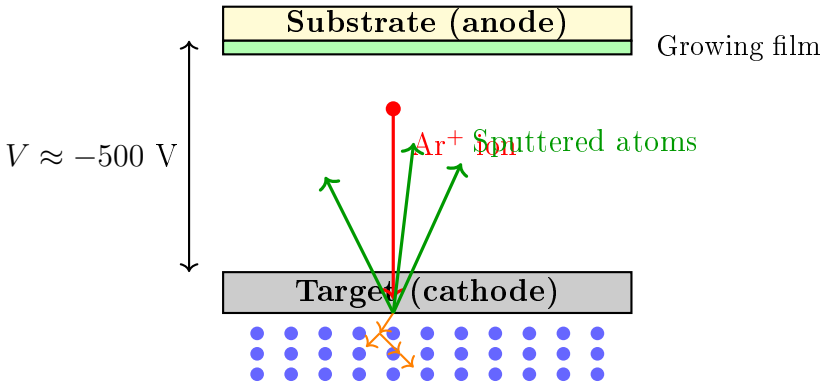

Figure 6.3: Schematic of sputtering process showing ion bombardment and atom ejection

Types of Sputtering

Table 6.2: Comparison of sputtering techniques

Type	Mechanism	Advantages	Applications
DC sputtering	Direct current discharge	Simple, low cost	Conductive films
RF sputtering	Radio frequency (13.56 MHz)	Insulators possible	Oxides, nitrides
Magnetron	Magnetic field traps electrons	High rate, low temp	Industrial coating
Reactive	Reaction with gas	Compound films	TiN, Al_2O_3

Deposition Rate

The deposition rate R_d (nm/s):

$$R_d = \frac{Y \cdot J \cdot M}{e \cdot N_A \cdot \rho} \cdot \cos\theta \tag{6.8}$$

where:

- J is ion current density (A/cm^2)
- M is atomic mass
- e is elementary charge
- N_A is Avogadro's number
- ρ is film density
- θ is angle from target normal

Typical rates: 0.1-10 nm/s

6.2.3 Pulsed Laser Deposition (PLD)

PLD uses high-power laser pulses to ablate material from a target, creating a plume that deposits on a substrate.

PLD Process

1. Laser pulse ($\sim$ 10-30 ns) focused on target
2. Intense energy absorption ($> 10^8$ W/cm^2)
3. Rapid heating, melting, vaporization
4. Plasma plume formation with ions, atoms, clusters
5. Plume expansion toward substrate
6. Film nucleation and growth

Ablation threshold fluence:

$$\Phi_{th} = \frac{E_{pulse}}{A_{spot}} \tag{6.9}$$

Typical values: 0.5-5 J/cm^2

Ablation depth per pulse:

$$d = \frac{1}{\alpha} \ln\left(\frac{\Phi}{\Phi_{th}}\right) \tag{6.10}$$

where α is optical absorption coefficient.

Plume Dynamics

The plume expansion can be modeled by adiabatic expansion:

$$R(t) = R_0 \left(1 + \frac{\gamma - 1}{2} v_s \frac{t}{R_0}\right)^{2/(\gamma-1)} \tag{6.11}$$

where:

- $R(t)$ is plume radius at time t
- v_s is sound velocity in plasma
- γ is adiabatic index

Typical plume velocities: 10^4-10^6 cm/s

Table 6.3: PLD process parameters

Parameter	**Effect**	**Typical Value**
Laser wavelength	Absorption, ablation	193 nm (ArF), 248 nm (KrF)
Pulse energy	Ablation rate	100-500 mJ
Fluence	Stoichiometry, rate	1-5 J/cm^2
Repetition rate	Deposition rate	1-50 Hz
Background pressure	Film properties	10^{-6}-10^{-1} Torr
Substrate temperature	Crystallinity	25-800°C
Target-substrate distance	Film uniformity	4-8 cm

Advantages and Limitations

Advantages:

- Stoichiometric transfer (complex oxides)
- High purity (vacuum environment)
- Wide material range
- Energetic species (better adhesion)

Limitations:

- Particulates ("splashing")
- Small area coverage
- High equipment cost
- Non-uniform thickness

6.2.4 Atomic Layer Deposition (ALD)

ALD is a variant of CVD that deposits films one atomic layer at a time through sequential, self-limiting surface reactions.

ALD Principles

ALD cycle consists of four steps:

1. **Precursor A exposure:** Chemisorption until surface saturation
2. **Purge:** Remove excess precursor A and byproducts
3. **Precursor B exposure:** Reaction with adsorbed species
4. **Purge:** Remove excess precursor B and byproducts

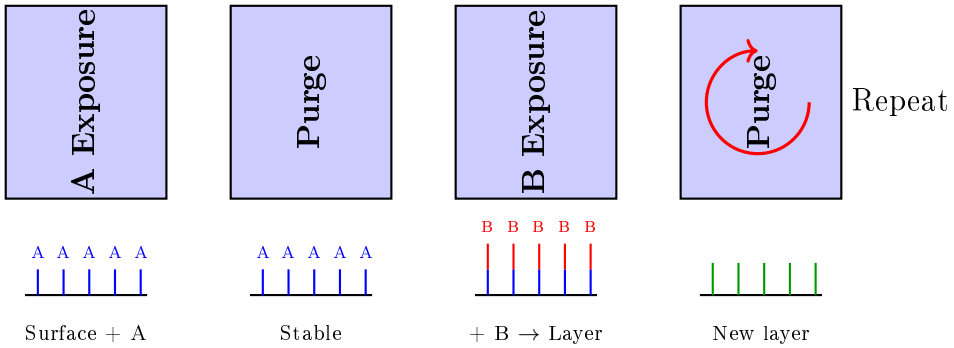

Figure 6.4: ALD cycle showing self-limiting surface reactions

Growth Per Cycle (GPC)

The growth per cycle is a fundamental parameter:

$$\text{GPC} = \frac{M}{\rho \cdot N_A \cdot \sigma} \tag{6.12}$$

where:

- M is molecular weight of deposited material
- ρ is film density
- σ is surface site density (atoms/cm^2)

Typical GPC: 0.1-0.3 nm/cycle
Total film thickness after n cycles:

$$t = n \times \text{GPC} \tag{6.13}$$

Temperature Window

ALD requires operation within a specific temperature window:

- **Too low:** Incomplete reactions, physisorption
- **Optimal:** Self-limiting chemisorption
- **Too high:** Precursor decomposition, CVD-like growth

Example

ALD of Al_2O_3 using TMA and H_2O

Half-reactions:

Cycle A:

$$-OH^* + Al(CH_3)_3 \longrightarrow -O-Al(CH_3)_2^* + CH_4 \tag{6.14}$$

Cycle B:

$$-Al(CH_3)_2^* + 2\,H_2O \longrightarrow -Al(OH)_2^* + 2\,CH_4 \tag{6.15}$$

Net reaction:

$$2\,Al(CH_3)_3 + 3\,H_2O \longrightarrow Al_2O_3 + 6\,CH_4 \tag{6.16}$$

Parameters:

- Temperature: 200-300°C
- GPC: 0.11 nm/cycle
- Pulse times: TMA (0.02 s), H_2O (0.02 s)
- Purge times: 5-10 s each

For 50 nm film: $n = 50/0.11 \approx 455$ cycles

Table 6.4: Comparison of thin film deposition techniques

Technique	Rate	Temp (°C)	Uniformity	Conformality	Cost	Scalability
Spin coating	Fast	20-150	Good	Poor	Low	High
Sputtering	Medium	25-500	Good	Medium	Medium	High
PLD	Medium	25-800	Medium	Poor	High	Low
ALD	Slow	150-400	Excellent	Excellent	High	Medium

6.3 Nanocomposites

Nanocomposites combine a matrix material with nanoscale fillers to achieve superior properties. They are classified based on matrix type and filler dimensionality.

6.3.1 Polymer-Based Nanocomposites

Polymer nanocomposites incorporate nanofillers (0D particles, 1D fibers/tubes, 2D platelets) into polymer matrices.

Types and Classification

Table 6.5: Polymer nanocomposite classification

Filler Type	Example	Loading (%)	Property Enhancement
0D Nanoparticles	SiO_2, TiO_2, Au	1-20	Mechanical, optical
1D Nanofibers	CNT, cellulose	0.5-5	Mechanical, electrical
2D Nanoplates	Graphene, clay	1-10	Barrier, mechanical

Dispersion and Interfacial Adhesion

The effectiveness of nanocomposites depends critically on:

1. Dispersion quality:

Characterized by inter-particle distance d:

$$d = D\left[\left(\frac{\phi_m}{\phi}\right)^{1/3} - 1\right] \tag{6.17}$$

where D is particle diameter, ϕ is volume fraction, ϕ_m is maximum packing.

For good dispersion: $d/D > 1$ (no touching)

2. Interfacial interaction:

Interfacial shear strength τ_i measured by micromechanical tests.

Work of adhesion:

$$W_a = \gamma_p + \gamma_m - \gamma_{pm} \tag{6.18}$$

where γ represents surface/interfacial energies.

Mechanical Properties

Young's modulus enhancement:

Halpin-Tsai model for aligned fiber composites:

$$\frac{E_c}{E_m} = \frac{1 + \xi\eta\phi}{1 - \eta\phi} \tag{6.19}$$

where:

$$\eta = \frac{(E_f/E_m) - 1}{(E_f/E_m) + \xi} \tag{6.20}$$

- E_c, E_m, E_f are moduli of composite, matrix, fiber
- ϕ is fiber volume fraction
- ξ is shape parameter (2×aspect ratio for fibers)

For spherical particles: $\xi = 2$

Strength enhancement:

Mixing rule with efficiency factor η_o:

$$\sigma_c = \eta_o \sigma_f \phi + \sigma_m (1 - \phi) \tag{6.21}$$

Efficiency factor accounts for:

- Orientation distribution
- Length distribution
- Interfacial strength

Application

Carbon Nanotube-Polymer Composites
Material: MWCNT in epoxy resin
Properties at 1 wt% CNT:

- Young's modulus: +30% (2.8 → 3.6 GPa)
- Tensile strength: +25%
- Electrical conductivity: Insulator → 10^{-3} S/m
- Thermal conductivity: +20%

Percolation threshold: ∼0.5 wt% for electrical conductivity
Applications:

- EMI shielding
- Conductive adhesives
- Structural composites (aerospace)
- Sensors (strain, chemical)

6.3.2 Ceramic Nanocomposites

Ceramic matrix nanocomposites incorporate nanoparticles or nanofibers into ceramic matrices to improve toughness and reliability.

Toughening Mechanisms

1. **Crack deflection:**
   Energy increase from crack path lengthening:

$$\frac{G_c}{G_0} = 1 + \frac{\Delta L}{L_0} \tag{6.22}$$

   where ΔL is additional crack length.
2. **Crack bridging:**
   Bridging stress reduces crack tip stress intensity:

$$K_{tip} = K_{applied} - K_{bridging} \tag{6.23}$$

3. Transformation toughening:
Volume expansion during phase transformation creates compressive stress.
Toughness increment:

$$\Delta K_{IC} = 0.22 E \varepsilon_T V_f^{1/2} \tag{6.24}$$

where ε_T is transformation strain, V_f is transformable fraction.

Example

Al_2O_3-SiC nanocomposite
Composition: 95% Al_2O_3 + 5 vol% SiC nanoparticles (100 nm)
Improvements over pure Al_2O_3:

- Fracture toughness: 3.5 → 5.8 MPa·m$^{1/2}$ (+66%)
- Hardness: 18 → 21 GPa (+17%)
- Strength: 350 → 650 MPa (+86%)

Mechanisms:

- Grain refinement (inhibited growth)
- Crack deflection at SiC particles
- Residual stresses from thermal expansion mismatch

6.3.3 Metal Oxide-Graphene Hybrids

Graphene and graphene oxide (GO) serve as versatile platforms for creating hybrid nanocomposites with metal oxides.

Synthesis Strategies

1. In-situ growth:
Metal oxide nanoparticles nucleate and grow on GO surface:

$$\text{GO} + \text{Metalprecursor} \longrightarrow \text{GO/MOnanocomposite} \tag{6.25}$$

Anchoring sites: -COOH, -OH groups on GO
2. Mixing and assembly:
Pre-formed nanoparticles mixed with GO sheets:

- Electrostatic assembly (opposite charges)
- Hydrophobic interactions
- Covalent linking

3. Hydrothermal co-synthesis:
Simultaneous formation of metal oxide and reduction of GO.

Synergistic Properties

The combination of graphene and metal oxides provides:

- **Enhanced electron transport:** Graphene as conductive network
- **Prevented agglomeration:** Graphene sheets separate nanoparticles
- **Increased surface area:** Both components contribute
- **Novel electronic properties:** Interfacial charge transfer

Electrical conductivity:
Percolation model:

$$\sigma = \sigma_0(V_f - V_c)^t \tag{6.26}$$

where V_c is percolation threshold (∼0.1-1 vol% for graphene) and $t \approx 2$ is critical exponent.

Application

TiO_2-Graphene Photocatalyst
Structure: TiO_2 nanoparticles (10-20 nm) on reduced graphene oxide
Enhanced photocatalytic activity:

- Dye degradation rate: 5× faster than pure TiO_2
- Extended light absorption (visible region)
- Reduced electron-hole recombination

Mechanism:

1. Photon absorption by TiO_2: $TiO_2 + h\nu \rightarrow e^- + h^+$
2. Electron transfer to graphene: e^- (TiO_2) → e^- (graphene)
3. Graphene stores electrons, reduces recombination
4. Enhanced reactive oxygen species generation

Applications:

- Water purification
- Air pollution control
- Self-cleaning surfaces
- Hydrogen production

6.4 Structure-Property Correlation in Composites

Understanding and predicting nanocomposite properties requires analyzing structure at multiple length scales.

6.4.1 Hierarchical Structure

Nanocomposite properties emerge from structure at:

1. **Atomic scale:** Interfacial bonding, crystallinity
2. **Nanoscale:** Filler size, shape, dispersion
3. **Microscale:** Aggregation, phase distribution
4. **Macroscale:** Overall composite architecture

6.4.2 Key Structure-Property Relationships

Mechanical Properties

Effect of particle size:
Hall-Petch type relationship for hardness:

$$H = H_0 + \frac{k}{\sqrt{d}} \tag{6.27}$$

Smaller nanoparticles → more grain boundaries → higher strength (to a limit).
Effect of aspect ratio:
For fiber reinforcement, critical length l_c:

$$l_c = \frac{\sigma_f d}{2\tau_i} \tag{6.28}$$

where σ_f is fiber strength, d is diameter, τ_i is interfacial shear strength.
Effective reinforcement requires: $l > l_c$

Electrical Properties

Percolation theory:
Conductivity transition at critical volume fraction:

$$\sigma_{dc} \propto (V - V_c)^t \quad \text{for } V > V_c \tag{6.29}$$

For random networks: $V_c \propto \frac{1}{\text{aspect ratio}}$
High aspect ratio fillers (CNT, graphene) achieve conductivity at very low loadings (<1%).

Thermal Properties

Effective thermal conductivity:
Maxwell model for spherical particles:

$$k_{eff} = k_m \frac{k_p + 2k_m + 2\phi(k_p - k_m)}{k_p + 2k_m - \phi(k_p - k_m)} \tag{6.30}$$

where k_m, k_p are matrix and particle conductivities.
For high aspect ratio fillers, enhanced along alignment direction.

Optical Properties

Effective refractive index:
Maxwell-Garnett approximation:

$$\frac{n_{eff}^2 - n_m^2}{n_{eff}^2 + 2n_m^2} = \phi \frac{n_p^2 - n_m^2}{n_p^2 + 2n_m^2} \tag{6.31}$$

Transparency:
Rayleigh scattering for particles $<< \lambda$:

$$I_{scattered} \propto \frac{d^6}{\lambda^4} \tag{6.32}$$

Nanoparticles < 20 nm maintain transparency in visible range.

6.4.3 Interface Engineering

The filler-matrix interface governs load transfer and property enhancement.

Interfacial strength measurement:
Single fiber pullout test gives interfacial shear strength:

$$\tau_i = \frac{F_{max}}{\pi d l} \tag{6.33}$$

Surface modification strategies:

- Silane coupling agents for oxides
- Polymer grafting
- Plasma treatment
- Functionalization (graphene, CNT)

Improved interface increases τ_i by 2-10×.

6.5 Experiment: Preparation of GO-MgO Nanocomposites

Experiment

Objective

To synthesize graphene oxide-magnesium oxide (GO-MgO) nanocomposites via in-situ precipitation method and characterize their structure and properties.

Background

GO-MgO nanocomposites combine the high surface area and electrical properties of graphene oxide with the catalytic, antibacterial, and optical properties of MgO nanoparticles. The oxygen-containing functional groups on GO serve as nucleation sites for MgO formation, resulting in uniform nanoparticle distribution.

Materials

- Graphene oxide (GO) dispersion (2 mg/mL in water)
- Magnesium nitrate hexahydrate, $Mg(NO_3)_2 \cdot 6H_2O$
- Sodium hydroxide (NaOH) pellets
- Distilled water
- Ethanol (95%)

Equipment

- Magnetic stirrer with hot plate
- Beakers (250 mL)
- pH meter
- Centrifuge
- Vacuum oven
- Muffle furnace
- Sonicator

Procedure

Step 1: GO dispersion preparation

1. Prepare GO dispersion by dispersing GO powder in distilled water (2 mg/mL)
2. Sonicate for 30 minutes to ensure complete dispersion
3. Measure 50 mL GO dispersion (100 mg GO total)

Step 2: Precursor solution

1. Dissolve 2.56 g $Mg(NO_3)_2 \cdot 6H_2O$ in 50 mL distilled water (0.2 M solution)
2. Stir for 10 minutes at room temperature

6.6 Summary

This chapter has explored thin film deposition techniques and nanocomposite materials:

Key Point

Key Takeaways:

- **Thin film deposition** methods span solution-based (spin coating) to physical (sputtering, PLD) to chemical (ALD) approaches, each with distinct advantages for specific applications
- **Spin coating** provides cost-effective uniform films with thickness controlled by $\omega^{-0.5}$
- **Sputtering** offers versatile high-quality films with controllable composition through magnetron and reactive variants
- **PLD** enables stoichiometric transfer of complex materials with energetic deposition
- **ALD** achieves atomic-level precision through self-limiting surface reactions
- **Nanocomposites** combine matrix and nanofiller to achieve synergistic properties exceeding individual components
- **Polymer nanocomposites** enhance mechanical, electrical, and thermal properties at low filler loadings through high aspect ratio reinforcement
- **Ceramic nanocomposites** improve toughness through crack deflection, bridging, and transformation toughening
- **Metal oxide-graphene hybrids** leverage graphene's conductivity with metal oxide functionality for catalysis, sensing, and energy applications
- **Structure-property relationships** are governed by filler size, shape, dispersion, and interfacial interactions across multiple length scales

Future directions include:

- Multifunctional nanocomposites with combined properties
- Hierarchical structures mimicking natural materials
- 3D printing of nanocomposites
- Self-healing and adaptive composites
- Sustainable and bio-based nanocomposites

Exercises

Conceptual Questions

1. Explain why thin films exhibit properties different from bulk materials. What are the critical thickness ranges for different effects?

2. Compare the four deposition techniques (spin coating, sputtering, PLD, ALD) in terms of cost, uniformity, conformality, and suitable applications.

3. Describe the four stages of spin coating. Which stage primarily determines the final film thickness?

4. Explain the concept of sputter yield. How does it depend on ion mass, energy, and target material?

5. What are the advantages of pulsed laser deposition for complex oxide films? What causes the "particulate" problem?

6. Explain the self-limiting nature of ALD. Why is temperature control critical?

7. Discuss the importance of nanoparticle dispersion in polymer nanocomposites. How does agglomeration affect properties?

8. Describe three toughening mechanisms in ceramic nanocomposites with mathematical expressions.

9. Why do graphene-metal oxide hybrids show enhanced photocatalytic activity compared to pure metal oxides?

10. Explain the percolation threshold concept for electrical conductivity in nanocomposites. Why do high aspect ratio fillers have lower percolation thresholds?

Numerical Problems

1. A photoresist solution (3 wt%, viscosity 8 cP) is spin-coated at 2500 rpm. Using the empirical relation $h_f = 100(C/\omega^{0.5})$ nm:

   (a) Calculate expected film thickness

   (b) If thickness should be 200 nm, what spin speed is needed?

   (c) How does doubling concentration affect thickness?

2. For sputtering of Cu target with Ar^+ ions:

   - Ion energy: 500 eV
   - Sputter yield: 2.5 atoms/ion
   - Ion current density: 5 mA/cm^2

   Calculate:

   (a) Deposition rate (nm/s) assuming Cu density 8.96 g/cm^3

   (b) Time to deposit 100 nm film

3. PLD of $YBa_2Cu_3O_7$ (YBCO) superconductor:

- Laser: KrF (248 nm), pulse energy 200 mJ
- Spot size: 2 mm × 3 mm
- Repetition rate: 10 Hz

(a) Calculate fluence (J/cm^2)

(b) If ablation threshold is 1 J/cm^2 and $\alpha = 10^6$ cm^{-1}, calculate ablation depth per pulse

(c) Estimate deposition time for 200 nm film (assume 30% material transfer)

4. ALD of HfO_2 with GPC = 0.12 nm/cycle at 250°C:

(a) How many cycles needed for 24 nm film?

(b) If each cycle takes 8 seconds (including purges), calculate total deposition time

(c) Compare with sputtering at 5 nm/min

5. MWCNT-epoxy composite with CNT properties:

- CNT modulus: $E_f = 1000$ GPa
- Epoxy modulus: $E_m = 3$ GPa
- CNT diameter: 20 nm, length: 5 μm
- Loading: 2 vol%

Using Halpin-Tsai model:

(a) Calculate aspect ratio

(b) Calculate η parameter

(c) Predict composite modulus E_c

(d) Calculate modulus enhancement percentage

6. Graphene-polymer composite for electrical conductivity:

- Percolation threshold: $V_c = 0.8$ vol%
- Critical exponent: $t = 2$
- Maximum conductivity (high loading): $\sigma_0 = 100$ S/m

(a) Calculate conductivity at 1.5 vol% graphene

(b) At what loading does conductivity reach 50 S/m?

(c) Plot conductivity vs. volume fraction (0-5 vol%)

7. Al_2O_3-SiC nanocomposite (5 vol% SiC, 50 nm particles):

- Pure Al_2O_3 toughness: $K_{IC} = 3.5$ MPa·m$^{1/2}$
- Composite shows 60% enhancement

(a) Calculate composite toughness

(b) If grain size reduces from 5 μm to 0.8 μm, estimate additional hardness increase using Hall-Petch ($k = 0.5$ MPa·m$^{1/2}$)

8. GO-MgO synthesis:

   - Starting GO: 100 mg
   - $Mg(NO_3)_2 \cdot 6H_2O$: 2.56 g (0.01 mol)

   (a) Calculate theoretical yield of MgO

   (b) If MgO loading in composite is 70 wt%, calculate expected total product mass

   (c) If experimental yield is 250 mg, calculate percentage yield

9. Thermal conductivity of Al-graphene composite:

   - Al matrix: $k_m = 237$ W/m·K
   - Graphene: $k_p = 5000$ W/m·K
   - Graphene loading: 3 vol%

   Using Maxwell model, calculate effective thermal conductivity.

10. Optical transparency of polymer-TiO_2 nanocomposite:

    - TiO_2 particle size: 15 nm
    - Light wavelength: 550 nm
    - Loading: 5 vol%

    (a) Estimate Rayleigh scattering intensity relative to 100 nm particles

    (b) Will the composite remain transparent? Justify.

Advanced Problems

1. Design a multilayer thin film coating for anti-reflection on solar cells:

   - Substrate: Si ($n = 3.5$)
   - Target wavelength: 600 nm
   - Available materials: SiO_2 ($n = 1.46$), TiO_2 ($n = 2.4$)

   Specify layer thicknesses and recommend deposition method.

2. Develop a synthesis protocol for CNT-ceramic nanocomposite with target properties:

   - Matrix: Al_2O_3
   - Filler: MWCNTs
   - Target modulus increase: 40%
   - Maintain electrical conductivity > 10 S/m

   Include dispersion strategy, sintering conditions, and property characterization plan.

3. Compare cost and performance of depositing 50 nm Al_2O_3 on 1000 cm^2 substrate using:

   (a) Sputtering (rate: 3 nm/min, cost: \$50/hour)

   (b) ALD (GPC: 0.1 nm/cycle, 10 s/cycle, cost: \$100/hour)

   Include time, cost, and recommend method for (a) research, (b) industrial production.

4. Propose an experiment to determine the percolation threshold of graphene in PMMA. Include sample preparation (at least 8 different loadings), measurement techniques, and data analysis approach.

Bibliography

[1] Ohring, M. (2001). *Materials Science of Thin Films* (2nd ed.). Academic Press.

[2] Seshan, K. (Ed.). (2002). *Handbook of Thin Film Deposition Processes and Techniques* (2nd ed.). William Andrew Publishing.

[3] Mattox, D. M. (2010). *Handbook of Physical Vapor Deposition (PVD) Processing* (2nd ed.). Elsevier.

[4] George, S. M. (2010). Atomic layer deposition: An overview. *Chemical Reviews*, 110(1), 111-131.

[5] Leskelä, M., & Ritala, M. (2002). Atomic layer deposition (ALD): from precursors to thin film structures. *Thin Solid Films*, 409(1), 138-146.

[6] Hall, D. B., Underhill, P., and Torkelson, J. M. (1998). Spin coating of thin and ultrathin polymer films. *Polymer Engineering and Science*, 38(12), 2039-2045.

[7] Bhushan, B. (Ed.). (1999). *Handbook of Micro/Nanotribology* (2nd ed.). CRC Press.

[8] Chrisey, D. B., and Hubler, G. K. (Eds.). (1994). *Pulsed Laser Deposition of Thin Films*. Wiley-Interscience.

[9] Eason, R. (Ed.). (2007). *Pulsed Laser Deposition of Thin Films: Applications-Led Growth of Functional Materials*. Wiley-Interscience.

[10] Ajayan, P. M., Schadler, L. S., & Braun, P. V. (2003). *Nanocomposite Science and Technology*. Wiley-VCH.

[11] Tjong, S. C. (2006). Structural and mechanical properties of polymer nanocomposites. *Materials Science and Engineering: R: Reports*, 53(3-4), 73-197.

[12] Paul, D. R., & Robeson, L. M. (2008). Polymer nanotechnology: Nanocomposites. *Polymer*, 49(15), 3187-3204.

[13] Coleman, J. N., Khan, U., Blau, W. J., & Gun'ko, Y. K. (2006). Small but strong: A review of the mechanical properties of carbon nanotube–polymer composites. *Carbon*, 44(9), 1624-1652.

[14] Stankovich, S., Dikin, D. A., Dommett, G. H., et al. (2006). Graphene-based composite materials. *Nature*, 442(7100), 282-286.

[15] Kim, H., Abdala, A. A., and Macosko, C. W. (2010). Graphene/polymer nanocomposites. *Macromolecules*, 43(16), 6515-6530.

[16] Nieto, A., Bisht, A., Lahiri, D., Zhang, C., and Agarwal, A. (2017). Graphene reinforced metal and ceramic matrix composites: a review. *International Materials Reviews*, 62(5), 241-302.

[17] Ramanathan, T., Abdala, A. A., Stankovich, S., et al. (2008). Functionalized graphene sheets for polymer nanocomposites. *Nature Nanotechnology*, 3(6), 327-331.

[18] Huang, X., Qi, X., Boey, F., and Zhang, H. (2012). Graphene-based composites. *Chemical Society Reviews*, 41(2), 666-686.

[19] Zhu, Y., Murali, S., Cai, W., et al. (2010). Graphene and graphene oxide: synthesis, properties, and applications. *Advanced Materials*, 22(35), 3906-3924.

[20] Novoselov, K. S., Fal'ko, V. I., Colombo, L., et al. (2012). A roadmap for graphene. *Nature*, 490(7419), 192-200.

[21] Zhang, Y., Tan, Y. W., Stormer, H. L., and Kim, P. (2005). Experimental observation of the quantum Hall effect and Berry's phase in graphene. *Nature*, 438(7065), 201-204.

[22] Geim, A. K. (2009). Graphene: status and prospects. *Science*, 324(5934), 1530-1534.

[23] Cao, G., and Wang, Y. (2011). *Nanostructures and Nanomaterials: Synthesis, Properties, and Applications* (2nd ed.). World Scientific.

[24] Rao, C. N. R., Müller, A., & Cheetham, A. K. (Eds.). (2004). *The Chemistry of Nanomaterials: Synthesis, Properties and Applications*. Wiley-VCH.

[25] Hussain, F., Hojjati, M., Okamoto, M., & Gorga, R. E. (2006). Review article: Polymer-matrix nanocomposites, processing, manufacturing, and application. *Journal of Composite Materials*, 40(17), 1511-1575.

[26] Kickelbick, G. (Ed.). (2007). *Hybrid Materials: Synthesis, Characterization, and Applications*. Wiley-VCH.

[27] Mittal, V. (Ed.). (2009). *Polymer Nanocomposites: Synthesis, Microstructure, and Properties*. Momentum Press.

Part I

Characterization of Nanomaterials

Characterization is the cornerstone of nanomaterials science, providing the essential link between synthesis and application. Understanding the structure, morphology, composition, and properties of nanomaterials requires a comprehensive suite of analytical techniques. Part III explores the fundamental principles and practical applications of key characterization methods, enabling researchers to extract meaningful information from complex nanoscale systems.

Chapter 7

Structural Characterization Techniques

"The structure of a material determines its properties, and at the nanoscale, even subtle structural variations can lead to dramatic property changes."
— C. N. R. Rao

7.1 Introduction

Structural characterization is fundamental to understanding nanomaterials, as their unique properties arise directly from their atomic and molecular arrangements. At the nanoscale, crystal structure, defects, grain boundaries, phase composition, and crystallite size all play critical roles in determining material behavior.

The primary structural characterization techniques for nanomaterials include:

- **X-ray Diffraction (XRD):** Determines crystal structure, phase composition, crystallite size, and lattice parameters
- **Raman Spectroscopy:** Identifies molecular vibrations, crystal phases, defects, and stress states
- **Electron Diffraction:** Provides high-resolution structural information from individual nanoparticles
- **Neutron Diffraction:** Useful for light element detection and magnetic structure determination

This chapter focuses on XRD and Raman spectroscopy, the most widely accessible and versatile techniques for nanomaterial characterization.

Table 7.1: Comparison of major structural characterization techniques

Technique	Probe	Information	Sample Size	Resolution
XRD	X-rays	Crystal structure	Bulk (mg)	0.1-1 Å
Raman	Photons	Molecular vibrations	Micro (μm^3)	Molecular
TEM diffraction	Electrons	Local structure	Nano (nm)	< 0.1 Å
Neutron diffraction	Neutrons	Magnetic/light atoms	Bulk (g)	0.1-1 Å

7.2 X-ray Diffraction (XRD)

X-ray diffraction is the most widely used technique for determining crystal structure, phase identification, and quantitative analysis of crystalline materials. Its application to nanomaterials provides crucial information about crystallite size, lattice parameters, and structural perfection.

7.2.1 Fundamental Principles

Wave-Particle Duality of X-rays

X-rays are electromagnetic radiation with wavelengths in the range 0.01-10 nm, comparable to interatomic distances in crystals. The energy-wavelength relationship:

$$E = h\nu = \frac{hc}{\lambda} \tag{7.1}$$

For Cu Kα radiation (most common):

- Wavelength: $\lambda = 1.5406$ Å
- Energy: $E = 8.05$ keV

X-ray Generation

X-rays are produced by bombarding a metal target (Cu, Mo, Co) with high-energy electrons in an X-ray tube:

1. Electrons accelerated by voltage (30-50 kV)
2. Electrons strike metal target
3. Inner shell electrons ejected
4. Outer shell electrons fill vacancies
5. Characteristic X-rays emitted

For copper target:

- Kα_1: $\lambda = 1.54056$ Å (strongest)
- Kα_2: $\lambda = 1.54439$ Å
- Kβ: $\lambda = 1.39222$ Å (filtered out)

7.2.2 Bragg's Law

Definition

Bragg's Law describes the condition for constructive interference of X-rays scattered by parallel crystal planes:

$$n\lambda = 2d\sin\theta \tag{7.2}$$

where:

- n is the order of diffraction (integer)
- λ is the X-ray wavelength
- d is the interplanar spacing
- θ is the Bragg angle (angle of incidence)

Mathematical Derivation

Derivation of Bragg's Law

Consider two parallel crystal planes separated by distance d, with incident X-rays at angle θ.

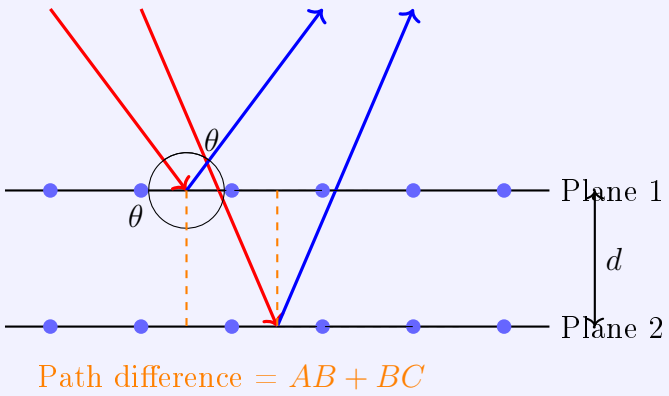

Figure 7.1: Geometry for derivation of Bragg's law

The path difference between rays reflected from adjacent planes:

$$\Delta = AB + BC \tag{7.3}$$

From geometry:

$$AB = BC = d\sin\theta \tag{7.4}$$

Therefore:

$$\Delta = 2d\sin\theta \tag{7.5}$$

For constructive interference, path difference must be an integer multiple of wavelength:

$$\Delta = n\lambda \tag{7.6}$$

Combining:

$$n\lambda = 2d\sin\theta \quad \text{(Bragg's Law)} \tag{7.7}$$

Miller Indices and d-spacing

Crystal planes are designated by Miller indices (hkl). For cubic crystal systems:

$$d_{hkl} = \frac{a}{\sqrt{h^2 + k^2 + l^2}} \tag{7.8}$$

where a is the lattice parameter.

For other crystal systems, the relationship is more complex. For hexagonal (wurtzite ZnO):

$$\frac{1}{d_{hkl}^2} = \frac{4}{3}\left(\frac{h^2 + hk + k^2}{a^2}\right) + \frac{l^2}{c^2} \tag{7.9}$$

7.2.3 XRD Instrumentation

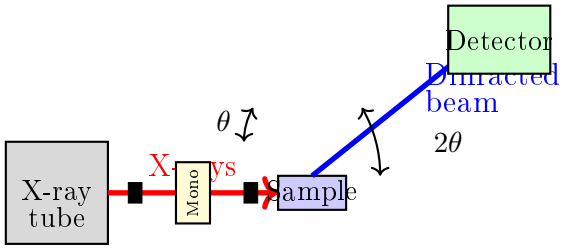

Figure 7.2: Schematic of X-ray diffractometer (Bragg-Brentano geometry)

Key components:

1. **X-ray source:** Sealed tube or rotating anode
2. **Monochromator:** Selects characteristic radiation
3. **Slits:** Collimate and define beam
4. **Sample holder:** Rotates at angle θ
5. **Detector:** Rotates at 2θ, measures intensity
6. **Goniometer:** Precision angle control

7.2.4 Debye-Scherrer Equation

For nanomaterials, XRD peaks are broadened due to finite crystallite size. The Debye-Scherrer equation relates peak broadening to crystallite size.

$$D = \frac{K\lambda}{\beta \cos\theta} \tag{7.10}$$

where:

- D is the mean crystallite size (volume-weighted)
- K is the shape factor (typically 0.89-0.94, often 0.9 for spheres)
- λ is the X-ray wavelength
- β is the full width at half maximum (FWHM) in radians
- θ is the Bragg angle

Mathematical Derivation

Physical Basis of Scherrer Equation

Peak broadening arises from destructive interference when the number of scattering planes is finite.

For a crystallite with N scattering planes, the intensity distribution:

$$I(\Delta\theta) = I_0 \frac{\sin^2(N\pi\Delta\theta/\lambda)}{\sin^2(\pi\Delta\theta/\lambda)} \tag{7.11}$$

The FWHM occurs when the numerator first becomes zero:

$$N\pi\beta/\lambda = \pi \tag{7.12}$$

Therefore:

$$\beta = \frac{\lambda}{Nd} \tag{7.13}$$

Since crystallite size $D = Nd$:

$$D = \frac{\lambda}{\beta} \tag{7.14}$$

Including geometric factors and using β measured in 2θ space:

$$D = \frac{K\lambda}{\beta\cos\theta} \tag{7.15}$$

The shape factor K accounts for crystallite shape and varies from 0.89 (cubic) to 0.94 (spherical).

Instrumental Broadening Correction

Measured peak width contains both sample and instrumental contributions:

$$\beta^2_{measured} = \beta^2_{sample} + \beta^2_{instrumental} \tag{7.16}$$

Or using Lorentzian approximation:

$$\beta_{sample} = \beta_{measured} - \beta_{instrumental} \tag{7.17}$$

$\beta_{instrumental}$ is determined from a standard (e.g., LaB_6, Si).

Strain Broadening

Lattice strain also causes peak broadening:

$$\beta_{strain} = 4\varepsilon\tan\theta \tag{7.18}$$

where ε is the microstrain.

Williamson-Hall analysis separates size and strain:

$$\beta\cos\theta = \frac{K\lambda}{D} + 4\varepsilon\sin\theta \tag{7.19}$$

Plotting $\beta\cos\theta$ vs. $\sin\theta$ gives:

- Intercept: $K\lambda/D \rightarrow$ crystallite size
- Slope: $4\varepsilon \rightarrow$ microstrain

Example

Crystallite size calculation for ZnO
Given XRD data for ZnO (101) peak:

- Peak position: $2\theta = 36.25°$
- FWHM: $\beta = 0.43° = 0.0075$ rad
- Wavelength: $\lambda = 1.5406$ Å
- Shape factor: $K = 0.9$

Solution:

$$D = \frac{K\lambda}{\beta \cos\theta} = \frac{0.9 \times 1.5406}{0.0075 \times \cos(36.25°/2)} \tag{7.20}$$

$$D = \frac{1.387}{0.0075 \times 0.9455} = \frac{1.387}{0.00709} = 195.6 \text{ Å} \approx 19.6 \text{ nm} \tag{7.21}$$

The ZnO nanoparticles have an average crystallite size of approximately 20 nm.

7.2.5 Rietveld Refinement

Rietveld refinement is a powerful method for extracting quantitative structural information from powder XRD patterns through least-squares fitting of a calculated pattern to experimental data.

Principles of Rietveld Method

The method minimizes the residual:

$$S_y = \sum_i w_i[y_i(obs) - y_i(calc)]^2 \tag{7.22}$$

where:

- $y_i(obs)$ is observed intensity at point i
- $y_i(calc)$ is calculated intensity
- $w_i = 1/y_i(obs)$ is statistical weight

Calculated Intensity

The calculated intensity at point i:

$$y_i(calc) = s \sum_K L_K |F_K|^2 \phi(2\theta_i - 2\theta_K) P_K A + y_{bi} \tag{7.23}$$

where:

- s is scale factor
- K represents Miller indices (hkl)
- L_K contains Lorentz, polarization, multiplicity factors
- F_K is structure factor
- ϕ is reflection profile function
- P_K is preferred orientation function
- A is absorption factor
- y_{bi} is background intensity

Structure Factor

$$F_K = \sum_n f_n \exp[2\pi i(hx_n + ky_n + lz_n)] \exp[-M_n] \tag{7.24}$$

where:

- f_n is atomic scattering factor for atom n
- (x_n, y_n, z_n) are fractional coordinates
- M_n is Debye-Waller temperature factor

Profile Functions

Common peak shape functions:

Gaussian:

$$G = \frac{\sqrt{4\ln 2}}{\pi^{1/2} H_K} \exp\left[-4\ln 2 \frac{(2\theta_i - 2\theta_K)^2}{H_K^2}\right] \tag{7.25}$$

Lorentzian:

$$L = \frac{2}{\pi H_K}\left[1 + 4\frac{(2\theta_i - 2\theta_K)^2}{H_K^2}\right]^{-1} \tag{7.26}$$

Pseudo-Voigt (combination):

$$\phi = \eta L + (1-\eta)G \tag{7.27}$$

where η is the mixing parameter.

Refinable Parameters

Parameters refined in Rietveld analysis:

1. **Scale factor:** Overall intensity
2. **Lattice parameters:** $a, b, c, \alpha, \beta, \gamma$
3. **Atomic positions:** x, y, z for each atom

4. **Atomic displacement parameters:** Thermal vibration
5. **Profile parameters:** Peak width, shape
6. **Background:** Polynomial or manual points
7. **Preferred orientation:** Texture correction
8. **Crystallite size/strain:** Via peak broadening

Goodness-of-Fit Indicators

R-weighted pattern:

$$R_{wp} = \sqrt{\frac{\sum_i w_i[y_i(obs) - y_i(calc)]^2}{\sum_i w_i y_i(obs)^2}} \tag{7.28}$$

R-expected:

$$R_{exp} = \sqrt{\frac{N - P}{\sum_i w_i y_i(obs)^2}} \tag{7.29}$$

where N is number of data points, P is number of parameters.

Goodness of fit:

$$\chi^2 = \left(\frac{R_{wp}}{R_{exp}}\right)^2 \tag{7.30}$$

Good refinement: $\chi^2 \approx 1 - 2$

R-Bragg:

$$R_B = \frac{\sum_K |I_K(obs) - I_K(calc)|}{\sum_K I_K(obs)} \tag{7.31}$$

Excellent fit: $R_B < 5\%$

Table 7.2: Quality indicators for Rietveld refinement

Parameter	Good Refinement	Excellent Refinement
R_{wp}	10-15%	$< 10\%$
R_B	5-10%	$< 5\%$
χ^2	1-2	≈ 1
Residuals	Random	No systematic trends

Crystallite Size from Rietveld

Rietveld refines parameters in the Lorentzian size broadening term:

$$\text{FWHM}_{size} = \frac{K\lambda}{D\cos\theta} \tag{7.32}$$

This provides volume-weighted mean crystallite size more accurately than Scherrer for multi-peak analysis.

7.3 Raman Spectroscopy

Raman spectroscopy probes vibrational modes of molecules and crystals through inelastic scattering of monochromatic light, providing fingerprint identification of materials and information about crystal structure, defects, and stress.

7.3.1 Fundamental Principles

Light Scattering Phenomena

When light interacts with matter, several scattering processes occur:

1. **Rayleigh scattering:** Elastic (no energy change)
2. **Raman scattering:** Inelastic (energy exchange)
   - Stokes: Energy loss (phonon creation)
   - Anti-Stokes: Energy gain (phonon annihilation)

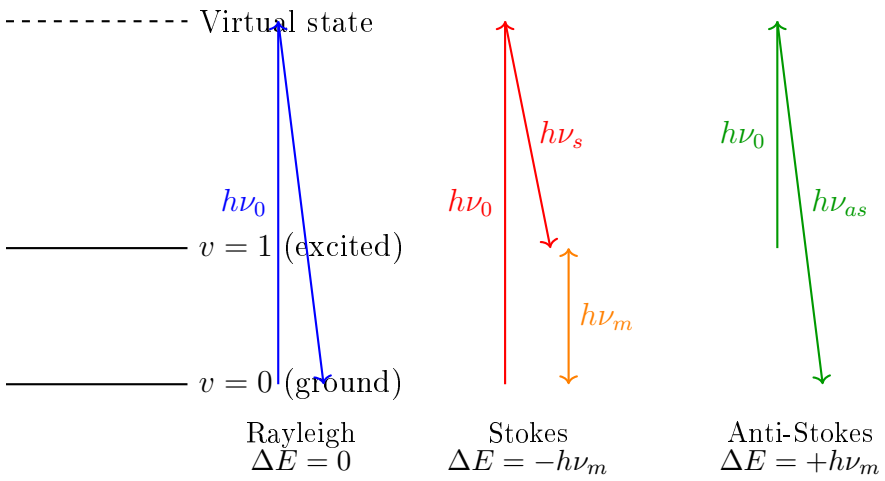

Figure 7.3: Energy level diagram for Rayleigh and Raman scattering processes

Energy relationships:
Stokes: $h\nu_s = h\nu_0 - h\nu_m$
Anti-Stokes: $h\nu_{as} = h\nu_0 + h\nu_m$
where ν_0 is incident frequency, ν_m is vibrational frequency.

Raman Shift

Raman spectra are reported as Raman shift $\tilde{\nu}$ (wavenumber, cm^{-1}):

$$\tilde{\nu} = \frac{1}{\lambda_0} - \frac{1}{\lambda_s} = \nu_0 - \nu_s \tag{7.33}$$

This is independent of excitation wavelength, making it a molecular/crystal fingerprint.

Classical Theory of Raman Scattering

The induced dipole moment:

$$\vec{P} = \alpha \vec{E} \tag{7.34}$$

where α is polarizability tensor.
For oscillating electric field:

$$E = E_0 \cos(2\pi\nu_0 t) \tag{7.35}$$

And molecular vibration:

$$Q = Q_0 \cos(2\pi\nu_m t) \tag{7.36}$$

Expanding polarizability:

$$\alpha = \alpha_0 + \left(\frac{\partial \alpha}{\partial Q}\right)_0 Q + ... \tag{7.37}$$

The induced dipole:

$$P = \alpha_0 E_0 \cos(2\pi\nu_0 t) + \frac{1}{2}\left(\frac{\partial \alpha}{\partial Q}\right)_0 Q_0 E_0 [\cos(2\pi(\nu_0 - \nu_m)t) + \cos(2\pi(\nu_0 + \nu_m)t)] \tag{7.38}$$

Terms represent:

- First: Rayleigh scattering (ν_0)
- Second: Stokes Raman ($\nu_0 - \nu_m$)
- Third: Anti-Stokes Raman ($\nu_0 + \nu_m$)

Raman selection rule:

$$\left(\frac{\partial \alpha}{\partial Q}\right)_0 \neq 0 \tag{7.39}$$

Vibration must change polarizability to be Raman active.

7.3.2 Raman Instrumentation

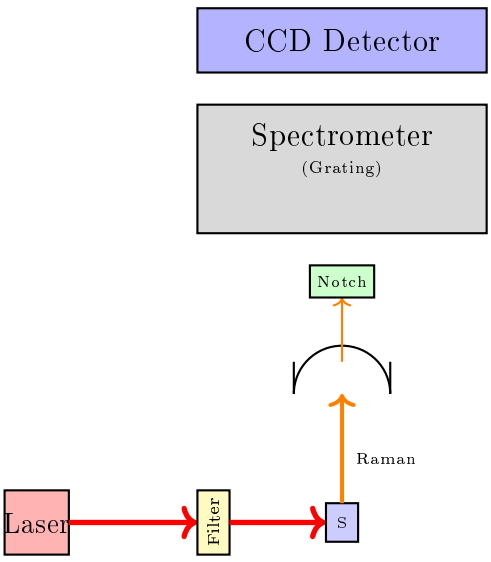

Figure 7.4: Schematic of Raman spectroscopy system

Key components:

1. **Laser source:**
   - Visible: 532 nm (green), 633 nm (red)
   - NIR: 785 nm, 1064 nm (reduced fluorescence)
   - UV: 244 nm (resonance Raman)
2. **Notch/Edge filter:** Removes Rayleigh scattering
3. **Spectrometer:** Disperses wavelengths (grating)
4. **Detector:** CCD (charge-coupled device)

7.3.3 Raman Spectroscopy for Phase Identification

Different crystal phases exhibit distinct Raman spectra due to different symmetries and vibrational modes.

Group Theory and Selection Rules

Crystal symmetry determines allowed Raman modes. For a crystal with point group symmetry, irreducible representations predict active modes.

For wurtzite ZnO (C_{6v} symmetry):
Mechanical representation:

$$\Gamma_{mech} = 2A_1 + 2E_1 + 2E_2 + 2B_1 \tag{7.40}$$

Acoustic modes: $A_1 + E_1$
Optical modes: $A_1 + E_1 + 2E_2 + 2B_1$
Raman active: $A_1 + 2E_1 + 2E_2$
Silent: $2B_1$

Characteristic Raman Modes

Table 7.3: Raman modes of ZnO (wurtzite)

Mode	Frequency (cm^{-1})	Symmetry	Description
E_2^{low}	101	E_2	Zn sublattice
$A_1(TO)$	380	A_1	Transverse optical
$E_1(TO)$	410	E_1	Transverse optical
E_2^{high}	437	E_2	Oxygen vibration
$A_1(LO)$	574	A_1	Longitudinal optical
$E_1(LO)$	583	E_1	Longitudinal optical

The E_2^{high} mode at 437 cm^{-1} is the strongest and most characteristic for wurtzite ZnO.

Size and Defect Effects

Phonon confinement:

For nanocrystals, Raman peaks broaden and shift due to phonon confinement. The intensity:

$$I(\omega) \propto \int_0^{2\pi/a} \frac{|C(q)|^2}{[\omega - \omega(q)]^2 + (\Gamma/2)^2} d^3q \tag{7.41}$$

where $C(q)$ is confinement function.

Peak shift:

$$\Delta\omega \approx -A \left(\frac{a}{D}\right)^2 \tag{7.42}$$

where D is crystallite size, a is lattice constant, A is material constant.

Defects and disorder:

Structural defects activate forbidden modes and broaden peaks:

- Oxygen vacancies in ZnO activate A_{1g} mode
- Lattice disorder broadens E_2^{high}
- Surface modes appear in nanoparticles

7.4 Data Analysis: XRD Pattern Interpretation of ZnO Nanoparticles

Data Analysis

Objective

Comprehensive analysis of XRD pattern for ZnO nanoparticles synthesized by co-precipitation method, including phase identification, lattice parameter determination, and crystallite size estimation.

Sample Information

- Material: ZnO nanoparticles
- Synthesis: Coprecipitation at pH 12, calcined at 500 °C
- Instrument: PANalytical X'Pert Pro
- Radiation: Cu Kα ($\lambda = 1.5406$ Å)
- Range: $2\theta = 20 - 80°$
- Step size: 0.02°

Experimental XRD Pattern

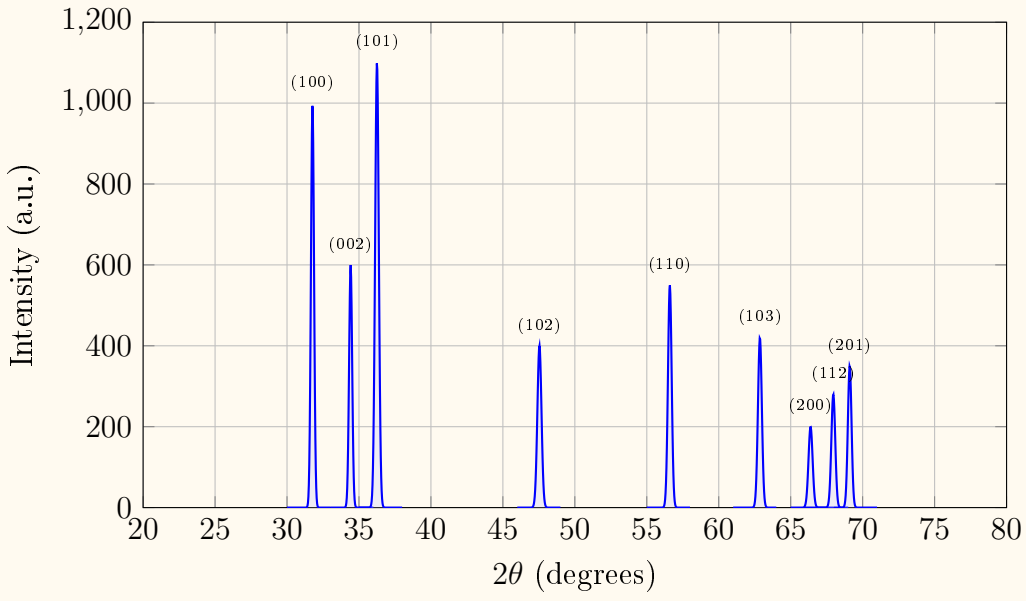

Figure 7.5: Simulated XRD pattern of ZnO nanoparticles (wurtzite structure)

Step 1: Phase Identification

Compare experimental peak positions with standard JCPDS/ICDD card for ZnO:

Table 7.4: Peak positions: Experimental vs. Standard (JCPDS 36-1451)

(hkl)	$2\theta_{exp}$	$2\theta_{std}$	I_{exp}	I_{std}	d_{exp} **(Å)**
(100)	31.77°	31.77°	91%	57	2.814
(002)	34.42°	34.42°	55%	44	2.603

7.5 Summary

This chapter has provided comprehensive coverage of structural characterization techniques for nanomaterials:

Key Point

Key Takeaways:

- **X-ray diffraction** is the primary technique for determining crystal structure, phase identification, and quantitative structural analysis
- **Bragg's law** ($n\lambda = 2d\sin\theta$) provides the fundamental relationship between X-ray wavelength, interplanar spacing, and diffraction angle
- **Debye-Scherrer equation** ($D = K\lambda/\beta\cos\theta$) enables crystallite size estimation from peak broadening
- **Rietveld refinement** offers comprehensive structural analysis through least-squares fitting of calculated to observed patterns
- **Raman spectroscopy** provides complementary molecular and crystal vibrational information for phase identification and defect analysis
- **Williamson-Hall analysis** separates size and strain contributions to peak broadening
- **Integrated analysis** combining multiple techniques provides the most complete structural characterization

Proper structural characterization is essential for:

- Quality control in nanomaterial synthesis
- Understanding structure-property relationships
- Optimizing processing conditions
- Publishing credible research results
- Developing commercial applications

Exercises

Conceptual Questions

1. Explain why X-rays are ideal for crystal structure determination. What properties make them suitable?

2. Derive Bragg's law starting from the path difference between rays reflected from adjacent crystal planes.

3. Why do nanoparticles show broader XRD peaks compared to bulk materials? Explain both physically and mathematically.
4. Distinguish between crystallite size and particle size. Can they be different? Give examples.
5. Explain the physical basis of the Debye-Scherrer equation. What assumptions are made?
6. What is the difference between Stokes and anti-Stokes Raman scattering? Which is more intense and why?
7. How does Rietveld refinement differ from simple peak fitting? What additional information does it provide?
8. Explain why certain vibrational modes are Raman active while others are IR active. What determines the selection rules?
9. Describe how phonon confinement affects Raman spectra of nanoparticles.
10. Why is the (101) peak typically strongest in wurtzite ZnO? Relate to structure factor.

Numerical Problems

1. For Cu Kα radiation ($\lambda = 1.5406$ Å) incident on Si (111) planes:
   (a) Calculate the d-spacing for Si (cubic, $a = 5.431$ Å)
   (b) Determine the Bragg angle for first-order diffraction
   (c) At what angle would second-order diffraction occur?
2. An XRD peak for Au (200) appears at $2\theta = 44.39$ using Cu Kα radiation:
   (a) Calculate the d-spacing
   (b) Determine the lattice parameter (Au is FCC)
   (c) Compare with literature value (4.078 Å)
3. A ZnO nanoparticle shows (101) peak at $2\theta = 36.25$ with FWHM = 0.52°:
   (a) Calculate crystallite size using Scherrer equation ($K = 0.9$)
   (b) If instrumental broadening is 0.08°, what is the corrected crystallite size?
   (c) Estimate the number of unit cells along the diffracting direction
4. For TiO_2 anatase, the following peaks are observed:

(hkl)	2θ (°)	FWHM (°)
(101)	25.28	0.65
(004)	37.80	0.70
(200)	48.05	0.75

   (a) Calculate crystallite size from each peak

(b) Determine average size with standard deviation

(c) Perform Williamson-Hall analysis

5. In a Raman spectrum of ZnO:

   - Laser wavelength: 532 nm
   - E_2^{high} mode observed at: 437 cm^{-1}

   (a) Calculate the frequency of this vibrational mode (Hz)

   (b) Determine the wavelength of Stokes-scattered light

   (c) Calculate the energy of the phonon (eV)

6. For graphene, the G-band appears at 1580 cm^{-1}:

   (a) Using laser at 633 nm, calculate Raman shift wavelength

   (b) If peak shifts to 1590 cm^{-1} under strain, calculate the strain (use strain coefficient 10 cm^{-1}/%)

   (c) Determine compressive or tensile strain

7. A Rietveld refinement of ZnO yields:

   - $R_{wp} = 8.5\%$
   - $R_{exp} = 6.2\%$
   - $R_B = 4.8\%$

   (a) Calculate goodness of fit χ^2

   (b) Assess the quality of refinement

   (c) What improvements would you suggest if $R_{wp} = 25\%$?

8. For hexagonal ZnO ($a = 3.25$ Å, $c = 5.21$ Å):

   (a) Calculate d-spacing for (100), (002), and (101) planes

   (b) Determine 2θ for each using Cu Kα

   (c) Calculate structure factors assuming Zn at (1/3, 2/3, 0) and O at (1/3, 2/3, u) with $u = 0.382$

9. The intensity ratio $I_{Anti-Stokes}/I_{Stokes}$ for a Raman mode at 520 cm^{-1}:

   (a) Calculate the ratio at 300 K

   (b) At what temperature would the ratio become 0.5?

   (c) Use: $I_{AS}/I_S = \exp(-h\nu/k_BT)$

10. Given XRD data for mixed phase TiO_2 (anatase + rutile):

    - Anatase (101): $I_A = 800$, $I_A^0 = 100$ (reference)
    - Rutile (110): $I_R = 300$, $I_R^0 = 100$ (reference)

    Calculate weight fraction of anatase using:

$$X_A = \frac{1}{1 + 1.26(I_R/I_A)}$$

Advanced Problems

1. Design a complete XRD experiment to characterize unknown oxide nanoparticles. Include:
   - Measurement parameters (range, step, time)
   - Phase identification strategy
   - Quantitative analysis plan
   - Expected challenges and solutions

2. Perform a full Williamson-Hall analysis on the following data for SnO_2:

(hkl)	2θ (°)	FWHM (°)	I_{rel} (%)
(110)	26.61	0.45	100
(101)	33.89	0.48	65
(200)	37.95	0.50	30
(211)	51.78	0.55	50

   Plot, determine size and strain, interpret results.

3. Compare XRD and Raman for characterizing:
   (a) Carbon nanotubes
   (b) Mixed-phase TiO_2
   (c) Strained Si thin films

   Which technique is more suitable for each case and why?

4. Propose a comprehensive structural characterization protocol for a new nanomaterial combining XRD, Raman, and complementary techniques (TEM, XPS). Justify the sequence and integration of results.

Bibliography

[1] Cullity, B. D., & Stock, S. R. (2001). *Elements of X-Ray Diffraction* (3rd ed.). Prentice Hall.

[2] Pecharsky, V. K., & Zavalij, P. Y. (2009). *Fundamentals of Powder Diffraction and Structural Characterization of Materials* (2nd ed.). Springer.

[3] Warren, B. E. (1990). *X-Ray Diffraction*. Dover Publications.

[4] Jenkins, R., & Snyder, R. L. (1996). *Introduction to X-Ray Powder Diffractometry*. Wiley-Interscience.

[5] Klug, H. P., & Alexander, L. E. (1974). *X-Ray Diffraction Procedures for Polycrystalline and Amorphous Materials* (2nd ed.). Wiley.

[6] Rietveld, H. M. (1969). A profile refinement method for nuclear and magnetic structures. *Journal of Applied Crystallography*, 2(2), 65-71.

[7] Young, R. A. (Ed.). (1995). *The Rietveld Method*. Oxford University Press.

[8] McCusker, L. B., Von Dreele, R. B., Cox, D. E., Louër, D., & Scardi, P. (1999). Rietveld refinement guidelines. *Journal of Applied Crystallography*, 32(1), 36-50.

[9] Scherrer, P. (1918). Bestimmung der Größe und der inneren Struktur von Kolloidteilchen mittels Röntgenstrahlen. *Nachrichten von der Gesellschaft der Wissenschaften zu Göttingen*, 2, 98-100.

[10] Williamson, G. K., & Hall, W. H. (1953). X-ray line broadening from filed aluminium and wolfram. *Acta Metallurgica*, 1(1), 22-31.

[11] Langford, J. I., & Wilson, A. J. C. (1978). Scherrer after sixty years: a survey and some new results in the determination of crystallite size. *Journal of Applied Crystallography*, 11(2), 102-113.

[12] Larson, A. C., & Von Dreele, R. B. (2004). *General Structure Analysis System (GSAS)*. Los Alamos National Laboratory Report LAUR 86-748.

[13] Ferrari, A. C., & Robertson, J. (2000). Interpretation of Raman spectra of disordered and amorphous carbon. *Physical Review B*, 61(14), 14095.

[14] Smith, E., & Dent, G. (2005). *Modern Raman Spectroscopy: A Practical Approach*. Wiley.

[15] Ferraro, J. R., Nakamoto, K., & Brown, C. W. (2003). *Introductory Raman Spectroscopy* (2nd ed.). Academic Press.

[16] Long, D. A. (2002). *The Raman Effect: A Unified Treatment of the Theory of Raman Scattering by Molecules*. Wiley.

[17] Cardona, M., & Güntherodt, G. (Eds.). (1982). *Light Scattering in Solids II: Basic Concepts and Instrumentation*. Springer.

[18] Alim, K. A., Fonoberov, V. A., Shamsa, M., & Balandin, A. A. (2005). Micro-Raman investigation of optical phonons in ZnO nanocrystals. *Journal of Applied Physics*, 97(12), 124313.

[19] Bundesmann, C., Ashkenov, N., Schubert, M., et al. (2003). Raman scattering in ZnO thin films doped with Fe, Sb, Al, Ga, and Li. *Applied Physics Letters*, 83(10), 1974-1976.

[20] Richter, H., Wang, Z. P., & Ley, L. (1981). The one phonon Raman spectrum in microcrystalline silicon. *Solid State Communications*, 39(5), 625-629.

[21] Campbell, I. H., & Fauchet, P. M. (1986). The effects of microcrystal size and shape on the one phonon Raman spectra of crystalline semiconductors. *Solid State Communications*, 58(10), 739-741.

[22] Cao, G., & Wang, Y. (2011). *Nanostructures and Nanomaterials: Synthesis, Properties, and Applications* (2nd ed.). World Scientific.

[23] Rao, C. N. R., Müller, A., & Cheetham, A. K. (Eds.). (2004). *The Chemistry of Nanomaterials: Synthesis, Properties and Applications*. Wiley-VCH.

[24] Suryanarayana, C., Norton, M. G. (1998). *X-Ray Diffraction: A Practical Approach*. Plenum Press.

[25] Bish, D. L., Post, J. E. (Eds.). (1989). *Modern Powder Diffraction*. Mineralogical Society of America.

[26] Dinnebier, R. E., & Billinge, S. J. (Eds.). (2008). *Powder Diffraction: Theory and Practice*. Royal Society of Chemistry.

Chapter 8

Morphological and Elemental Characterization

"Seeing is believing, but at the nanoscale, seeing requires sophisticated eyes."
— Ernst Ruska (Nobel Prize 1986, Electron Microscopy)

8.1 Introduction

Morphological and elemental characterization techniques are essential tools for understanding nanomaterials at multiple length scales, from atomic resolution to mesoscopic structures. These techniques provide complementary information about:

- **Morphology:** Size, shape, surface topography, and distribution
- **Structure:** Crystal orientation, defects, and interfaces
- **Composition:** Elemental distribution and chemical state
- **Properties:** Mechanical, electrical, and magnetic at the nanoscale

The primary techniques covered in this chapter form the cornerstone of nanomaterial characterization:

1. **Scanning Electron Microscopy (SEM):** Surface imaging with nanometer resolution
2. **Transmission Electron Microscopy (TEM):** Atomic-scale imaging and diffraction
3. **Atomic Force Microscopy (AFM):** Three-dimensional surface profiling
4. **Energy Dispersive X-ray Spectroscopy (EDX):** Elemental composition analysis

Table 8.1: Comparison of morphological characterization techniques

Parameter	SEM	TEM	AFM	EDX
Resolution	1-10 nm	0.1-0.2 nm	0.1-1 nm (lateral) 0.01 nm (vertical)	∼1 μm
Magnification	10-500,000×	50-10^6×	N/A	N/A
Sample type	Bulk, powder	Thin (<100 nm)	Any surface	With SEM/TEM
Vacuum	Required	High vacuum	Air/liquid OK	Required
Information	Surface morphology	Internal structure	Topography 3D profile	Composition (Z ≥ 5)

This chapter provides the theoretical foundations, practical applications, and data interpretation skills necessary for effective nanomaterial characterization.

8.2 Scanning Electron Microscopy (SEM)

SEM is one of the most versatile and widely used techniques for imaging surfaces and near-surface regions of solid materials at high magnification.

8.2.1 Fundamental Principles

Electron-Matter Interactions

When a focused beam of energetic electrons (typically 1-30 keV) strikes a specimen, various signals are generated through elastic and inelastic scattering events.

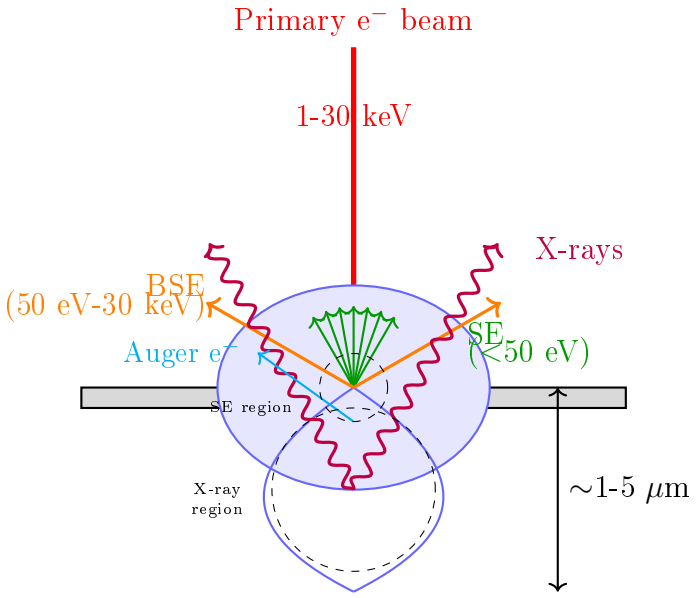

Figure 8.1: Electron-specimen interaction volume showing various signals generated in SEM

Key signals for imaging:

1. **Secondary Electrons (SE):**

- Energy: < 50 eV
- Escape depth: 5-50 nm
- Provide topographic contrast
- Most common imaging mode

2. **Backscattered Electrons (BSE):**
   - Energy: 50 eV to beam energy
   - Escape from deeper regions
   - Provide atomic number (Z) contrast
   - Useful for compositional imaging

Resolution and Magnification

The resolution δ of an SEM is determined by several factors:

$$\delta = \sqrt{\delta_d^2 + \delta_s^2 + \delta_c^2} \tag{8.1}$$

where:

- δ_d is diffraction limit
- δ_s is probe diameter (source size contribution)
- δ_c is chromatic aberration

Probe diameter:

$$d_p = \frac{4I}{\pi^2 \alpha^2 \beta} \tag{8.2}$$

where I is beam current, α is convergence angle, β is brightness.
Rayleigh criterion for resolution:

$$\delta_R = \frac{0.61\lambda}{\alpha} \tag{8.3}$$

For 30 keV electrons: $\lambda = 0.007$ nm
Magnification:

$$M = \frac{\text{CRT display size}}{\text{Scan width on specimen}} \tag{8.4}$$

Modern field-emission SEMs achieve:

- Resolution: 1-2 nm at 1 keV, < 1 nm at 15 keV
- Magnification: $10\times$ to $500{,}000\times$
- Depth of field: Much larger than optical microscopy

8.2.2 SEM Instrumentation

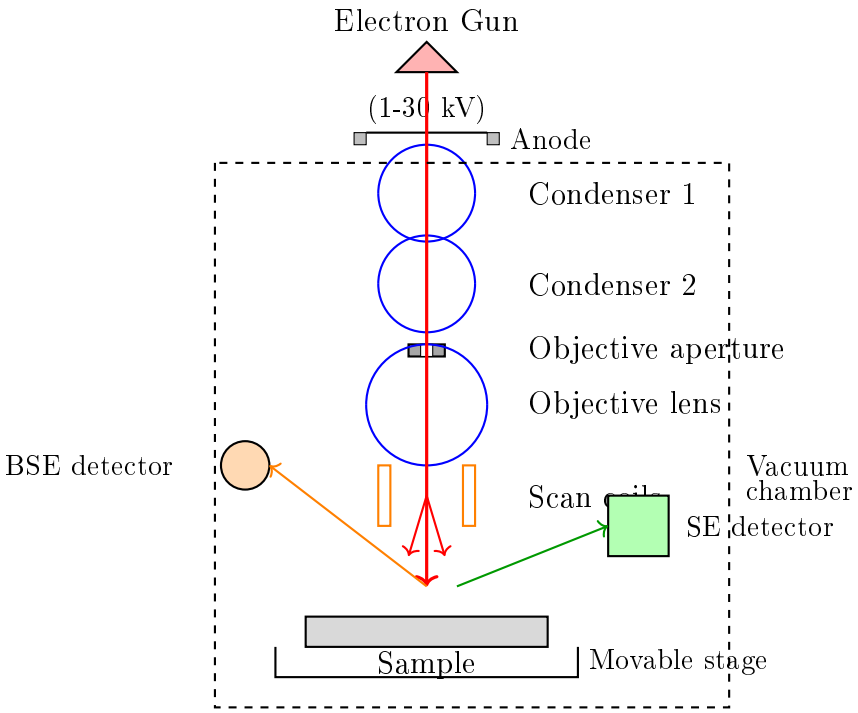

Figure 8.2: Schematic diagram of SEM instrumentation

Main components:

1. **Electron source:**
   - Thermionic: Tungsten filament (brightness: 10^5 A/cm^2/sr)
   - Field emission: LaB_6 or cold FE (brightness: 10^9 A/cm^2/sr)
2. **Electromagnetic lenses:** Focus and demagnify beam
3. **Scan coils:** Raster beam across sample
4. **Detectors:**
   - Everhart-Thornley detector (SE)
   - Solid-state detector (BSE)
5. **Vacuum system:** 10^{-4} to 10^{-7} Pa

8.2.3 Imaging Modes and Contrast Mechanisms

Secondary Electron Imaging

SE yield δ_{SE} depends on:

$$\delta_{SE} = \delta_0 \sec\theta \tag{8.5}$$

where θ is angle between beam and surface normal.
This creates strong **topographic contrast**:

- Edges and protrusions appear bright
- Valleys appear dark
- Excellent for surface morphology

Backscattered Electron Imaging

BSE coefficient η increases with atomic number:

$$\eta \approx -0.0254 + 0.016Z - 1.86 \times 10^{-4} Z^2 + 8.3 \times 10^{-7} Z^3 \tag{8.6}$$

Provides **compositional contrast**:

- Heavy elements (high Z): Bright
- Light elements (low Z): Dark

Table 8.2: Backscatter coefficient for selected elements at 20 keV

Element	Z	η	Relative brightness
Carbon (C)	6	0.05	Dark
Aluminum (Al)	13	0.11	
Silicon (Si)	14	0.12	Medium
Iron (Fe)	26	0.22	
Copper (Cu)	29	0.24	
Silver (Ag)	47	0.33	Bright
Gold (Au)	79	0.42	Very bright

8.3 Transmission Electron Microscopy (TEM)

TEM achieves atomic-scale resolution by transmitting electrons through ultra-thin specimens, providing structural information unattainable by other techniques.

8.3.1 Fundamental Principles

Wave Nature of Electrons

The de Broglie wavelength:

$$\lambda = \frac{h}{p} = \frac{h}{\sqrt{2m_0 eV(1 + eV/2m_0c^2)}} \tag{8.7}$$

For non-relativistic approximation ($V < 100$ kV):

$$\lambda \approx \frac{1.226}{\sqrt{V}} \text{ nm} \tag{8.8}$$

For 200 keV electrons: $\lambda = 0.00251$ nm (much smaller than atomic spacings!)

Abbe Resolution Criterion

$$\delta = \frac{0.61\lambda}{\mu \sin \beta} \tag{8.9}$$

where μ is refractive index (1 for electrons) and β is collection angle. Modern aberration-corrected TEMs achieve < 0.1 nm resolution.

8.3.2 TEM Instrumentation

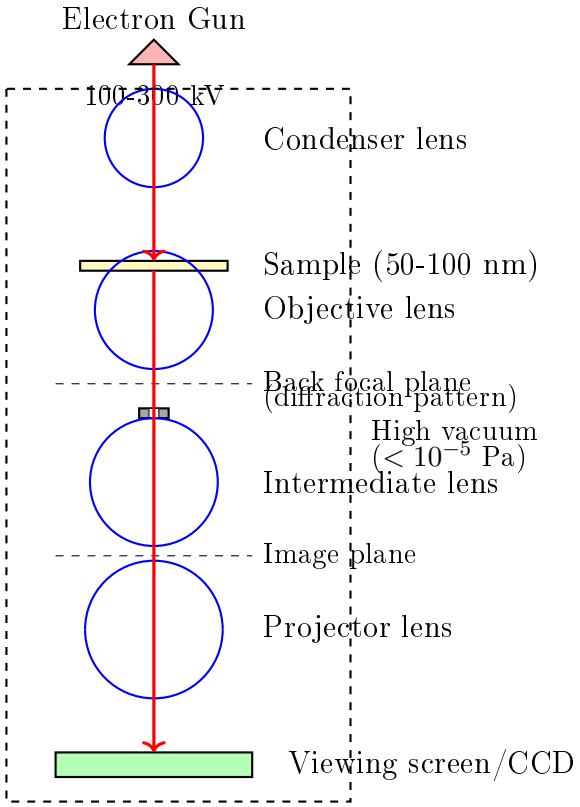

Figure 8.3: Schematic of TEM column showing ray paths

8.3.3 Imaging Modes

Bright-Field (BF) Imaging

Only transmitted beam forms image. Dark regions indicate:

- Mass-thickness contrast: Thicker/denser areas
- Diffraction contrast: Crystalline regions

Image intensity:

$$I_{BF} = I_0 e^{-\mu t} \tag{8.10}$$

where μ is scattering coefficient, t is thickness.

Dark-Field (DF) Imaging

Only diffracted beams form image. Bright regions show:

- Specific crystal orientations
- Defects and strain fields

High-Resolution TEM (HRTEM)

Multiple beams interfere to form lattice images. Resolution:

$$\delta_{HRTEM} = 0.65 C_s^{1/4} \lambda^{3/4} \tag{8.11}$$

where C_s is spherical aberration coefficient.
For $C_s = 0.5$ mm, $\lambda = 0.0025$ nm at 200 keV:

$$\delta_{HRTEM} = 0.65 \times (0.5)^{0.25} \times (0.0025)^{0.75} \approx 0.19 \text{ nm} \tag{8.12}$$

8.3.4 Selected Area Diffraction (SAD)

Diffraction patterns provide crystallographic information.
Bragg's law in reciprocal space:

$$\lambda = 2 d_{hkl} \sin \theta_B \tag{8.13}$$

For small angles: $\sin \theta_B \approx \theta_B$
Camera length L and diffraction spot distance R:

$$R = L\lambda / d_{hkl} \tag{8.14}$$

Camera constant:

$$K = L\lambda = R \cdot d_{hkl} \tag{8.15}$$

Measure R to determine d-spacings and identify crystal structure.

Example

Determining lattice spacing from SAD
Given:

- Camera constant: $K = 2.5$ nm·mm
- Measured spot distance: $R = 8.3$ mm

Calculate d-spacing:

$$d = \frac{K}{R} = \frac{2.5}{8.3} = 0.301 \text{ nm} \tag{8.16}$$

This matches Si (111) planes ($d_{111} = 0.314$ nm in literature).

8.4 Atomic Force Microscopy (AFM)

AFM provides three-dimensional surface profiles by scanning a sharp probe across a surface and measuring tip-sample interaction forces.

8.4.1 Fundamental Principles

Interatomic Forces

The tip-sample force can be approximated by Lennard-Jones potential:

$$V(r) = 4\varepsilon \left[\left(\frac{\sigma}{r}\right)^{12} - \left(\frac{\sigma}{r}\right)^{6} \right] \tag{8.17}$$

Force:

$$F(r) = -\frac{dV}{dr} = \frac{24\varepsilon}{\sigma} \left[2\left(\frac{\sigma}{r}\right)^{13} - \left(\frac{\sigma}{r}\right)^{7} \right] \tag{8.18}$$

- $r < r_0$: Repulsive (contact regime)
- $r > r_0$: Attractive (van der Waals)

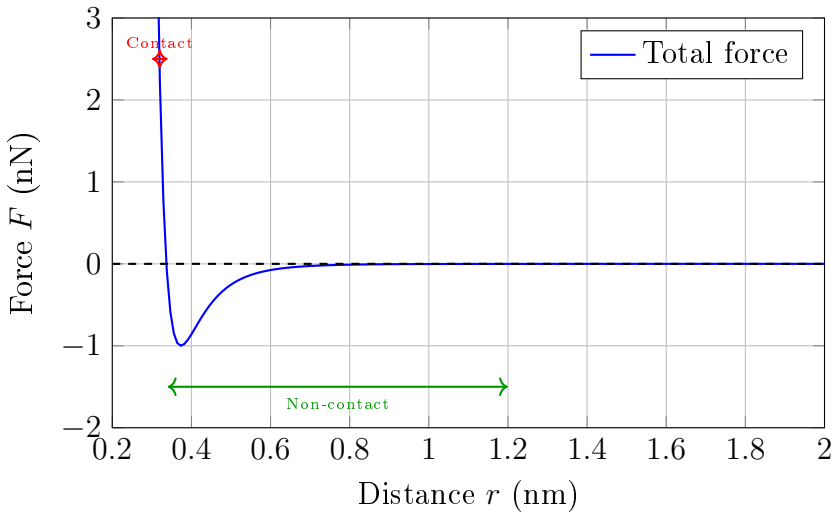

Figure 8.4: Tip-sample force vs. distance showing contact and non-contact regimes

Cantilever Mechanics

The cantilever acts as a spring with force constant k:

$$k = \frac{Ewt^3}{4L^3} \tag{8.19}$$

where E is Young's modulus, w is width, t is thickness, L is length.
Typical values: $k = 0.01 - 100$ N/m
Resonance frequency:

$$f_0 = \frac{1}{2\pi}\sqrt{\frac{k}{m_{eff}}} \approx \frac{0.162t}{L^2}\sqrt{\frac{E}{\rho}} \tag{8.20}$$

Typical $f_0 = 10 - 400$ kHz

8.4.2 Operating Modes

Table 8.3: AFM operating modes

Mode	Principle	Advantages	Applications
Contact	Tip in constant repulsive contact	High resolution, simple	Hard surfaces
Non-contact	Tip oscillates above surface	No damage, soft samples	Biological
Tapping	Tip oscillates, intermittent contact	Best for most samples	General purpose
Lateral force	Measure friction	Material contrast	Composites
Magnetic	Magnetic tip	Magnetic domains	Magnetic materials

Contact Mode

Cantilever deflection z measured by optical lever:

$$F = kz \tag{8.21}$$

Feedback maintains constant force (constant deflection).

Tapping Mode (Dynamic)

Cantilever driven near resonance. Amplitude A changes with tip-sample interaction:

$$A = A_0 \exp\left(-\frac{Q}{\pi f_0}\int F(z)dz\right) \tag{8.22}$$

where Q is quality factor (typically 100-500 in air, 10,000-100,000 in vacuum).
Feedback maintains constant amplitude $\rightarrow$ constant average force.

8.4.3 Resolution and Artifacts

Lateral resolution:

$$\delta_{lateral} \approx \sqrt{2Rd} \tag{8.23}$$

where R is tip radius (5-50 nm) and d is feature height.
For $R = 10$ nm, $d = 1$ nm: $\delta \approx 4.5$ nm
Vertical resolution: Limited by thermal noise, typically 0.01-0.1 nm
Common artifacts:

- Tip convolution: Features appear broader
- Tip asymmetry: Directional distortion
- Multiple tips: Ghost images

8.5 Energy Dispersive X-ray (EDX) Analysis

EDX spectroscopy provides elemental composition by analyzing characteristic X-rays emitted from electron-bombarded samples.

8.5.1 Fundamental Principles

X-ray Generation

When inner-shell electrons are ejected by incident electrons, outer-shell electrons fill vacancies, emitting characteristic X-rays.

X-ray energy:

$$E_X = E_i - E_j = h\nu \tag{8.24}$$

where E_i and E_j are energy levels.
For Kα transition (L $\rightarrow$ K):

$$E_{K\alpha} \approx 10.2(Z - \sigma)^2 \text{ eV} \tag{8.25}$$

where Z is atomic number, $\sigma \approx 1 - 2$ is screening constant.

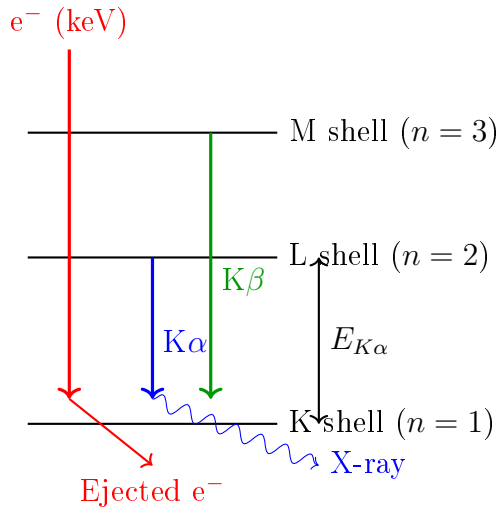

Figure 8.5: Characteristic X-ray generation: electron transitions and energy levels

Detection and Spectrum

EDX detector (Si(Li) or silicon drift detector) converts X-ray photons to electronic pulses.
Energy resolution: $\Delta E \approx 130$ eV at Mn Kα (5.9 keV)

Table 8.4: Characteristic X-ray energies for selected elements

Element	**Z**	**Kα (keV)**	**Lα (keV)**
Carbon (C)	6	0.277	–
Oxygen (O)	8	0.525	–
Silicon (Si)	14	1.740	–
Iron (Fe)	26	6.404	0.705
Copper (Cu)	29	8.048	0.930
Silver (Ag)	47	22.163	2.984
Gold (Au)	79	68.803	9.713

8.5.2 Quantitative Analysis

ZAF Correction

Raw X-ray intensities must be corrected for:

1. **Z - Atomic number effect:** Backscatter and stopping power
2. **A - Absorption:** X-rays absorbed in sample
3. **F - Fluorescence:** Secondary X-ray excitation

Concentration:

$$C_A = \frac{(I_A/I_A^{std})}{ZAF} \tag{8.26}$$

For thin samples (TEM-EDX), ZAF ≈ 1.

Cliff-Lorimer Method (Thin Film)

For elements A and B:

$$\frac{C_A}{C_B} = k_{AB}\frac{I_A}{I_B} \tag{8.27}$$

where k_{AB} is sensitivity factor (tabulated or measured from standards).

8.5.3 Spatial Resolution

X-ray generation volume limits resolution. For bulk sample at accelerating voltage E_0 (keV):

Kanaya-Okayama range:

$$R_{KO} = \frac{0.0276 A E_0^{1.67}}{Z^{0.89}\rho} \ (\mu\text{m}) \tag{8.28}$$

where A is atomic weight, ρ is density (g/cm^3).
For Al at 20 keV:

$$R_{KO} = \frac{0.0276 \times 26.98 \times 20^{1.67}}{13^{0.89} \times 2.7} \approx 2.1 \ \mu\text{m} \tag{8.29}$$

Spatial resolution $\approx 1 - 2$ μm for bulk SEM-EDX

For thin TEM samples ($<$ 100 nm), resolution approaches beam diameter ($\sim$ 1-10 nm).

8.6 Hands-On: Interpreting SEM/EDX Images and Particle Size Distribution

Hands-On Analysis

Objective

Learn to analyze SEM images and EDX spectra to characterize nanoparticle morphology, size distribution, and elemental composition.

Case Study: ZnO Nanoparticles

Sample Information

- Material: ZnO nanoparticles synthesized by coprecipitation
- SEM: 15 kV acceleration voltage, SE detector
- EDX: 20 kV, acquisition time 60 seconds

Task 1: SEM Image Analysis

Observations from SEM image:

SEM Image: ZnO Nanoparticles

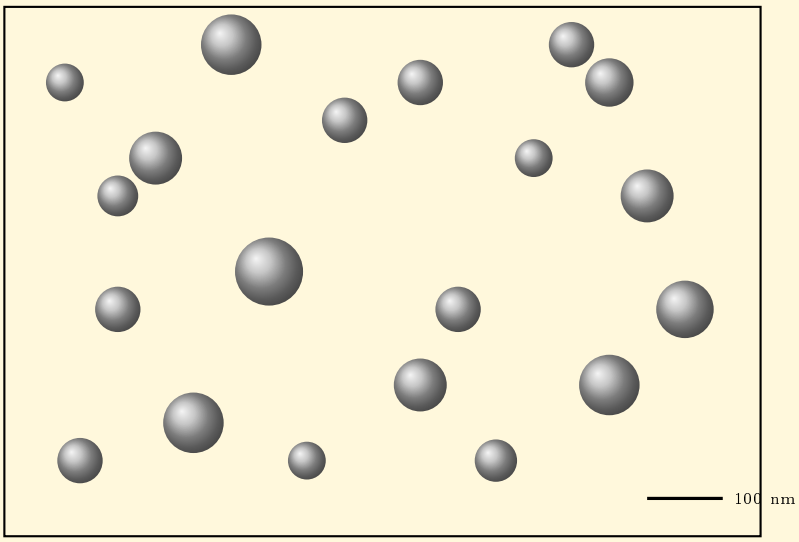

Scale bar: 200 nm

Figure 8.6: Simulated SEM image of ZnO nanoparticles

Image characteristics:

1. **Morphology:** Roughly spherical particles
2. **Size range:** 20-50 nm (visual estimate)
3. **Distribution:** Relatively uniform, some agglomeration
4. **Surface:** Smooth, well-defined boundaries

Task 2: Particle Size Distribution

Measure diameters of 50+ particles using ImageJ software:

8.7 Summary

This chapter has provided comprehensive coverage of morphological and elemental characterization:

Key Point

Key Takeaways:

- **SEM** provides high-resolution surface imaging (1-10 nm) with large depth of field, ideal for morphology studies
- **TEM** achieves atomic-scale resolution (< 0.1 nm) for internal structure, diffraction, and crystallography
- **AFM** offers three-dimensional surface profiling with sub-nanometer vertical resolution and can operate in various environments
- **EDX** enables elemental composition analysis with spatial resolution from μm (SEM) to nm (TEM) scale
- **Complementary techniques** provide complete characterization: SEM (morphology) + EDX (composition) + XRD (structure)
- **Quantitative analysis** requires understanding of electron-matter interactions, resolution limits, and correction procedures
- **Practical skills** in image analysis and spectrum interpretation are essential for materials characterization

Practical Tip

Best Practices for Nanomaterial Characterization:

1. Use multiple techniques for comprehensive analysis
2. Measure sufficient particles (50-100+) for statistical validity
3. Consider beam damage for sensitive materials
4. Calibrate instruments regularly
5. Report imaging/analysis conditions clearly
6. Compare SEM particle size with XRD crystallite size
7. Use standards for quantitative EDX
8. Consider sample preparation artifacts

Exercises

Conceptual Questions

1. Explain why SEM has much larger depth of field than optical microscopy. Derive the relationship mathematically.

2. Compare secondary electron and backscattered electron imaging. Which is better for: (a) topographic imaging, (b) compositional contrast? Explain.

3. Why must TEM samples be ultra-thin (< 100 nm)? What happens if the sample is too thick?

4. Describe the difference between bright-field and dark-field TEM imaging. When would you use each?

5. Explain how AFM can measure forces at the nanoscale. What is the role of the cantilever?

6. Why is EDX detection limit for light elements ($Z < 11$) poor? How can this be overcome?

7. Discuss why XRD crystallite size often differs from SEM particle size. Give three possible explanations.

8. Explain the ZAF correction in EDX. Why is it unnecessary for thin TEM samples?

9. How does specimen charging affect SEM imaging? Propose solutions for insulating samples.

10. Compare the information obtained from selected area diffraction (SAD) in TEM versus XRD.

Numerical Problems

1. Calculate the de Broglie wavelength for:

   (a) 100 keV electrons

   (b) 200 keV electrons

   (c) 300 keV electrons

   Compare with typical atomic spacings ($\sim$0.2 nm).

2. An SEM operates at 15 kV with spot size 5 nm. If the scan width is 10 μm on the specimen and display is 10 cm:

   (a) Calculate magnification

   (b) Determine pixel resolution if display is 1024×768 pixels

   (c) Is the pixel size smaller than spot size?

3. For silicon at 20 keV electron beam energy:

   (a) Calculate the Kanaya-Okayama range ($A = 28.09$, $Z = 14$, $\rho = 2.33$ g/cm^3)

   (b) Estimate the EDX spatial resolution

(c) How would resolution change at 5 keV?

4. In TEM, a diffraction spot is measured at distance $R = 12.5$ mm from the central spot. Camera constant is $K = 2.8$ nm·mm:

   (a) Calculate the d-spacing

   (b) Identify the crystal planes if the sample is FCC Au ($a = 4.08$ Å)

   (c) What would be R for the (200) reflection?

5. An AFM cantilever has: $L = 200$ μm, $w = 40$ μm, $t = 2$ μm, $E = 150$ GPa, $\rho = 2330$ kg/m^3:

   (a) Calculate spring constant k

   (b) Determine resonance frequency f_0

   (c) If deflection is 10 nm, calculate force

6. EDX spectrum shows Fe Kα at 6.404 keV with 5000 counts and O Kα at 0.525 keV with 3000 counts. Using Cliff-Lorimer with $k_{Fe,O} = 2.5$:

   (a) Calculate atomic ratio Fe:O

   (b) Determine the oxide formula

   (c) Calculate weight percentages (Fe = 55.85, O = 16.00)

7. SEM image shows particles with measured diameters (nm): 25, 30, 28, 35, 32, 27, 33, 29, 31, 26, 34, 28, 30, 29, 32:

   (a) Calculate mean and standard deviation

   (b) Determine coefficient of variation

   (c) Create histogram with 5 nm bins

   (d) Is the distribution normal?

8. For HRTEM with $C_s = 1.2$ mm and $\lambda = 0.00251$ nm (200 keV):

   (a) Calculate point resolution

   (b) How does resolution change if C_s is reduced to 0.001 mm (aberration-corrected)?

   (c) At what voltage would uncorrected resolution equal corrected at 200 keV?

9. The BSE coefficient for a two-phase sample (50% Cu, 50% Al by area) at 20 keV:

   (a) Calculate individual η values using the formula in text

   (b) Determine the average image brightness

   (c) Calculate contrast between phases

10. AFM tapping mode with $k = 40$ N/m, $Q = 400$, $f_0 = 300$ kHz, free amplitude $A_0 = 50$ nm, setpoint amplitude $A_{sp} = 40$ nm:

    (a) Calculate quality factor effect on force sensitivity

    (b) Estimate average interaction force

    (c) Determine appropriate feedback gain

Advanced Problems

1. Design a comprehensive characterization protocol for unknown oxide nanoparticles combining SEM, TEM, AFM, and EDX. Specify:

   - Sequence of measurements
   - Sample preparation for each technique
   - Expected information from each
   - How to integrate results

2. Compare the advantages and limitations of SEM-EDX vs. TEM-EDX for analyzing:

   (a) Core-shell nanoparticles (10 nm core, 2 nm shell)

   (b) Nanocomposite with 5% carbon nanotubes

   (c) Doped semiconductor nanocrystals

3. Develop a method to measure the thickness of a thin film on a substrate using:

   (a) Cross-sectional SEM

   (b) AFM step height

   (c) TEM cross-section

   Compare accuracy and difficulty of each method.

4. Propose an experiment to distinguish between:

   - Single-crystal particles vs. polycrystalline particles
   - Solid particles vs. hollow particles
   - Crystalline vs. amorphous nanoparticles

   using the techniques in this chapter.

Bibliography

[1] Goldstein, J. I., Newbury, D. E., Michael, J. R., et al. (2017). *Scanning Electron Microscopy and X-Ray Microanalysis* (4th ed.). Springer.

[2] Williams, D. B., & Carter, C. B. (2009). *Transmission Electron Microscopy: A Textbook for Materials Science* (2nd ed.). Springer.

[3] Reimer, L., & Kohl, H. (2008). *Transmission Electron Microscopy: Physics of Image Formation* (5th ed.). Springer.

[4] Eaton, P., & West, P. (2010). *Atomic Force Microscopy*. Oxford University Press.

[5] Binnig, G., Quate, C. F., & Gerber, C. (1986). Atomic force microscope. *Physical Review Letters*, 56(9), 930-933.

[6] Meyer, G., Amer, N. M. (1988). Novel optical approach to atomic force microscopy. *Applied Physics Letters*, 53(12), 1045-1047.

[7] García, R., Pérez, R. (2002). Dynamic atomic force microscopy methods. *Surface Science Reports*, 47(6-8), 197-301.

[8] Egerton, R. F. (2011). *Electron Energy-Loss Spectroscopy in the Electron Microscope* (3rd ed.). Springer.

[9] Reimer, L. (1985). *Scanning Electron Microscopy: Physics of Image Formation and Microanalysis*. Springer.

[10] Joy, D. C., Romig, A. D., Goldstein, J. I. (Eds.). (1986). *Principles of Analytical Electron Microscopy*. Plenum Press.

[11] Reed, S. J. B. (2005). *Electron Microprobe Analysis and Scanning Electron Microscopy in Geology* (2nd ed.). Cambridge University Press.

[12] Leng, Y. (2008). *Materials Characterization: Introduction to Microscopic and Spectroscopic Methods*. Wiley.

[13] Brandon, D., Kaplan, W. D. (2008). *Microstructural Characterization of Materials* (2nd ed.). Wiley.

[14] Amelinckx, S., van Dyck, D., van Landuyt, J., van Tendeloo, G. (Eds.). (1997). *Handbook of Microscopy: Applications in Materials Science, Solid-State Physics and Chemistry*. VCH.

[15] Fultz, B., Howe, J. M. (2013). *Transmission Electron Microscopy and Diffractometry of Materials* (4th ed.). Springer.

[16] Kirkland, E. J. (2010). *Advanced Computing in Electron Microscopy* (2nd ed.). Springer.

[17] Pennycook, S. J., Nellist, P. D. (Eds.). (2011). *Scanning Transmission Electron Microscopy: Imaging and Analysis*. Springer.

[18] Yao, N., Wang, Z. L. (Eds.). (2005). *Handbook of Microscopy for Nanotechnology*. Springer.

[19] Wang, Z. L. (Ed.). (2000). *Characterization of Nanophase Materials*. Wiley-VCH.

[20] Giannuzzi, L. A., Stevie, F. A. (Eds.). (2005). *Introduction to Focused Ion Beams: Instrumentation, Theory, Techniques and Practice*. Springer.

[21] Butt, H. J., Cappella, B., Kappl, M. (2005). Force measurements with the atomic force microscope. *Surface Science Reports*, 59(1-6), 1-152.

[22] Magonov, S. N., Whangbo, M. H. (1996). *Surface Analysis with STM and AFM*. VCH.

[23] Bhushan, B. (Ed.). (2010). *Springer Handbook of Nanotechnology* (3rd ed.). Springer.

[24] Cao, G., Wang, Y. (2011). *Nanostructures and Nanomaterials: Synthesis, Properties, and Applications* (2nd ed.). World Scientific.

[25] Rao, C. N. R., Müller, A., Cheetham, A. K. (Eds.). (2004). *The Chemistry of Nanomaterials: Synthesis, Properties and Applications*. Wiley-VCH.

[26] Banfield, J. F., Navrotsky, A. (Eds.). (2001). *Nanoparticles and the Environment*. Mineralogical Society of America.

[27] Baraton, M. I. (Ed.). (2002). *Synthesis, Functionalization and Surface Treatment of Nanoparticles*. American Scientific Publishers.

Chapter 9

Optical and Magnetic Characterization

"Light and magnetism reveal what the eye cannot see—the electronic structure and magnetic order that define nanomaterials."
— Adapted from Richard Feynman

9.1 Introduction

Optical and magnetic characterization techniques provide essential information about the electronic structure, energy levels, luminescence properties, and magnetic behavior of nanomaterials. These properties are intimately connected to applications in optoelectronics, photocatalysis, data storage, biomedicine, and energy conversion.

The primary techniques covered in this chapter include:

1. **UV-Vis Spectroscopy:** Electronic transitions and band gap determination
2. **Photoluminescence (PL):** Radiative recombination and defect states
3. **Vibrating Sample Magnetometry (VSM):** Magnetic properties and hysteresis
4. **Fourier Transform Infrared (FTIR):** Molecular vibrations and chemical bonding

Table 9.1: Comparison of optical and magnetic characterization techniques

Parameter	UV-Vis	PL	VSM	FTIR
Energy range	1-6 eV	1-6 eV	N/A	0.05-0.5 eV
Information	Band gap absorption	Luminescence defects	Magnetization hysteresis	Bonding vibrations
Sample type	Solid, liquid	Solid, powder	Solid, powder	Solid, liquid
Sensitivity	High	Very high	mg samples	μg samples
Quantitative	Yes	Semi	Yes	Yes
Applications	Catalysis solar cells	Displays sensors	Data storage biomedicine	Chemical ID surface groups

These complementary techniques enable comprehensive understanding of structure-property relationships in nanomaterials.

9.2 UV-Vis Spectroscopy and Tauc Plot

UV-Vis spectroscopy measures the absorption or transmission of ultraviolet and visible light by materials, providing information about electronic band structure and optical transitions.

9.2.1 Fundamental Principles

Light-Matter Interaction

When electromagnetic radiation interacts with matter, several processes occur:

1. **Absorption:** Photon energy matches electronic transition energy
2. **Transmission:** Photons pass through without interaction
3. **Reflection:** Photons bounce off surface
4. **Scattering:** Photons deflected by particles

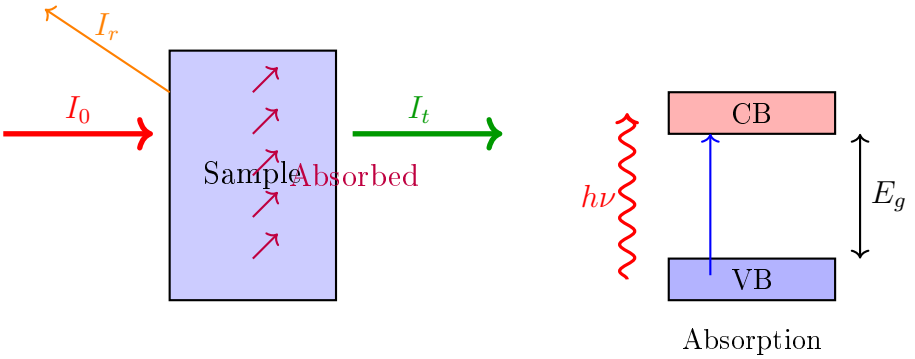

Figure 9.1: Light-matter interaction and electronic transition in semiconductors

Beer-Lambert Law

The relationship between absorption and concentration:

$$A = \log_{10}\left(\frac{I_0}{I_t}\right) = \varepsilon \cdot c \cdot l \tag{9.1}$$

where:

- A is absorbance (dimensionless)
- I_0 is incident intensity
- I_t is transmitted intensity
- ε is molar absorptivity ($\mathrm{M^{-1}cm^{-1}}$)

- c is concentration (M)
- l is path length (cm)

For solid samples, absorption coefficient α (cm^{-1}):

$$I_t = I_0 e^{-\alpha l} \tag{9.2}$$

Converting to absorbance:

$$\alpha = \frac{2.303A}{l} \tag{9.3}$$

9.2.2 Band Gap Determination

Direct and Indirect Transitions

For semiconductors, the absorption coefficient near the band edge follows different relationships:

Direct band gap:

$$\alpha h\nu = A(h\nu - E_g)^{1/2} \tag{9.4}$$

Indirect band gap:

$$\alpha h\nu = A(h\nu - E_g)^2 \tag{9.5}$$

where A is a constant depending on transition probability.

Mathematical Derivation

Tauc Relation for Direct Band Gap

Starting from quantum mechanics, the probability of optical transition depends on:

$$P \propto |\langle \psi_f | \hat{H}_{int} | \psi_i \rangle|^2 \tag{9.6}$$

For direct transitions, both electron and hole at same k-vector. The joint density of states:

$$g(E) \propto (E - E_g)^{1/2} \tag{9.7}$$

Absorption coefficient:

$$\alpha(h\nu) = \frac{4\pi^2 e^2}{ncm^2\omega^2} |\langle \psi_c | \vec{p} | \psi_v \rangle|^2 g(E) \tag{9.8}$$

For parabolic bands near band edge:

$$\alpha h\nu = A(h\nu - E_g)^{1/2} \tag{9.9}$$

Squaring both sides gives the Tauc relation:

$$(\alpha h\nu)^2 = A^2(h\nu - E_g) \tag{9.10}$$

9.2.3 Tauc Plot Analysis

The Tauc plot method determines band gap by plotting $(\alpha h\nu)^n$ vs. $h\nu$ where:

- $n = 2$ for direct allowed transitions
- $n = 1/2$ for indirect allowed transitions
- $n = 2/3$ for direct forbidden
- $n = 1/3$ for indirect forbidden

Procedure:

1. Measure absorbance vs. wavelength
2. Convert wavelength to energy: $E(eV) = 1240/\lambda(nm)$
3. Calculate α from absorbance
4. Plot $(\alpha h\nu)^2$ vs. $h\nu$ (for direct gap)
5. Extrapolate linear portion to $(\alpha h\nu)^2 = 0$
6. Intercept gives E_g

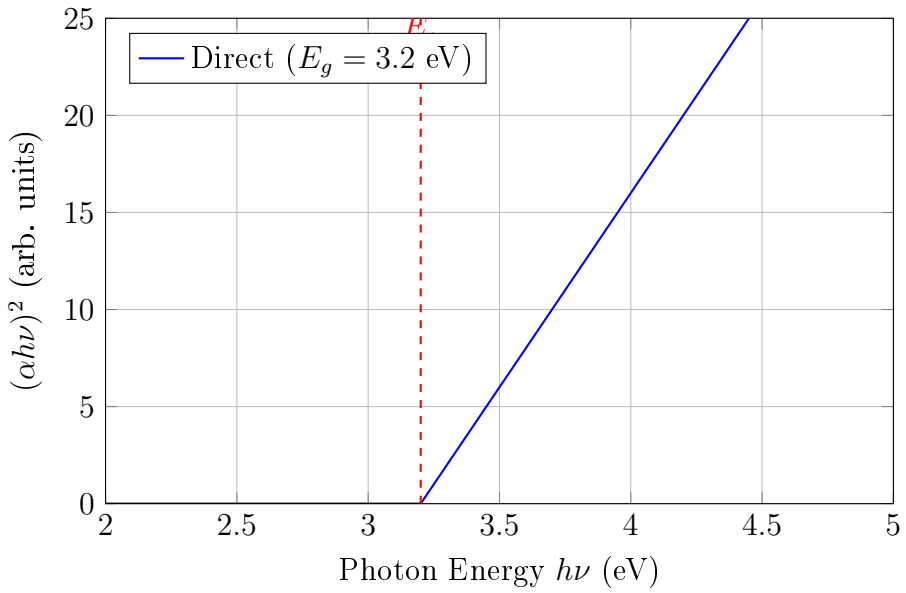

Figure 9.2: Tauc plot for direct band gap determination showing linear extrapolation

Example

Band gap calculation for ZnO
Given UV-Vis data for ZnO nanoparticles:

λ (nm)	A	$h\nu$ (eV)	$(\alpha h\nu)^2$
400	0.05	3.10	0.024
380	0.12	3.26	0.153
370	0.45	3.35	0.567
360	0.85	3.44	1.015
350	1.20	3.54	1.440

Plotting and extrapolating the linear region gives:
Band gap: $E_g = 3.28$ **eV**
This is consistent with bulk ZnO (3.37 eV) with slight blue-shift due to quantum confinement.

9.2.4 Size-Dependent Band Gap

For semiconductor nanoparticles, quantum confinement causes band gap widening:

$$E_g(R) = E_g^{bulk} + \frac{\hbar^2\pi^2}{2R^2}\left(\frac{1}{m_e^*} + \frac{1}{m_h^*}\right) - \frac{1.8e^2}{4\pi\varepsilon_0\varepsilon_r R} \tag{9.11}$$

The first term is kinetic energy (quantum confinement), the second is Coulombic attraction.

Effective mass approximation:

$$\Delta E_g \approx \frac{\hbar^2\pi^2}{2\mu R^2} \tag{9.12}$$

where μ is reduced mass.

9.3 Photoluminescence Spectroscopy

Photoluminescence (PL) measures light emission from materials following optical excitation, providing information about electronic structure, defects, and radiative recombination.

9.3.1 Fundamental Principles

PL Mechanism

1. **Photoexcitation:** Absorption of photon with $h\nu > E_g$
2. **Thermalization:** Carriers relax to band edges (10^{-12} s)
3. **Radiative recombination:** Electron-hole pair recombines emitting photon
4. **Non-radiative processes:** Energy dissipated as heat/phonons

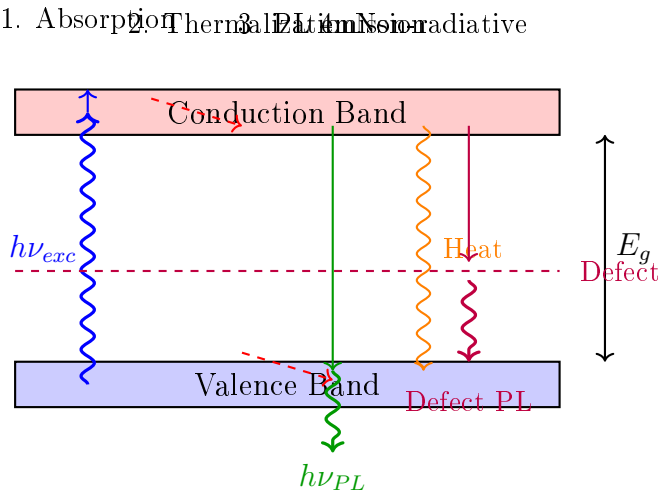

Figure 9.3: Photoluminescence processes: excitation, thermalization, and radiative/non-radiative recombination

Quantum Yield

Photoluminescence quantum yield (PLQY):

$$\Phi_{PL} = \frac{\text{photons emitted}}{\text{photons absorbed}} = \frac{\Gamma_{rad}}{\Gamma_{rad} + \Gamma_{non-rad}} \tag{9.13}$$

where Γ are radiative and non-radiative recombination rates.
PL lifetime:

$$\tau_{PL} = \frac{1}{\Gamma_{rad} + \Gamma_{non-rad}} \tag{9.14}$$

Internal quantum efficiency:

$$\eta_{int} = \frac{\Gamma_{rad}}{\Gamma_{rad} + \Gamma_{non-rad}} \tag{9.15}$$

9.3.2 PL Spectral Features

Band Edge Emission

Near-band-edge (NBE) emission occurs from direct band-to-band or excitonic recombination:

$$h\nu_{NBE} \approx E_g \tag{9.16}$$

For excitonic emission:

$$h\nu_{exc} = E_g - E_b \tag{9.17}$$

where E_b is exciton binding energy.

Defect Emission

Deep-level defects create states within band gap:

- Oxygen vacancies: Often cause green/yellow emission
- Metal vacancies: Trap states
- Interstitials: Donor/acceptor levels
- Surface states: Non-radiative centers

Stokes Shift

Energy difference between absorption and emission maxima:

$$\Delta E_{Stokes} = h\nu_{abs} - h\nu_{PL} \tag{9.18}$$

Originates from:

- Lattice relaxation (Franck-Condon)
- Energy transfer
- Thermalization

9.3.3 Temperature-Dependent PL

PL intensity and peak position vary with temperature:

Thermal quenching:

$$I(T) = \frac{I_0}{1 + C\exp(-E_a/k_B T)} \tag{9.19}$$

where E_a is activation energy for quenching.

Band gap temperature dependence:

Varshni equation:

$$E_g(T) = E_g(0) - \frac{\alpha T^2}{T + \beta} \tag{9.20}$$

where α and β are material constants.

9.4 Vibrating Sample Magnetometer (VSM)

VSM measures magnetic properties by detecting the voltage induced in pickup coils by a vibrating magnetized sample.

9.4.1 Fundamental Principles

Operating Principle

1. Sample placed in uniform magnetic field H
2. Sample vibrates vertically at frequency f (typically 50-90 Hz)
3. Magnetic moment m induces AC voltage in detection coils
4. Voltage proportional to magnetic moment

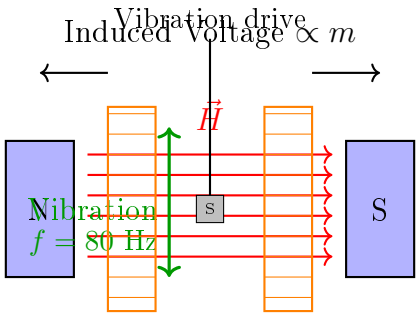

Figure 9.4: Schematic of VSM showing vibrating sample between detection coils

Faraday's Law

Induced voltage in pickup coils:

$$V = -\frac{d\Phi}{dt} = -\frac{d}{dt}(B \cdot A) \tag{9.21}$$

For vibrating sample with displacement $z = z_0 \sin(2\pi f t)$:

$$V = -2\pi f z_0 m \frac{dG}{dz} \tag{9.22}$$

where G is geometric factor of coil system.
Measured voltage proportional to magnetic moment:

$$V \propto m \tag{9.23}$$

9.4.2 Magnetic Properties Measured

Magnetization vs. Field: M-H Curve

The hysteresis loop provides key parameters:

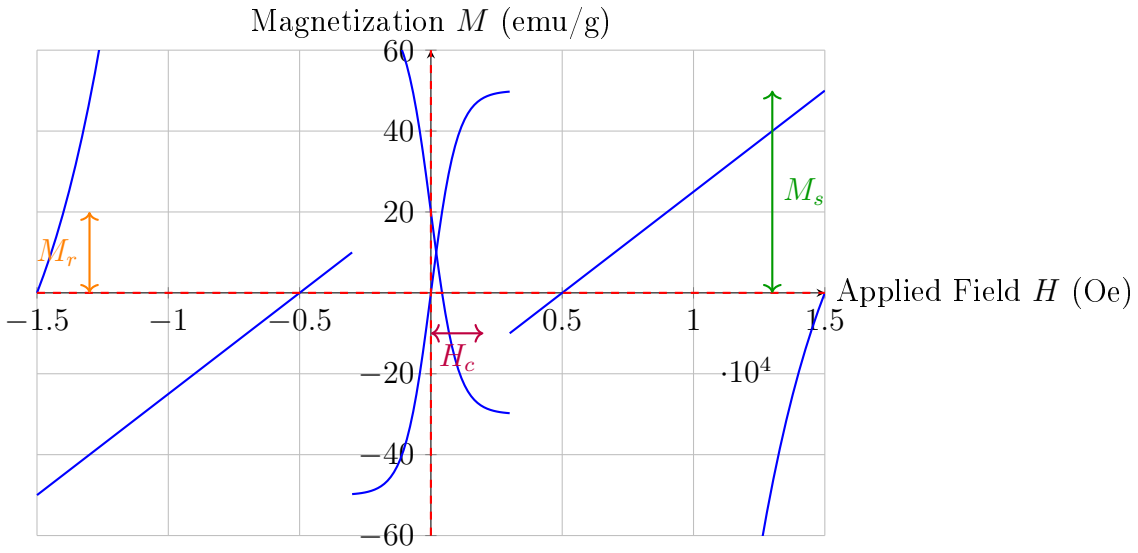

Figure 9.5: Ferromagnetic hysteresis loop showing key magnetic parameters

Key parameters:

1. **Saturation magnetization (M_s):** Maximum magnetization at high field
2. **Remanent magnetization (M_r):** Magnetization at zero field after saturation
3. **Coercivity (H_c):** Field required to reduce M to zero
4. **Squareness ratio:** $S = M_r/M_s$ (0.5-1.0 for hard magnets)
5. **Energy product:** $(BH)_{max}$ for permanent magnets

9.4.3 Types of Magnetic Behavior

Table 9.2: Classification of magnetic materials

Type	χ	H_c	**Examples**
Diamagnetic	-10^{-5}	0	Au, Cu, Bi
Paramagnetic	$+10^{-5}$ to 10^{-3}	0	Al, Pt, O_2
Ferromagnetic	$>> 1$	> 0	Fe, Co, Ni
Antiferromagnetic	Small +	0	MnO, NiO, Cr
Ferrimagnetic	$>> 1$	> 0	Ferrites
Superparamagnetic	$>> 1$	0	Nanoparticles < 20 nm

Superparamagnetism

For nanoparticles below critical size:

$$D_c \approx \frac{18\sqrt{K_1 A}}{\mu_0 M_s^2} \tag{9.24}$$

Thermal energy overcomes anisotropy barrier:

$$E_b = KV \tag{9.25}$$

Relaxation time:

$$\tau = \tau_0 \exp\left(\frac{KV}{k_B T}\right) \tag{9.26}$$

Blocking temperature:

$$T_B = \frac{KV}{25 k_B} \tag{9.27}$$

For $T > T_B$: Superparamagnetic (no hysteresis)
For $T < T_B$: Blocked (shows hysteresis)

9.5 FTIR Spectroscopy for Bonding Analysis

Fourier Transform Infrared (FTIR) spectroscopy identifies molecular vibrations and chemical bonds by measuring infrared absorption.

9.5.1 Fundamental Principles

Molecular Vibrations

Molecules undergo various vibrational modes when absorbing IR radiation:

1. **Stretching:** Bond length changes
    - Symmetric
    - Asymmetric
2. **Bending:** Bond angle changes
    - Scissoring
    - Rocking
    - Wagging
    - Twisting

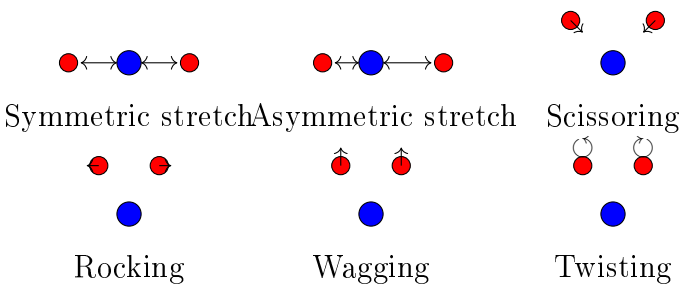

Figure 9.6: Molecular vibrational modes detected in FTIR spectroscopy

Harmonic Oscillator Model

Vibrational frequency for diatomic molecule:

$$\nu = \frac{1}{2\pi}\sqrt{\frac{k}{\mu}} \tag{9.28}$$

where k is force constant, μ is reduced mass:

$$\mu = \frac{m_1 m_2}{m_1 + m_2} \tag{9.29}$$

Wavenumber (cm^{-1}):

$$\tilde{\nu} = \frac{\nu}{c} = \frac{1}{2\pi c}\sqrt{\frac{k}{\mu}} \tag{9.30}$$

Selection rule: Vibration must change dipole moment:

$$\left(\frac{\partial \mu}{\partial Q}\right)_0 \neq 0 \tag{9.31}$$

9.5.2 FTIR Instrumentation

Michelson Interferometer:

1. IR source emits broadband radiation
2. Beam splitter divides beam
3. Fixed and moving mirrors create interference
4. Sample absorbs specific frequencies
5. Detector measures interferogram
6. Fourier transform converts to spectrum

Advantages of FT over dispersive:

- Multiplex advantage (Fellgett)
- Throughput advantage (Jacquinot)
- Better signal-to-noise ratio
- Faster acquisition

9.5.3 Spectral Analysis

Table 9.3: Characteristic FTIR absorption bands

Functional Group	**Wavenumber (cm^{-1})**	**Mode**
O-H (alcohol)	3200-3600	Stretching
O-H (carboxylic acid)	2500-3300	Stretching (broad)
C-H (alkane)	2850-2960	Stretching
C=O (carbonyl)	1700-1750	Stretching
C=C (alkene)	1620-1680	Stretching
N-H (amine)	3300-3500	Stretching
C-O (ether)	1000-1300	Stretching
Metal-O	400-700	Stretching
Si-O-Si	1000-1100	Asymmetric stretch

9.6 Case Study: Magnetic Analysis of Ni-Zn Ferrite Nanoparticles

Case Study

Background

Nickel-zinc ferrites ($Ni_xZn_{1-x}Fe_2O_4$) are soft magnetic materials with applications in transformers, inductors, and electromagnetic interference (EMI) shielding. Their magnetic properties are highly composition and size dependent.

Sample Preparation

Composition: $Ni_{0.5}Zn_{0.5}Fe_2O_4$ nanoparticles
Synthesis: Coprecipitation method

- Precursors: $Ni(NO_3)_2$, $Zn(NO_3)_2$, $Fe(NO_3)_3$
- Precipitant: NaOH (pH = 12)
- Temperature: 80°C
- Calcination: 600°C for 4 hours

Characterization results:

- XRD: Cubic spinel structure, crystallite size = 28 nm
- SEM: Particle size = 35-45 nm
- BET surface area: 48 m^2/g

VSM Analysis

Measurement conditions:

- Temperature: 300 K (room temperature)
- Applied field: ±15 kOe
- Sample mass: 12 mg

M-H Hysteresis Loop

$Ni_{0.5}Zn_{0.5}Fe_2O_4$ Nanoparticles at 300 K

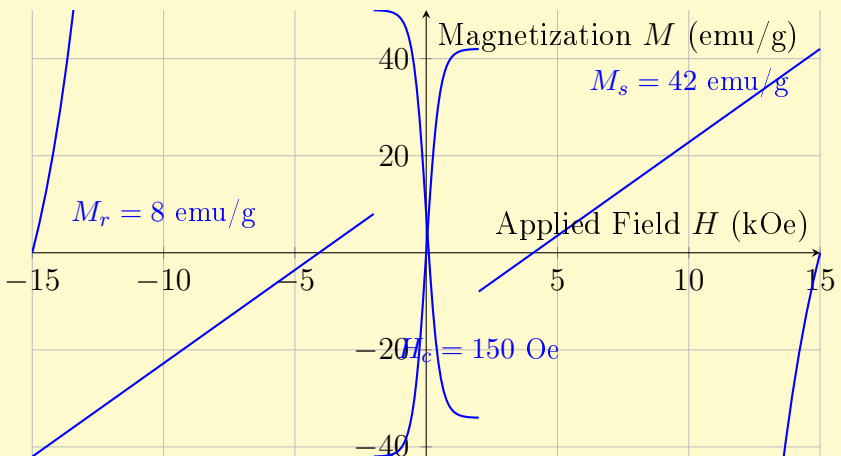

9.7 Summary

This chapter has covered essential optical and magnetic characterization techniques:

Key Point

Key Takeaways:

- **UV-Vis spectroscopy** determines band gap through Tauc plot analysis, with quantum confinement causing blue-shift in nanoparticles
- **Photoluminescence** reveals radiative recombination processes, defect states, and quantum efficiency
- **VSM** measures magnetic properties including saturation magnetization, coercivity, and hysteresis behavior
- **FTIR** identifies chemical bonds and functional groups through molecular vibrations
- **Complementary analysis** combining multiple techniques provides comprehensive material understanding
- **Size-dependent properties** are crucial in nanomaterials: band gap widens, magnetization decreases, coercivity increases
- **Case study approach** demonstrates practical application of VSM for ferrite characterization

These techniques are essential for:

- Materials quality control
- Property optimization
- Application-specific characterization
- Structure-property correlation
- Research publication

Exercises

Conceptual Questions

1. Explain why quantum confinement causes blue-shift in UV-Vis absorption spectra of semiconductor nanoparticles.
2. Describe the difference between direct and indirect band gap transitions. How does this affect the Tauc plot?
3. Why do defect states in nanomaterials often cause visible emission despite UV excitation?

4. Explain the concept of superparamagnetism. At what particle size does it typically occur?
5. Compare photoluminescence quantum yield in bulk vs. nanoparticles. What factors affect efficiency?
6. Describe how surface effects reduce saturation magnetization in magnetic nanoparticles.
7. Why is FTIR particularly useful for identifying surface functionalization of nanoparticles?
8. Explain the relationship between blocking temperature and particle size in magnetic nanoparticles.
9. How does the Stokes shift provide information about energy relaxation processes?
10. Discuss why single-domain particles have higher coercivity than multi-domain particles.

Numerical Problems

1. A CdSe quantum dot shows absorption onset at 520 nm:
   (a) Calculate the band gap in eV
   (b) If bulk CdSe has $E_g = 1.74$ eV, estimate the quantum dot diameter using effective mass approximation ($m_e^* = 0.13m_0$, $m_h^* = 0.45m_0$)
   (c) Determine expected PL emission wavelength (assume 30 meV Stokes shift)
2. UV-Vis data for ZnO nanoparticles:

λ (nm)	Absorbance
400	0.08
380	0.25
370	0.65
360	1.10
350	1.42

   (a) Create Tauc plot
   (b) Determine band gap
   (c) Compare with bulk ZnO (3.37 eV)
3. For Fe_3O_4 nanoparticles with anisotropy constant $K = 1.1 \times 10^4$ J/m^3:
   (a) Calculate energy barrier for 10 nm diameter particles
   (b) Determine blocking temperature (assume $\tau_0 = 10^{-10}$ s, $\tau_m = 100$ s)
   (c) At what temperature will particles be superparamagnetic?
4. VSM measurement shows:
   - $M_s = 55$ emu/g

- $M_r = 12$ emu/g
- $H_c = 250$ Oe

(a) Calculate squareness ratio

(b) Classify as soft or hard magnet

(c) Determine energy product $(BH)_{max}$ estimate

5. FTIR shows strong absorption at 550 cm^{-1} for metal-oxygen bond:

   (a) Calculate vibrational frequency in Hz

   (b) If force constant $k = 200$ N/m, determine reduced mass

   (c) Identify the metal if bonded to oxygen

6. A PL spectrum shows peak at 450 nm with FWHM = 40 nm:

   (a) Calculate emission energy in eV

   (b) Determine energy width of emission (FWHM in eV)

   (c) If excitation is at 350 nm, calculate Stokes shift

7. For $Ni_{0.3}Zn_{0.7}Fe_2O_4$ with particle size 25 nm and dead layer 1.5 nm:

   (a) Estimate M_s if bulk value is 70 emu/g

   (b) Calculate critical single-domain size ($K_1 = 2 \times 10^4$ J/m^3, $A = 10^{-11}$ J/m)

   (c) Determine if particles are single or multi-domain

8. Temperature-dependent PL shows intensity decreases from 1000 (at 10 K) to 200 (at 300 K):

   (a) Fit to thermal quenching model

   (b) Determine activation energy

   (c) Predict intensity at 150 K

9. For harmonic oscillator model of C=O bond:

   (a) Given $\tilde{\nu} = 1700$ cm^{-1}, calculate force constant

   (b) Determine reduced mass of C=O

   (c) Calculate zero-point energy

10. A magnetic nanoparticle sample shows $T_B = 280$ K with volume 500 nm^3:

    (a) Calculate anisotropy constant

    (b) Determine coercivity at 100 K if $M_s = 400$ kA/m

    (c) Estimate relaxation time at 300 K

Advanced Problems

1. Design an experiment to distinguish between:
   (a) Band-edge emission vs. defect emission using PL
   (b) Ferromagnetic vs. superparamagnetic using VSM
   (c) Surface-bound vs. bulk-phase groups using FTIR
2. Develop a comprehensive optical characterization protocol for unknown semiconductor nanoparticles. Include UV-Vis, PL, and data analysis steps.
3. Propose a method to measure the distribution of blocking temperatures in a polydisperse magnetic nanoparticle sample.
4. Compare the magnetic properties expected for:
   (a) 5 nm particles at 300 K
   (b) 50 nm particles at 300 K
   (c) 5 nm particles at 10 K

   Explain using superparamagnetic theory.
5. Design a quality control procedure for commercial ZnO nanoparticles using UV-Vis and FTIR. Specify acceptance criteria.

Bibliography

[1] Pavia, D. L., Lampman, G. M., Kriz, G. S., & Vyvyan, J. R. (2014). *Introduction to Spectroscopy* (5th ed.). Cengage Learning.

[2] Atkins, P., & de Paula, J. (2010). *Physical Chemistry* (9th ed.). Oxford University Press.

[3] Sze, S. M., & Ng, K. K. (2006). *Physics of Semiconductor Devices* (3rd ed.). Wiley-Interscience.

[4] Yu, P. Y., & Cardona, M. (2010). *Fundamentals of Semiconductors: Physics and Materials Properties* (4th ed.). Springer.

[5] Fox, M. (2010). *Optical Properties of Solids* (2nd ed.). Oxford University Press.

[6] Jiles, D. (1998). *Introduction to Magnetism and Magnetic Materials* (2nd ed.). Chapman Hall.

[7] Cullity, B. D., Graham, C. D. (2008). *Introduction to Magnetic Materials* (2nd ed.). Wiley-IEEE Press.

[8] Stuart, B. H. (2004). *Infrared Spectroscopy: Fundamentals and Applications*. Wiley.

[9] Smith, B. C. (2011). *Fundamentals of Fourier Transform Infrared Spectroscopy* (2nd ed.). CRC Press.

[10] Lakowicz, J. R. (2006). *Principles of Fluorescence Spectroscopy* (3rd ed.). Springer.

[11] Valeur, B., Berberan-Santos, M. N. (2012). *Molecular Fluorescence: Principles and Applications* (2nd ed.). Wiley-VCH.

[12] Reitz, J. R., Milford, F. J., Christy, R. W. (2008). *Foundations of Electromagnetic Theory* (4th ed.). Addison-Wesley.

[13] Brus, L. E. (1984). Electron-electron and electron-hole interactions in small semiconductor crystallites. *Journal of Chemical Physics*, 80(9), 4403-4409.

[14] Tauc, J., Grigorovici, R., Vancu, A. (1966). Optical properties and electronic structure of amorphous germanium. *Physica Status Solidi (b)*, 15(2), 627-637.

[15] Davis, E. A., Mott, N. F. (1970). Conduction in non-crystalline systems. *Philosophical Magazine*, 22(179), 0903-0922.

[16] Néel, L. (1949). Théorie du traînage magnétique des ferromagnétiques en grains fins avec applications aux terres cuites. *Annales de Géophysique*, 5, 99-136.

[17] Bean, C. P., Livingston, J. D. (1959). Superparamagnetism. *Journal of Applied Physics*, 30(4), S120-S129.

[18] Leslie-Pelecky, D. L., Rieke, R. D. (1996). Magnetic properties of nanostructured materials. *Chemistry of Materials*, 8(8), 1770-1783.

[19] Kodama, R. H. (1999). Magnetic nanoparticles. *Journal of Magnetism and Magnetic Materials*, 200(1-3), 359-372.

[20] Laurent, S., Forge, D., Port, M., et al. (2008). Magnetic iron oxide nanoparticles: synthesis, stabilization, vectorization, physicochemical characterizations, and biological applications. *Chemical Reviews*, 108(6), 2064-2110.

[21] Goldman, A. (2006). *Modern Ferrite Technology* (2nd ed.). Springer.

[22] Smit, J., Wijn, H. P. J. (1959). *Ferrites*. Wiley.

[23] Valenzuela, R. (1994). *Magnetic Ceramics*. Cambridge University Press.

[24] Cao, G., & Wang, Y. (2011). *Nanostructures and Nanomaterials: Synthesis, Properties, and Applications* (2nd ed.). World Scientific.

[25] Rao, C. N. R., Müller, A., Cheetham, A. K. (Eds.). (2004). *The Chemistry of Nanomaterials: Synthesis, Properties and Applications*. Wiley-VCH.

[26] Ozin, G. A., Arsenault, A. C. (2009). *Nanochemistry: A Chemical Approach to Nanomaterials* (2nd ed.). Royal Society of Chemistry.

[27] Bhushan, B. (Ed.). (2017). *Springer Handbook of Nanotechnology* (4th ed.). Springer.

Part IV

Applications of Nanomaterials

The emergence of nanomaterials has revolutionized diverse fields ranging from energy harvesting to biomedicine, and from electronics to environmental remediation. The unique properties exhibited at the nanoscale—including quantum confinement effects, enhanced surface-to-volume ratios, and tunable optical and electronic characteristics—enable unprecedented functionalities that are unattainable in bulk materials. This part of the textbook explores three major application domains of nanomaterials, providing both fundamental understanding and practical insights into their implementation.

In Chapter 10, we delve into energy and environmental applications, examining how nanomaterials address critical challenges in sustainable energy production, storage, and environmental protection. Chapter 11 focuses on biomedical and pharmaceutical applications, where nanomaterials are transforming diagnostics, therapeutics, and biosensing technologies. Finally, Chapter 12 explores electronic and photonic applications, highlighting the role of nanomaterials in next-generation computing, communication, and optoelectronic devices.

Each chapter integrates theoretical foundations with practical examples, mathematical formulations, and experimental insights to provide a comprehensive understanding of how nanomaterials are being deployed to solve real-world problems.

Chapter 10

Energy and Environmental Applications

10.1 Introduction

The global energy crisis and environmental degradation demand innovative solutions that can provide sustainable, clean, and efficient technologies. Nanomaterials, with their exceptional physical and chemical properties, have emerged as promising candidates for addressing these challenges. The high surface area, quantum effects, and tunable properties of nanomaterials enable enhanced performance in photocatalysis, energy conversion, storage devices, and thermal management systems.

This chapter explores four critical areas where nanomaterials are making significant contributions:

- Photocatalytic degradation of pollutants and wastewater treatment
- Advanced solar energy conversion and supercapacitive energy storage
- Hydrogen production and storage for clean energy
- Thermal and electrical transport in energy devices

10.2 Photocatalysis and Wastewater Remediation

10.2.1 Fundamental Principles of Photocatalysis

Photocatalysis is a light-driven catalytic process that utilizes semiconductor nanomaterials to accelerate chemical reactions, particularly the degradation of organic pollutants in wastewater.

Definition

Photocatalysis is the acceleration of a photoreaction in the presence of a catalyst (photocatalyst). In heterogeneous photocatalysis, semiconductor nanoparticles absorb photons with energy equal to or greater than their band gap, generating electron-hole pairs that participate in redox reactions.

Mechanism of Photocatalytic Degradation

The photocatalytic process involves several sequential steps:

1. **Photoexcitation**: When a photon with energy $h\nu \geq E_g$ (where E_g is the band gap) irradiates the semiconductor, electrons are promoted from the valence band (VB) to the conduction band (CB):

$$\text{Photocatalyst} + h\nu \rightarrow e^-_{\text{CB}} + h^+_{\text{VB}} \tag{10.1}$$

2. **Charge Separation**: The photogenerated electron-hole pairs migrate to the surface or recombine:

$$e^-_{\text{CB}} + h^+_{\text{VB}} \rightarrow \text{heat (recombination)} \tag{10.2}$$

3. **Surface Reactions**: The separated charges participate in redox reactions:

$$h^+_{\text{VB}} + \text{H}_2\text{O} \rightarrow \text{OH}^\bullet + \text{H}^+ \tag{10.3}$$
$$h^+_{\text{VB}} + \text{OH}^- \rightarrow \text{OH}^\bullet \tag{10.4}$$
$$e^-_{\text{CB}} + \text{O}_2 \rightarrow \text{O}_2^{-\bullet} \tag{10.5}$$

4. **Pollutant Degradation**: Reactive oxygen species (ROS) attack organic pollutants:

$$\text{OH}^\bullet + \text{Pollutant} \rightarrow \text{Degradation products} \rightarrow \text{CO}_2 + \text{H}_2\text{O} \tag{10.6}$$

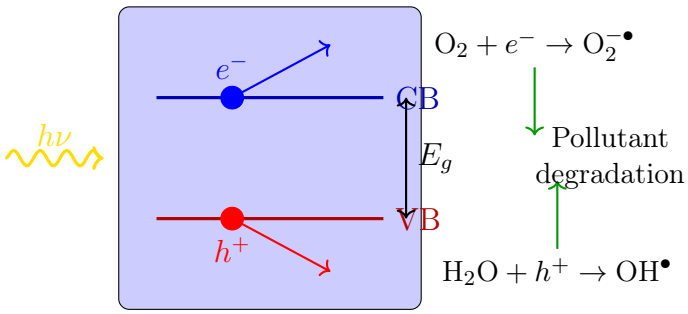

Figure 10.1: Schematic representation of photocatalytic mechanism in semiconductor nanoparticles showing photoexcitation, charge separation, and surface redox reactions.

10.2.2 Kinetics of Photocatalytic Degradation

The photocatalytic degradation typically follows pseudo-first-order kinetics described by the Langmuir-Hinshelwood model:

$$r = -\frac{dC}{dt} = \frac{k_r K_{\text{ad}} C}{1 + K_{\text{ad}} C} \tag{10.7}$$

where r is the degradation rate, C is the pollutant concentration, k_r is the reaction rate constant, and K_{ad} is the adsorption equilibrium constant.

For low concentrations ($K_{\text{ad}} C \ll 1$), this simplifies to:

$$-\frac{dC}{dt} = k_{\text{app}} C \tag{10.8}$$

where $k_{\text{app}} = k_r K_{\text{ad}}$ is the apparent rate constant. Integration yields:

$$\ln\left(\frac{C_0}{C}\right) = k_{\text{app}} t \tag{10.9}$$

The degradation efficiency is defined as:

$$\eta = \frac{C_0 - C}{C_0} \times 100\% \tag{10.10}$$

10.2.3 Quantum Efficiency

The quantum efficiency (QE) measures the effectiveness of photon utilization:

$$\text{QE} = \frac{\text{Number of degraded molecules}}{\text{Number of absorbed photons}} \times 100\% \tag{10.11}$$

For practical purposes, the apparent quantum efficiency is:

$$\Phi = \frac{\text{Rate of pollutant degradation}}{\text{Rate of photon absorption}} \tag{10.12}$$

10.2.4 Nanomaterial Photocatalysts

Table 10.1: Properties of common photocatalytic nanomaterials

Material	Band Gap (eV)	Active Region	Advantages
TiO_2	3.0–3.2	UV	High stability, non-toxic
ZnO	3.2–3.3	UV	High electron mobility
WO_3	2.6–2.8	Visible	Visible light active
g-C_3N_4	2.7	Visible	Metal-free, stable
$BiVO_4$	2.4	Visible	Excellent visible response
CdS	2.4	Visible	Narrow band gap

Key Point

Nanostructured photocatalysts offer several advantages over bulk materials:

- Higher surface area for enhanced adsorption
- Shorter charge carrier diffusion paths, reducing recombination
- Tunable band gap through quantum confinement
- Enhanced light harvesting through scattering effects

10.2.5 Strategies for Enhanced Photocatalytic Performance

Doping and Heterostructure Formation

Doping introduces impurity levels within the band gap, enabling visible light absorption:

$$E_g^{\text{eff}} = E_g - E_{\text{dopant}} \tag{10.13}$$

Heterostructures facilitate charge separation. For a Type-II heterojunction:

$$\Delta E_C = \chi_A - \chi_B \tag{10.14}$$

where χ represents electron affinity and the subscripts denote different materials.

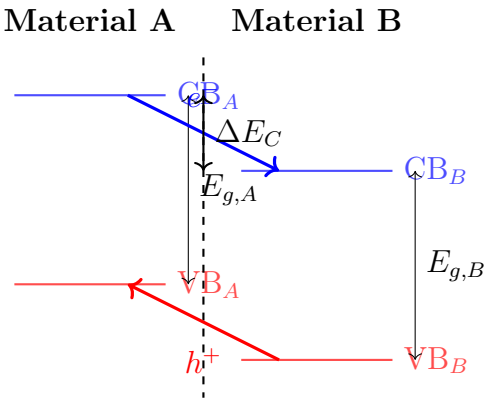

Figure 10.2: Type-II heterojunction showing band alignment and charge transfer mechanism promoting charge separation.

10.2.6 Example: Photocatalytic Degradation using Ferrite Nanocomposites

Hands-On Analysis

Case Study: $CoFe_2O_4$/g-C_3N_4 Nanocomposite for Methylene Blue Degradation

Background: Ferrite nanoparticles (MFe_2O_4, M = Co, Ni, Zn) possess magnetic properties facilitating easy recovery and exhibit photocatalytic activity. Coupling with graphitic carbon nitride (g-C_3N_4) creates a heterojunction enhancing charge separation.

Experimental Setup:

- Photocatalyst: $CoFe_2O_4$/g-C_3N_4 (30 wt% ferrite)
- Pollutant: Methylene Blue (MB), $C_0 = 10$ mg/L
- Catalyst loading: 1 g/L
- Light source: Visible light (500 W xenon lamp, $\lambda > 420$ nm)
- Reaction time: 120 minutes

Kinetic Analysis:
The degradation follows pseudo-first-order kinetics. Experimental data:

Time (min)	C/C$_0$	$\ln(C_0/C)$	Efficiency (%)
0	1.000	0.000	0
20	0.823	0.195	17.7
40	0.651	0.429	34.9
60	0.487	0.719	51.3
80	0.342	1.072	65.8
100	0.228	1.478	77.2
120	0.142	1.952	85.8

From the linear plot of $\ln(C_0/C)$ vs. t:

$$k_{\text{app}} = 0.0163 \text{ min}^{-1} \quad (R^2 = 0.995) \tag{10.15}$$

The half-life is calculated as:

$$t_{1/2} = \frac{\ln 2}{k_{\text{app}}} = \frac{0.693}{0.0163} = 42.5 \text{ min} \tag{10.16}$$

Mechanism: The enhanced performance is attributed to:

1. Z-scheme electron transfer reducing recombination
2. Magnetic properties enabling catalyst recovery (>95% after 5 cycles)
3. Synergistic effects between ferrite and g-C_3N_4

Comparison with Controls:

10.3 Solar Cells and Supercapacitors

10.3.1 Nanomaterials in Photovoltaic Devices

Solar cells convert light energy into electrical energy through the photovoltaic effect. Nanomaterials enhance solar cell efficiency through improved light absorption, charge transport, and reduced recombination.

Solar Cell Operating Principles

The current-voltage characteristics of a solar cell are described by the Shockley diode equation:

$$I = I_L - I_0 \left[\exp\left(\frac{qV}{nk_BT} \right) - 1 \right] - \frac{V}{R_{sh}} \tag{10.17}$$

where:

- I_L = photogenerated current
- I_0 = reverse saturation current
- q = elementary charge
- n = ideality factor
- k_B = Boltzmann constant
- T = temperature
- R_{sh} = shunt resistance

The power conversion efficiency (PCE) is:

$$\eta = \frac{P_{\max}}{P_{\text{in}}} = \frac{V_{oc} \times I_{sc} \times FF}{P_{\text{in}}} \tag{10.18}$$

where V_{oc} is open-circuit voltage, I_{sc} is short-circuit current, and FF is the fill factor:

$$FF = \frac{V_{mp} \times I_{mp}}{V_{oc} \times I_{sc}} \tag{10.19}$$

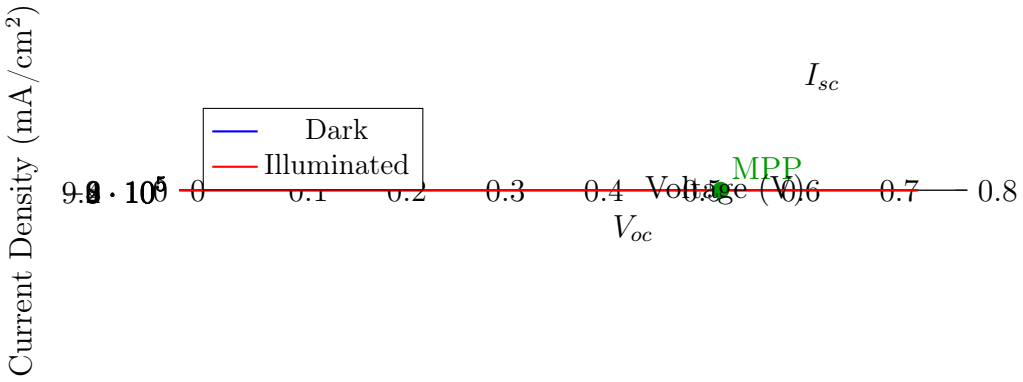

Figure 10.3: Current-voltage (I-V) characteristics of a solar cell under dark and illuminated conditions, showing key parameters.

Quantum Dot Solar Cells

Quantum dots (QDs) enable tunable band gaps through size control:

$$E_g(r) = E_g^{\text{bulk}} + \frac{\hbar^2\pi^2}{2r^2}\left(\frac{1}{m_e^*} + \frac{1}{m_h^*}\right) - \frac{1.8e^2}{4\pi\epsilon\epsilon_0 r} \tag{10.20}$$

where r is QD radius, m_e^* and m_h^* are effective masses, and ϵ is the dielectric constant.

The theoretical maximum efficiency for QD solar cells with multiple exciton generation (MEG) can exceed the Shockley-Queisser limit:

$$\eta_{\text{MEG}} = \frac{\sum_i N_{\text{ex}}(E_i) \cdot \Phi(E_i) \cdot E_g}{E_{\text{solar}}} \tag{10.21}$$

where N_{ex} is the number of excitons generated per photon and $\Phi(E_i)$ is the photon flux.

10.3.2 Supercapacitors with Nanomaterial Electrodes

Supercapacitors (electrochemical capacitors) store energy through electrostatic charge accumulation (EDLCs) or fast redox reactions (pseudocapacitors).

Energy Storage Mechanisms

The total capacitance can be expressed as:

$$C_{\text{total}} = C_{\text{EDLC}} + C_{\text{pseudo}} \tag{10.22}$$

For EDLCs, the capacitance is given by:

$$C_{\text{EDLC}} = \frac{\epsilon_r \epsilon_0 A}{d} \tag{10.23}$$

where A is the electrode surface area and d is the charge separation distance (Debye length).

The energy density (E) and power density (P) are:

$$E = \frac{1}{2}CV^2 \tag{10.24}$$

$$P = \frac{V^2}{4R_{ESR}} \tag{10.25}$$

where V is the operating voltage and R_{ESR} is the equivalent series resistance.

Nanomaterial Electrodes

Table 10.2: Specific capacitance of nanomaterial electrodes

Material	Type	Specific Capacitance (F/g)	Voltage Window (V)
Graphene	EDLC	100–300	3.5 (organic)
CNTs	EDLC	50–200	3.0
RuO_2	Pseudo	600–900	1.2
MnO_2	Pseudo	200–400	1.0
Conducting polymers	Pseudo	300–500	0.8
MXenes	Hybrid	300–900	1.0

Key Point

Nanomaterials enhance supercapacitor performance through:

- High specific surface area (up to 2630 m^2/g for graphene)
- Short ion diffusion paths enabling high power density
- Exposed active sites for pseudocapacitive reactions
- Hierarchical pore structures optimizing ion transport

10.4 Hydrogen Production and Storage

10.4.1 Photocatalytic Water Splitting

Water splitting for hydrogen production is described by:

$$2H_2O \xrightarrow{h\nu} 2H_2 + O_2 \quad \Delta G^0 = 237 \text{ kJ/mol} \tag{10.26}$$

Thermodynamic Requirements

The minimum photon energy required is:

$$E_{\text{photon}} = \frac{\Delta G^0}{nF} = \frac{237000}{2 \times 96485} = 1.23 \text{ V} \tag{10.27}$$

Accounting for overpotentials and losses:

$$E_g \geq 1.23 + \eta_{\text{HER}} + \eta_{\text{OER}} + \eta_{\text{loss}} \approx 1.8\text{–}2.0 \text{ eV} \tag{10.28}$$

The band edges must straddle the water redox potentials:

$$E_{\text{CB}} < E(H^+/H_2) = 0 \text{ V vs. NHE} \tag{10.29}$$

$$E_{\text{VB}} > E(O_2/H_2O) = 1.23 \text{ V vs. NHE} \tag{10.30}$$

Solar-to-Hydrogen Efficiency

The STH efficiency is calculated as:

$$\eta_{\text{STH}} = \frac{r_{\text{H}_2} \times \Delta G^0}{P_{\text{solar}} \times A} \times 100\% \tag{10.31}$$

where r_{H_2} is the hydrogen production rate (mol/s), P_{solar} is incident solar power (typically 100 mW/cm^2), and A is the illuminated area.

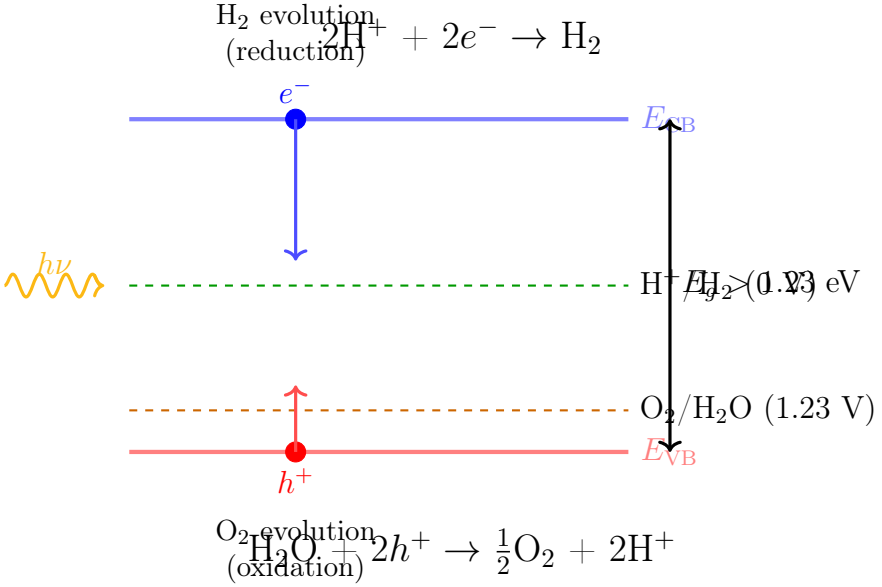

Figure 10.4: Energy diagram for photocatalytic water splitting showing band edge positions relative to water redox potentials.

10.4.2 Hydrogen Storage in Nanomaterials

Nanomaterials offer enhanced hydrogen storage through:

- Physisorption in high surface area materials (MOFs, carbon nanostructures)
- Chemisorption in metal hydrides
- Spillover mechanisms

The gravimetric storage capacity is:

$$\text{Capacity (wt\%)} = \frac{m_{\text{H}_2}}{m_{\text{H}_2} + m_{\text{storage material}}} \times 100\% \tag{10.32}$$

The U.S. Department of Energy (DOE) targets for 2025:

- System gravimetric capacity: 5.5 wt%
- System volumetric capacity: 40 g/L
- Operating temperature: -40 to 60 °C

Table 10.3: Hydrogen storage capacities of nanomaterials

Material	Gravimetric (wt%)	Volumetric (g/L)	Mechanism
SWCNTs	1–2	10–20	Physisorption
Graphene	1–5	15–30	Physisorption
MOF-5	7.1	42	Physisorption
MgH_2 nanoparticles	7.6	110	Chemisorption
Complex hydrides	5–10	80–120	Chemical

10.5 Thermal and Electrical Conductivity in Energy Devices

10.5.1 Thermal Conductivity of Nanomaterials

Thermal conductivity (κ) in nanomaterials is modified by phonon boundary scattering. The kinetic theory gives:

$$\kappa = \frac{1}{3} C_v v_s \Lambda \tag{10.33}$$

where C_v is heat capacity, v_s is sound velocity, and Λ is phonon mean free path.

For nanostructures with characteristic dimension d:

$$\frac{1}{\Lambda_{\text{eff}}} = \frac{1}{\Lambda_{\text{bulk}}} + \frac{1}{d} \tag{10.34}$$

This leads to thermal conductivity reduction:

$$\frac{\kappa_{\text{nano}}}{\kappa_{\text{bulk}}} = \frac{\Lambda_{\text{eff}}}{\Lambda_{\text{bulk}}} = \frac{1}{1 + \Lambda_{\text{bulk}}/d} \tag{10.35}$$

10.5.2 Electrical Conductivity and Thermoelectric Figure of Merit

The thermoelectric figure of merit is:

$$ZT = \frac{S^2 \sigma T}{\kappa} \tag{10.36}$$

where S is the Seebeck coefficient, σ is electrical conductivity, and T is absolute temperature.

Nanomaterials can enhance ZT by:

- Reducing κ through phonon scattering (quantum confinement)
- Maintaining or increasing S through density of states modifications
- Maintaining σ through quantum well effects

Practical Tip

For thermoelectric applications, aim for "phonon-glass electron-crystal" behavior: low thermal conductivity like amorphous materials, but high electrical conductivity like crystalline materials. Nanostructuring is a key strategy to approach this ideal.

10.6 Chapter Summary

This chapter has explored the diverse energy and environmental applications of nanomaterials:

- **Photocatalysis**: Nanomaterials enable efficient pollutant degradation through enhanced light absorption and charge separation. The Langmuir-Hinshelwood kinetic model describes degradation rates, with ferrite-based nanocomposites showing exceptional performance.
- **Solar Energy**: Quantum dots and nanostructured materials improve photovoltaic efficiency through tunable band gaps and reduced recombination. Supercapacitors using nanomaterial electrodes achieve high power density and cyclic stability.
- **Hydrogen Economy**: Photocatalytic water splitting and enhanced hydrogen storage in nanomaterials provide pathways for clean energy. Band edge engineering is critical for efficient photocatalysts.
- **Thermal Management**: Nanostructuring allows independent tuning of thermal and electrical transport, enabling high-performance thermoelectric devices.

The mathematical frameworks presented—from reaction kinetics to quantum efficiency calculations—provide quantitative tools for designing and optimizing nanomaterial-based energy technologies. The integration of experimental examples demonstrates the practical implementation of these concepts.

References

[1] Fujishima, A., & Honda, K. (1972). Electrochemical photolysis of water at a semiconductor electrode. *Nature*, 238(5358), 37-38.

[2] Hoffmann, M. R., Martin, S. T., Choi, W., & Bahnemann, D. W. (1995). Environmental applications of semiconductor photocatalysis. *Chemical Reviews*, 95(1), 69-96.

[3] Cao, G., & Wang, Y. (2011). *Nanostructures and Nanomaterials: Synthesis, Properties, and Applications* (2nd ed.). World Scientific.

[4] Gratzel, M. (2001). Photoelectrochemical cells. *Nature*, 414(6861), 338-344.

[5] Simon, P., & Gogotsi, Y. (2008). Materials for electrochemical capacitors. *Nature Materials*, 7(11), 845-854.

[6] Chen, X., Shen, S., Guo, L., & Mao, S. S. (2010). Semiconductor-based photocatalytic hydrogen generation. *Chemical Reviews*, 110(11), 6503-6570.

[7] Sakintuna, B., Lamari-Darkrim, F., & Hirscher, M. (2007). Metal hydride materials for solid hydrogen storage: A review. *International Journal of Hydrogen Energy*, 32(9), 1121-1140.

[8] Snyder, G. J., & Toberer, E. S. (2008). Complex thermoelectric materials. *Nature Materials*, 7(2), 105-114.

[9] Pelaez, M., et al. (2012). A review on the visible light active titanium dioxide photocatalysts for environmental applications. *Applied Catalysis B: Environmental*, 125, 331-349.

[10] Schüth, F., Bogdanović, B., & Felderhoff, M. (2004). Light metal hydrides and complex hydrides for hydrogen storage. *Chemical Communications*, (20), 2249-2258.

Chapter 11

Biomedical and Pharmaceutical Applications

11.1 Introduction

Nanomaterials have revolutionized biomedical science and pharmaceutical technology by enabling unprecedented control over drug delivery, diagnostics, and therapy at the molecular and cellular levels. The unique properties of nanomaterials—including high surface-to-volume ratios, tunable surface chemistry, quantum effects, and the ability to cross biological barriers—make them ideal candidates for addressing critical challenges in medicine.

This chapter explores four major areas of biomedical nanomaterial applications:

- Targeted drug delivery systems and controlled release mechanisms
- Antibacterial and antifungal nanoparticles for infection control
- Biosensors and bioimaging technologies
- Toxicological considerations and regulatory frameworks

Each section integrates fundamental principles with practical applications, emphasizing the interdisciplinary nature of nanomedicine.

11.2 Drug Delivery and Targeted Therapy

11.2.1 Fundamentals of Nanoparticle Drug Delivery

Drug delivery systems using nanoparticles offer several advantages over conventional formulations:

Key Point

Advantages of Nanoscale Drug Carriers:

- Enhanced permeability and retention (EPR) effect in tumor tissues
- Protection of drugs from degradation
- Controlled and sustained release kinetics
- Active targeting through surface functionalization
- Reduced systemic toxicity
- Improved bioavailability of poorly soluble drugs

The Enhanced Permeability and Retention (EPR) Effect

Tumor tissues exhibit abnormal vasculature with pore sizes of 100–800 nm, compared to normal tissues with pores < 6 nm. This enables passive targeting of nanoparticles.

The accumulation rate in tumors can be modeled as:

$$\frac{dC_{\text{tumor}}}{dt} = k_{\text{in}} C_{\text{blood}} - k_{\text{out}} C_{\text{tumor}} \tag{11.1}$$

where k_{in} is the extravasation rate and k_{out} is the clearance rate. At steady state:

$$C_{\text{tumor}} = \frac{k_{\text{in}}}{k_{\text{out}}} C_{\text{blood}} \tag{11.2}$$

The targeting ratio is:

$$TR = \frac{C_{\text{tumor}}}{C_{\text{normal tissue}}} = \frac{(k_{\text{in}}/k_{\text{out}})_{\text{tumor}}}{(k_{\text{in}}/k_{\text{out}})_{\text{normal}}} \tag{11.3}$$

For effective passive targeting, $TR > 5$ is typically desired.

11.2.2 Drug Release Kinetics

Several mathematical models describe drug release from nanocarriers:

Zero-Order Release

$$\frac{dM_t}{dt} = k_0 \quad \Rightarrow \quad M_t = k_0 t \tag{11.4}$$

where M_t is the amount of drug released at time t.

First-Order Release (Diffusion-Controlled)

$$\frac{dM_t}{dt} = k_1(M_0 - M_t) \quad \Rightarrow \quad \ln\left(\frac{M_0}{M_0 - M_t}\right) = k_1 t \tag{11.5}$$

Higuchi Model (Matrix Diffusion)

For drug dispersed in a matrix:

$$M_t = k_H \sqrt{t} \tag{11.6}$$

where k_H is the Higuchi constant:

$$k_H = \sqrt{D(2C_0 - C_s)C_s} \tag{11.7}$$

with D = diffusion coefficient, C_0 = initial drug concentration, C_s = drug solubility.

Korsmeyer-Peppas Model

$$\frac{M_t}{M_\infty} = k_{KP} t^n \tag{11.8}$$

The release exponent n indicates the mechanism:

- $n = 0.5$: Fickian diffusion (spherical geometry)
- $0.5 < n < 1$: Anomalous transport
- $n = 1$: Case-II transport (swelling-controlled)

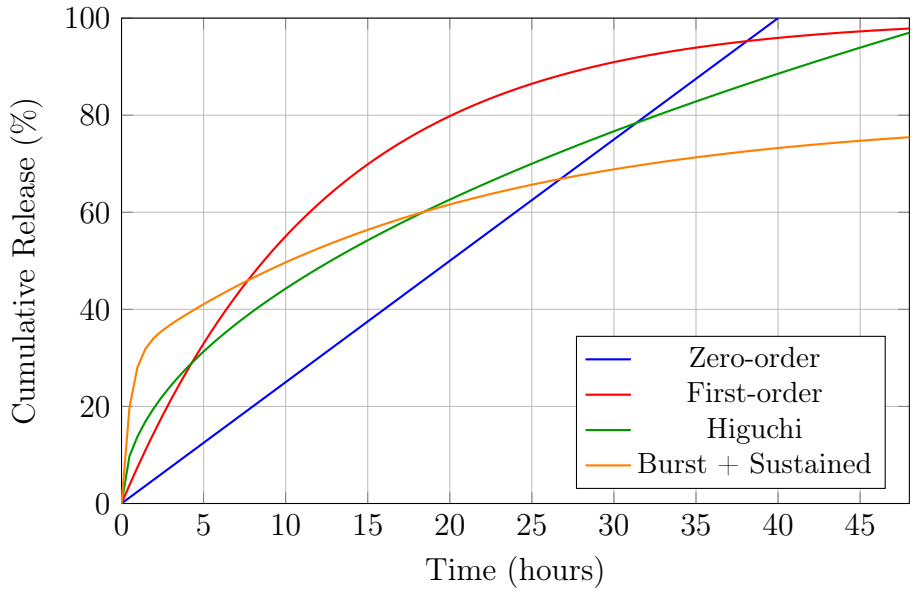

Figure 11.1: Drug release profiles following different kinetic models. Real systems often exhibit combination behaviors.

11.2.3 Types of Nanocarriers

Table 11.1: Common nanoparticle drug delivery systems

Nanocarrier	**Size Range**	**Drug Loading**	**Applications**
Liposomes	50–500 nm	Hydrophilic core, lipophilic bilayer	Cancer therapy, vaccines
Polymeric NPs	10–1000 nm	Encapsulation or conjugation	Sustained release, targeting
Dendrimers	1–15 nm	Surface/interior loading	Gene delivery, imaging
Metallic NPs	1–100 nm	Surface conjugation	Photothermal therapy, diagnostics
Quantum dots	2–10 nm	Conjugation	Imaging, theranostics
Carbon nanotubes	1–5 nm × 100–1000 nm	Interior/exterior loading	Drug/gene delivery

11.2.4 Active Targeting Strategies

Surface functionalization with targeting ligands enhances cellular uptake through receptor-mediated endocytosis.

The binding affinity is characterized by the dissociation constant:

$$K_d = \frac{[\text{Receptor}][\text{Ligand}]}{[\text{Complex}]} \tag{11.9}$$

Lower K_d values indicate stronger binding. Typical targeting ligands include:

- Folic acid ($K_d \approx 10^{-9}$ M) for folate receptor
- Transferrin for transferrin receptor
- Antibodies (e.g., anti-HER2) for cancer cells
- Peptides (e.g., RGD) for integrin receptors

The cellular uptake rate following receptor-mediated endocytosis:

$$\frac{dN_{\text{cell}}}{dt} = k_{\text{on}} N_{\text{receptor}} C_{\text{NP}} - k_{\text{off}} N_{\text{cell}} \tag{11.10}$$

where N_{cell} is the number of internalized nanoparticles and N_{receptor} is the number of available receptors.

11.3 Antibacterial and Antifungal Nanoparticles

11.3.1 Mechanisms of Antimicrobial Action

Nanoparticles exhibit antimicrobial activity through multiple mechanisms:

1. **Reactive Oxygen Species (ROS) Generation**

$$\mathrm{NP} + \mathrm{O_2} + e^- \rightarrow \mathrm{NP^+} + \mathrm{O_2^{-\bullet}} \tag{11.11}$$

$$\mathrm{O_2^{-\bullet}} + 2\mathrm{H^+} + e^- \rightarrow \mathrm{H_2O_2} \rightarrow \mathrm{OH^\bullet} \tag{11.12}$$

2. **Metal Ion Release**

$$\text{Ag-NP} \xrightarrow{\text{oxidation}} \mathrm{Ag^+} + e^- \tag{11.13}$$

3. **Membrane Disruption**: Electrostatic interaction and physical penetration

4. **Protein Denaturation and DNA Damage**: Through oxidative stress

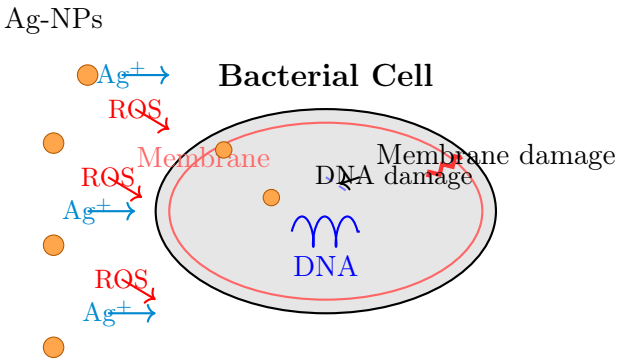

Figure 11.2: Multifaceted mechanisms of antibacterial action by metal nanoparticles including ROS generation, ion release, membrane disruption, and DNA damage.

11.3.2 Quantifying Antibacterial Activity

Minimum Inhibitory Concentration (MIC)

MIC is the lowest concentration that prevents visible bacterial growth after incubation (typically 24 hours):

$$\mathrm{MIC} = \frac{\text{Mass of antibacterial agent}}{\text{Volume of culture medium}} \tag{11.14}$$

Units are typically µg/mL or µM.

Zone of Inhibition (ZOI)

For disk diffusion assays, the ZOI diameter is measured. The inhibition zone area scales with concentration:

$$\text{ZOI Area} = \pi r^2 = k \log C + b \tag{11.15}$$

where C is the antibacterial agent concentration.

Bacterial Viability

The reduction in viable bacteria follows first-order kinetics:

$$\frac{dN}{dt} = -k_{\text{kill}} N \tag{11.16}$$

Solution:

$$\ln\left(\frac{N_0}{N}\right) = k_{\text{kill}} t \tag{11.17}$$

The log reduction value (LRV) is:

$$\text{LRV} = \log_{10}\left(\frac{N_0}{N}\right) \tag{11.18}$$

A 99.9% reduction corresponds to LRV = 3.

11.3.3 Example: Ag-Doped ZnO Nanoparticles

Hands-On Analysis

Antibacterial Performance of Ag-Doped ZnO Nanoparticles

Synthesis: Ag-doped ZnO nanoparticles (Ag:ZnO = 1, 3, 5 mol%) prepared via co-precipitation method.

Characterization:

- Average size: 25–35 nm (TEM)
- Crystalline structure: Wurtzite (XRD)
- Band gap: 3.28 eV (pure ZnO) → 3.15 eV (5% Ag-ZnO)
- Zeta potential: +18 mV (pH 7)

Antibacterial Testing:
Test organisms: Escherichia coli (Gram-negative), *Staphylococcus aureus* (Gram-positive)
Method: Disk diffusion and colony counting

Results:

Sample	ZOI (mm)		MIC (µg/mL)	
	E. coli	*S. aureus*	*E. coli*	*S. aureus*
Pure ZnO	8.5	7.2	125	150
1% Ag-ZnO	12.3	11.5	62.5	75
3% Ag-ZnO	15.8	14.6	31.25	37.5
5% Ag-ZnO	18.2	17.4	15.63	18.75

Time-Kill Kinetics (5% Ag-ZnO, 50 µg/mL):

Time (h)	CFU/mL	N/N_0	$\ln(N_0/N)$	LRV
0	1.2×10^8	1.000	0.000	0.00
1	4.8×10^7	0.400	0.916	0.40
2	1.5×10^7	0.125	2.079	0.90
3	3.6×10^6	0.030	3.526	1.53
4	6.0×10^5	0.005	5.298	2.30
6	2.4×10^4	0.0002	8.611	3.74

From linear regression of $\ln(N_0/N)$ vs. t:

$$k_{\text{kill}} = 1.42 \text{ h}^{-1} \quad (R^2 = 0.989) \tag{11.19}$$

Mechanism Analysis:
ROS generation measured by DCFH-DA assay showed 3.8-fold increase for 5% Ag-ZnO compared to pure ZnO. Ag^+ release in physiological medium: 8.2 µg/mL after 24 h from 100 µg/mL Ag-ZnO suspension.

Enhanced Activity Factors:

11.4 Biosensors and Bioimaging

11.4.1 Nanomaterial-Based Biosensors

Biosensors are analytical devices that convert biological responses into measurable signals. Nanomaterials enhance biosensor performance through:

Definition

A **biosensor** consists of three main components:

1. **Biorecognition element**: Enzyme, antibody, nucleic acid, or cell
2. **Transducer**: Converts biochemical interaction to measurable signal (optical, electrochemical, piezoelectric)
3. **Signal processor**: Amplifies and displays the output

Performance Metrics

Sensitivity: The slope of the calibration curve

$$S = \frac{d(\text{Signal})}{d(\text{Analyte concentration})} \tag{11.20}$$

Limit of Detection (LOD):

$$\text{LOD} = \frac{3\sigma_{\text{blank}}}{S} \tag{11.21}$$

where σ_{blank} is the standard deviation of blank measurements.

Dynamic Range: The concentration range over which the sensor responds linearly, typically expressed as LOD to upper limit of quantification.

Response Time: Time to reach 90% of steady-state signal, often modeled by:

$$I(t) = I_{\max}\left(1 - e^{-t/\tau}\right) \tag{11.22}$$

where τ is the time constant.

11.4.2 Types of Nanomaterial Biosensors

Table 11.2: Nanomaterial-based biosensing platforms

Nanomaterial	**Transduction**	**Analyte Examples**	**Key Advantage**
Gold NPs	Optical (SPR, colorimetric)	DNA, proteins, glucose	Simple readout, no instrumentation
Quantum dots	Fluorescence	Biomarkers, pH, ions	Photostability, multiplexing
Carbon nanotubes	Electrochemical	Glucose, dopamine, H_2O_2	Fast electron transfer
Graphene	Electrochemical, FET	DNA, proteins, cells	High surface area, conductivity
Magnetic NPs	MRI, magnetic	Tumor markers, bacteria	Separation, enrichment
Plasmonic NPs	SERS, LSPR	Trace analytes	Ultra-high sensitivity

Electrochemical Glucose Biosensor

Glucose oxidase (GOx)-functionalized carbon nanotubes on electrodes:

$$\text{Glucose} + \text{GOx(ox)} \rightarrow \text{Gluconic acid} + \text{GOx(red)} \tag{11.23}$$

$$\text{GOx(red)} + O_2 \rightarrow \text{GOx(ox)} + H_2O_2 \tag{11.24}$$

The current response follows the Cottrell equation:

$$i(t) = \frac{nFAD^{1/2}C_0}{\pi^{1/2}t^{1/2}} \tag{11.25}$$

where n = electrons transferred, F = Faraday constant, A = electrode area, D = diffusion coefficient.

For enzyme kinetics, the Michaelis-Menten model applies:

$$i = \frac{i_{\max}[S]}{K_M + [S]} \tag{11.26}$$

At low substrate concentrations ($[S] \ll K_M$), the response is linear:

$$i \approx \frac{i_{\max}}{K_M}[S] \tag{11.27}$$

11.4.3 Bioimaging with Nanomaterials

Quantum Dots for Fluorescence Imaging

Quantum dots offer advantages over organic dyes:

- Broad absorption, narrow emission (25–40 nm FWHM)
- Size-tunable emission wavelength
- High quantum yield (30–80%)
- Photostability (no photobleaching)
- Multiplexing capability

The emission wavelength depends on QD size:

$$\lambda_{\text{em}} = \frac{hc}{E_g(r)} \approx \frac{hc}{E_g^{\text{bulk}} + \frac{\hbar^2\pi^2}{2\mu r^2}} \tag{11.28}$$

where μ is the reduced mass: $1/\mu = 1/m_e^* + 1/m_h^*$.

Contrast Enhancement Factor

For imaging, the contrast-to-noise ratio (CNR) is:

$$\text{CNR} = \frac{S_{\text{target}} - S_{\text{background}}}{\sigma_{\text{noise}}} \tag{11.29}$$

Nanoparticle contrast agents increase S_{target} through:

- High payload of imaging agents (e.g., Gd^{3+} for MRI)
- Enhanced cellular uptake and retention
- Reduced background through targeting

Two-Photon Imaging

For deep tissue imaging, two-photon excitation uses near-IR light:

$$F \propto \langle I^2 \rangle \sigma_2 \phi \tag{11.30}$$

where $\langle I^2 \rangle$ is the time-averaged intensity squared, σ_2 is the two-photon absorption cross-section (in GM, 1 GM = 10^{-50} cm^4 s photon^{-1}), and ϕ is the quantum yield.

Gold nanorods and upconversion nanoparticles exhibit large σ_2 values (>1000 GM).

11.5 Toxicological Aspects and Safety Regulations

11.5.1 Nanotoxicology: Fundamental Concepts

Nanoparticle toxicity depends on physicochemical properties:

- **Size**: Smaller particles have higher cellular uptake and can cross blood-brain barrier (BBB)
- **Surface area**: Higher surface area increases reactivity and ROS generation
- **Surface charge**: Cationic NPs show higher toxicity than anionic or neutral

- **Shape**: High aspect ratio NPs (e.g., nanotubes) show different biodistribution
- **Composition**: Heavy metal-based NPs may release toxic ions
- **Surface coating**: PEGylation reduces protein adsorption and immune recognition

11.5.2 Toxicity Assessment Methods

In Vitro Cytotoxicity

MTT Assay: Measures mitochondrial activity

$$\text{Cell Viability (\%)} = \frac{\text{Abs}_{\text{sample}} - \text{Abs}_{\text{blank}}}{\text{Abs}_{\text{control}} - \text{Abs}_{\text{blank}}} \times 100 \tag{11.31}$$

The half-maximal inhibitory concentration (IC_{50}) is determined from the dose-response curve:

$$\text{Viability} = \frac{100}{1 + \left(\frac{[\text{NP}]}{IC_{50}}\right)^{h}} \tag{11.32}$$

where h is the Hill slope.

Oxidative Stress

ROS generation measured by fluorescent probes (DCFH-DA):

$$\text{ROS Level} = \frac{F_{\text{sample}} - F_{\text{control}}}{F_{\text{control}}} \times 100\% \tag{11.33}$$

Genotoxicity

Comet assay quantifies DNA damage:

$$\text{Tail Moment} = \text{Tail Length} \times \frac{\text{Tail DNA (\%)}}{\text{Total DNA (\%)}} \tag{11.34}$$

11.5.3 Biodistribution and Clearance

The biodistribution of nanoparticles is described by pharmacokinetic models. For a two-compartment model:

$$\frac{dC_{\text{blood}}}{dt} = -(k_{12} + k_{10})C_{\text{blood}} + k_{21}C_{\text{tissue}} \tag{11.35}$$

$$\frac{dC_{\text{tissue}}}{dt} = k_{12}C_{\text{blood}} - k_{21}C_{\text{tissue}} \tag{11.36}$$

where k_{12} is the distribution rate constant, k_{21} is the redistribution rate, and k_{10} is the elimination rate.

The area under the curve (AUC) relates to total exposure:

$$\text{AUC} = \int_0^{\infty} C_{\text{blood}}(t)\, dt = \frac{\text{Dose}}{CL} \tag{11.37}$$

where CL is total body clearance.

11.5.4 Regulatory Framework

Table 11.3: Regulatory guidelines for nanomedicine

Agency	Region	Key Requirements
FDA	USA	Physicochemical characterization (size, surface properties), safety pharmacology, biocompatibility (ISO 10993)
EMA	Europe	Quality by Design (QbD), risk assessment, nano-specific guidance for product development
PMDA	Japan	GLP-compliant toxicity studies, quality consistency, stability data
ISO	International	ISO/TS 80004 (terminology), ISO/TR 13014 (endotoxin testing), ISO 19010 (characterization)

Key Point

Critical Characterization Parameters for Regulatory Approval:

- Size distribution (DLS, TEM, NTA)
- Surface charge (zeta potential)
- Morphology (SEM, AFM)
- Chemical composition and purity
- Surface chemistry and functionalization
- Stability in biological media
- Drug loading and release kinetics
- Sterility and endotoxin levels

11.6 Chapter Summary

This chapter has explored the transformative applications of nanomaterials in biomedicine and pharmaceutics:

- **Drug Delivery**: Nanocarriers enable targeted delivery through EPR effects and active targeting, with controlled release kinetics modeled by various mathematical frameworks (zero-order, Higuchi, Korsmeyer-Peppas). The ability to tune surface properties and loading mechanisms provides unprecedented control over therapeutic outcomes.

- **Antimicrobial Applications**: Metal and metal oxide nanoparticles exhibit potent antibacterial activity through multiple mechanisms including ROS generation and ion release. The example of Ag-doped ZnO demonstrates synergistic enhancement with quantifiable metrics (MIC, ZOI, kill kinetics).

- **Biosensing and Imaging**: Nanomaterials enhance sensitivity, selectivity, and signal quality in biosensors. Quantum dots and plasmonic nanoparticles enable advanced imaging modalities with superior photostability and multiplexing capabilities.

- **Safety and Regulation**: Comprehensive toxicological evaluation and adherence to regulatory frameworks ensure safe translation of nanomedicines. Understanding structure-toxicity relationships guides the design of biocompatible nanomaterials.

The integration of nanomaterials in medicine represents a paradigm shift from conventional therapies to precision medicine, offering solutions to previously intractable challenges in drug delivery, diagnostics, and therapeutics.

References

[1] Peer, D., et al. (2007). Nanocarriers as an emerging platform for cancer therapy. *Nature Nanotechnology*, 2(12), 751-760.

[2] Maeda, H., Wu, J., Sawa, T., Matsumura, Y., & Hori, K. (2000). Tumor vascular permeability and the EPR effect in macromolecular therapeutics: a review. *Journal of Controlled Release*, 65(1-2), 271-284.

[3] Siepmann, J., & Peppas, N. A. (2011). Higuchi equation: Derivation, applications, use and misuse. *International Journal of Pharmaceutics*, 418(1), 6-12.

[4] Lemire, J. A., Harrison, J. J., Turner, R. J. (2013). Antimicrobial activity of metals: mechanisms, molecular targets and applications. *Nature Reviews Microbiology*, 11(6), 371-384.

[5] Raghunath, A., Perumal, E. (2017). Metal oxide nanoparticles as antimicrobial agents: a promise for the future. *International Journal of Antimicrobial Agents*, 49(2), 137-152.

[6] Saha, K., Agasti, S. S., Kim, C., Li, X., Rotello, V. M. (2012). Gold nanoparticles in chemical and biological sensing. *Chemical Reviews*, 112(5), 2739-2779.

[7] Resch-Genger, U., Grabolle, M., Cavaliere-Jaricot, S., Nitschke, R., Nann, T. (2008). Quantum dots versus organic dyes as fluorescent labels. *Nature Methods*, 5(9), 763-775.

[8] Nel, A., Xia, T., Mädler, L., Li, N. (2006). Toxic potential of materials at the nanolevel. *Science*, 311(5761), 622-627.

[9] Dobrovolskaia, M. A., McNeil, S. E. (2007). Immunological properties of engineered nanomaterials. *Nature Nanotechnology*, 2(8), 469-478.

[10] Etheridge, M. L., Campbell, S. A., Erdman, A. G., Haynes, C. L., Wolf, S. M., McCullough, J. (2013). The big picture on nanomedicine: the state of investigational and approved nanomedicine products. *Nanomedicine: Nanotechnology, Biology and Medicine*, 9(1), 1-14.

Chapter 12

Electronic and Photonic Applications

12.1 Introduction

The relentless miniaturization of electronic devices and the growing demand for high-speed, energy-efficient information processing and communication technologies have driven extensive research into nanomaterial-based electronic and photonic systems. At the nanoscale, materials exhibit unique quantum mechanical, optical, and transport properties that enable revolutionary device architectures beyond the capabilities of conventional silicon technology.

This chapter explores four critical areas where nanomaterials are advancing electronic and photonic applications:

- Nanoelectronics and logic devices approaching quantum limits
- Graphene-based photonic structures for ultrafast optoelectronics
- Terahertz metamaterials and plasmonic devices
- Quantum dots in optoelectronic applications

Each section integrates fundamental physics with device operation principles, providing both theoretical frameworks and practical implementation strategies.

12.2 Nanoelectronics and Logic Devices

12.2.1 Scaling and Quantum Effects

The semiconductor industry has followed Moore's Law, doubling transistor density approximately every two years. However, as feature sizes approach atomic dimensions, quantum mechanical effects become dominant.

Classical Scaling Theory

Dennard scaling predicts that as transistor dimensions scale by factor κ:

$$L, W, t_{ox} \to L/\kappa, W/\kappa, t_{ox}/\kappa \tag{12.1}$$
$$V_{DD} \to V_{DD}/\kappa \tag{12.2}$$
$$I_D \to I_D/\kappa \tag{12.3}$$
$$\text{Power density} \to \text{constant} \tag{12.4}$$

However, below 10 nm, quantum effects violate these assumptions.

Quantum Tunneling

For ultra-thin gate oxides, direct tunneling current density is:

$$J_{\text{tunnel}} \propto \exp\left(-\frac{4\pi t_{ox}\sqrt{2m^*\phi_B}}{h}\right) \tag{12.5}$$

where t_{ox} is oxide thickness, m^* is effective mass, and ϕ_B is barrier height.
When $t_{ox} < 2$ nm, leakage becomes prohibitive, necessitating high-κ dielectrics:

$$C_{ox} = \frac{\kappa\epsilon_0 A}{t_{ox}} \tag{12.6}$$

Replacing SiO_2 ($\kappa = 3.9$) with HfO_2 ($\kappa = 25$) allows thicker physical layers while maintaining capacitance.

12.2.2 Carbon Nanotube Field-Effect Transistors (CNTFETs)

Single-walled carbon nanotubes (SWCNTs) exhibit ballistic transport with mean free paths exceeding 1 µm at room temperature.

Electronic Structure of CNTs

The band gap of a semiconducting CNT is:

$$E_g = \frac{2\gamma_0 a_{C-C}}{d} = \frac{2\gamma_0 a_{C-C}\pi}{3L_{ch}} \tag{12.7}$$

where $\gamma_0 \approx 2.9$ eV is the C-C tight-binding overlap energy, $a_{C-C} = 0.142$ nm, and d is the CNT diameter.
For a (n,m) CNT:

$$d = \frac{a_{C-C}\sqrt{n^2 + nm + m^2}}{\pi} \tag{12.8}$$

Metallic when $(n - m)/3$ is integer; semiconducting otherwise.

CNTFET Current-Voltage Characteristics

In the ballistic regime, the on-current is:

$$I_{ON} = \frac{4q}{h}k_B T \ln\left(1 + \exp\left(\frac{q(V_{GS} - V_T)}{k_B T}\right)\right) \tag{12.9}$$

The ON/OFF ratio is:

$$\frac{I_{ON}}{I_{OFF}} \approx \exp\left(\frac{E_g}{k_B T}\right) \tag{12.10}$$

For $E_g = 0.6$ eV at 300 K: $I_{ON}/I_{OFF} \approx 10^{10}$.

Performance Metrics

The intrinsic delay time is:

$$\tau = \frac{C_g V_{DD}}{I_{ON}} \tag{12.11}$$

The cutoff frequency:

$$f_T = \frac{g_m}{2\pi C_g} = \frac{1}{2\pi}\frac{\partial I_D}{\partial V_{GS}}\frac{1}{C_g} \tag{12.12}$$

State-of-the-art CNTFETs demonstrate $f_T > 100$ GHz.

12.2.3 Graphene Transistors

Graphene's linear dispersion relation near the Dirac points:

$$E(\mathbf{k}) = \pm\hbar v_F |\mathbf{k}| \tag{12.13}$$

where $v_F \approx 10^6$ m/s is the Fermi velocity, gives it exceptional carrier mobility ($> 100,000$ cm^2/V·s).

Ambipolar Transport

The conductivity of graphene is:

$$\sigma = \sigma_{\min} + \frac{e\mu}{1}\sqrt{\pi|n|} \tag{12.14}$$

where $n = C_g(V_G - V_{Dirac})/e$ is the carrier density. The minimum conductivity $\sigma_{\min} \approx 4e^2/h$ persists at the Dirac point.

Opening a Band Gap

Pristine graphene's zero band gap limits digital logic applications. Band gaps can be engineered via:

- **Quantum confinement**: Graphene nanoribbons (GNRs)

$$E_g^{\text{GNR}} \approx \frac{\pi\hbar v_F}{W} \tag{12.15}$$

  where W is ribbon width. For $W = 10$ nm, $E_g \approx 0.2$ eV.

- **Bilayer graphene with vertical field**:

$$E_g \approx \gamma_1 \frac{eEd}{\sqrt{\gamma_1^2 + (eEd)^2}} \tag{12.16}$$

  where $\gamma_1 = 0.39$ eV, E is electric field, $d = 0.335$ nm.

- **Chemical doping or functionalization**

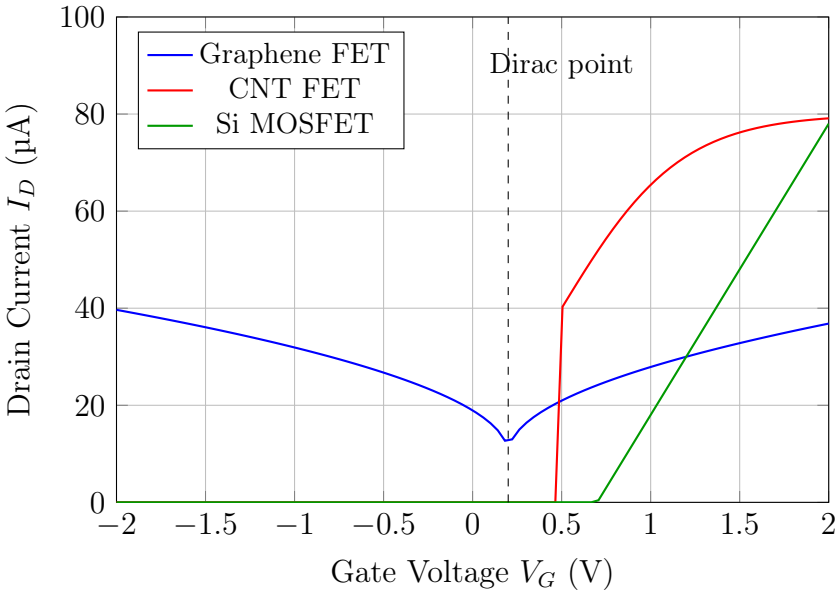

Figure 12.1: Transfer characteristics comparing graphene FET (ambipolar), CNT FET (unipolar), and Si MOSFET. The graphene device shows symmetric electron and hole conduction.

12.2.4 Quantum Dot Cellular Automata (QCA)

QCA represents a paradigm shift from current-based to charge-based computing.

Operating Principle

A QCA cell contains four quantum dots arranged in a square, with two mobile electrons. Coulombic repulsion creates two degenerate ground states representing binary "0" and "1".

The potential energy difference between polarizations is:

$$\Delta E = \frac{2e^2}{4\pi\epsilon\epsilon_0 a}\left(\frac{1}{\sqrt{2}} - 1\right) \approx -1.17\frac{e^2}{4\pi\epsilon\epsilon_0 a} \tag{12.17}$$

where a is the cell size.

For reliable operation at temperature T:

$$\frac{\Delta E}{k_B T} > 10 \quad \Rightarrow \quad a < \frac{e^2}{40\pi\epsilon\epsilon_0 k_B T} \tag{12.18}$$

At room temperature (300 K): $a < 10$ nm for $\epsilon = 10$.

Logic Gates

Majority gate: The output cell polarization follows:

$$P_{\text{out}} = \text{sgn}(P_A + P_B + P_C) \tag{12.19}$$

This implements: AND ($C = -1$), OR ($C = +1$), NOT (one input inverted).

12.3 Graphene-Based Photonic Structures

12.3.1 Optical Properties of Graphene

Graphene's optical conductivity in the infrared and terahertz regions is described by the Kubo formula:

$$\sigma(\omega) = \sigma_{\text{intra}}(\omega) + \sigma_{\text{inter}}(\omega) \tag{12.20}$$

Intraband Contribution (Drude Model)

$$\sigma_{\text{intra}}(\omega) = \frac{ie^2 k_B T}{\pi\hbar^2(\omega + i\tau^{-1})}\left[\frac{\mu_c}{k_B T} + 2\ln\left(e^{-\mu_c/k_B T} + 1\right)\right] \tag{12.21}$$

where μ_c is chemical potential and τ is relaxation time.

Interband Contribution

$$\sigma_{\text{inter}}(\omega) = \frac{ie^2}{4\pi\hbar}\ln\left[\frac{2|\mu_c| - \hbar(\omega + i\tau^{-1})}{2|\mu_c| + \hbar(\omega + i\tau^{-1})}\right] \tag{12.22}$$

At optical frequencies, graphene absorbs:

$$A = \pi\alpha \approx 2.3\% \tag{12.23}$$

per layer, where $\alpha = e^2/(4\pi\epsilon_0\hbar c) \approx 1/137$ is the fine structure constant.

12.3.2 Graphene Photodetectors

Photocurrent Generation Mechanisms

1. **Photovoltaic effect**: Built-in electric field at junctions
2. **Photothermoelectric effect**: Temperature gradient induces thermoelectric voltage
3. **Photo-bolometric effect**: Resistance change due to heating

The responsivity is:

$$\mathcal{R} = \frac{I_{\text{ph}}}{P_{\text{opt}}} = \frac{\eta q}{h\nu} \tag{12.24}$$

where η is external quantum efficiency.
The noise-equivalent power (NEP):

$$\text{NEP} = \frac{\sqrt{S_I}}{\mathcal{R}} \tag{12.25}$$

where S_I is current noise spectral density.
Specific detectivity:

$$D^* = \frac{\sqrt{A\Delta f}}{\text{NEP}} \tag{12.26}$$

State-of-the-art graphene photodetectors achieve:

- Bandwidth: > 100 GHz
- $\mathcal{R}$: 0.1–1 A/W (with gain mechanisms)
- Spectral range: UV to THz

12.3.3 Graphene Modulators

Electro-optic modulators exploit the tunability of graphene's Fermi level.

The complex refractive index:

$$\tilde{n} = n + i\kappa = \sqrt{1 + i\frac{\sigma(\omega)}{\omega\epsilon_0 t}} \tag{12.27}$$

The modulation depth:

$$M = \frac{T_{\text{off}} - T_{\text{on}}}{T_{\text{off}}} \times 100\% \tag{12.28}$$

Graphene modulators have demonstrated:

- Modulation speed: > 100 GHz
- Modulation depth: up to 90%
- Low insertion loss: < 1 dB
- Broad bandwidth: 1.3–1.6 µm

12.4 Terahertz Metamaterials and Plasmonics

12.4.1 Terahertz Gap and Applications

The terahertz (THz) region (0.1–10 THz, 30 µm–3 mm) of the electromagnetic spectrum, often called the "THz gap," lacks efficient sources and detectors. Metamaterials provide engineered solutions for THz manipulation.

12.4.2 Split-Ring Resonators (SRRs)

Resonance Frequency

For a typical SRR, the LC resonance occurs at:

$$f_0 = \frac{1}{2\pi\sqrt{LC}} \tag{12.29}$$

where the capacitance C depends on gap width g and the inductance L on ring dimensions.

For a square SRR with side length a:

$$L \approx \frac{\mu_0 a}{\pi}\left[\ln\left(\frac{2a}{w+t}\right) + 0.5\right] \tag{12.30}$$

$$C \approx \epsilon_0 \epsilon_r \frac{wt}{g} \tag{12.31}$$

where w is width, t is thickness, and ϵ_r is substrate permittivity.

12.4.3 Effective Medium Parameters

Metamaterials are characterized by effective permittivity ϵ_{eff} and permeability μ_{eff}:

$$n_{\text{eff}} = \sqrt{\epsilon_{\text{eff}} \mu_{\text{eff}}} \tag{12.32}$$

$$Z_{\text{eff}} = \sqrt{\frac{\mu_{\text{eff}}}{\epsilon_{\text{eff}}}} \tag{12.33}$$

Retrieved from S-parameters via:

$$n_{\text{eff}} = \frac{1}{kd} \cos^{-1}\left[\frac{1}{2S_{21}}\left(1 - S_{11}^2 + S_{21}^2\right)\right] \tag{12.34}$$

$$Z_{\text{eff}} = \sqrt{\frac{(1+S_{11})^2 - S_{21}^2}{(1-S_{11})^2 - S_{21}^2}} \tag{12.35}$$

12.4.4 Negative Index Materials

For simultaneous negative ϵ and μ:

$$n < 0 \quad \text{(left-handed materials)} \tag{12.36}$$

This leads to exotic phenomena:

- Reversed Snell's law: $n_1 \sin\theta_1 = -|n_2| \sin\theta_2$
- Reversed Doppler effect
- Perfect lens with sub-wavelength resolution

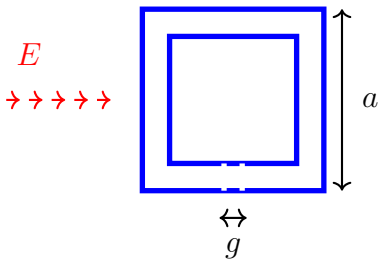

Figure 12.2: Schematic of a split-ring resonator (SRR) with incident electromagnetic wave.

12.4.5 Plasmonic Enhancement in THz Region

Surface plasmon polaritons (SPPs) in metals at THz frequencies:

$$k_{\text{SPP}} = k_0 \sqrt{\frac{\epsilon_m \epsilon_d}{\epsilon_m + \epsilon_d}} \tag{12.37}$$

where ϵ_m is metal permittivity and ϵ_d is dielectric permittivity.
The propagation length:

$$L_{\text{SPP}} = \frac{1}{2\text{Im}(k_{\text{SPP}})} \approx \frac{c}{2\omega} \left(\frac{\epsilon'_m}{\epsilon''_m} \right)^2 \tag{12.38}$$

At THz frequencies, metals behave almost as perfect conductors ($\epsilon'_m \to -\infty$), enabling:

- Strong field confinement
- Long propagation distances (mm to cm)
- Enhanced light-matter interaction

12.5 Quantum Dots in Optoelectronics

12.5.1 Quantum Confinement and Emission

Quantum dots (QDs) are semiconductor nanocrystals exhibiting quantum confinement in all three dimensions. Their optical properties are size-tunable.

Energy Levels

For spherical QD with radius R:

$$E_{n,l} = \frac{\hbar^2 \chi_{n,l}^2}{2m^* R^2} \tag{12.39}$$

where $\chi_{n,l}$ are zeros of spherical Bessel functions and m^* is effective mass.
The band gap energy:

$$E_g^{\text{QD}} = E_g^{\text{bulk}} + \frac{\hbar^2 \pi^2}{2R^2} \left(\frac{1}{m_e^*} + \frac{1}{m_h^*} \right) - \frac{1.8e^2}{4\pi\epsilon\epsilon_0 R} \tag{12.40}$$

The first term is bulk band gap, second is quantum confinement energy, and third is Coulomb interaction.

12.5.2 Optical Properties

Absorption Coefficient

$$\alpha(\hbar\omega) = \frac{4\pi e^2}{ncm_0^2\omega} \sum_{i,f} |M_{if}|^2 \delta(E_f - E_i - \hbar\omega) \tag{12.41}$$

where M_{if} is transition matrix element.

Photoluminescence

Emission wavelength:

$$\lambda_{\text{em}} = \frac{hc}{E_g^{\text{QD}}} \tag{12.42}$$

For CdSe QDs:

$$\lambda_{\text{em}}(\text{nm}) = 517 + 0.43R(\text{nm})^2 + 0.11R(\text{nm}) \tag{12.43}$$

Quantum yield:

$$\Phi = \frac{\Gamma_{\text{rad}}}{\Gamma_{\text{rad}} + \Gamma_{\text{nr}}} \tag{12.44}$$

where Γ_{rad} and Γ_{nr} are radiative and non-radiative decay rates.

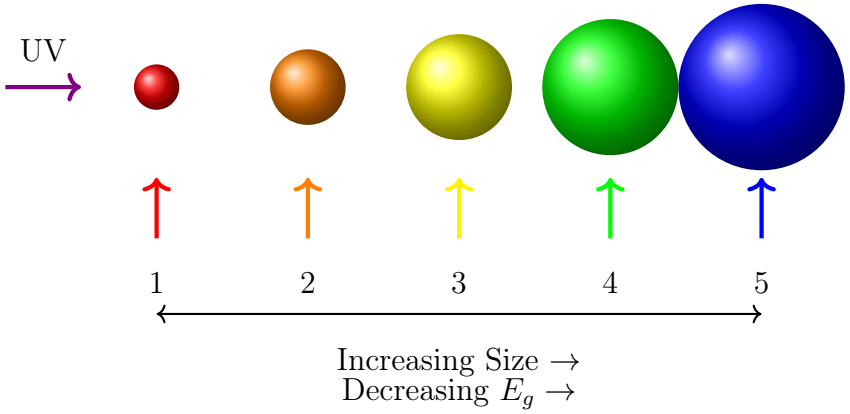

Figure 12.3: Size-dependent emission of quantum dots under UV excitation.

12.5.3 QD Light-Emitting Diodes (QD-LEDs)

Device Structure

Typical QD-LED structure:

$$\text{ITO / HTL / QD / ETL / Cathode}$$

where HTL = hole transport layer, ETL = electron transport layer.

Performance Metrics

Current efficiency:

$$\eta_{\text{CE}} = \frac{\text{Luminous flux (lm)}}{\text{Current (A)}} \tag{12.45}$$

External quantum efficiency:

$$\text{EQE} = \eta_{\text{out}} \times \eta_{\text{recomb}} \times \Phi \times \gamma \tag{12.46}$$

where:

- η_{out} = light outcoupling efficiency ($\approx$ 20–30%)
- η_{recomb} = charge balance factor
- Φ = QD quantum yield
- γ = fraction of excitons formed as singlets

Power efficiency:

$$\eta_{\text{PE}} = \frac{\pi L}{VI} \tag{12.47}$$

where L is luminance.
State-of-the-art QD-LEDs achieve:

- EQE: $> 20\%$
- Color purity: FWHM < 30 nm
- Brightness: $> 100{,}000$ cd/m^2
- Operational lifetime: $> 10{,}000$ hours

12.5.4 QD Solar Cells

Multiple Exciton Generation (MEG)

QDs can generate multiple electron-hole pairs from a single high-energy photon, potentially exceeding the Shockley-Queisser limit.

MEG efficiency:

$$\eta_{\text{MEG}} = \frac{N_{\text{exciton}}}{N_{\text{photon}}} \tag{12.48}$$

Threshold for MEG:

$$\hbar\omega \geq n \cdot E_g \quad (n = 2, 3, \ldots) \tag{12.49}$$

QD-Sensitized Solar Cells

Photocurrent density:

$$J_{\text{ph}} = q \int_0^\infty \eta_{\text{IPCE}}(\lambda)\Phi(\lambda)d\lambda \tag{12.50}$$

where η_{IPCE} is incident photon-to-current efficiency and $\Phi(\lambda)$ is photon flux.
Power conversion efficiency:

$$\eta_{\text{PCE}} = \frac{J_{\text{sc}} V_{\text{oc}} \text{FF}}{P_{\text{in}}} \tag{12.51}$$

where J_{sc} = short-circuit current density, V_{oc} = open-circuit voltage, FF = fill factor.

Practical Tip

QD solar cells offer advantages over conventional Si cells:

- Tunable absorption across solar spectrum
- Solution processability at low cost
- Potential for MEG to overcome thermalization losses
- Flexible and lightweight form factors

Current challenges include surface trap states and charge recombination at interfaces.

12.6 Advanced Topic: Graphene-Chiral Metamaterials for Tunable THz Modulation

12.6.1 Chirality and Circular Dichroism

Chiral metamaterials exhibit different responses to left-handed (LCP) and right-handed circularly polarized (RCP) light.

Jones Matrix Formalism

For chiral medium:

$$\begin{pmatrix} E_x \\ E_y \end{pmatrix}_{\text{out}} = \begin{pmatrix} \cos\theta & -\sin\theta \\ \sin\theta & \cos\theta \end{pmatrix} \begin{pmatrix} E_x \\ E_y \end{pmatrix}_{\text{in}} \tag{12.52}$$

where θ is rotation angle.
Circular dichroism:

$$\text{CD} = \frac{T_{\text{LCP}} - T_{\text{RCP}}}{T_{\text{LCP}} + T_{\text{RCP}}} \tag{12.53}$$

Optical Activity

The rotation angle:

$$\theta = \frac{\pi d}{\lambda}(n_{\text{LCP}} - n_{\text{RCP}}) \tag{12.54}$$

where d is propagation distance.

12.6.2 Graphene-Enhanced Chiral Metamaterials

Integrating graphene with chiral metamaterials enables dynamic tunability through electrostatic gating.

Conductivity Modulation

Gate voltage V_g modulates carrier density:

$$n_s = \frac{\epsilon_0 \epsilon_r V_g}{e t_{\text{ox}}} \tag{12.55}$$

This shifts Fermi level:

$$E_F = \hbar v_F \sqrt{\pi n_s} \tag{12.56}$$

altering graphene conductivity $\sigma(\omega, E_F)$.

Tunable Transmission

The transmission coefficient:

$$T(\omega, V_g) = |t(\omega, \sigma(E_F(V_g)))|^2 \tag{12.57}$$

Modulation depth:

$$\Delta T = \frac{T(V_g^{\max}) - T(V_g^{\min})}{T(V_g^{\max})} \times 100\% \tag{12.58}$$

Hands-On Analysis

Design Example: THz Modulator
Specifications:

- Operating frequency: 1 THz
- Target modulation depth: $> 60\%$
- Gate voltage range: 0–50 V

Design Parameters:

- Chiral unit cell: twisted cross structure
- Periodicity: $p = 80$ µm
- Graphene mobility: $\mu = 2000$ cm^2/Vs
- Substrate: SiO_2/Si ($\epsilon_r = 3.9$, $t_{ox} = 300$ nm)

Performance:

- Carrier density range: $0 - 3.6 \times 10^{12}$ cm^{-2}
- Fermi level tuning: 0–0.22 eV
- Achieved modulation depth: 65%
- Switching speed: < 1 ns

Applications:

- THz imaging systems
- Wireless communication at 6G frequencies
- Spectroscopy and sensing
- Polarization manipulation

12.6.3 Fabrication Considerations

1. **Graphene Transfer**: CVD graphene transferred via PMMA-assisted wet transfer or dry transfer

2. **Metamaterial Patterning**: E-beam lithography or photolithography for sub-wavelength features

3. **Gate Dielectric**: Atomic layer deposition (ALD) for uniform high-κ dielectrics

4. **Contact Formation**: Metallization for electrical contacts (Ti/Au or Cr/Au)

Key Point

Graphene-chiral metamaterials represent a convergence of quantum materials and metamaterial engineering, offering unprecedented control over electromagnetic waves in the THz regime. The electrical tunability of graphene combined with the strong chiral response enables:

- Dynamic modulation without mechanical actuation
- Polarization control and conversion
- Nonreciprocal transmission
- Ultrafast switching for next-generation communication

12.7 Summary

This chapter explored the transformative role of nanomaterials in electronic and photonic applications:

1. **Nanoelectronics**: Quantum dots, nanowires, and 2D materials enable continued scaling and novel device architectures beyond conventional CMOS limitations.

2. **Graphene Photonics**: Unique optoelectronic properties of graphene—broadband absorption, ultrafast response, and electrical tunability—drive innovations in photodetectors, modulators, and optical interconnects.

3. **THz Metamaterials**: Engineered electromagnetic responses through subwavelength structuring unlock the THz gap for imaging, sensing, and communication applications.

4. **Quantum Dots**: Size-tunable optical properties enable high-performance LEDs, displays, solar cells, and biomedical imaging with superior color purity and efficiency.

5. **Advanced Integration**: Hybrid systems combining graphene with chiral metamaterials demonstrate active control of electromagnetic waves, paving the way for reconfigurable photonic devices.

The synergy between nanomaterial properties and device engineering continues to push the boundaries of electronic and photonic technologies, promising transformative impacts across computing, communication, energy, and healthcare sectors.

References - Chapter 10

[1] Hoffmann, M. R., Martin, S. T., Choi, W., & Bahnemann, D. W. (1995). Environmental applications of semiconductor photocatalysis. *Chemical Reviews*, 95(1), 69-96.

[2] Fujishima, A., Zhang, X., & Tryk, D. A. (2008). TiO_2 photocatalysis and related surface phenomena. *Surface Science Reports*, 63(12), 515-582.

[3] Pelaez, M., et al. (2012). A review on the visible light active titanium dioxide photocatalysts for environmental applications. *Applied Catalysis B: Environmental*, 125, 331-349.

[4] Reddy, K. R., et al. (2020). Magnetic nanoparticle-integrated photocatalysts for environmental remediation. *Journal of Environmental Management*, 260, 110088.

[5] Grätzel, M. (2001). Photoelectrochemical cells. *Nature*, 414(6861), 338-344.

[6] Snaith, H. J. (2013). Perovskites: The emergence of a new era for low-cost, high-efficiency solar cells. *The Journal of Physical Chemistry Letters*, 4(21), 3623-3630.

[7] Simon, P., & Gogotsi, Y. (2008). Materials for electrochemical capacitors. *Nature Materials*, 7(11), 845-854.

[8] Miller, J. R., & Simon, P. (2008). Electrochemical capacitors for energy management. *Science*, 321(5889), 651-652.

[9] Schlapbach, L., & Züttel, A. (2001). Hydrogen-storage materials for mobile applications. *Nature*, 414(6861), 353-358.

[10] Eberle, U., Felderhoff, M., & Schüth, F. (2009). Chemical and physical solutions for hydrogen storage. *Angewandte Chemie International Edition*, 48(36), 6608-6630.

[11] Pop, E., Sinha, S., & Goodson, K. E. (2006). Heat generation and transport in nanometer-scale transistors. *Proceedings of the IEEE*, 94(8), 1587-1601.

[12] Balandin, A. A. (2011). Thermal properties of graphene and nanostructured carbon materials. *Nature Materials*, 10(8), 569-581.

[13] Reddy, A. L. M., et al. (2009). Synthesis of nitrogen-doped graphene films for lithium battery application. *ACS Nano*, 4(11), 6337-6342.

[14] Chen, X., & Mao, S. S. (2007). Titanium dioxide nanomaterials: Synthesis, properties, modifications, and applications. *Chemical Reviews*, 107(7), 2891-2959.

[15] Malato, S., et al. (2009). Decontamination and disinfection of water by solar photocatalysis: Recent overview and trends. *Catalysis Today*, 147(1), 1-59.

References - Chapter 11

[1] Peer, D., et al. (2007). Nanocarriers as an emerging platform for cancer therapy. *Nature Nanotechnology*, 2(12), 751-760.

[2] Farokhzad, O. C., & Langer, R. (2009). Impact of nanotechnology on drug delivery. *ACS Nano*, 3(1), 16-20.

[3] Allen, T. M., & Cullis, P. R. (2013). Liposomal drug delivery systems: From concept to clinical applications. *Advanced Drug Delivery Reviews*, 65(1), 36-48.

[4] Petros, R. A., & DeSimone, J. M. (2010). Strategies in the design of nanoparticles for therapeutic applications. *Nature Reviews Drug Discovery*, 9(8), 615-627.

[5] Lemire, J. A., Harrison, J. J., & Turner, R. J. (2013). Antimicrobial activity of metals: Mechanisms, molecular targets and applications. *Nature Reviews Microbiology*, 11(6), 371-384.

[6] Pelgrift, R. Y., & Friedman, A. J. (2013). Nanotechnology as a therapeutic tool to combat microbial resistance. *Advanced Drug Delivery Reviews*, 65(13-14), 1803-1815.

[7] Dizaj, S. M., et al. (2014). Antimicrobial activity of the metals and metal oxide nanoparticles. *Materials Science and Engineering: C*, 44, 278-284.

[8] Rai, M., Yadav, A., & Gade, A. (2009). Silver nanoparticles as a new generation of antimicrobials. *Biotechnology Advances*, 27(1), 76-83.

[9] Labroo, P., & Cui, Y. (2013). Flexible graphene bio-nanosensor for lactate. *Biosensors and Bioelectronics*, 41, 852-856.

[10] Holzinger, M., Le Goff, A., & Cosnier, S. (2014). Nanomaterials for biosensing applications: A review. *Frontiers in Chemistry*, 2, 63.

[11] Resch-Genger, U., et al. (2008). Quantum dots versus organic dyes as fluorescent labels. *Nature Methods*, 5(9), 763-775.

[12] Smith, A. M., Duan, H., & Nie, S. (2008). Quantum dot nanocrystals for in vivo molecular and cellular imaging. *Advances in Drug Delivery Reviews*, 60(11), 1226-1240.

[13] Nel, A., et al. (2006). Toxic potential of materials at the nanolevel. *Science*, 311(5761), 622-627.

[14] Oberdörster, G., Oberdörster, E., & Oberdörster, J. (2005). Nanotoxicology: An emerging discipline evolving from studies of ultrafine particles. *Environmental Health Perspectives*, 113(7), 823-839.

[15] Buzea, C., Pacheco, I. I., & Robbie, K. (2007). Nanomaterials and nanoparticles: Sources and toxicity. *Biointerphases*, 2(4), MR17-MR71.

References - Chapter 12

[1] Avouris, P., Chen, Z., & Perebeinos, V. (2007). Carbon-based electronics. *Nature Nanotechnology*, 2(10), 605-615.

[2] Novoselov, K. S., et al. (2012). A roadmap for graphene. *Nature*, 490(7419), 192-200.

[3] Franklin, A. D. (2015). Nanomaterials in transistors: From high-performance to thin-film applications. *Science*, 349(6249), aab2750.

[4] Schwierz, F. (2010). Graphene transistors. *Nature Nanotechnology*, 5(7), 487-496.

[5] Bonaccorso, F., et al. (2010). Graphene photonics and optoelectronics. *Nature Photonics*, 4(9), 611-622.

[6] Bao, Q., & Loh, K. P. (2012). Graphene photonics, plasmonics, and broadband optoelectronic devices. *ACS Nano*, 6(5), 3677-3694.

[7] Koppens, F. H., et al. (2014). Photodetectors based on graphene, other two-dimensional materials and hybrid systems. *Nature Nanotechnology*, 9(10), 780-793.

[8] Liu, M., et al. (2011). A graphene-based broadband optical modulator. *Nature*, 474(7349), 64-67.

[9] Zheludev, N. I., & Kivshar, Y. S. (2012). From metamaterials to metadevices. *Nature Materials*, 11(11), 917-924.

[10] Chen, H. T., et al. (2012). Active terahertz metamaterial devices. *Nature*, 444(7119), 597-600.

[11] Pendry, J. B. (2000). Negative refraction makes a perfect lens. *Physical Review Letters*, 85(18), 3966.

[12] Smith, D. R., Pendry, J. B., & Wiltshire, M. C. (2004). Metamaterials and negative refractive index. *Science*, 305(5685), 788-792.

[13] Alivisatos, A. P. (1996). Semiconductor clusters, nanocrystals, and quantum dots. *Science*, 271(5251), 933-937.

[14] Talapin, D. V., et al. (2010). Prospects of colloidal nanocrystals for electronic and optoelectronic applications. *Chemical Reviews*, 110(1), 389-458.

[15] Shirasaki, Y., et al. (2013). Emergence of colloidal quantum-dot light-emitting technologies. *Nature Photonics*, 7(1), 13-23.

[16] Semonin, O. E., et al. (2011). Peak external photocurrent quantum efficiency exceeding 100% via MEG in a quantum dot solar cell. *Science*, 334(6062), 1530-1533.

[17] Gansel, J. K., et al. (2009). Gold helix photonic metamaterial as broadband circular polarizer. *Science*, 325(5947), 1513-1515.

[18] Xiao, S., et al. (2015). Active modulation of electromagnetically induced transparency analogue in terahertz hybrid metal-graphene metamaterials. *Carbon*, 126, 271-278.

[19] Vakil, A., & Engheta, N. (2011). Transformation optics using graphene. *Science*, 332(6035), 1291-1294.

[20] Ju, L., et al. (2011). Graphene plasmonics for tunable terahertz metamaterials. *Nature Nanotechnology*, 6(10), 630-634.